Universite du Quebec
Institut National de la Recherche Scientifique
Centre Energie, Materiaux et Telecommunications

Research on the effect of heterobimetallic sites nitrogen-oxygen doping catalyst for nitrogen reduction reaction.

Par

Na Xu

These presentee pour l'obtention du grade
de Philosophiae Doctor (Ph.D.)
en sciences de l'énergie et des matériaux

Jury d'évaluation

Président du jury et examinateur interne	Prof. Daniel Guay INRS-EMT
Examinateur externe	Prof. Makhsud Saidaminov University of Victoria
Examinateur externe	Prof. Nhat Truong Nguyen Concordia University
Directeur de recherche	Prof. Federico Rosei University of Trieste
Directeur de recherche	Prof. Shuhui Sun INRS-EMT

ACKNOWLEDGEMENTS

Upon the completion of the thesis, I would like to thank all people who have encouraged and supported me during the past seven years. First and foremost, I would like to show my sincere gratitude to my supervisor Prof. Federico Rosei, and co-supervisor Prof. Chenglin Yan for their continual support, patience, motivation, immense knowledge, and guidance in the research. Prof. Federico Rosei offered an enabling and supportive research environment for me to finish my PhD study in INRS and provided me with the chance to participate in the academic organizations where I have developed my social skills. During my two-year academic exchange in China, Prof. Chenglin Yan guided me in my scientific research and academic direction and provided me with an excellent experimental and office environment at Soochow University. The professional guidance and encouragement in my PhD study and the valuable advice for my future academic career from both Prof. Federico Rosei and Prof. Chenglin Yan would be a great fortune in my life and will boost my confidence in my future career. I feel very lucky to have them as my supervisor and it is my honor to accomplish my PhD study with their help.

Secondly, I`m very grateful to my husband Bluce Li, and my parents. During the 7 years of studying in Canada, we lived in two countries in the eastern and western hemispheres. The 12-hour time difference made it difficult for us to contact. But they have been supporting me with their selfless love and firm trust to help me go through the difficult moments in my life. I would also like to thank my best friend as well as my roommate Yuting Lei. She has given me a lot of help in life and scientific research and has been by my side for 6 years. I would also like to thank my two team leaders Dr. Daniele Benetti and Prof. Tao Qian who are like friends and teachers. They have given me a lot of help in both scientific research and life. Daniele encouraged me to talk in Canada and gave me a lot of help in improving my English speaking. He also gave me a lot of help in revising the manuscript. Prof. Tao Qian from Suzhou University has inspired me a lot in experiments and gave me a lot of inspiration when I encountered a bottleneck in my experiments.

I would also like to thank my administrative supervisor Prof. Shuhui Sun for his help and suggestions and thank the group members in NanoFemtoLab at INRS-EMT and Soochow University, Dr. Mengfan Wang, Dr. Lei Jin, Dr. Sisi Liu, Dr. Daling Cui, Dr. Xin Liu. Dr. Li Shi, Dr. Tingzhou Yang, Dr. Faying Li, Dr. Min Zhang, Dr. Yuanfu Zhang, Chao Wang, Qiyang Cheng, and Yanzheng He for their kind help and assistance in the lab and the useful comments during the group meetings. I feel lucky to know a lot of friends to share life and feelings during the past

years, particularly Xiaoying Zheng, Ting Yu, Wanting He, Xin Tong, Jiyun Chen, Xianglei Liu, Cheng Jiang, and many others. Many thanks to the administration and technician staff at INRS-EMT and characterization technicians at Université de Montréal and Université du Québec à Montréal.

I would like to thank Prof. Daniel Guay, Prof. Makhsud Saidaminov and Prof. Nhat Truong Nguyen for being the members of my thesis committee and offering their precious comments and valuable time.

RÉSUMÉ

La réaction de réduction électrocatalytique de l'azote (NRR) en tant qu'approche alternative au procédé Haber-Bosch, à forte intensité énergétique, pour la synthèse artificielle de l'ammoniac a suscité une grande attention. Cependant, le processus NRR ne se limite pas à l'adsorption, mais également au clivage et à l'hydrogénation ultérieurs de l'azote, qui posent encore de grands défis. Il existe un besoin urgent d'un électrocatalyseur hautement actif doté de multiples fonctions pour réduire considérablement la résistance à la réaction et favoriser la synthèse d'ammoniac dans l'environnement. Dans cette thèse, nous avons mené trois projets visant à améliorer l'efficacité du NRR, notamment une stratégie de confinement de l'azote obtenue par gravure plasma, le dopage de l'oxygène dans du carbone dopé à l'azote en tant qu'hétéroatome secondaire pour déclencher un effet de promotion électronique synergique, ainsi que la proposition de sites FeCo hétérobimétalliques asymétriques pour rompre les relations d'échelle dans NRR.

Dans le premier projet, nous avons utilisé la gravure au plasma pour construire in situ un grand nombre de vides dans le plan basal du catalyseur. Les défauts ressemblant à des vides induiraient une hétérogénéité de surface et amélioreraient efficacement les interactions de Van der Waals entre l'électrocatalyseur et les molécules d'azote, déclenchant ainsi un transfert directionnel d'azote vers le catalyseur. Les nanobulles d'azote venant en sens inverse peuvent être efficacement capturées par les vides, fournissant ainsi un apport abondant de réactifs et stimulant ainsi l'ensemble du processus NRR. Comme prévu, le catalyseur gravé au plasma de preuve de concept offre un taux de rendement en ammoniac supérieur de 35,24 μg h^{-1} mg^{-1} et une efficacité Faradaïque exceptionnelle de 53,99 % à -0,3 V par rapport à une électrode à hydrogène réversible.

Dans le deuxième projet, en dopant l'oxygène dans du carbone dopé à l'azote en tant qu'hétéroatome secondaire, un effet de promotion électronique synergique est déclenché pour stimuler la synthèse d'ammoniac ambiant. La structure électronique et la polarité des atomes de carbone adjacents sont encore optimisées, réduisant considérablement la barrière énergétique du processus global de réduction de l'azote. Comme prévu, le catalyseur au carbone dopé à l'azote, enrichi en oxygène et dopé à l'azote, offre des performances bien améliorées par rapport à son homologue, avec un taux de rendement en ammoniac de 67,3 μg h^{-1} mg^{-1} et une efficacité Faradaïque correspondante de 36,2 % à -0,2 V par rapport à une électrode à hydrogène réversible.

Dans le troisième projet, nous avons proposé des sites FeCo hétérobimétalliques asymétriques pour rompre les relations d'échelle dans le NRR et stimuler la synthèse d'ammoniac ambiant. Selon les calculs de la théorie fonctionnelle de la densité, les sites dimères hétéronucléaires FeCo présentant la surface polarisée avec des sites multiélectroniques permettent un affaiblissement de la liaison N≡N et une activation maximisée de N_2. L'optimisation des énergies d'adsorption de certains intermédiaires devient ainsi réalisable, contribuant à réduire considérablement la barrière énergétique du processus global de réduction de l'azote. Comme prévu, le catalyseur de validation de principe offre un taux de rendement en ammoniac supérieur de 70,11 μg h^{-1} mg^{-1} avec une efficacité faradique correspondante de 32,16 % à -0,2 V par rapport à une électrode à hydrogène réversible.

Mots-clés: gravure au plasma, confinement de N_2, défauts de type vide, sites hétérobimétalliques asymétriques, réaction multi-intermédiaire, effet promoteur électronique synergique, dopage à l'oxygène, électrocatalyseur sans métal, réaction de réduction de l'azote, synthèse d'ammoniac.

ABSTRACT

Electrocatalytic nitrogen reduction reaction (NRR) as an alternative approach to the energy-intensive Haber-Bosch process for artificial ammonia synthesis has attracted extensive attention. However, the NRR process is more than just adsorption, but also subsequent nitrogen cleavage and hydrogenation, which still pose a great challenge. There is an urgent need for a highly active electrocatalyst with multiple functions to greatly reduce reaction resistance and promote environmental ammonia synthesis. In this thesis, we conducted three projects to improve NRR efficiencies including nitrogen confining strategy achieved by plasma etching, doping oxygen into nitrogen-doped carbon as secondary heteroatom to trigger synergistic electronic promoting effect as well as proposing asymmetrical heterobimetallic FeCo sites to break scaling relations in NRR.

In the first project, we used plasma etching to in situ construct a large number of voids in the basal plane of the catalyst. The void-like defects would induce surface heterogeneity and effectively enhance the van der Waals interactions between the electrocatalyst and the nitrogen molecules, triggering directional nitrogen transfer toward the catalyst. The oncoming nitrogen nanobubbles can be effectively captured by the voids, providing abundant reactant supply and thus boosting the whole NRR process. As expected, the proof-of-concept plasma etched catalyst delivers a superior ammonia yield rate of 35.24 μg h^{-1} mg^{-1} and an outstanding Faradaic efficiency of 53.99 % at -0.3 V versus reversible hydrogen electrode.

In the second project, through doping oxygen into nitrogen-doped carbon as the secondary heteroatom, a synergistic electronic promoting effect is triggered to boost ambient ammonia synthesis. The electronic structure and the polarity of adjacent carbon atoms are further optimized, significantly lowering the energy barrier of the overall nitrogen reduction process. As expected, the proof-of-concept oxygen-enriched nitrogen-doped carbon catalyst delivers a much-enhanced performance with respect to the counterpart, with an ammonia yield rate of 67.3 μg h^{-1} mg^{-1} and a corresponding Faradaic efficiency of 36.2% at -0.2 V versus reversible hydrogen electrode.

In the third project, we proposed asymmetrical heterobimetallic FeCo sites to break scaling relations in NRR and boost ambient ammonia synthesis. According to the density functional theory calculations, the heteronuclear FeCo dimer sites featuring the polarized surface with multielectron sites enable the weakening of N≡N bond and maximized activation of N_2. The optimization of the adsorption energies of certain intermediates thus becomes feasible,

contributing to significantly reduced energy barrier of the overall nitrogen reduction process. As expected, the proof-of-concept catalyst delivers a superior ammonia yield rate of 70.11 μg h^{-1} mg^{-1} with a corresponding Faradaic efficiency of 32.16 % at -0.2 V versus reversible hydrogen electrode.

Keywords: plasma etching, N_2 confining, void-like defects, asymmetrical heterobimetallic sites, multi-intermediate reaction, synergistic electronic promoting effect, oxygen doping, metal-free electrocatalyst, nitrogen reduction reaction, ammonia synthesis.

TABLE OF CONTENTS

ACKNOWLEDGEMENTS I
RÉSUMÉ III
ABSTRACT V
TABLE OF CONTENTS VII
LIST OF FIGURES IX
LIST OF TABLES XIII
LIST OF SYMBOLS AND CHEMICAL FORMULA XV
LIST OF ABBREVIATIONS AND ACRONYMS XIX
1 INTRODUCTION 1
1.1 Background and Motivations 1
1.2 Nitrogen reduction reaction mechanism 3
1.3 Research strategies for electrocatalytic NRR 6
1.3.1 Guidelines for NRR experiments. 6
1.3.2 Reactor configurations 8
1.3.3 Electrochemical measurements 9
1.3.4 Ammonia detection 9
1.3.5 Activity 16
1.4 NRR catalyst 17
1.4.1 metal-based electrocatalysts 17
1.4.2 non-metal-based electrocatalysts 21
1.4.3 carbon-based electrocatalysts 21
1.5 Challenges in electrocatalytic NRR 25
1.6 Strategies for NRR 26
1.6.1 Doping 26
1.6.2 Single Atom Catalysts 27
1.6.3 Surface Modification 28
1.7 Thesis Objectives and Organizations 29
1.7.1 Thesis objectives 29
1.7.2 Thesis organizations 30
2 EXPERIMENTAL 33
2.1 Chemicals and Materials 33
2.2 Synthesis of catalyst 33
2.2.1 Synthesis of catalyst WFeNC and P-WFeNC 33
2.2.2 Synthesis of catalyst FeNC 34

2.2.3 Synthesis of catalyst FeCoNC *34*
2.2.4 Synthesis of catalyst OENC, ONC, and NC *34*
2.3 CHARACTERIZATIONS 35
2.3.1 Physical characterizations *35*
2.3.2 Electrochemical characterizations *36*
2.4 THEORETICAL CALCULATIONS AND MOLECULAR DYNAMICS 38
2.4.1 DFT computational method and model. *38*
2.4.2 Molecular dynamics (MD) simulations model and method *39*

3 CONFINING NITROGEN NANOBUBBLES WITHIN PLASMA ETCHED VOIDS 40
3.1 INTRODUCTION 41
3.2 RESULTS AND DISCUSSIONS 42
3.3 CONCLUSION 50
3.4 SUPPORTING INFORMATION 50

4 OENC CATALYST WITH SYNERGISTIC ELECTRON PROMOTION FOR NRR 67
4.1 INTRODUCTION 68
4.2 RESULTS AND DISCUSSION 69
4.3 CONCLUSION 80
4.4 SUPPORTING INFORMATION 81

5 BREAKING SCALING RELATIONS IN NRR WITH FECONC CATALYST 87
5.1 INTRODUCTION 88
5.2 RESULTS AND DISCUSSION 89
5.3 CONCLUSION 98
5.4 SUPPORTING INFORMATION 99

6 CONCLUSION 107
6.1 CONCLUSION 107
6.2 PERSPECTIVES 109

7 BIBLIOGRAPHIE 111
8 SOMMAIRE RÉCAPITULATIF 125

LIST OF FIGURES

Figure 1.1 A Schematic Diagram of an Industrial Plant for the Production of Ammonia via the Haber-Bosch Process. Ref.[6] 2

Figure 1.2 Timeline of theoretical and experimental breakthroughs in electrocatalytic NRR for ammonia synthesis. 3

Figure 1.3 The possible reaction mechanism of NRR including dissociative pathway, associative distal, and alternating pathways. * represents an adsorption site. Ref. [26] 5

Figure 1.4 Guidelines to conduct electrochemical NRR experiments for ammonia generation. Here, cyclic voltammetry (CV), linear sweep voltammetry (LSV). Ref.[27] 6

Figure 1.5 Multiple cell configurations for NRR in a schematic view under standard conditions (RE stands for the reference electrode, WE stand for the working electrode, and CE stands for the counter electrode). Ref. [29] 9

Figure 1.6 (a) Schematic illustration of UV-vis spectrophotometer for double beam instrument. Ref. [31] The tungsten lamp and D2 lamp emit visible and ultraviolet lights, respectively. The light is directed to the monochromator, which determines the wavelength of the sample. Adapted with permission from Ref. [32] (b) UV-vis spectra of standard solutions with different concentrations, and (c) corresponding calibration curve. The absorbance values for the calibration curve were obtained from a wavelength of 655 nm. Inset of (c) is the photograph of the standard solutions after 2 h of reaction with indophenol reagent. Adapted with permission from Ref. [33] (d) UV-vis spectra of the standard solution with different concentrations, and (e) corresponding calibration curve. The absorbance values for the calibration curve were obtained from the wavelength of 420 nm. Inset of (e) is the photograph of the standard solution after 20 min of reaction with Nessler's reagent. Adapted with permission from Ref. [34] 12

Figure 1.7 (a) Absorption process in NMR. (b) Schematic representation of a typical NMR spectrometer. Ref. [39] (c) ^{1}H NMR spectra of $^{14}NH^{4+}$ and $^{15}NH^{4+}$ produced from NRR reaction using $^{14}N_2$ and $^{15}N_2$ isotopes. Ref. [33] (d) ^{1}H NMR spectra of 15NH4+ standard solutions with various concentrations and (e) corresponding calibration curve. Ref. [40] 14

Figure 1.8 (a)Synthetic strategy used for the synthesis of Fe(II)Cu(II)Fe(III)-LDH and Cu(II)Fe(III)-LDH. Ref. [46] (b)Schematic illustration of the preparation of Fe/Fe_3O_4/PC-800. Ref. [47] (c)Schematic illustration of the processes for preparing layered iron hydroxide series with the oxidation degree increased gradually. Ref. [48] (d)Synthetic Processes of Fe-N/C-CPs. Ref. [49] 19

FIGURE 1.9 (A) ILLUSTRATION OF THE FORMATION OF W-NO/NC. REF. [53] (B)SCHEMATIC DIAGRAM FOR THE PREPARATION OF WO_x/NPC. REF. [54] 20

FIGURE 1.10 (A) CORRESPONDING NH_3 PRODUCTION RATES AND FES MEASURED WITH VARIOUS CATALYSTS. (B) ATOMIC STRUCTURE DIAGRAM FOR NRR ON N_3 SITES (UP); AND (DOWN) FREE ENERGY DIAGRAM FOR NRR ON N_3 SITES IN N-DOPED CARBON. REF. [62] (C) SCHEMATIC ILLUSTRATION OF NPC PREPARATION. REF. [63] ...23

FIGURE 1.11 (A) CORRESPONDING NH_3 PRODUCT EFFICIENCY AND FES AT VARIOUS APPLIED POTENTIALS FOR O–G/CP. REF. [66] (B) SCHEMATIC REPRESENTATION OF O-CNTS MODEL WITH VARIOUS OXYGEN GROUPS AND N_2 INTERACTIONS. REF. [67] (C) THE NΞN BOND LENGTHS, C═O BOND LENGTHS, AND C═O VIBRATION FREQUENCIES BEFORE AND AFTER N_2 ADSORPTION. (D) PDOS FOR THE COMPLEX. REF. [68] 24

FIGURE 1.12 MECHANISTIC INSIGHTS INTO ELECTROCATALYTIC NRR. (A) PARTIAL POURBAIX DIAGRAM FOR THE N_2–H_2O SYSTEM. REF 72 (B) THE CALCULATED ONSET POTENTIALS FOR NRR AND HER OF DIFFERENT MATERIALS. REF. 73 25

FIGURE 3.1 SCHEMATIC ILLUSTRATION OF THE MECHANISM FOR IMPROVING THE ELECTROCHEMICAL AMMONIA SYNTHESIS BY CONFINING NITROGEN CLUSTERS WITHIN PLASMA ETCHED VOIDS. 42

FIGURE 3.2 (A) MD SIMULATION SNAPSHOTS OF N_2 DISTRIBUTION IN 0.1 M HCL AT 2, 3, 4, AND 5 NS. (B) THE AVERAGE DIAMETER OF THE REPRESENTATIVE N_2 CLUSTER VERSUS TIME IN THREE SEPARATE SIMULATIONS. .. 43

FIGURE 3.3 (A) SEM AND (B) TEM IMAGES OF WFENC. (C) SEM AND (D) TEM IMAGES OF P-WFENC. (E) HRTEM IMAGE AND CORRESPONDING ELEMENT MAPS OF P-WFENC. 44

FIGURE 3.4 (A) THE PORE SIZE DISTRIBUTION CURVES, (B) THE XRD PATTERNS, AND (C) THE RAMAN SPECTRA OF WFENC AND P-WFENC. 46

FIGURE 3.5 A SERIES OF OPTICAL IMAGES SHOWING THE N_2 DIFFUSION PROCESS ON THE SURFACE OF (A) WFENC AND (B) P-WFENC MEASURED BY THE CAPTIVE BUBBLE METHOD. (C) IN SITU XRD INTENSITY MAPS OF P-WFENC UNDER ELECTROCHEMICAL TESTING AS A FUNCTION OF TIME. (D) DOUBLE-LAYER CHARGING CURRENT PLOTTED AGAINST THE CV SCAN RATE FOR DIFFERENT ELECTRODES. 47

FIGURE 3.6 (A) NH_3 YIELD RATES AND (B) CORRESPONDING FARADAIC EFFICIENCIES OF WFENC AND P-WFENC AT VARIOUS POTENTIALS. 48

FIGURE 3.7 (A) THE UV-VIS ABSORPTION SPECTRA THE ELECTROLYTES UNDER DIFFERENT CONDITIONS. (B) ^1H NMR SPECTRA OF THE ELECTROLYTE TESTED WITH DIFFERENT FEEDING GASES. 49

FIGURE 3.8 (A) COMPARISON OF OUR RESULTS WITH STATE-OF-THE-ART ELECTROCATALYSTS IN TERMS OF NH_3 YIELD RATE AND FARADAIC EFFICIENCY. (B) THE NRR PERFORMANCE OF P-WFENC IN THE DURABILITY TEST. 49

FIGURE 4.1 (A) SCANNING ELECTRON MICROSCOPY IMAGE, (B) TRANSMISSION ELECTRON MICROSCOPY IMAGE, AND (C) CORRESPONDING ELEMENTAL MAPPING IMAGES OF ONC. 70

FIGURE 4.2 (A) XRD PATTERNS AND (B) RAMAN SPECTRA OF ONC AND NC. 71

FIGURE 4.3 (A) THE SURVEY XPS SPECTRA OF ONC AND NC. HIGH-RESOLUTION (B) C 1S, (C) N 1S AND (D) O 1S SPECTRA OF ONC AND NC. 72

FIGURE 4.4 N_2 SORPTION ISOTHERMS OF ONC AND NC. 73

FIGURE 4.5 CHRONOAMPEROMETRY RESULTS OF (A) ONC AND (B) NC TESTED IN 0.1 M HCL AT DIFFERENT APPLIED POTENTIALS. 75

FIGURE 4.6 (A) NH_3 YIELD RATES AND (B) CORRESPONDING FARADAIC EFFICIENCIES OF ONC AND NC MEASURED AT ALL GIVEN POTENTIALS. 76

FIGURE 4.7 H_2 SELECTIVITY OF ONC AND NC MEASURED AT ALL GIVEN POTENTIALS. 76

FIGURE 4.8 (A) NH_3 YIELD RATE AND FARADAIC EFFICIENCY OF ONC COMPARED WITH OTHER STATE-OF-THE-ARTS; DETAILED DATA ARE PROVIDED IN TABLE 4.1. (B) THE NRR PERFORMANCE IN THE DURABILITY TEST OF ONC. 77

FIGURE 4.9 (A) THE UV-VIS ABSORPTION SPECTRA OF THE ELECTROLYTES UNDER DIFFERENT CONDITIONS. (B) COMPARISON OF THE NH_3 YIELD RATE AND FARADAIC EFFICIENCY USING DIFFERENT FEEDING GASES FOR NRR AT -0.2 V VS. RHE AND OPEN-CIRCUIT POTENTIAL. (C) ^1H NMR SPECTRA OF THE NRR PRODUCTS USING DIFFERENT FEED GASES. (D) COMPARISON OF THE NH_3 YIELD RATE AND FARADAIC EFFICIENCY USING DIFFERENT FEEDING GASES FOR NRR AT -0.2 V VS. RHE EITHER BY COLORIMETRIC OR NMR METHOD. 79

FIGURE 5.1 CONFIGURATIONS OF (A) FENC AND (B) FECONC. (C) THE ELECTROSTATIC POTENTIAL OF FECONC. THE ELECTRON DENSITY DIFFERENCE AFTER NITROGEN ADSORBED AT (D) FENC AND (E) FECONC. (F) COMPARISON OF NITROGEN BOND LENGTH AFTER ADSORPTION AT THE CORRESPONDING ACTIVE SITE. 90

FIGURE 5.2 (A) FREE ENERGY OF AMMONIA SYNTHESIS ON FECONC AND FENC THROUGH THE ALTERNATING PATHWAY AND THE CORRESPONDING CONFIGURATIONS OF ADSORBATES ON FECONC. (B) FREE ENERGY OF AMMONIA SYNTHESIS ON FECONC AND FENC THROUGH THE DISTAL PATHWAY AND THE CORRESPONDING CONFIGURATIONS OF ADSORBATES ON FECONC. THE LIGHT BLUE, BLUE, GREEN, PINK, AND WHITE SPHERES REPRESENT C, N, FE, CO, AND H ATOMS, RESPECTIVELY. 91

FIGURE 5.3 (A) SCANNING ELECTRON MICROSCOPY IMAGE, (B) TRANSMISSION ELECTRON MICROSCOPY IMAGE, AND (C) ELEMENT MAPPINGS OF FECONC. (D) ABERRATION-CORRECTED HIGH-ANGLE ANNULAR DARK-FIELD SCANNING TRANSMISSION ELECTRON MICROSCOPY IMAGE OF FECONC. 92

FIGURE 5.4 (A) XRD PATTERN AND (B) RAMAN SPECTRA OF FECONC AND FENC. 93

FIGURE 5.5 (A) X-RAY ABSORPTION NEAR-EDGE STRUCTURE (XANES) SPECTRA OF FECONC AND FE FOIL. (B) XANES SPECTRA OF FECONC AND CO FOIL. (C) EXTENDED X-RAY ABSORPTION FINE STRUCTURE (EXAFS) SPECTRA AT THE FE K-EDGE OF FECONC AND FE FOIL. (D) EXAFS SPECTRA AT THE CO K-EDGE OF FECONC AND CO FOIL. 94

FIGURE 5.6 CHRONOAMPEROMETRY RESULTS OF (A) FECONC AND (B) FNCNTESTED IN THE H-CELL WITH 0.1 M HCL AT DIFFERENT APPLIED POTENTIALS. 95

FIGURE 5.7 (A) NH_3 YIELD RATES, (B) CORRESPONDING FARADAIC EFFICIENCIES, AND (C) H_2 SELECTIVITY OF FENC AND FECONC MEASURED AT ALL GIVEN POTENTIALS. 95

FIGURE 5.8 (A) THE NH_3 PRODUCTION PERFORMANCE IN THE DURABILITY TEST OF FECONC. (B) NH_3 YIELD RATE AND FARADAIC EFFICIENCY OF FECONC COMPARED WITH OTHER STATE-OF-THE-ARTS; DETAILED DATA ARE PROVIDED IN TABLE 5.1. 96

FIGURE 5.9 (A) THE UV-VIS ABSORPTION SPECTRA OF THE ELECTROLYTES UNDER DIFFERENT CONDITIONS. (B) COMPARISON OF THE NH_3 YIELD RATE AND FARADAIC EFFICIENCY USING DIFFERENT FEEDING GASES FOR NRR AT -0.2 V VS. RHE AND OPEN-CIRCUIT POTENTIAL. (C) ^1H NMR SPECTRA OF THE NRR PRODUCTS USING DIFFERENT FEED GASES. (D) COMPARISON OF THE NH_3 YIELD RATE AND FARADAIC EFFICIENCY USING DIFFERENT FEEDING GASES FOR NRR AT -0.2 V VS. RHE EITHER BY COLORIMETRIC OR NMR METHOD. 98

LIST OF TABLES

TABLE 1.1 REACTION MECHANISMS FOR THE ELECTROCATALYTIC NRR. 5

TABLE 4.1 COMPARISON OF THE ELECTROCATALYTIC NRR PERFORMANCE AT AMBIENT CONDITIONS. 77

TABLE 5.1 COMPARISON OF THE ELECTROCATALYTIC NRR PERFORMANCE AT AMBIENT CONDITIONS. 96

LIST OF SYMBOLS AND CHEMICAL FORMULA

A	absorbance value
Ag	Silver
AgCl	Silver chloride
$c(NH_3)$	measured ammonia concentration
C_{dl}	double-layer capacitance
cm^2	square centimeter
CO_2	carbon dioxide
E_*	energies of the surface without adsorbed molecules
$E_{*+intermediate}$	energies of the surface with adsorbed molecules
$E_{molecule}$	energy of the molecule in the gas phase
eV	electron volts
F	Faraday constant (96,485 C mol^{-1})
GeV	Giga - electron volts
h	hour
H_2	hydrogen
H_2O	water
H_2O_2	hydrogen peroxide
HCl	hydrochloric acid
I_D	intensity of D band

I_G	intensity of G band
I_{total}	recording current
K	Kelvins
k_B	Boltzmann constant
KCL	Potassium chloride
$KMnO_4$	Potassium permanganate
KOH	potassium hydroxide
kV	Kilovolt
M	mol/L
m	loading mass of the catalysts
mA	milliampere
mg	milligram
MHz	Mega Hertz
ml	milliliter
ms	millisecond
N_2	nitrogen
N_2H_4	hydrazine
NH_3	ammonia
nm	nanometer
NO	Nitric oxide

NO_2	nitrogen dioxide
NO_2^-	nitrite
NO_3^-	Nitrate
NO_x	Nitrogen oxides
ns	nanosecond
P	atmospheric pressure (101.325 KPa)
ps	picosecond
Q	total charge passed through the electrode
R	gas constant (8.314 J mol^{-1} K^{-1})
s	second
S_A	average span
S_x	span of the nitrogen cluster in the direction of x axis
S_y	span of the nitrogen cluster in the direction of y axis
S_z	span of the nitrogen cluster in the direction of z axis
t	time
T	temperature in Kelvin (298.15 K)
t_H	time required to fill the sampling loop
V	volt
V	volume of the electrolyte
V_j	volume percentage obtained from the GC analysis of H_2

wt%	weight percent
℃	degree c
Å	10-10m
ΔE	total energy difference between reactants and products
ΔG	Gibbs free energy change
ΔG_{pH}	contribution of H^+ and is equal to $-k_BT\times\ln(10)\times pH$
ΔS	entropy change
ΔZPE	zero-point energy correction
μg	microgram
μl	microliter
R_{ct}	charge transfer resistance

LIST OF ABBREVIATIONS AND ACRONYMS

*N_2@FeCoNC	N_2 adsorbed on FeCoNC configuration
*N_2@FeNC	N_2 adsorbed on FeNC configuration
AC-HAADF-STEM	aberration-corrected high-angle annular dark field scanning transmission electron microscopy
BET	Brunauer-Emmett-Teller
CA	contact angle
CE	counter electrode
COFs	covalent organic frameworks
CP	carbon paper
CPs	carbon papers
CV	cyclic voltammetry
DFT	density functional theory
ECSA	electrochemical active surface area
EIS	electrochemical impedance spectroscopy
ENRR	electrochemical nitrogen reduction reaction
EXAFS	extended X-ray absorption fine structure
FE	Faradaic efficiency
FeCoNC	asymmetrical Fe-Co dimers anchored on nitrogen-doped carbon
FeNC	single Fe atoms anchored on nitrogen-doped carbon

FESEM	field emission scanning electron microscope
FETEM	field emission transmission electron microscope
GC	gas chromatography
GDY	Graphdiyne
GGA	generalized gradient approximation
HB	Haber-Bosch
HER	hydrogen evolution reaction
HRTEM	high-resolution transmission electron microscopy
IC	ion chromatography
ISE	ion selective electrodes
LDH	layered double hydroxide
LSV	linear sweep voltammetry
MD	Molecular dynamics
NC	nitrogen-doped carbon
NMR	nuclear magnetic resonance
NPC	nitrogen-doped porous carbon
NPs	nano particles
NRR	nitrogen reduction reaction
OENC	oxygen-enriched nitrogen-doped carbon
PEM	proton exchange membrane

P-WFeNC	plasma-etched WFeNC
RDS	rate-determining step
RE	reference electrode
RF	radio frequency
RHE	reversible hydrogen electrode
SACs	Single-atom catalysts
sccm	standard cubic cm per min
SEM	scanning electron microscopy
TEM	transmission electron microscopy
TM	transition-metal
TPB	three-phase boundary
VASP	Vienna ab initio simulation package
vdW	van der Waals
vs.	versus
WE	working electrode
WFeNC	tungsten cluster and single Fe atoms anchored on nitrogen-doped carbon
XANES	X-ray absorption near-edge structure
XPS	X-ray photoelectron spectroscopy
XRD	X-ray diffraction
ZIF	zeolite imidazolate framework

1 INTRODUCTION

1.1 Background and Motivations

As a basic chemical, ammonia is one of the most produced chemical products in the world. It is also an important raw material for synthetic fertilizers, drugs, and fine chemicals.[1] It is widely used in chemical industry, agriculture, and other fields. Therefore, it occupies an important position in the global economy. Ammonia is vital to many industrial production processes and even the entire human life and is one of the key factors determining the progress of human society.[2] The main sources of ammonia in nature are the release of plants, evaporation from the ocean or other waters, volatilization of soil, animal urine and feces, and lightning.[3] But the ammonia produced by these processes is negligible compared to global demand. The Haber-Bosch process, developed by German chemists Fritz Haber and Carl Bosch in the first decade of the 20th century, is the primary industrial procedure for producing ammonia.[4] So far, the traditional Haber-Bosch method is still the main way for the synthesis of NH_3. The process converts atmospheric nitrogen (N_2) to ammonia (NH_3) by a reaction with hydrogen (H_2) using an iron metal catalyst shown in Figure 1.1.[5,6] However, it is hard to gently reduce N_2 to NH_3 owing to the strong N triple bond (941 kJ mol^{-1}).[7] Therefore, the current industrial Haber-Bosch process requires the synthesis of ammonia under high temperature (400~450℃) and high pressure (10-30 MPa) conditions where high temperature for accelerated kinetics and high pressure for favorably shifting the equilibrium.[8] In 2021, global ammonia production reached 182 million tons through the Haber-Bosch process. Among them, about 70% of ammonia is used in chemical fertilizer production, and about 50% of global food production relies on ammonia-derived chemical fertilizers.[9] The above data clearly shows the great impact of ammonia synthesis technology on human beings. However, the Haber process for ammonia synthesis has high energy consumption and serious pollution. The high-purity hydrogen used not only consumes a large amount of fossil fuel natural gas to convert but also releases about 1.6 tons of carbon dioxide greenhouse gas for every ton of ammonia produced.[10] The energy consumption of this process accounts for 1% of global energy consumption and carbon dioxide emissions account for 1.5% of total global emissions.[11] Therefore, finding a green, environmentally friendly and low-energy-consumption method for ammonia synthesis is of great significance to the sustainable development of the environment and energy.

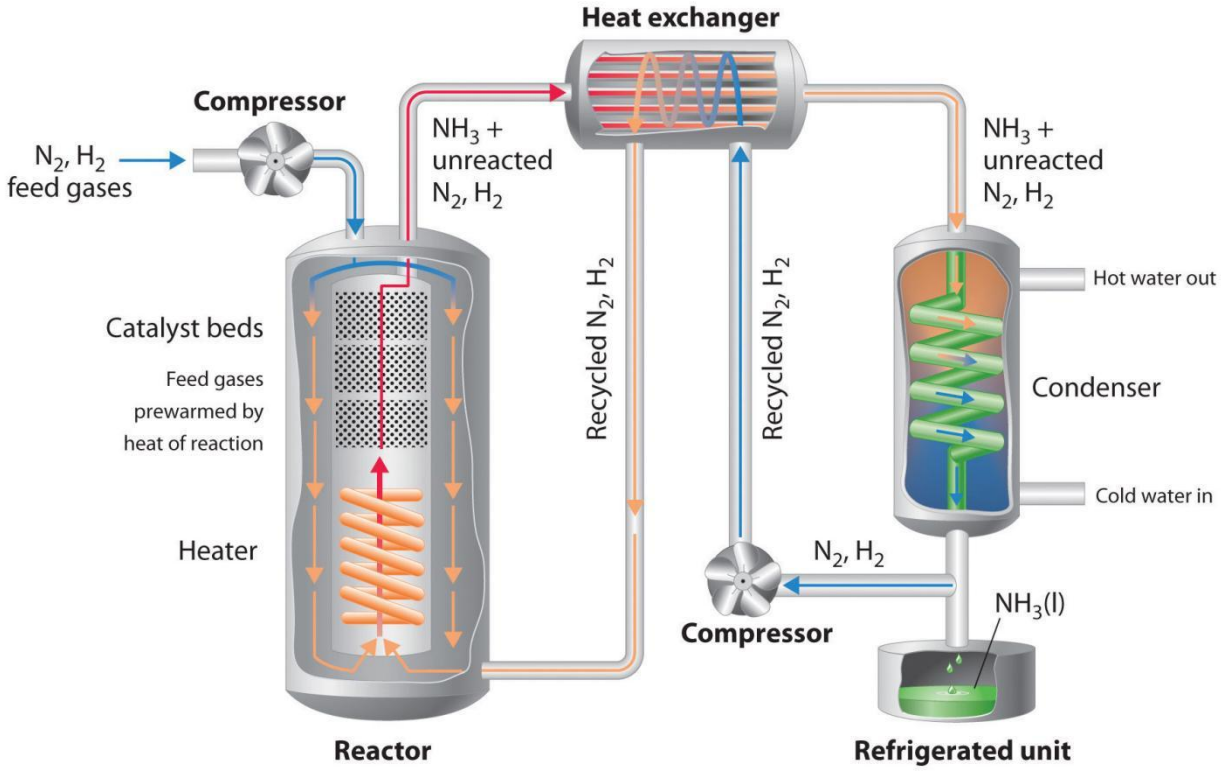

Figure 1.1 A Schematic Diagram of an Industrial Plant for the Production of Ammonia via the Haber-Bosch Process. Ref.[6]

Traditional ammonia synthesis technology is intensive production of ammonia, and fertilizers are transported to users. Currently, as the price of renewable electricity continues to decrease, electrochemical ammonia synthesis directly from nitrogen and water is one of the potential ammonia synthesis routes, driven by renewable energy.[12] This process can be used to synthesize ammonia in a decentralized manner using decentralized renewable energy in smaller-scale devices and is expected to bring huge economic and social benefits, such as lowering the price of fertilizers in developing countries and remote areas that lack transportation networks or infrastructure. In recent years, electrochemical ammonia synthesis and electrocatalytic ammonia synthesis have received widespread attention and exploration in the scientific community. It is expected that the electrochemical ammonia synthesis route can replace or supplement the Haber-Bosch process. The electrochemical ammonia synthesis method can enable the thermodynamically non-spontaneous ammonia synthesis reaction to be driven by electric energy without being limited or less limited by thermodynamic equilibrium, and realize the synthesis of ammonia at normal temperature and pressure.[13] Electrocatalytic

nitrogen reduction reaction (NRR) is a green, sustainable process that directly converts N_2 into NH_3 using water as a proton and electron source at a lower potential. Electrocatalytic NRR has the advantages of utilizing renewable energy (wind energy, solar energy, etc.), wide sources of raw materials (N_2 and H_2O) and reaction at room temperature and pressure. Figure 1.2 summarizes part of a timeline of theoretical and experimental breakthroughs in electrocatalytic NRR for ammonia synthesis.[13-25]

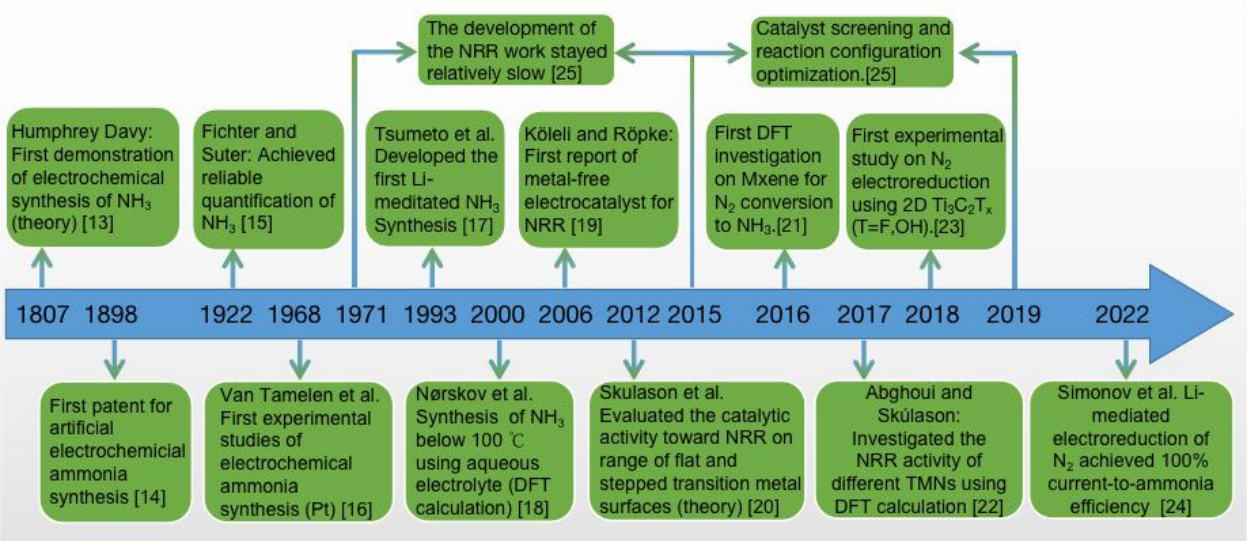

Figure 1.2 Timeline of theoretical and experimental breakthroughs in electrocatalytic NRR for ammonia synthesis.

1.2 Nitrogen reduction reaction mechanism

Learning the underlying mechanisms of a reaction can lead to profound insights into the catalytic process and, in turn, provide guidance for developing catalysts with superior performances. The mechanism for nitrogen reduced to ammonia under electrochemical conditions is shown in Figure 1.3.[26] The reaction of nitrogen gas being reduced to ammonia gas on a non-uniform surface has two different reaction mechanisms: dissociative and associative mechanisms with different involved intermediates (Table 1.1). According to the dissociative mechanism, the N≡N triple bond is first cleaved, and the hydrogenation steps subsequently take place over the adsorbed N atoms. It should be noted that such a mechanism is uncommon in NH_3 electrosynthesis under ambient conditions due to the rather high energy

required for the cleavage of the N≡N bond and this also explains why harsh conditions are required for the Haber–Bosch process following the dissociative pathway. In the case of the associative mechanism, the N_2 molecule is first adsorbed and keeps two N atoms bound to each other before the formation of the first NH_3 molecule. Considering different sequences of the addition of H to the N atoms, the hydrogenation process in the associative mechanism can proceed via two ways, including the distal pathway and alternating pathway. In the distal pathway, the distal N atom far away from the adsorption site firstly undergoes the hydrogenation process until the release of the NH_3 molecule, and then the remaining N atom repeats the same hydrogenation process to produce the second NH_3 molecule. In comparison, the alternating pathway proceeds with the two N atoms of the N_2 molecule adsorbed through an end-on mode alternately undergoing the hydrogenation process until an NH_3 molecule is released and the N–N bond is broken. It should be pointed out that alternating or distal pathways greatly depend on the electrocatalysts in the real NRR process at present.

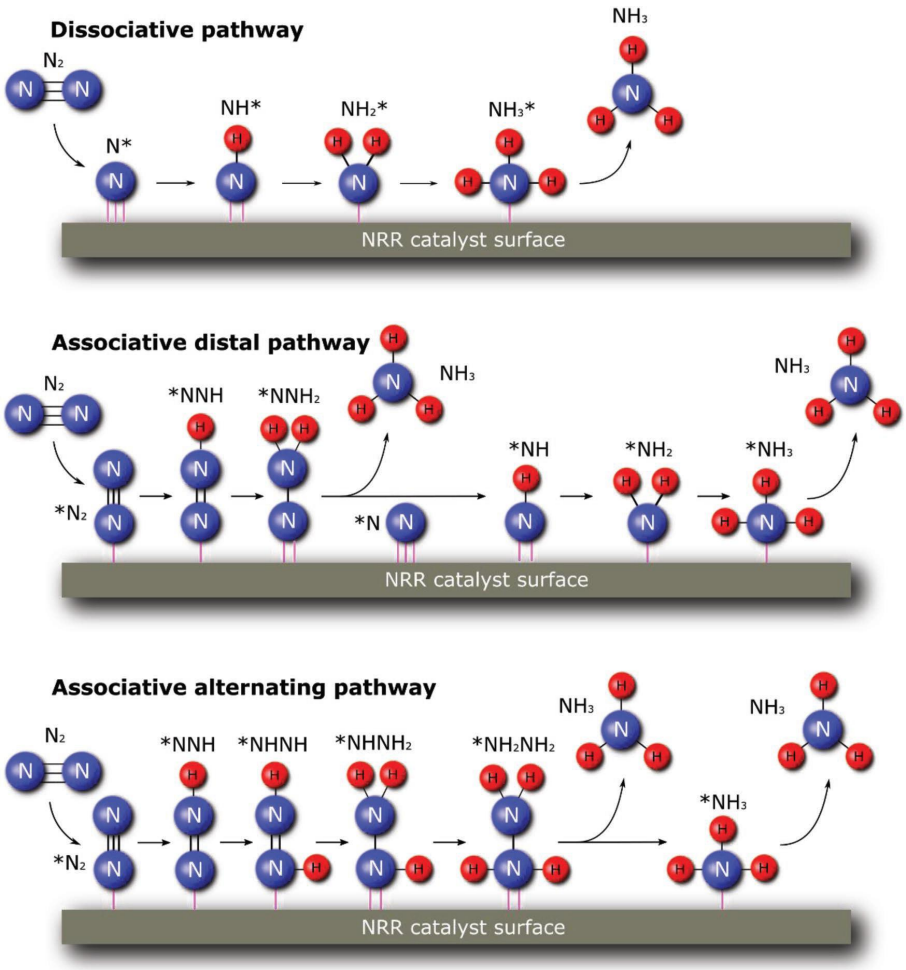

Figure 1.3 The possible reaction mechanism of NRR including dissociative pathway, associative distal, and alternating pathways. * represents an adsorption site. Ref. [26]

Table 1.1 Reaction mechanisms for the electrocatalytic NRR.

Mechanism	Primary reactions stages
Dissociative pathway	$N_2 + 2^* \rightarrow 2^*N$ $2^*N + 2e^- + 2H^+ \rightarrow 2^*NH$ $2^*NH + 2e^- + 2H^+ \rightarrow 2^*NH_2$ $2^*NH_2 + 2e^- + 2H^+ \rightarrow 2NH_3 + 2^*$
Associative distal pathway	$N_2 + * \rightarrow *N_2$ $*N_2 + e^- + H^+ \rightarrow *NNH$ $*NNH + e^- + H^+ \rightarrow *NNH_2$ $*NNH_2 + e^- + H^+ \rightarrow *N + NH_3$ $*N + e^- + H^+ \rightarrow *NH$ $*NH + e^- + H^+ \rightarrow *NH_2$ $*NH_2 + e^- + H^+ \rightarrow NH_3 + *$
Associative alternating pathway	$N_2 + * \rightarrow *N_2$ $*N_2 + e^- + H^+ \rightarrow *NNH$ $*NNH + e^- + H^+ \rightarrow *NHNH$ $*NHNH + e^- + H^+ \rightarrow *NHNH_2$ $*NHNH_2 + e^- + H^+ \rightarrow *NH_2NH_2$ $*NH_2NH_2 + e^- + H^+ \rightarrow *NH_2 + NH_3$ $*NH_2 + e^- + H^+ \rightarrow NH_3 + *$

***Represents a surface adsorption site on an electrocatalyst.**

In the electrochemical system, protons and electrons can be obtained through the electrolysis reaction of water. In acidic and alkaline electrolytes, nitrogen reduction reactions at the anode and cathode are as follows:

Under acidic conditions:

Anodic reaction: $3H_2O \rightarrow 3/2O_2 + 6H^+ + 6e^-$

Cathodic reaction: $N_2 + 6H^+ + 6e^- \rightarrow 2NH_3$

Under alkaline conditions:

Anodic reaction: $6OH^- \rightarrow 3H_2O + 3/2O_2 + 6e^-$

Cathodic reaction: $N_2 + 6H_2O + 6e^- \rightarrow 2NH_3 + 6OH^-$

1.3 Research strategies for electrocatalytic NRR

1.3.1 Guidelines for NRR experiments.

NH_3 contamination can be found in the environment, ion exchange membranes, and even within electrocatalysts. As a result, determining the exact concentration of generated NH_3 is a difficult task. New protocols have been devised by researchers to ensure correct and accurate NH_3 measurements under controlled environments, such as in an Ar atmosphere, an open-circuit potential, without catalysts, and under a $^{15}N_2$ environment, to minimize the risk of NH_3 contamination (Figure 1.4).[27]

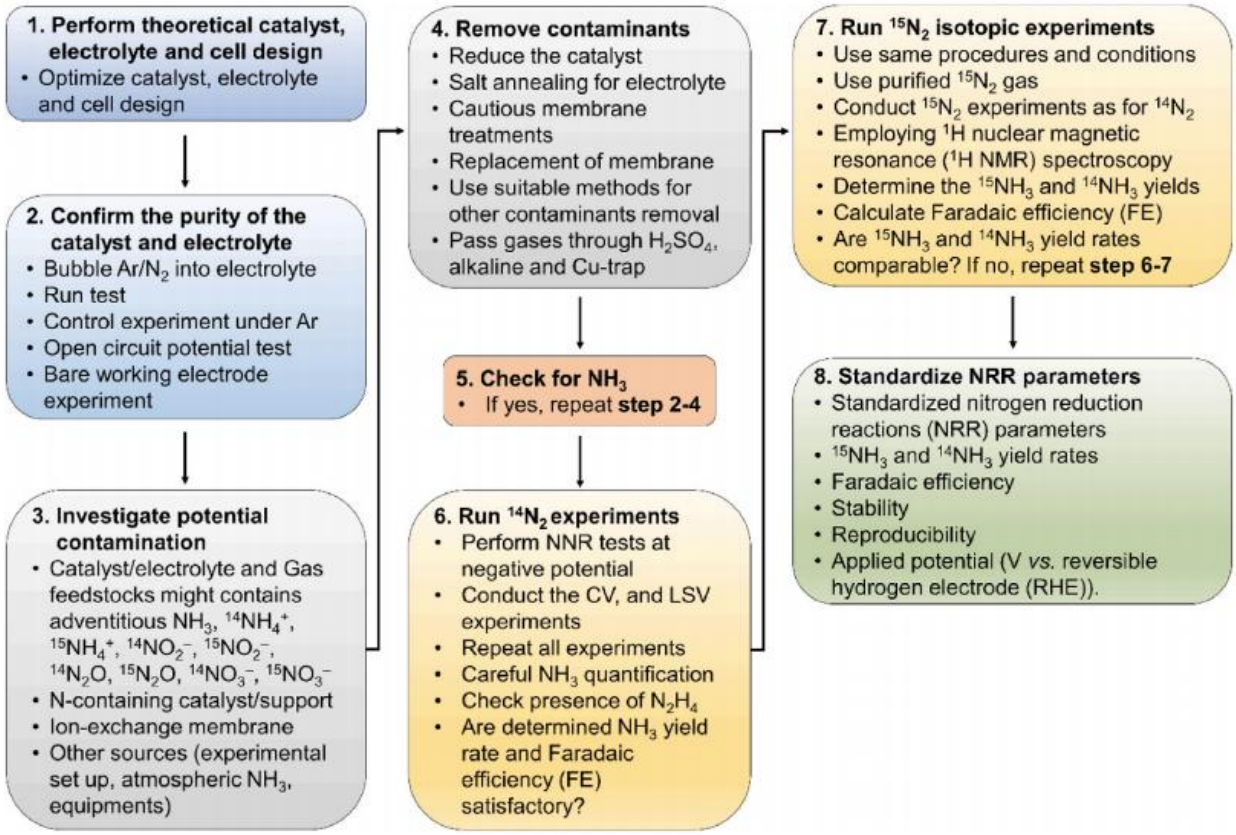

Figure 1.4 Guidelines to conduct electrochemical NRR experiments for ammonia generation. Here, cyclic voltammetry (CV), linear sweep voltammetry (LSV). Ref.[27]

The first step is to design theoretical catalysts, electrolytes, and batteries. The catalyst should be favorable for NRR, and the choice of electrolyte should be suitable for the catalyst. The reaction cell should be selected to suit the catalyst reaction mechanism.

The second step is to determine the purity of the entire testing process and remove contaminants. It should be ensured that contaminants do not come from the experimental setup including working electrode, reference electrode, counter electrode, ion-exchange membrane, and reaction cell. Catalyst, electrolyte and feeding gas might contains adventitious NH_3, NH^{4+}, NO^{2-}, N_2O, NO^{3-}. Catalysts should be washed repeatedly to remove ammonia that may be carried during the synthesis process. For N-containing catalyst, isotopic testing should be used to determine that the ammonia produced is not coming from the catalyst. The catalyst and its working electrode should be tested under argon conditions to determine that ammonia in the electrolyte does not come from the catalyst or working electrode. The purification of the electrolyte includes: (I) If aqueous electrolyte is used for testing, ultra-pure water should be used to prepare the electrolyte. (II) Control the entire test process to test in Ar or N_2 environment to prevent the electrolyte from adsorbing ammonia in the air. (III) It should be ensured that the purity of feeding gas does not contain contaminants. The purification of the feeding gas contains sequentially flowed through acid, oxidizing agent, and alkaline traps to remove possible contaminants. Then, the gas was passed through a drying tube to prevent water vapor from entering the electrochemical cell.

After confirming that there are no contaminants in the entire reaction process, proceed to the third step, which is to run $^{14}N_2$ experiments. Including: (I) Perform NRR tests at negative potential. (II) Conducting the CV and LSV experiments. (III) Repeat all experiments to make sure their repeatability. (IV) Perform NH_3 quantification carefully. (V) Check the presence of N_2H_4 (VI)Determine the ammonia yield rate and FE to be satisfactory.

The fourth step is run $^{15}N_2$ isotopic experiments. Including: (I) Use the same procedures and conditions. (II) Use purified $^{15}N_2$ feeding gas. (III) Conduct $^{15}N_2$ experiments as for $^{14}N_2$. (IV) Employing ^{1}H nuclear magnetic resonance (^{1}H NMR) spectroscopy. (V) Determine the$^{15}NH_3$ and $^{14}NH_3$ yields rate and FE (VI) Make sure that the$^{15}NH_3$ and $^{14}NH_3$ yields rate and FE are comparable.

At last, standardize NRR parameters including $^{15}NH_3$ and $^{14}NH_3$ yields rate, FE, stability, reproducibility, and applied potential (V *vs.* reversible hydrogen electrode (RHE)).

1.3.2 Reactor configurations

The electrochemical reactor setup utilized in the NRR study is mainly of four types: the back-to-back cell, the proton exchange membrane (PEM) cell, the ‘‘H”-type cell, and the single-chamber cell.[28] In the back-to-back cell, the cathode and the anode gas diffusion electrodes, which are filled with N_2 gas and H_2O, respectively, are separated by a proton exchange membrane or an anion exchange membrane (Figure 1.5a). Although similar to the back-to-back cell, the PEM-type cell has one key distinction: its anode is loaded with an aqueous electrolyte (Figure 1.5b). Both the PEM-type cell and the back-to-back cell are effective at inhibiting the HER due to the non-direct contact of the electrolyte with the cathode, whereas the efficiency of gas–solid reactions occurring in the cathode chamber is relatively low under ambient conditions. Single chamber and ‘‘H”-type cells are usually filled with liquid electrolytes. For the former, the cathodic and anodic reactions take place in the same electrolyte medium, which might result in a simultaneous decomposition/oxidation of cathodic product (ammonia) onto the anode leading to a low yield (Figure 1.5d). This shortage can be eliminated using an ‘‘H”-type cell (Figure 1.5c), the most frequently used reactor design under relative conditions, where the anodic and cathodic reactions are separated by a membrane. However, in both the single chamber cell and the ‘‘H”-type cell, the interaction between the cathode and the aqueous electrolyte may lead to a low FE of NH_3 because of the competing HER.

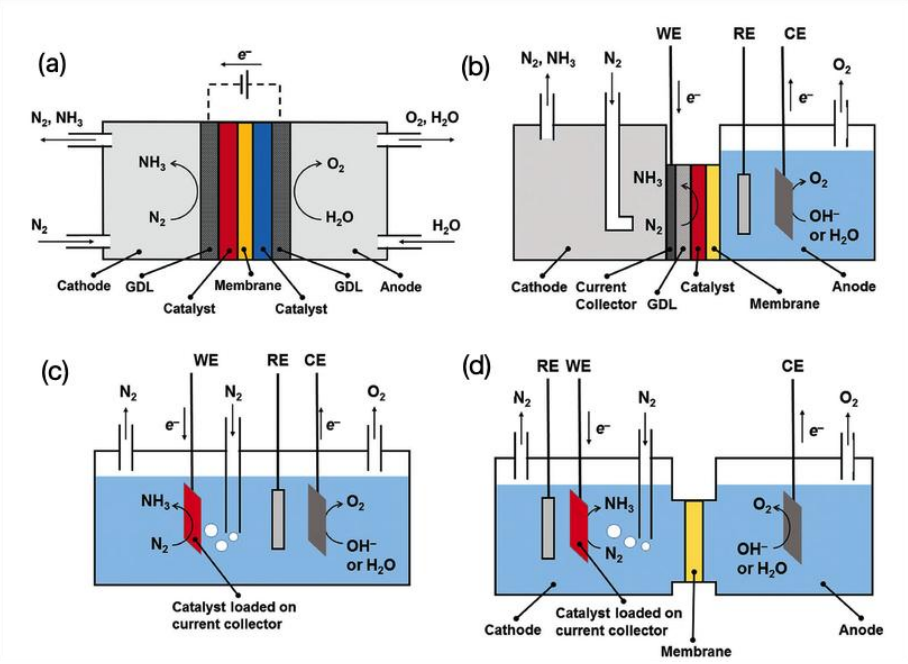

Figure 1.5 Multiple cell configurations for NRR in a schematic view under standard conditions (RE stands for the reference electrode, WE stand for the working electrode, and CE stands for the counter electrode). Ref. [29]

1.3.3 Electrochemical measurements

The NRR electrocatalyst performance is typically evaluated using electrochemical techniques such as cyclic voltammetry (CV), linear sweep voltammetry (LSV), chronoamperometry (CA), and electrochemical impedance spectroscopy (EIS) via an electrochemical workstation with a three-electrode configuration. The LSV curve describes the galvanic response to the linear change in potential, which can be used to identify the occurrence of NRR by comparing the current density acquired from Ar or N_2-saturated electrolyte media. CA is a potentiostatic approach that analyzes the variation of current density within a reaction period under a fixed applied potential. The acquired CA values provide information about the FE, the yield of the product, and the durability of catalysts during prolonged reactions. The repetition of CV measurements also allows for estimating the durability of the electrocatalysts. In addition, using CV measurements in the non-Faradic range with various scan rates, it is possible to determine the electrochemically active surface area (ECSA), which is directly related to a double-layer capacitance (C_{dl}). This allows one to compare the performance of different catalysts. The EIS

measurements are usually conducted to analyze the charge transfer dynamics at the solid–liquid interface extracted from the Nyquist semi-circle diameter; the smaller the charge transfer resistance (R_{ct}), the faster the rate of reaction.

1.3.4 Ammonia detection

There are several methods and analytical instruments that can be used for ammonia quantification. These include, but are not limited to, colorimetric methods, ion chromatography (IC), ^{1}H nuclear magnetic resonance (^{1}H NMR), ion selective electrodes (ISE), fluorometric, enzymatic, conductivity, and titrimetric methods. Among these methods, colorimetric methods are widely used for ammonia quantification in NRR due to their high accuracy, low detection limits, reproducibility, and simplicity. The colorimetric methods, including the indophenol blue approach depending on the Berthelot reaction and Nessler's reagent method depending on the reaction between NH_3 and the Nessler's reagent to induce a color indicator, are the most

employed methods to determine NH_3-N in the electrocatalytic NRR. In recent years, the IC method and 1H NMR have also been used. IC has the advantages of good reproducibility and precision, but its apparatus is costly and sophisticated. Combining with $^{15}N_2$ isotopes as a feed gas during the NRR, the 1H NMR method can verify the origin of the produced ammonia. Here we will introduce in detail the testing methods used in this thesis: indophenol blue and ^{1}H NMR method.

Indophenol Blue Method

The indophenol blue method is based on the reaction of ammonia with hypochlorite and phenol in an alkaline condition, which produces blue-colored indophenol. This reaction is called the Berthelot reaction, and because it involves the use of phenol, the indophenol blue method is also known as the phenate method. The reaction in the indophenol blue method proceeds via several steps, including the reaction between ammonia and hypochlorite at pH 9.7–11.5 as the first step. This reaction produces monochloramine, which further reacts with the phenol, producing quinone chloramine. The formation of quinone chloramine is facilitated by the addition of sodium nitroprusside or sodium nitroferricyanide as a catalyst. Subsequently, the quinone chloramine further reacts with phenol to form indophenol, which dissociates in the alkaline solution resulting in a blue color. Therefore, the indophenol product can be quantitatively determined using a UV-vis spectrophotometer at a wavelength of 630–655 nm. The overall process of the reaction in the indophenol blue method is presented in Equation (1.1).[30]

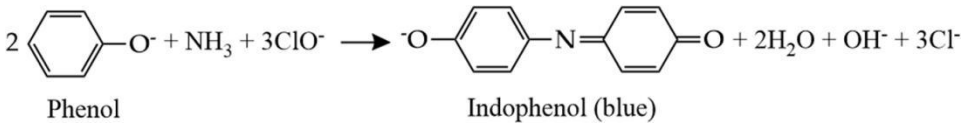

(1.1)

Modification of the indophenol blue method was then developed, specifically by substituting the phenol using sodium salicylate or salicylic acid. This modified method is also known as the “salicylate method”. In addition to being less harmful than phenol, the use of salicylate compounds is to avoid the formation of a harmful substance, such as *o*-chlorophenol, during the process. However, because of the lower reactivity of the salicylate compared to phenol, the salicylate method requires a much higher concentration of salicylate to reach a similar sensitivity as phenol. The reaction involves the same reaction step between the ammonia and hypochlorite to form monochloramine, as in the original indophenol blue method. However, in the salicylate method, the monochloramine reacts with salicylate, producing 5-aminosalicylate. The 5-aminosalicylate is oxidized, and it further reacts with salicylate, forming a colored compound. The apparent color may be varied depending on the ammonia concentration in the sample. The color may change from yellow to green and

then to blue, along with increasing ammonia concentration (Figure 1.6 b, c). The overall reaction is shown in Equation (1.2).

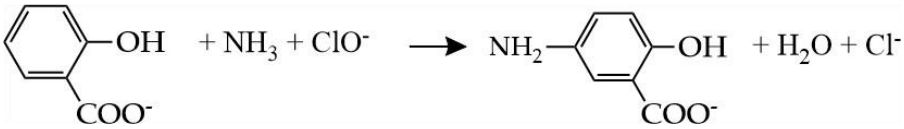

(1.2)

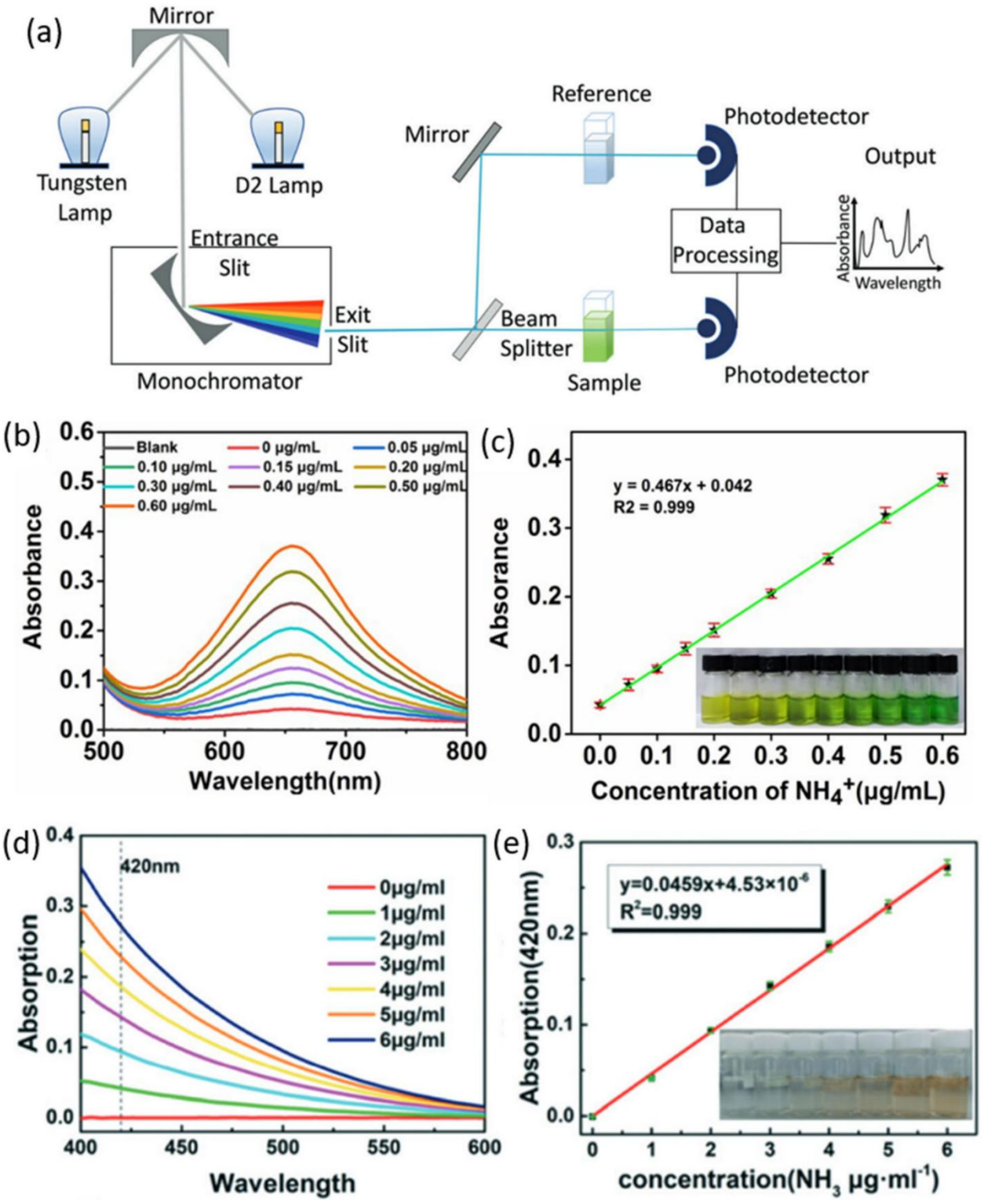

Figure 1.6 (a) Schematic illustration of UV-vis spectrophotometer for double beam instrument. Ref. [31] The tungsten lamp and D2 lamp emit visible and ultraviolet lights, respectively. The light is directed to the monochromator, which determines the wavelength of the sample. Adapted with permission from Ref. [32] (b) UV-vis spectra of standard solutions with different concentrations, and (c) corresponding

calibration curve. The absorbance values for the calibration curve were obtained from a wavelength of 655 nm. Inset of (c) is the photograph of the standard solutions after 2 h of reaction with indophenol reagent. Adapted with permission from Ref. [33] (d) UV-vis spectra of the standard solution with different concentrations, and (e) corresponding calibration curve. The absorbance values for the calibration curve were obtained from the wavelength of 420 nm. Inset of (e) is the photograph of the standard solution after 20 min of reaction with Nessler's reagent. Adapted with permission from Ref. [34]

In both the indophenol blue method and the salicylate method, citrate buffer is often used to stabilize the pH and prevent the precipitation of hardness cations, such as magnesium or calcium ions, at a high pH.[35,36] The indophenol blue method and the salicylate method are able to measure ammonia at low concentrations (0-0.6 mg L^{-1} of NH_3-N) with good accuracy and repeatability.[37] However, it takes a relatively long time for the samples to be ready for measurement (1–2 h). It is worth noting that most of the NRR and NO_3^-RR reports employed the salicylate method to quantify the produced ammonia, according to the reagent that they used (they used a salicylate compound instead of phenol). However, they referred to their method as the indophenol blue method instead of the salicylate method, possibly due to the origin of the salicylate method derived from the indophenol blue method and the same principle between them, or just for simplification purposes. Therefore, we will use the term indophenol blue method in the following discussion.

^{1}H NMR Method

Many nuclear isotopes, including ^{1}H, ^{14}N, and ^{15}N, are magnetically active with nonzero spin and the NMR instruments measure the radio frequency (RF) associated with those nuclei. Similar to other spectroscopy methods, the NMR analyzes the structure or chemical composition of molecules based on their absorption of electromagnetic radiation. In this case, the NMR specifically works at the radio-wave frequency, which affects a transition in the nuclear spin level.

Many atomic nuclei have a property called spin, by which we can illustrate as if they are spinning. The energy of spin states is not equal in an applied magnetic field. Because nuclei are charged particles, they have their own magnetic moments (μ), which are generated by their charge and spin. In an applied magnetic field, there are two magnetic moment alignments of nuclei. The alignment can be in the same direction ($+\frac{1}{2}$ spin state) or in the opposite direction ($-\frac{1}{2}$ spin state) relative to the magnetic field direction. The $+\frac{1}{2}$ spin state has a lower energy level.[38] The resonance occurs when the nuclei with the same alignment as the applied

magnetic field absorb energy, which changes their orientation (Figure 5a). The absorbed energy must be equal to the difference between the two states, as shown in Equation (1.3).

$$E_{absorbed} = (E_{-\frac{1}{2}state} - E_{+\frac{1}{2}state}) = h\nu \qquad (1.3)$$

where $E_{absorbed}$ is the energy absorbed by the nuclei, $E_{-\frac{1}{2}state}$ is the energy of $-\frac{1}{2}$ spin state(opposite direction against the magnetic field direction), $E_{+\frac{1}{2}state}$ is the energy of $+\frac{1}{2}$ spin state (same direction as the magnetic field direction), *h* is the Planck constant, and *v* is the frequency of the electromagnetic radiation.

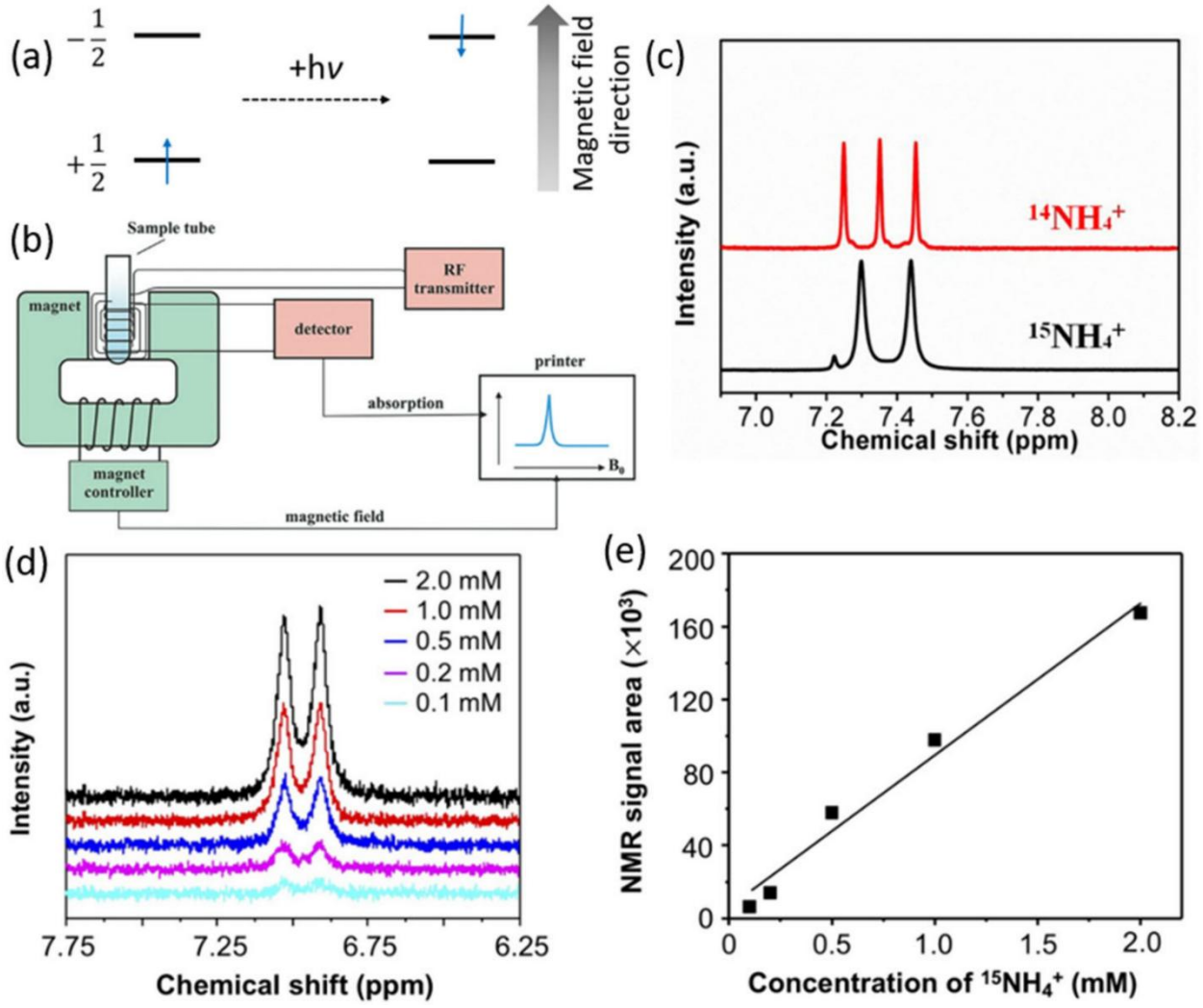

Figure 1.7 (a) Absorption process in NMR. (b) Schematic representation of a typical NMR spectrometer. Ref. [39] (c) ^{1}H NMR spectra of $^{14}NH^{4+}$ and $^{15}NH^{4+}$ produced from NRR reaction using $^{14}N_2$ and $^{15}N_2$ isotopes.

Ref. [33] (d) ^{1}H NMR spectra of 15NH4+ standard solutions with various concentrations and (e) corresponding calibration curve. Ref. [40]

In practice, energy difference in the energy levels (and therefore, the nuclei population) is a function of the applied magnetic field. The stronger the magnetic field, the higher the energy difference between the possible spin states. In an applied magnetic field, the nuclei precess in their axis with various alignments. The frequency at which a nucleus precess is proportional to the strength of the applied magnetic field. In this case, each isotope has its characteristic frequency. For example, in a 7.5 T of magnetic field, the 1H nucleus precesses at 300 MHz, while at 21.1 T, ^{1}H precesses at 900 MHz.[41]

The resonance occurs when external electromagnetic radiation matches with the nucleus precession. As also shown in Figure 1.7a, during this resonance process, the spin alignment of the nuclei changes from $+\frac{1}{2}$ spin state to $-\frac{1}{2}$ spin state, which increases the population of higher energy spin states. This process continues until the population of the high energy spin states is equal to the lower energy spin states. This condition is called saturation, which should be avoided as no net signal can be observed. At this stage, external electromagnetic radiation is turned off. Therefore, the resonance stops. With cessation of resonance, the system changes back to the initial condition, where the high energy spin state ($-\frac{1}{2}$) nuclei relax to the lower energy ($+\frac{1}{2}$) spin state. The relaxation process is accompanied by RF emission. Therefore, the detector can record the intensity of RF from each nucleus. This process is reiterated, which strengthens the signal from each nucleus and reduces the noise. The software then calculates peak properties, such as chemical shift, intensity, multiplicity, and J-coupling (Figure 1.7b).[38]

In NRR and NO_3^-RR, 1H NMR is mostly used, instead of ^{15}N NMR, to detect $^{15}NH_3$ because of the extremely low gyromagnetic ratio of ^{15}N. In this case, 1H NMR can differentiate the $^{15}NH^{4+}$ and $^{14}NH^{4+}$ because $^{14}NH^{4+}$ is a spin-1 nucleus and $^{15}NH^{4+}$ is a spin$-\frac{1}{2}$ nucleus. Therefore, the coupling between ^{1}H and ^{15}N in $^{15}NH^{4+}$ will generate a doublet signal with a spacing of 73 Hz. Meanwhile, the coupling between ^{1}H and ^{14}N in $^{14}NH^{4+}$ results in a triplet signal with a spacing of 52 Hz (Figure 1.7c)[42] [36].

Measurement using ^{1}H NMR in NRR usually aims to confirm the origin of the produced ammonia. Before ^{1}H NMR detection, the NRR experiments are first performed by using the $^{15}N_2$ as an N source instead of $^{14}N_2$. Therefore, the detection of $^{15}NH_3$ in NMR spectra verifies that

the produced ammonia is originated from N_2 gas instead of other impurities. In addition to confirming the origin of ammonia qualitatively, more recently, ^{1}H NMR was also used for $^{15}NH_3$ quantification, as reported by Jang et al. For this purpose, measurements of a series of standard solutions were performed. The peak area of the ^{1}H NMR spectra was then plotted as a function of concentration to obtain the calibration curve (Figure 1.7d, e). Before measurements, the sample solutions were acidified to reach a pH of ~3 by adding HCl to convert $^{15}NH_3$ to $^{15}NH^{4+}$.[40]

The ^{1}H NMR method offers high sensitivity, appreciable repeatability, and straightforward discrimination against the contaminant ammonia.[43] Furthermore, it does not need any advanced chemical manipulation, as required in the spectrophotometric method. However, it requires complex and expensive instrumentation.

1.3.5 Activity

The NH3 production rate and the FE are two important and common descriptors to estimate the NRR efficiency of the catalysts. The NH_3 formation rate is defined as the yield of ammonia per unit time and unit working electrode geometric area or unit sample mass loading, which are calculated using Eq. (1.4) or (1.5). The FE refers to the ratio of the charge from ammonia production to the overall charge flowing over the circuit, revealing the desired selectivity of ammonia formation in the electrocatalytic NRR processes and is calculated using Eq. (1.6).

$$R_{NH3}(\text{mol}\cdot\text{cm}^{-2}\cdot\text{s}^{-1}) = [17c(NH_3) \times V] / (t \times A) \quad (1.4)$$

$$R_{NH3}(\mu\text{g}\cdot\text{mg}_{cat}^{-1}\cdot\text{h}^{-1}) = [17c(NH_3) \times V] / (t \times m) \quad (1.5)$$

$$\text{Faradaic efficiency } (NH_3) = [zF \times c(NH_3) \times V] / Q \quad (1.6)$$

Where c_{NH3} (μg mL^{-1}) is the obtained NH_3 amount, V (mL) is the electrolyte volume, t (s or h) is the reaction time; A (cm^{-2}) is the geometric electrode surface area; m (mg) is the mass loading of the catalyst; z is the number of transferred electrons in the reduction of N atom (3 e$^-$ per mole of NH_3), F is the Faraday constant equal to 96,485 C mol^{-1}, and Q is the total charge passed over the electrode.

In addition, the over potential (η), which is the difference between the thermodynamic potential and the applied potential to initiate the NRR, is another important indicator of catalytic activity, revealing the faster kinetics of the NRR in a system with the smaller η.

1.4 NRR catalyst

Electrocatalysts for the electrochemical NRR have been developed using metals (Ag, Cu, W, Mo Co, Fe, etc.), non-metals (Cl, B, F, P, S, O, N, etc.), metal oxides (TiO_2, $Bi_4V_2O_{11}$, etc.), metal sulfide (MoS_2), and carbon-based materials (graphdiyne, g-C_3N_4, N-doped carbon, etc.).

1.4.1 metal-based electrocatalysts

Fe-based electrocatalysts

Iron (Fe) is the second-most plentiful metal in the earth's crust (after Al) and a crucial component of the nitrogenase catalytic sites that are crucial for biological N_2 reduction, which makes it the center of attention for use as an efficient electrocatalyst for NRR.[44,45] Four Fe based catalyst for ENRR will be introduced here (Figure 1.8). For example, Kong et al.[46] proposed a simple and valid strategy of ferrous iron replacing copper to regulate the electronic structure of layered double hydroxide (LDH) for boosting the NRR activity. Thanks to the ferrous iron, the Fe(II)Cu(II)Fe(III)-LDH catalyst attains a NH_3 yield rate of 33.1 ± 2.5 μg h^{-1} $mg_{cat.}^{-1}$ and a desirable Faradaic efficiency (FE) of 21.7 ± 1.8% in a neutral electrolyte of 0.1 M Na_2SO_4, outclassing the Cu(II)Fe(III)-LDH catalyst without Fe(II). Wei et al.[47] prepared Fe supported by porous carbon (denoted as Fe/Fe_3O_4/PC-800) composite with a high specific surface area of 1004.1 m^2g^{-1} via a simple template method. On one hand, the high surface area of Fe/Fe_3O_4/PC-800 provides a large area to enhance N_2 adsorption and promote more protons and electrons to accelerate the reaction, thereby greatly improving the dynamics. On the other hand, mesoporous Fe/Fe_3O_4/PC-800 provides high electrochemically active surface area for promoting the occurrence of catalytic kinetics. As a result, Fe/Fe_3O_4/PC-800 exhibited significantly enhanced NRR performance with an ammonia yield of 31.15 $\mu g h^{-1} mg^{-1}_{cat.}$ and faraday efficiency of 22.26% at -0.1 V vs. reversible hydrogen electrode (RHE). Jia et al.[48] reported the synthesis of porous and positively charged iron oxyhydroxide nanosheets by using layered ferrous hydroxide as a starting precursor, which undergoes topochemical oxidation, partial dehydrogenated reaction, and final delamination. As the electrocatalyst of ENRR, the

obtained nanosheets with a monolayer thickness and 10-nm mesopores display exceptional NH_3 yield rate (28.5 μg h^{-1} $mg_{cat.}^{-1}$) and FE (13.2%) at a potential of −0.4 V versus RHE in a phosphate buffered saline (PBS) electrolyte. The values are much higher than those of the undelaminated bulk iron oxyhydroxide. The larger specific surface area and positive charge of the nanosheets are beneficial for providing more exposed reactive sites as well as retarding hydrogen evolution reaction. This study highlights the rational control on the electronic structure and morphology of porous iron oxyhydroxide nanosheets, expanding the scope of developing non-precious iron-based highly efficient ENRR electrocatalysts. Liu et al.[49] reported an atomically dispersed Fe-N_4 fixed on a carbon substrate (Fe-N/C) with the Fe single atom loading up to 3.5 wt % and the specific surface area reaching up to 1088.96 m^2 g^{-1}. Furthermore, Fe-N/C was modified on carbon papers (CPs) to form Fe-N/C-CPs as effective electrochemical nitrogen reduction reaction (NRR) catalysts, achieving an R_{NH3} of 2.27 μg h^{-1} mg^{-1} with an FE of 7.67% at −0.2 V (vs RHE). The uniformly dispersed and high ratio Fe single atoms in Fe-N/C ensure that the active sites can be fully exposed, which has the ability to reduce the stable N≡N triple bond and facilitate subsequent activation and hydrogenation of nitrogen molecules, improving the electrocatalytic NRR activity.

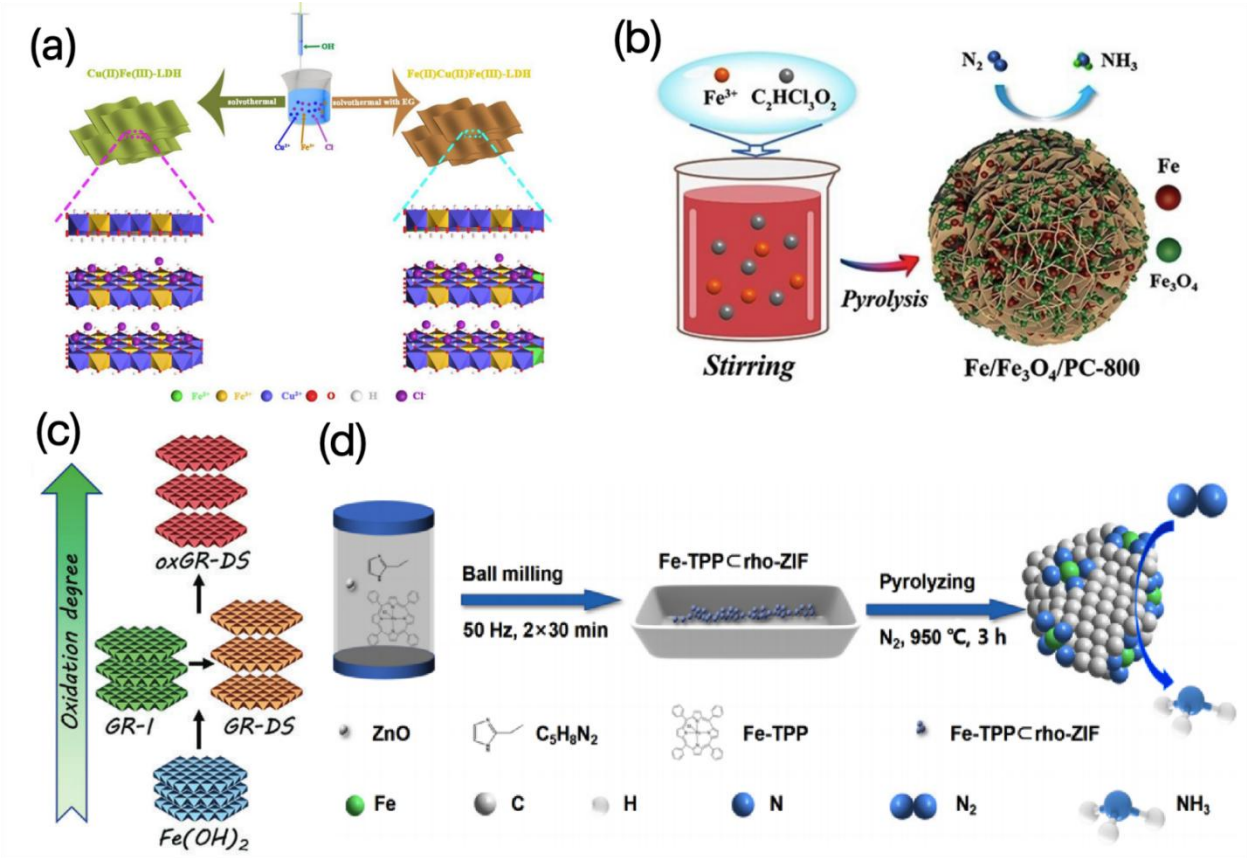

Figure 1.8 (a)Synthetic strategy used for the synthesis of Fe(Ⅱ)Cu(Ⅱ)Fe(Ⅲ)-LDH and Cu(Ⅱ)Fe(Ⅲ)-LDH. Ref. [46] (b)Schematic illustration of the preparation of Fe/Fe_3O_4/PC-800. Ref. [47] (c)Schematic illustration of the processes for preparing layered iron hydroxide series with the oxidation degree increased gradually. Ref. [48] (d)Synthetic Processes of Fe-N/C-CPs. Ref. [49]

W-based electrocatalysts

According to previous theoretical investigations, in a series of pure metal catalysts, the W atoms have high NRR activity and selectivity for N_2 fixation.[50] Chen et al. theoretically studied a series of single metal atoms on g-C_3N_4 substrate and found that W@C_3N_4 exhibit the outstanding NRR catalytic activity with a low limiting potential, and can well suppress the competing HER.[51] Du et al. reported that the excellent NRR catalytic activity of W atoms anchored on N-doped graphene is derived from the inherent properties of W atoms, such as significant positive charge, large spin moment, moderate binding energy strength of NRR intermediates.[52] Gu et al.[53] prepared a new kind of W SACs with oxygen and nitrogen coordination (W-NO/NC) and a high metal loading over 10 wt% by introducing an oxygenbridged [WO_4] tetrahedron(Figure 1.9 a). The catalyst shows excellent selectivity and

activity for the electrochemical nitrogen reduction reaction (NRR). This work also offers a versatile synthesis approach for well-defined and high-metal-loading SACs. Lu et al.[54] prepared a high-performance ENRR catalyst WO_x nanoparticle/nitrogen-doped porous carbon (WO_x/NPC) by a one-step thermal pyrolysis method shown in Figure 1.9 b. The results reveal that WO_x gradually changes from the dominant WO_2 phase to the WO_3 phase. WO_x/NPC-700 °C with WO_2 NPs anchored on the surfaces of NPC via W–N bonding could deliver a high NH_3 yield of 46.8 μg h^{-1} mg^{-1} and a high faradaic efficiency (FE) of 10.2%. The edge W atomic site on WO_x/NPC is demonstrated to be the active center which could activate a stable N≡N triple bond with an electron-donating ability. Benefiting from the covalent interaction between the WO_x nanoparticles and NPC, WO_x/NPC also shows high electrocatalytic stability.

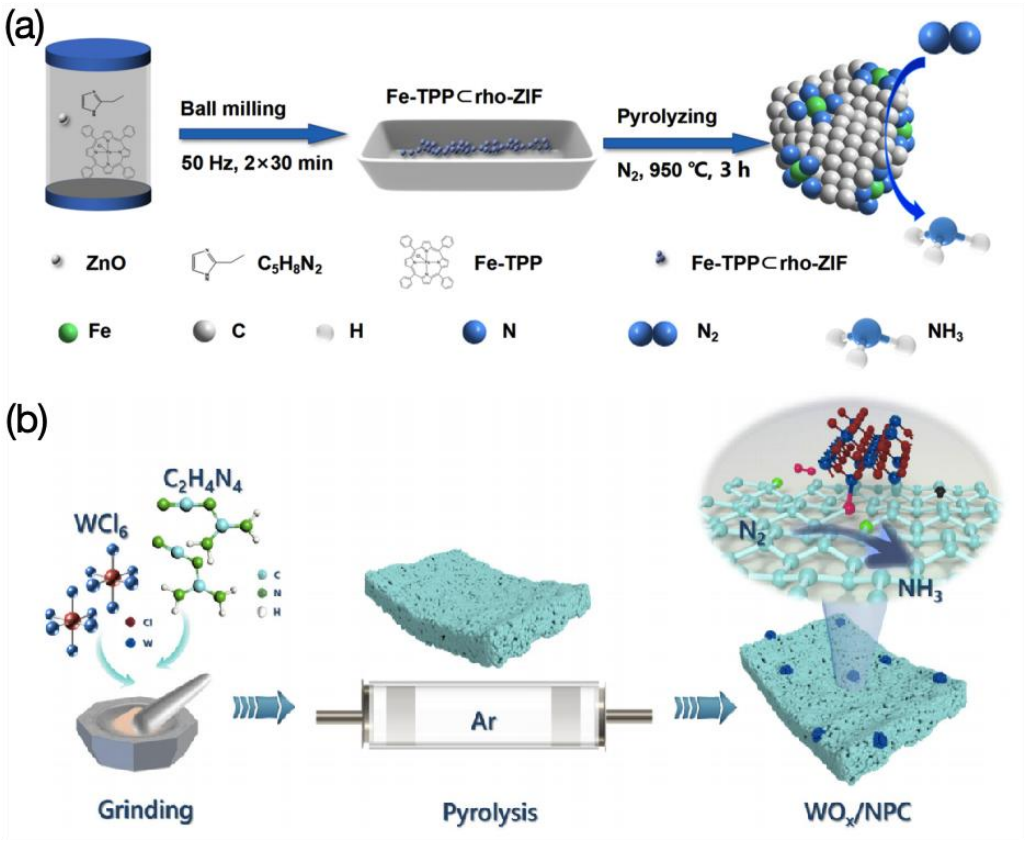

Figure 1.9 (a) Illustration of the formation of W-NO/NC. Ref. [53] (b)Schematic diagram for the preparation of WO_x/NPC. Ref. [54]

Co-based electrocatalysts

Quan et al.[55] reported utilization of a cobalt-based zeolite imidazolate framework (ZIF) to synthesize an atomically dispersed Co electrocatalyst with Co-N_4 active sites for the NRR,

giving an NH3 yield rate of 0.86 μmol cm^{-2} h^{-1} and a Faradaic efficiency (FE) of 10.5% at −0.2 V (vs RHE) in 0.05 M Na_2SO_4 solution. Sun et al.[56] also utilized a cobalt-based zeolite imidazolate framework (ZIF-67) to fabricate a Co single-atom electrocatalyst for the NRR, exhibiting a maximum NH3 yield rate of 5.1 μg_{NH3} h^{-1} $mg_{cat.}^{-1}$ at −0.4 V (vs RHE) and an FE of up to 10.1% at −0.1 V (vs RHE) in 0.1 M KOH solution. Zhang et al.[57] synthesized Co single atoms anchored on N-doped carbon (Co-SAs/NC) by carbonizing a mixture of cobalt acetate, tartaric acid, and polyvinylpyrrolidone. After laser-irradiation treatment, the Co-SAs/NC indicates an enhanced NH_3 yield rate (16.9 μg h^{-1} $mg_{cat.}^{-1}$) and FE (18.8%) at −0.25 V (vs RHE). The improved NRR activity is due to more exposed Co-N_3 sites on Co-SAs/NC after the laser-irradiation treatment. Their studies demonstrated that single Co atoms bound with pyrrolic N (Co-N_4) are major catalytic active sites for N_2 adsorption and activation.

1.4.2 non-metal-based electrocatalysts

So far, transition-metal (TM)-based catalysts have been used in the utmost theoretical and practical analysis for electrocatalytic N_2 reduction. However, most TMs attach N_2 molecules inadequately to stimulate them, resulting in low FE due to the competitive HER side reaction. Non-metal-based electrocatalysts could open up novel avenues for the development of extremely effective electrocatalysts for NRR with minimal HER interaction.[58] In order to reduce the proton supply and increase the diffusion of nitrogen, a new study developed a thermodynamic modulation technique that may be used to impose tunable diffusional constraints on the reactants. Based on a proof-of-concept, a system consisting of proton-filtering covalent organic frameworks (COFs) as a traditional carbon-based electrocatalyst exhibited extremely high activity and selectivity for NRR.[59]

1.4.3 carbon-based electrocatalysts

Due to their affordability, abundance, electric stability, and versatile crystal structures, carbon-based materials are creating a huge demand for electrocatalysis. Graphdiyne (GDY), a recently emerging 2D carbon resource, is also regarded as excellent support for NRR metal-based catalysts due to its special polyyne configuration.[60] Additionally, heteroatom doping is the most practical way of boosting the efficiency of carbon-based NRR catalysts, which can tune the electronic and electrochemical properties of the materials.[61]

Nitrogen (N) doping

The defect-rich N-doped nano-porous carbon (C-ZIF) catalyst was prepared from a zinc-containing zeolitic imidazolate framework (ZIF-8) via a simple heat activation process.[62] The authors heated the ZIF-8 at different temperatures (700-1000 ℃) at different times. As temperature and time increased, highly disordered carbon structures formed with low N-doping content. As demonstrated in Figure 1.10a, the catalyst that was treated at 1100 ℃ temperature for 1 h showed a notable FE of 10.2% and a maximum NH_3 formation efficiency of 3.4×10^{-6} mol cm^{-2} h^{-1} at -0.3 V when tested in KOH (0.1 M) media. To prove the effectiveness of the catalyst, they used DFT calculations that suggested pyridinic N_3 moieties induced thermally in the graphitic layer were highly active sites. According to Figure 1.10b, this pyridinic N_3 moiety consists of one protonated pyridinic nitrogen and one adjacent vacancy that is generated from the removal of one pyridinic nitrogen due to high-temperature treatment. The DFT calculations also imply that, with the help of pyridinic N, the vacancy can effectively adsorb and reduce N_2 molecules to initiate the NRR. Similarly, Liu et al.[63] attained the electrochemical production of NH_3 from N_2 by using ZIF-8-derived N-doped porous carbon (NPC) (Figure 1.10c), which showed a robust activity with an NH_3 product rate of 1.40 mmol g^{-1} h^{-1} at -0.9 V_{RHE}. The high pyrrolic and pyridinic N composition of NPC were the catalytically active centers for NH_3 formation, and the promising route for NH_3 production was $*N\equiv N \rightarrow *NH = NH \rightarrow *NH_2 - NH_2 \rightarrow 2NH_3$, according to the theoretical and experimental analysis. An effective and reliable electrocatalyst for NRR has also been demonstrated by Chen and his team[64] using nanocomposites of nickel oxide encapsulated with N-doped porous carbon (N-PC) dispersed on graphite paper (NAC@NiO/GP). The experimental and theoretical results showed the high performance of NAC@NiO/GP mainly due to the equal contribution of N-PC, NiO NSs coated with N-PC, and GP NiO nanosheets coated with N-PC causing high charge transfer, while N-PC facilitates the NH_3 production by coordination, and finally, NAC@NiO/GP with a vast specific surface area and porosity have more exposed catalytically active centers for NRR. Although N-doping has demonstrated its effect on improving N_2 adsorption on carbon-based catalysts, the restricted electron insertion into adsorbed N_2 by N-doped carbon-based materials severely limits its electrocatalytic NRR performance.

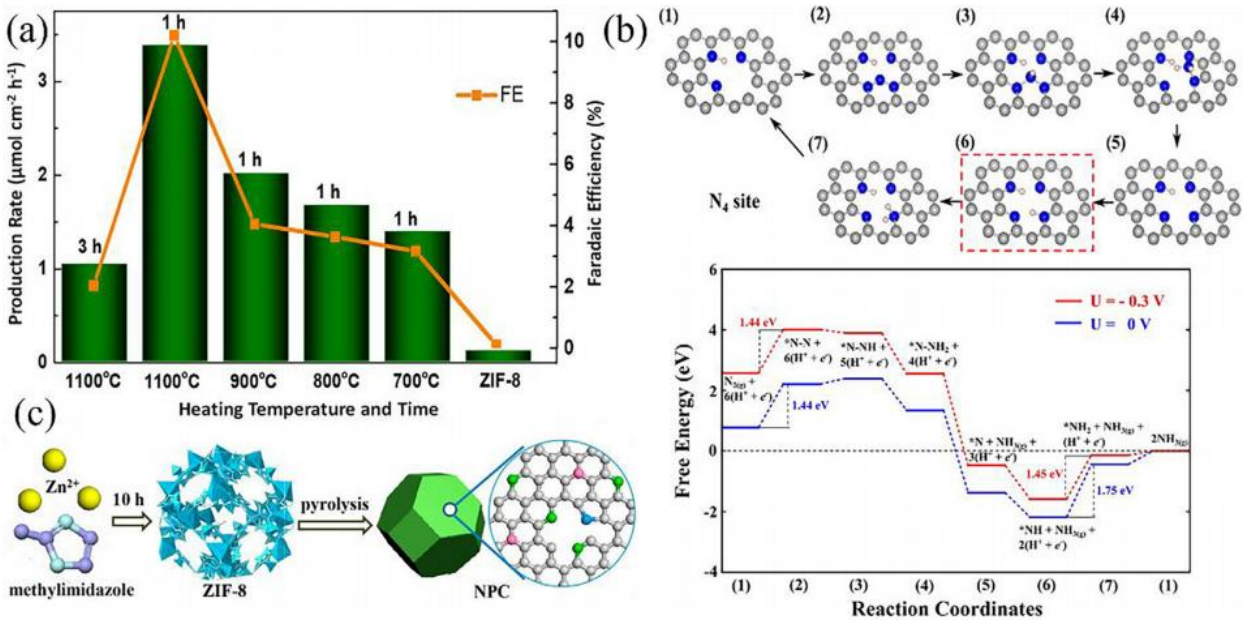

Figure 1.10 (a) Corresponding NH_3 production rates and FEs measured with various catalysts. (b) Atomic structure diagram for NRR on N_3 sites (up); and (down) free energy diagram for NRR on N_3 sites in N-doped carbon. Ref. [62] (c) Schematic illustration of NPC preparation. Ref. [63]

Oxygen (O) doping

The doping of carbon-based compounds with oxygen to adjust their asymmetric charge distribution has a wide range of applications. According to the literature, when oxygen atoms are added to carbon-based materials, they can change the hybridization state from sp^2 to sp^3 and cause structural distortions on the graphitic plane, which results in an altered charge distribution for N_2 activation.[65] Wang et al.[66] annealed sodium gluconate under the Ar atmosphere to prepare O-doped graphene (O-G) for NRR. The test results demonstrated that the highly stable O-doped graphene had the highest FE of 12.6 % and the greater NH_3 product efficiency of 21.3 μg h^{-1} $mg_{cat.}^{-1}$ (Figure 1.11a). Conferring to the DFT calculations, the oxygen containing species support the NRR, and in contrast to the C-O species, the C=O and O-C=O species effectively reduce the energy gap for the rate-determining step. Likewise, Zhao reported a chemically oxidized carbon nanotube(O-CNT) as a highly active catalyst for NRR in $LiClO_4$ solution. The experimental results showed that the C-O species is the main contributor to electrochemical N_2 fixation, giving the maximum FE of 12.50% and the notable NH_3 results of 32.33μg h^{-1} $mg_{cat.}^{-1}$ at 0.4 V. The C-O species in O-CNT exhibits superior N_2 adsorption energy compared to OH, COOH, and C=O species, which differs from O-doped graphene and is crucial for NRR (Figure 1.11b).[67] Wang et al.[68] determined the N_2 fixed sites on different oxygen-containing groups.

DFT results showed that the N≡N and C=O bond lengths increase after the adsorption of N_2, while the vibrational frequency of C=O bonds decreases. According to the results, C=O groups not only show weak adsorption of the intermediate *NH_2 but also provide more hybridization with N_2, revealing key importance in N_2 fixation and activation (Figure 1.11c&d).

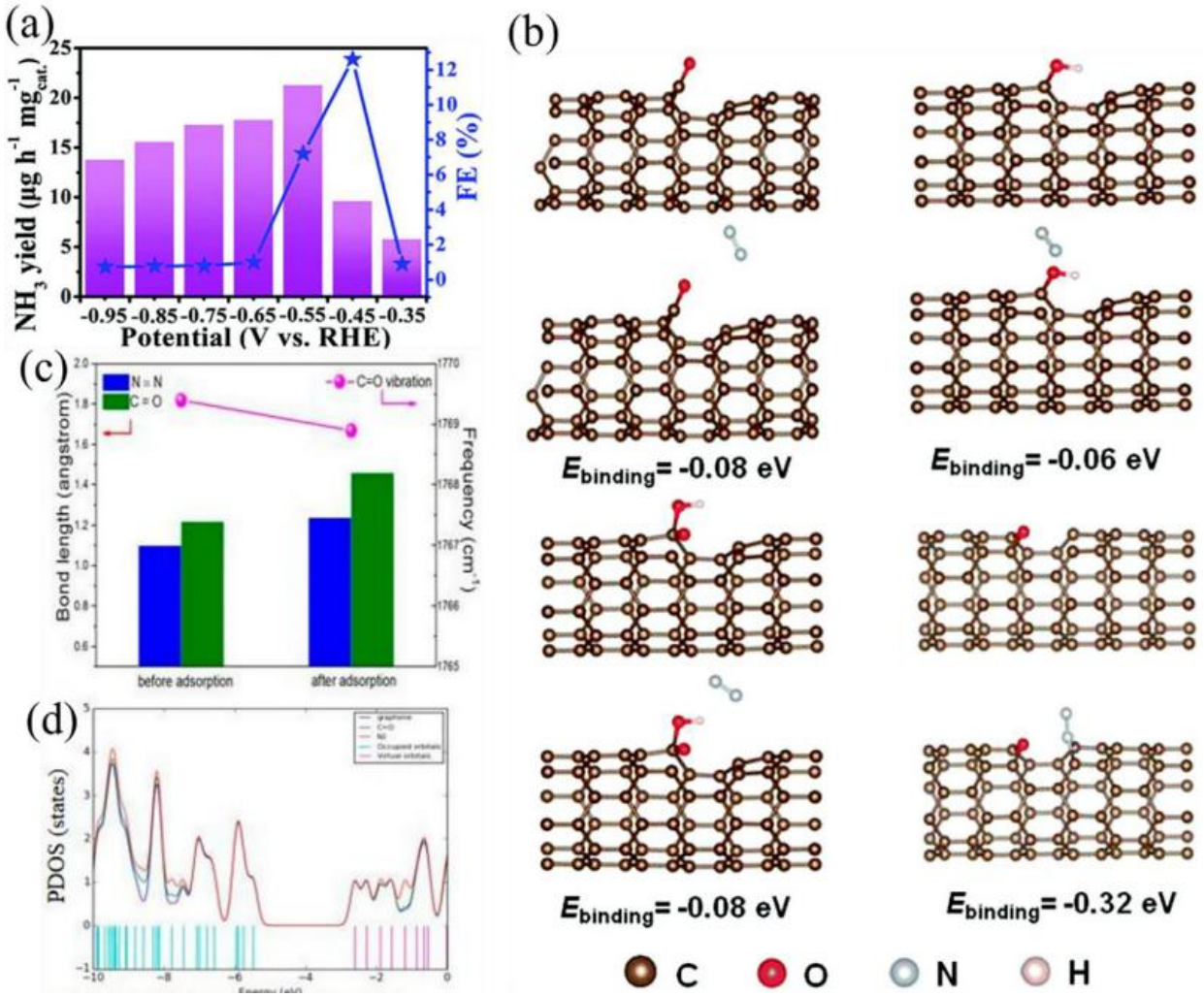

Figure 1.11 (a) Corresponding NH_3 product efficiency and FEs at various applied potentials for O–G/CP. Ref. [66] (b) Schematic representation of O-CNTs model with various oxygen groups and N_2 interactions. Ref. [67] (c) The N≡N bond lengths, C═O bond lengths, and C═O vibration frequencies before and after N_2 adsorption. (d) PDOS for the complex. Ref. [68]

1.5 Challenges in electrocatalytic NRR

In general, the major challenges we face in pursuit of breakthroughs in ambient electrocatalytic NRR can be classified as inherent limitations and technical puzzles. On the one hand, though it is thermodynamically possible to reduce N_2 to NH_3 or NH^{4+} under moderate conditions, the potential window between the NRR and hydrogen evolution reaction (HER) is quite narrow throughout the whole pH range (Figure 1.12a).[69] This means that a highly active electrocatalyst should be explored if NRR was operated at a small overpotential (above line in Figure 1.12a), while an extremely selective one would be required for more negative potentials (below line in Figure 1.12a). In fact, the vast majority of investigated materials were calculated to exhibit more negative onset potentials for NRR compared to those for HER (above the dashed line in Figure 1.12b), especially for the most commonly reported d-block transition metals (blue colored).[14] Besides, the low solubility of N_2 in water (0.66 mmol L^{-1} under ambient conditions[70]) significantly limits the NRR performance compared with the parasitic HER process, which further challenges the possibility for high NRR activity and selectivity simultaneously.

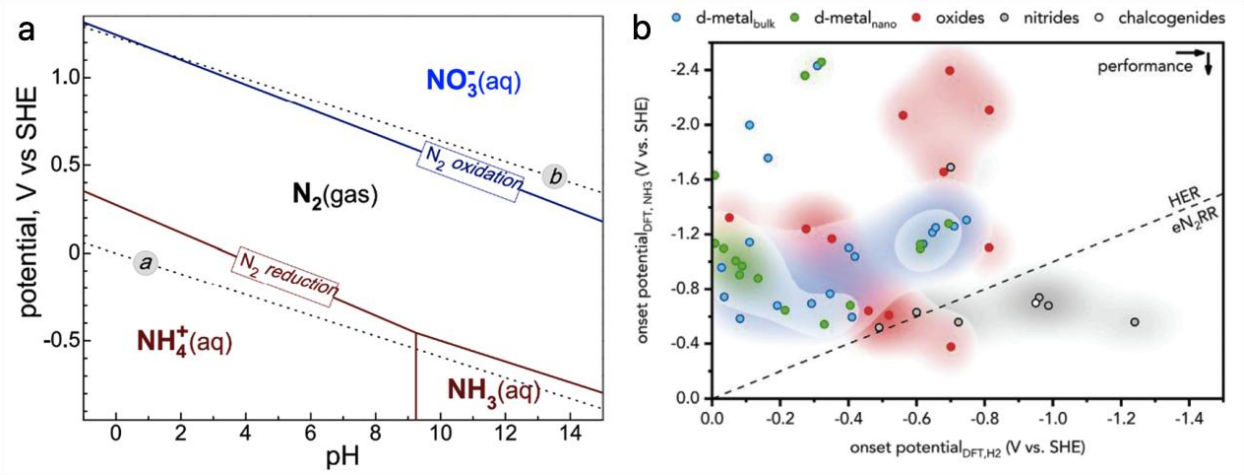

Figure 1.12 Mechanistic insights into electrocatalytic NRR. (a) Partial Pourbaix diagram for the N_2–H_2O system. Ref 72 (b) The calculated onset potentials for NRR and HER of different materials. Ref. 73

On the other hand, ambient ammonia contamination during experiments is inevitable and significant, thus making it difficult to detect NRR-generated ammonia accurately.[71] Due to its high polarity and aqueous solubility, ammonia (in the form of NH_3 or NH^{4+}) can be ubiquitous in all aqueous solutions and many surfaces, including atmosphere, oven, human respiration, latex

glove, lab coat, sample tubing, Nafion membrane, stored samples, stale Milli-Q water, etc. For example, the dissolved ammonia (32 wt%) in a Nafion 117 membrane (1 cm^2×25 μm) was estimated to be 136.4 μg;[72] acid trapped (50 mL of 0.01 M HCl) ammonia under an air-conditioner for 12 h can be 7.65 μg; and latex gloves can provide 41.70 μg of ammonia as new and ~15 μg after washing.[73] Considering a relatively good NRR performance with NH_3 yield of 3×10^{-10} mol s^{-1} cm^{-2} for a 1×1 cm^2 electrode and 2 h reaction time, the NRR-generated ammonia is only 36.72 μg. Therefore, ambient ammonia contamination could very likely lead to uncertainty, non-repeatability, and even false positives of results if the experiment wasn't conducted properly and carefully.[74-76]

Although an attractive subfield of electrocatalysis, ambient electrocatalytic NRR still suffers from a lack of benchmarking and best practices. To date, there is not yet a suitable catalyst that can be employed as the standard catalyst for ambient electrocatalytic NRR research. The electrochemical cell configuration and test techniques also vary between different research groups, and are not fully described in most literature with omissions in gas flow rate, electrolyte volume, sampling methods, *etc.* The influences of some critical experimental parameters on the measured activity and selectivity remain to be thoroughly investigated. This causes remarkable challenges and unreliability when directly comparing the results obtained by different groups. It can also substantially mask the problems that require attention, reduce the impact of our individual research, and hinder the anticipated progress in this field.

1.6 Strategies for NRR

Some representative strategies to improve ENRR by promoting N_2 activation and inhibiting competing responses have been proposed.

1.6.1 Doping

Doping with atoms of different sizes and charge to the original electrocatalyst has been widely suggested in various electrocatalytic applications. The dopants can alter the electrocatalyst's electronic structure and change the binding strength of the reactant, intermediate, or product at active sites. Thus, they govern the electrocatalytic performance. [77,78]

Mukherjee et al. prepared defect-rich N-doped nano-porous carbon (C-ZIF) catalyst which showed a notable FE of 10.2% and a maximum NH_3 formation efficiency of 3.4×10^{-6} mol cm^{-2} h^{-1} at -0.3 V when tested in KOH (0.1 M) media. Wang et al.[66] annealed sodium gluconate under

the Ar atmosphere to prepare O-doped graphene (O-G) for NRR. The test results demonstrated that the highly stable O-doped graphene had the highest FE of 12.6 % and the greater NH_3 product efficiency of 21.3 μg h^{-1} $mg_{cat.}^{-1}$. Wei et al.[79] employed spin-polarized density functional theory to proposed Fe-doped monolayer phosphorene (Fe–P) as catalyst for NRR. Their results show that single-atom Fe is the active site, cooperating with P to activate the inert N–N triple bond and reduce N_2 to NH_3 via three reliable pathways.

These reports demonstrated that the doping strategy could adjust key factors for the ENRR by developing defect sites, providing, or inducing neighbor's active sites, ordering/disordering the shift, surface area, and so on.

1.6.2 Single Atom Catalysts

Single atom catalyst (SAC) synthesis has been regarded as a promising technique for catalyst development. The prepared SACs show outstanding catalytic performances with an extremely high number of active sites and unique electronic properties affecting catalytic pathways.[80] Metal SACs — such as Au, Cu, Fe, and so on — have been proposed and exhibited excellent ENRR performances.

Naturally, NH_3 can be produced by the biological N_2 fixation over nitrogenase enzyme comprising Fe metal with ligands.[81] Xijun Liu et al. synthesized a Fe single atom on N-doped carbon frameworks (FeSA-NC) inspired by the nitrogenase using the hydrothermal method followed by carbonization.[82] The FeSA-NC exhibited an FE of 18.6% and an NH_3 production rate of 62.9 μg h^{-1} cm^{-2} at -0.4 V_{RHE} in 0.1 M phosphate buffer solution. The ENRR performance of FeSA-NC was highly advanced compared to that of FeNPs-NC. The presence of single Fe atoms on NC was revealed by EXAFS, where the Fe-N bond was shown with a negligible Fe-Fe bond, representing the Fe atom's coordination with the nitrogen atoms but not between the Fe atoms. This result indicates that the Fe-N sites provide an active site for N_2 adsorption and that Fe single atoms contribute to weakening the triple-bond length of N_2 from 1.098 to 1.134 Å.

This subsection demonstrated that SACs have various properties compared to nanoparticle catalysts. For example, SACs change their oxidation state or those of surrounding materials, effectively adsorbing N_2 and weakening the triple bond, consequently enhancing the ENRR.

1.6.3 Surface Modification

The formation of the three-phase boundary (TPB) of N_2(g)-catalyst(s)-H_2O(l) is critical for the actual ENRR.[83] The advanced TPB can effectively suppress HER, the representative competitive reaction, and develop the NH_3 production rate. In typical aqueous ENRR systems, the low N_2 solubility (0.0126 mg g^{-1}) prevents the effective transfer of N_2, unlike the free accessibility of H_2O, causing a significantly lower N_2 concentration near catalysts than H_2O.[84] It provides an insufficient TPB condition, resulting in an ineffective FE and production rate for ENRR.

One strategy to advance the TPB is modifying the electrode's surface which has a partial hydrophobic nature. Xing Yi Ling et al. suggested coating over the Ag-Au catalyst with the hydrophobic zeolitic imidazolate framework-71 (ZIF-71) (Ag-Au@ZIF-71) by a wet chemical deposition.[85] The distinct characteristics of ZIF-71, having a unique pore structure comprising metal centers and hydrophobic functional groups of dichloroimidazole linkers provides a superhydrophobic barrier, effectively suppressing the free access of H_2O to catalysts.[86] Furthermore, the N_2 molecules can freely diffuse through the ZIF-71 layer and thus be concentrated near the catalyst surface. The relatively reduced H_2O concentration and increased N_2 concentration on catalysts by surface modification with ZIF-71 develop the TPB, effectively resulting in an enhanced ENRR. Ag-Au@ZIF-71 electrode exhibited an advanced FE of 18 ± 4% and an NH_3 production rate of ~0.648 μg h^{-1} cm^{-2} at −2.9 $V_{Ag/AgCl}$ in the solution of 0.2 M $LiCF_3SO_3$ added to ethanol containing dry tetrahydrofuran (TPB), whereas the uncoated Ag-Au electrode showed an FE of only 9% and an NH_3 production rate of 0.1296 μg h^{-1} cm^{-2}. Furthermore, continuous local N_2 saturation led to long-term stability with improved accessibility of N_2 to the catalyst's surface by ZIF-71. The Ag-Au@ZIF-71 represented constant CV features during 45 consecutive potential sweeps between −3 and −0.5 $V_{Ag/AgCl}$. On the other hand, the Ag-Au catalyst showed that the shape of CV was continuously deformed during the consecutive experiments, gradually flattening.

Furthermore, Pei Kang Shen et al. suggested a way for accumulating N_2 molecules to increase the relative N_2 concentration, resulting in superior TPB for ENRR.[87] They prepared an aerobic-hydrophilic hetero-structured electrocatalyst using ultrathin Bi_5O_7I nanotubes (UP-BOIN) and carbon spheres. The UP-BOIN served as the active sites and showed a highly porous surface structure with a diameter of about 5 nm with a hollow tubular geometry. This morphological trait provides a super-aerophilic nature. Then, the UP-BOIN was combined with the hydrophilic carbon sphere, modified by immersing them in H_2O_2 and 70 wt % H_2SO_4 in

series. The combined aerophilic UP-BOIN and hydrophilic carbon sphere can control N_2 accumulation and H_2O accessibility, affecting the superior TPB formation. For example, the 75% UP-BOIN with the 25% carbon sphere sample shows an FE of 6.10% and an NH_3 production rate of 2.286 μg h^{-1} cm^{-2} at −0.4 V_{RHE} in 0.1 M Na_2SO_4. On the other hand, the electrode of 0% UP-BOIN with a 100% carbon sphere shows an FE and a production rate close to 0, indicating that UP-BOIN is a key electrocatalyst providing active sites. Furthermore, the sole UP-BOIN showed a significantly lower 5.19% FE and 0.796 μg h^{-1} cm^{-2} NH_3 production rate compared to the carbon sphere combined UP-BOIN. This indicates that the effective control of reactant concentration, including H_2O, is critical for providing a sufficient TPB for the ENRR.

1.7 Thesis Objectives and Organizations

1.7.1 Thesis objectives

This paper aims to optimize the yield rate and Faradaic efficiency of ammonia synthesis at normal temperature and pressure by developing a series of NC-based NRR catalysts doped with other elements, such as OENC, WFeNC, FeCoNC.

(1) In this work, a bimetallic nitrogen-doped carbon NRR catalyst (WFeNC) is synthesized, and a nitrogen limitation strategy is proposed by plasma etching the catalyst to solve the problem of limited reactant supply for NRR under ambient conditions. After plasma etching, a large number of voids appear on the catalyst P-WFeNC, which are fully sufficient to serve as a reservoir for N_2 nanobubbles. A large number of characterization methods are used to verify the above conclusions. First, we use molecular simulations to understand the agglomeration state of nitrogen in 0.1M HCl solution and the size of the agglomerates. BET is then used to test whether the size of the voids in the material after plasma etching matched the size of the nitrogen agglomerates in the molecular simulation. Then, we characterize the surface of the catalyst undergoing NRR through in-situ XRD technology to confirm whether nitrogen is adsorbed and stored in it. Subsequently, whether P-WFeNC can effectively trap N_2 nanobubble is evaluated based on trapping bubble experiments. Finally, by comparing whether the NH_3 yield rate and Faradaic efficiency of the catalyst before and after plasma etching are improved to verified whether this strategy is suitable for NRR.

(2) In this work, we design a catalyst (OENC) doped with oxygen as a secondary heteroatom that can promote ambient ammonia synthesis on nitrogen-doped carbon by triggering a

cooperative electron promotion effect. To gain deeper insight into the involved reaction mechanisms of NRR on OENC, DFT calculations are performed to study the free energy profiles, including the distal pathway and the alternating pathway. Through Raman testing, the intensity ratio of the D band and G band (I_D/I_G) for NC ONC and OENC is compared to confirm the presence of enriched oxygen. Subsequently, the chemical nature and bond structure of different structures are investigated by X-ray photoelectron spectroscopy (XPS). Subsequently, by testing and comparing the NH_3 yield, Faradaic efficiency, and H_2 selectivity of NC ONC and OENC to verify whether the electronic promoting effect will boost ambient ammonia synthesis. Finally, ^{15}N isotope labeling experiments is conducted to further investigate the N source of the produced ammonia.

(3) Since the two occupied d orbital heteronuclear metal atoms in the dimer site can simultaneously trap two lone-pair electrons at two ends of the N_2 molecule and enable the asymmetrical electron backdonation, which is beneficial to the polarization of N≡N bond and thus facilitates its weakening. In this work, asymmetrical heterobimetallic (Fe, Co) sites is proposed to break the inherent scaling relations between the binding strength of intermediates of NRR as multi-intermediate reaction. Density functional theory (DFT) calculations is used to verify whether the strong electronic interaction between N_2 and dimer sites enables maximized activation of N_2 and regulation of the binding strength of the key intermediates, thereby greatly reducing the energy barrier of the overall NRR process. The aberration-corrected high-angle annular dark field scanning transmission electron microscopy (AC-HAADF-STEM) is then conducted to elucidate the existential form of Fe and Co atoms. To further confirm FeCoNC structure in atomic level, we will take X-ray absorption near-edge structure (XANES) and extended X-ray absorption fine structure (EXAFS) analyses with Fe foil and Co foil as references. Subsequently, by testing and comparing the NH_3 yield, Faradaic efficiency, and H_2 selectivity of FeNC and FeCoNC to verify whether the electronic promoting effect will boost ambient ammonia synthesis. Finally, ^{15}N isotope labeling experiments is conducted to further investigate the N source of the produced ammonia.

1.7.2 Thesis organizations

Chapter 1 Introduction： This chapter provides the general introduction, introduces the background and motivation of my research, research progresses and the existing challenges in NRR field, following with the objectives of my projects.

Chapter 2 Experimental: This chapter provides the experimental and computational details. Synthesis methods of all the samples, physical and electrochemical characterization information, N_2 reduction products analysis, adopted models and parameters for theoretical calculations are all provided.

Chapter 3 corresponds to the first objective. A nitrogen confining strategy achieved by plasma etching has been proposed to address the challenge of limited reactant supply for nitrogen reduction reaction under ambient conditions. Upon plasma etching, a large number of voids appeared on catalyst P-WFeNC, which were totally sufficient to serve as the reservoir for N_2 nanobubbles. The publication related to this chapter is:

Na Xu, Daniele Benetti, Chenglin Yan, Federico Rosei, Confining nitrogen nanobubbles within plasma etched voids to promote reactant supply for enhanced electrochemical nitrogen reduction reaction under ambient conditions. *Chemical Engineering Journal,* 2023, 474, 145830.

Chapter 4 corresponds to the second objective. Synergistic electronic promoting effect is deliberately triggered through doping oxygen as secondary heteroatom to boost ambient ammonia synthesis on nitrogen-doped carbon. The electronic structure and the polarity of adjacent carbon atoms are further optimized, significantly lowing the energy barrier of the overall nitrogen reduction process. The publication related to this chapter is:

Na Xu, Qiyang Cheng, Mengfan Wang, Yanzheng He, Haoqing Ji, Federico Rosei, Triggering synergistic electronic promoting effect through oxygen doping to promote electrochemical nitrogen reduction on metal-free electrocatalyst. *Inorganic Chemistry Frontiers,* 2023, 10, 7010-7017.

Chapter 5 corresponds to the third objective. Asymmetrical heterobimetallic FeCo sites is proposed to break scaling relations in NRR and boost ambient ammonia synthesis. According to the DFT calculations, the heteronuclear FeCo dimer sites featuring the polarized surface with multielectron sites enable weakening of N≡N bond and maximized activation of N_2. The optimization of the adsorption energies of certain intermediates thus become feasible, contributing to significantly reduced energy barrier of the overall nitrogen reduction process. The publication related to this chapter is:

Na Xu, Yanzheng He, Mengfan Wang, Chen Cheng, Qiyang Cheng, Sisi Liu, Haoqing Ji, Chenglin Yan, Federico Rosei, Breaking scaling relations in nitrogen reduction with asymmetrical heterobimetallic FeCo sites to boost ammonia synthesis. *Materials Chemistry Frontiers,* 2024, 8, 851-858.

Chapter 6 Conclusions and perspectives: This chapter briefly summarizes the main conclusions of my research and provides the challenges and perspectives toward this field.

2 EXPERIMENTAL

2.1 Chemicals and Materials

Pyrrole (C_4H_5N,>99.7%), sodium chloride (NaCl, 99.8%), potassium permanganate ($KMnO_4$,99.5%), potassium hydroxide (KOH, 99.99%), silicon dioxide (SiO_2), hydrogen peroxide (H_2O_2, 30 wt. % in H_2O), sodium hypochlorite solution (NaClO, 6-14% active chlorine basis), hydrochloric acid (HCl, 37%), ethanol (CH_3CH_2OH, 95%) and hydrofluoric acid (HF, >40%) were purchased from Shanghai Aladdin Biochemical Technology Co. Ltd. Iron(II) chloride ($FeCl_2$, 99.5%), cobalt(II) chloride ($CoCl_2$, 99.7%), zinc chloride ($ZnCl_2$, 99.95%), trisodium citrate ($C_6H_5O_7Na_3$, 99%), nafion solution (5 wt%) and salicylic acid ($C_7H_6O_3$, 99%) were purchased from Alfa Aesar. Tungsten (VI) chloride (WCl_6, ≥99.9%), sodium nitroferricyanide dihydrate ($Na_2[Fe(CN)_5NO] \cdot 2H_2O$, 99%) and 4-(Dimethylamino)benzaldehyde ($(CH_3)_2NC_6H_4CHO$, 98%) were purchased from Sigma-Aldrich. Carbon paper was purchased from CeTech Co., LTD. Argon (Ar, 99.99%) was purchased form Air Liquid. H_2 was manual sampling and analyzed by gas chromatography (GC-2014, Shimadzu). The $^{14}N_2$ commercially purchased from Messer Gas Product Co., Ltd. (Germany) and $^{15}N_2$ commercially purchased from Newradar Special Gas Co., Ltd. (China). Deionized water was purified by a Millipore Ultrapure water system in our lab.

2.2 Synthesis of catalyst

2.2.1 Synthesis of catalyst WFeNC and P-WFeNC

First, pyrrole was dispersed evenly in deionized water with rapid stirring of the magnet. A bright yellow and transparent solution was formed after several hours of reaction with ferrous chloride and hydrogen peroxide. After drying at 100 ℃ over 24 h, the brown powders were collected for further use. Subsequently, the brown powder, sodium chloride, zinc chloride, and tungsten pentachloride were dissolved in deionized water and stirred for 24 h. The solution was dried product was at 100 °C until obtaining the mixture powders, followed by pyrolysis at 600 °C for two hours while being protected by Ar. The carbonized product was sufficiently washed with a lot of water and ethanol to remove the salt templates and then acid-washed to remove metal oxide, and the final WFeNC catalyst was obtained by freeze-drying. P-WFeNC was obtained by using a plasma cleaner to irradiate WFeNC at 20 kV for 80 s.

2.2.2 Synthesis of catalyst FeNC

To prepare FeNC, 2 ml pyrrole was adequately dispersed in deionized water by ultrasonic vibration. Excess ferrous chloride and hydrogen peroxide were added, and the reaction lasted several hours until a bright yellow and transparent solution was obtained. Sodium chloride, zinc chloride, and silicon dioxide was further dissolved in the solution to be used as a template. The product was collected by freezedrying to obtain brown powders. The material was then placed in a ceramic boat and carbonized at 700 °C for 2 h under argon protection. The carbonized material was firstly washed with hydrofluoric acid to remove the silicon dioxide. Then, after removing the salt templates through sufficient washing with a lot of water and ethanol, the products were dried in a vacuum at 60 °C overnight prior to use.

2.2.3 Synthesis of catalyst FeCoNC

To prepare FeCoNC, 2ml pyrrole was adequately dispersed in deionized water by ultrasonic vibration. Excess ferrous chloride, cobalt chloride, and hydrogen peroxide were added, and the reaction lasted several hours until a bright yellow and transparent solution was obtained. Sodium chloride, zinc chloride, and silicon dioxide was further dissolved in the solution to be used as a template. The product was collected by freeze-drying to obtain brown powders. The material was then placed in a ceramic boat and carbonized at 700 °C for 2 h under argon protection. The carbonized material was firstly washed with hydrofluoric acid to remove the silicon dioxide. Then, after removing the salt templates through sufficient washing with a lot of water and ethanol, the products were dried in a vacuum at 60 °C overnight to obtain black powders.

2.2.4 Synthesis of catalyst OENC, ONC, and NC

Typically, pyrrole was dispersed in deionized water, followed by the dissolution of ferrous chloride and sodium chloride. After adding 20 ml H_2O_2 to the solution, pyrrole polymerization was initiated. The solution was freeze-dried after vigorous stirring for 24 h. Then, the obtained material was placed in a ceramic boat and carbonized at 800 °C for 2 h under argon protection. After removing the salt through aqueous washing, the samples were dried under vacuum to obtain black powders. Finally, the materials were treated with hydrochloric acid and washed successively with deionized water and ethyl alcohol, and then dried in vacuum at 60 °C overnight to obtain OENC. ONC was fabricated through the same strategy as OENC, except changing the added H_2O_2 to 10

ml. NC was further prepared by annealing the ONC at 300 ℃ for 2 h in Ar/H_2 atmosphere.

2.3 Characterizations

2.3.1 Physical characterizations

General characterization. The morphology was studied via a field emission scanning electron microscope (FESEM, SU8010, Japan) and a field emission transmission electron microscope (FETEM, FEI Tecnai G2 F20 S-TWIN TMP, Hongkong). The dispersion of single Fe and Co atoms was characterized by atomic resolution high-angle annular dark-field scanning transmission electron microscopy on a JEOL JEM-ARM200F instrument equipped with a probe spherical aberration corrector. The XANES and the EXAFS spectra were obtained at 1W1B station in Beijing Synchrotron Radiation Facility (BSRF). The storage rings of BSRF were operated at 2.5 GeV with a maximum current of 250 mA. The data collection was carried out in transmission mode using Si (111) double-crystal monochromator, ionization chamber for Fe foil, Co foil and in fluorescence excitation mode using a Lytle detector for FeCoNC. N_2 adsorption analysis was performed by an ASAP 2460 accelerated surface area and porosimetry instrument (Micromeritics) equipped with an automated surface area, using BET to calculate the surface area at 77 K. The catalyst was characterized by X-ray diffraction (XRD, D8 Advance, Bruker) and Raman spectroscopy (HR evolution, Horiba Jobin Yvon, France). Surface elemental analysis was performed on XPS (Kratos Axis Ultra Dld, Japan). The bubble contact angle (CA) was measured by the captive bubble method using a video optical contact angle measuring instrument (OCA20, Dataphysics Inc., Germany) under ambient conditions. A plasma cleaner (Tonson TS-PL02) was reconfigured for the plasma irradiation process.The absorption spectrum was measured using an ultraviolet-visible spectrophotometer (UV-2700i, Shimadzu).

In situ XRD characterization. A tailor-made cell was specially customized for electrochemical measurements. The Ag/AgCl (4 M KCl) and graphite rod were used as the reference and counter electrodes, respectively. 0.1 M HCl solution was used as the electrolyte. The catalyst ink was generated by ultrasonically dispersing 5 mg P-WFeNC in 475 μl ethanol and 25 μl Nafion solution (5 wt%) for at least 1 hour. The ink was deposited on carbon paper to serve as the working electrode. The in situ XRD measurements were performed using an X-ray powder

diffractometer (Bruker D8 Advance). The potentiostatic test was carried out using a CHI660E electrochemical workstation (Shanghai Chenhua Instrument Co., Ltd) at -0.3 V vs. RHE. During the in-situ characterization, the working electrode was constantly bubbled with N_2.

2.3.2 Electrochemical characterizations

Cathode preparation. First, 1 mg of catalyst was dispersed in 980 μl of ethanol, to which 20 μl of Nafion solution (5 wt. %) was added and sonicated for one hour. The mixed solution was used as homogeneous ink. Then, 50 μl of ink was evenly coated on the carbon paper over an area of 1×1 cm^2 and dried at 80 °C for three hours. The obtained electrode was used for electrochemical measurements.

Electrochemical NRR measurements. The reduction of N_2 gas was carried out at room temperature in a two-chamber cell which was separated by a Celgard membrane with hydrophilic treatment. A three-electrode system was used for electrochemical measurements, with a carbon rod as the counter electrode and Ag/AgCl (4 M KCl) as the reference electrode. All measured potentials are converted to standard potentials versus RHE by calibration. Purified N_2 was continuously fed into the cathode section at a certain flow rate through a suitable sprayer, ensuring that the entire working electrode is in full contact with N_2 gas bubbles during the experiment. Electrochemical NRR reactions were carried out in N_2-saturated 0.1 M HCl at ambient temperature and pressure. The potentiostatic tests were carried at different potentials including -0.1, -0.2, -0.3, -0.4, -0.5 V vs. RHE. After the electrochemical reduction reaction, the electrolyte was collected and quantitatively analyzed either by colorimetric method or ^1H NMR spectroscopy.

Determination of ammonia in the electrolyte. To ensure that no NH_3 remains in the purified gas, the gas is passed into ultrapure water at a flow rate of 50 standard cubic cm per min (sccm) for 1 h. The obtained solution was analyzed using the indophenol blue method with some improvements. Specifically, 2 ml of 1 M sodium hydroxide solution containing sodium citrate and salicylic acid were mixed with 2 ml of treated water. Then, 1 ml of 0.05 M sodium hypochlorite solution and 0.2 ml of 1 wt.% sodium nitroferricyanide were added into the solution. The above mixture was shaken well and left to stand in the darkness for 2 hours, then the UV-vis absorption spectrum was measured. The absorbance at 655 nm was used to determine the concentration of indophenol blue. Ultrapure water was used as a blank (zero) for the baseline. The concentration-absorbance curves were calibrated using a standard ammonium chloride solution with a series of concentrations in H_2O.

For quantitative ^{1}H NMR measurements, various concentrations of ammonium sulfate were used to prepare the standard curve. The electrolyte was removed after electrolysis at -0.2 V vs. RHE. Then, the solution was concentrated to 0.5 ml and was mixed with 0.1 ml of dimethylsulfoxide-d6. Maleic acid was used as the internal standard. The produced ammonia was quantified by using ^{1}H NMR spectroscopy (Agilent 600 MHz).

Determination of NO_x contamination in purified gas. NO and NO_2 can be converted into NO_2^- and NO_3^- and captured once passing through the oxidising and alkaline traps. NO_2^- was determined by Griess spectrophotometric method. The test gas was fed into 50 ml gas absorption solution with 30 sccm for 1 hour. 0.5 g sulfanilic acid was dissolved in a mixture of 5 ml acetic acid and 90 ml H_2O. Then, 5 mg N-(1-naphthyl)-ethylenediamine dihydrochloride was added and the solution was filled to 100 ml to obtain chromogenic agent. 4 ml chromogenic agent were added into the 1 ml gas absorption solution. After further standing for 15 min, the UV-vis absorption spectrum was measured at 540 nm. The concentration-absorbance curves were calibrated using standard sodium nitrite solution with a series of concentrations in H_2O. NO_3^- was determined by sulfamic acid method. In detail, the test gas was fed into 50 ml gas absorption solution with 30 sccm for 1 hour. 0.1 ml 1 M HCl and 0.01 ml 0.8 wt.% sulfamic acid solution were added into the gas absorption solution. The absorption spectrum was recorded using an UV-Vis spectrophotometer. The final absorbance value was calculated by this equation: $A = A_{220\ nm} - 2A_{275\ nm}$. The concentration-absorbance curves were calibrated using standard sodium nitrate solution with a series of concentrations in H_2O.

Determination of produced hydrazine. The hydrazine present in 0.1 M HCl was estimated by the Watt and Chrisp method. A mixture of para-(dimethylamino) benzaldehyde (5.99 g), HCl (concentrated, 30 ml), and ethanol (300 ml) was used as the chromogenic reagent. Next, 5 ml of the residual electrolyte after the NRR potentiostatic test was collected from the electrochemical reaction vessel. Then, 5 ml of the above prepared chromogenic reagent was added to the solution, and the mixture was stirred for 10 min at room temperature. The absorbance of the resulting solution was measured at a wavelength of 455 nm. The concentration-absorbance curves were calibrated using standard hydrazine monohydrate in 0.1 M HCl solution at a series of concentrations.

Determination of hydrogen evolution. The H_2 was manual sampling and analyzed by gas chromatography (GC-2014, Shimadzu).

Isotope labeling experiments. The ^{15}N isotopic labeling experiments with purified $^{15}N_2$ (99 atom% ^{15}N) as the feeding gas were conducted to clarify the source of ammonia. After NRR in

0.1 M HCl solution at -0.3 V vs. RHE, the obtained $^{15}NH_4^+$ in the electrolyte was identified by the ^1H NMR measurement.

Nitrogen purification. The $^{14}N_2$ commercially purchased from Messer Gas Product Co., Ltd. (Germany) and $^{15}N_2$ commercially purchased from Newradar Special Gas Co., Ltd. (China) were sequentially flowed through acid (0.1 M HCl), oxidising (0.1 M $KMnO_4$), and alkaline traps (0.1 M KOH) to remove possible contaminants, including NH_3, NO, and NO_2. Then, the gas was passed through a drying tube to prevent water vapor from entering the electrochemical cell.

Faradaic efficiency and the yield rate. The Faradaic efficiency and yield rate of NH_3 were calculated as follows:

$$\text{Faradaic efficiency } (NH_3) = [3F \times c(NH_3) \times V] / Q \qquad (2.1)$$

$$\text{Yield rate } (NH_3) = [17c(NH_3) \times V] / (t \times m) \qquad (2.2)$$

where F is the Faraday constant (96,485 C mol^{-1}), t is the electrolysis time (1 h), m is the loading mass of the catalysts, Q is the total charge passed through the electrode, V is the volume of the electrolyte, and $c(NH_3)$ is the measured ammonia concentration.

The Faradaic efficiency of H_2 was calculated as below:

$$\text{Faradaic efficiency } (H_2) = [2 \times V_j \times P \times V \times 10^{-3} / RT] / [I_{total} \times t_H / F] \qquad (2.3)$$

where V_j is volume percentage obtained from the GC analysis of H_2, P is the atmospheric pressure (101.325 KPa), R is the gas constant (8.314 J mol^{-1} K^{-1}), V is the volume of sampling loop (1 cm^3), T is the temperature in Kelvin (298.15 K), I_{total} is the recording current, and t_H is the time required to fill the sampling loop.

2.4 Theoretical calculations and molecular dynamics

2.4.1 DFT computational method and model.

The first-principles calculations were conducted using the Vienna ab initio simulation package (VASP). The Perdew-Burke-Ernzerhof with generalized gradient approximation (GGA) was adopted to describe the electron–electron interaction. An energy cutoff of 450 eV was used, and a k-point sampling set of 3 × 3 × 1 was tested to be converged. The criterion for all structural optimizations was set to 10^{-5} eV for electronic energy convergence and Hellmann−Feynman force less than 0.01 eV $Å^{-1}$ for ionic relaxation loop. The vacuum space along the z-direction is

set to be 15 Å. The Hubbard U correction was also employed within the DFT+U approach in all spin polarized calculations. The van der Waals dispersion forces was included using the zero damping DFT-D3 method of Grimme. The implicit solvent model, VASPsol, was applied to considered effects between the solute and solvent on the activation energies. The adsorption energy ΔE of the A group on the surface of the substrates was defined as:

$$E_{ads} = E_{*+intermediate} - E_{*} - E_{molecule} \quad (2.4)$$

where $E_{*+intermediate}$ and E_{*} are the energies of the surface with and without adsorbed molecules, respectively, and the $E_{molecule}$ is the energy of the molecule in the gas phase. Gibbs free energy change (ΔG) of each chemical reaction is calculated by:

$$\Delta G = \Delta E - T\Delta S + \Delta ZPE + \Delta G_{pH} \quad (2.5)$$

where ΔE is the total energy difference between reactants and products in a specific step, ΔZPE is the zero-point energy correction and ΔS is the entropy change in the reaction step. Here, T was set as room temperature (298.15 K). ΔG_{pH} is the contribution of H^+ and is equal to $-k_B T \times \ln(10) \times pH$, where k_B is the Boltzmann constant.

2.4.2 Molecular dynamics (MD) simulations model and method

All MD simulations were performed with Gromacs 2019.6.[88,89] The simulation system with an edge length of roughly 12 nm, including 9 N_2 columns run through the simulation box from the top to the bottom. In the study of distribution of N_2 molecules in 0.1 M HCl solution within 5 ns, 100 H^+, 100 Cl^- and 1350 N_2 molecules were initially added into the simulation box, and then the box was solvated with 54538 H_2O molecules. The above model construction processes were performed using the PACKMOL package.[90] snapshots of N_2 distribution in 0.1 M HCl at 2, 3, 4, and 5 ns

Water, nitrogen, and hydrogen chloride were described by the SPC/E model,[91] TraPPE rigid model,[92] and the parameters from Botti et al.,[93] respectively.

The average span S_A of nitrogen cluster is defined as:

$$S_A = (S_x + S_y + S_z) / 3 \quad (2.6)$$

where S_x, S_y, and S_z represent the span of the nitrogen cluster in the three directions of x, y, z axi.

3 Confining nitrogen nanobubbles within plasma etched voids

Confining nitrogen nanobubbles within plasma etched voids to promote reactant supply for enhanced electrochemical nitrogen reduction reaction under ambient conditions

Confinement des nanobulles d'azote dans des vides gravés au plasma pour favoriser l'apport de réactifs pour une réaction électrochimique améliorée de réduction de l'azote dans des conditions ambiantes

Authors:

Na Xu[a, b], Qiyang Cheng[a], Mengfan Wang[a], Daniele Benetti[b], Chenglin Yan[a], Federico Rosei[b]

a. Collaborative Innovation Center of Suzhou Nano Science and Technology, College of Energy, Soochow University, Suzhou 215006, China

b. Institut national de la recherche scientifique1650 Boul. Lionel-Boulet, Varennes, QC J3X1S2, Canada

Publication:

Chemical Engineering Journal

Publication date: 15 October 2023

Volume 474, Page 145830

DOI: https://doi.org/10.1016/j.cej.2023.145830

3.1 Introduction

Ammonia (NH_3) plays a critical role in the global economy and is widely utilized in industry and agriculture.[94-97] It is also recognized as a carrier for future renewable energy, which has been considered as a key option to lower the use of fossil fuels for daily life and industry.[98-100] To date, ammonia is produced primarily through the Haber-Bosch process, which demands not only a coupled steam reforming plant for hydrogen but also harsh conditions operating at high pressures (150-300 bar) and temperatures (300-500 °C).[101,102] Consequently, this typical strategy has to consume nearly 5.0 % of the world's natural gas and 1-2% of the global energy. It also results in large CO_2 emissions into the atmosphere (about 4 gigatonnes per year).[103] In this case, there is an urgent need for a clean and sustainable strategy to replace the century-old Haber-Bosch process. Nowadays, increasing attention has been put on several alternative methods, such as electrocatalysis and photocatalysis, for artificial ammonia production. Among various options, the electrocatalytic nitrogen (N_2) reduction reaction (NRR), which is an electrochemical process for the production of ammonia from nitrogen and water that only requires a thermodynamic minimum potential of 1.17 V under standard conditions, holds great potential and arouses interest of the scientific community in recent years.[104,105]

Up to now, a widespread array of materials, such as noble metal-based catalysts,[106] transition metal-based catalysts, and metal-free catalysts, have made great progress on electrocatalytic activity and selectivity for NRR. Various strategies including surface control,[107] defect engineering,[108,109] hybridization, etc. have been continuously proposed to increase the number of exposed active sites or enhance the intrinsic activity of single site, thus further improving the catalytic performance. However, although the high activation barrier of inert N_2 can be reduced to a certain extent or even eliminated by thermodynamic regulation, the actual electrochemical performance is still far from satisfactory, making it hard to achieve the goal set forth by the U.S. Department of Energy.[110,111] Considering that NRR is a three-phase interface reaction, the key challenge must be the limited supply of gaseous N_2 due to its low solubility in aqueous solution and the sluggish diffusion rate at the reaction interface.[112-114] That is, no matter how good the intrinsic activity of the catalyst is, it cannot be made full use of without the abundant supply of reactants.[115] During the actual electrochemical measurements, the nitrogen gas is continuously fed into the cathodic compartment with a properly positioned sparger to ensure the whole cathode was hit by the N_2 gas bubbles. Unfortunately, instead of getting access to the electrocatalyst, the majority of the gas bubbles would get away from the

working electrode.[25,116-118] Therefore, it would be an effective approach to empower the electrocatalyst to capture the N_2 gas bubbles and make full use of the active sites.

In this work, a nitrogen confining strategy achieved by plasma etching is proposed to address the problem of limited nitrogen supply for enhanced ammonia synthesis under ambient conditions (Figure 3.1). Upon plasma etching, numerous voids can be in situ constructed to serve as reservoirs for nitrogen nanobubbles. The nanobubbles can be effectively attracted by the defect-induced surface heterogeneity since it could generate van der Waals (vdW) interactions between the electrocatalyst and the nitrogen. Through directional transfer, the nitrogen nanobubbles can be captured by the voids, thereby providing a continuous nitrogen source for NRR as evidenced by the combination of captive bubble experiments and in-situ X-ray diffraction (XRD) observations. As expected, the synergy of highly active electrocatalyst with excellent intrinsic NRR activity and the abundant nitrogen supply after plasma modification would contribute to much enhanced NRR performance, with an ammonia yield rate of 35.24 μg h^{-1} mg^{-1} and a Faradaic efficiency of 53.99 % at -0.3 V versus the reversible hydrogen electrode (vs. RHE).

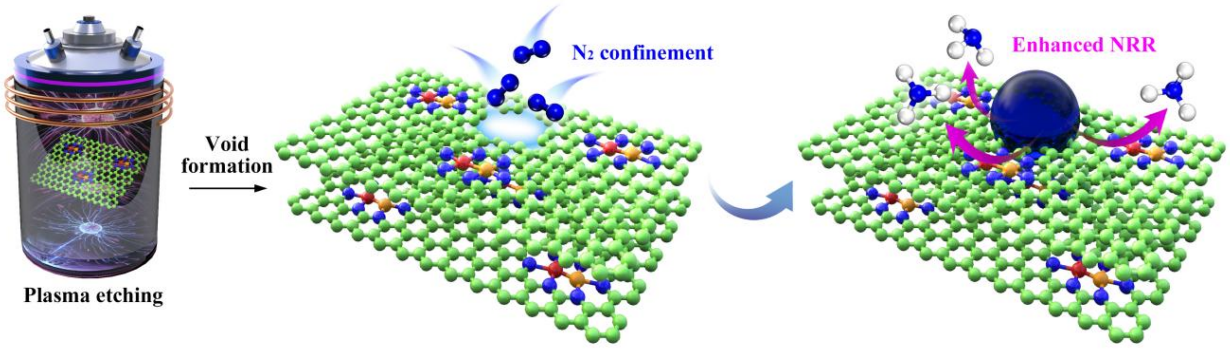

Figure 3.1 Schematic illustration of the mechanism for improving the electrochemical ammonia synthesis by confining nitrogen clusters within plasma etched voids.

3.2 Results and Discussions

In order to achieve precise capture of the N_2 gas, its existence form in the electrolyte was first investigated by MD simulations. Considering nitrogen is continuously fed into the system during the actual experiments, the initial model was constructed by uniformly setting 9 gas columns composed of nitrogen molecules in the simulation box with an edge length of 12 nm (Figure

S3.1). Such a model was first energy-minimized and equilibrated for 30 ps, followed by a 5 ns MD run. Snapshots of N_2 distribution at 2, 3, 4, and 5 ns are shown in Figure 3.2 a. From Figure 3.2 b, it can be clearly seen that nitrogen molecules tend to converge into nanobubbles with an average diameter of approximately 1.5 nm in a very short time, and then maintain this size during the simulation. Three separate simulations were conducted and the average diameter of the representative N_2 cluster versus time exhibits superior consistency. Under this prerequisite, voids larger than 1.5 nm should be constructed in the electrocatalyst to capture the nitrogen nanobubbles and serve as the nitrogen reservoir to supply for the NRR process.

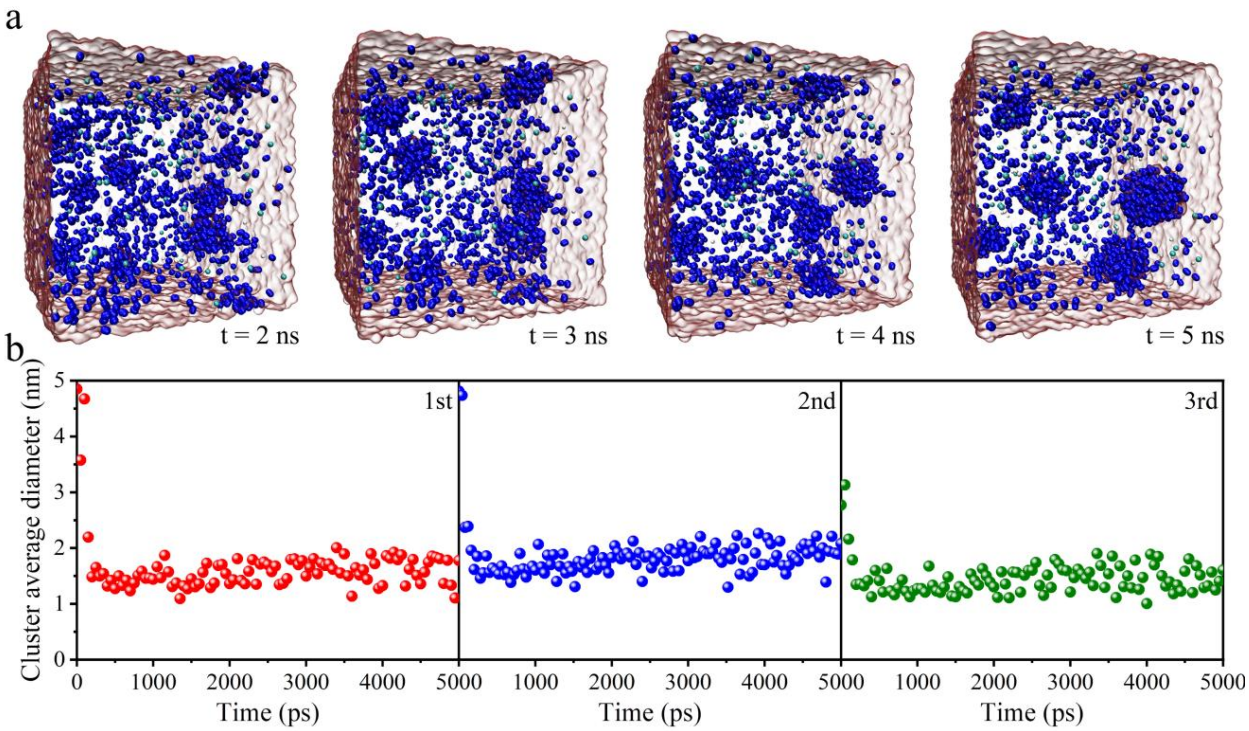

Figure 3.2 (a) MD simulation snapshots of N_2 distribution in 0.1 M HCl at 2, 3, 4, and 5 ns. (b) The average diameter of the representative N_2 cluster versus time in three separate simulations.

Plasma etching has been reported to be able to disrupt the basal surfaces of the carbon-based materials to generate a large number of void-like defects, and was applied here in this work.[119-123] Isolated single Fe atoms anchored on nitrogen-doped carbon (FeNC) is well-known to deliver certain degree of NRR performance.[124] The pristine WFeNC exhibits a graphene-like morphology as shown in scanning electron microscopy (SEM) and transmission

electron microscopy (TEM) images (Figure 3.3 a and b). Upon plasma etching, numerous voids were in situ constructed in the basal plane of WFeNC, triggering surface heterogeneity and leading to a mass of wrinkles in the graphene-like surface (Figure 3.3 c and d). The high-resolution TEM (HRTEM) image and the corresponding element maps of the plasma-etched WFeNC (P-WFeNC) describe the uniform distribution of C, N, O, Fe, and W elements over the entire architecture full of voids (Figure 3.3 e).

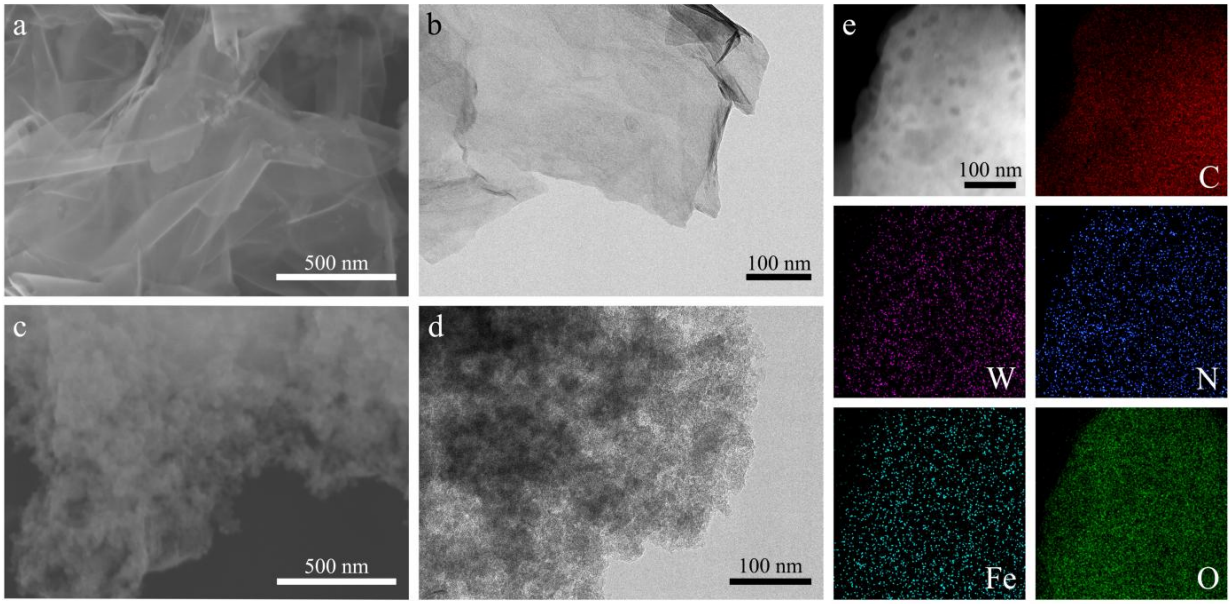

Figure 3.3 (a) SEM and (b) TEM images of WFeNC. (c) SEM and (d) TEM images of P-WFeNC. (e) HRTEM image and corresponding element maps of P-WFeNC.

To confirm the chemical state of Fe and W species in the sample, X-ray absorption near-edge structure (XANES) and extended X-ray absorption fine structure (EXAFS) analyses were carried out. The Fourier transformed EXAFS curve of P-WFeNC shows two peaks at approximately 1.51 Å and 1.05 Å, corresponding to the Fe–N and Fe-O scattering paths (Figure S3.22 b), and no obvious Fe–Fe peak (2.2 Å) or other peaks are observed. Moreover, no Fe peak shows up in XPS spectra from 700 to 750 eV which means that the iron element exists in the form of a single atom. According to the high-resolution N 1s spectra (Figure S3.20 b), the atomic structure of several nitrogen groups were further investigated by XPS and N-Fe peak show up at 398.5eV. Iron atoms in P-WFeNC are thus confirmed to be stabilized by N atoms and atomically dispersed on the supports. The XANES spectra of P-WFeNC about W L_3-edge is demonstrated

in Figure S21 b. To obtain an in-depth understanding of the atomic structure, EXAFS was then performed. The Fourier transform (FT) spectra from EXAFS at W L_3-edge in Figure S22 a indicate that the peaks of the W–W bond at 2.76 and 2.18 Å are divided. Another two peaks show up at 1.78 and 1.13 Å are considered as W-N/C bond and one tiny peak shows up at 1.44 Å is considered as W-O bond. W4f scan of P-WFeNC shows the characteristic W-O doublet at 35.9 and 33.8 eV respectively which may be originated from the plasma treated. Another doublet peaks show up at 30.7 and 32.8 eV represent W-W which shows that W is in the form of clusters.

Another significant issue in electrochemical nitrogen reduction is the catalytic activity of the catalyst. Thus, computational studies on both thermodynamics was carried out to investigate the mechanism of ammonia synthesis over the W-FeNC catalysts. The thermodynamic process of different models was first studied by DFT calculations. Accordingly, several possible models of tungsten cluster with different numbers of tungsten atoms on FeNC (FeNC-W_x, x = 1 to 6) were systematically proposed, and pure iron on nitrogen-doped carbon (FeNC) was also calculated for comparison (Figure S3.13). The limiting barrier for FeNC is 1.06 eV, and not all the introduction of tungsten clusters can reduce the rate-determining step. When the number of tungsten clusters is 1, 2, 4, 5, the limiting barrier of NRR is as high as 2.20, 2.87, 2.91, 2.43 eV, respectively. When the number of tungsten clusters is 6, the limiting barrier of NRR reaches the lowest, only 0.29 eV. As for the distal pathway, in addition to the dissociation of nitrogen as the reaction barrier, another bigger energy barrier during the following hydrogenation process have to be overcome, thus excluding it from the potential pathway. Free energy diagram and models represent the corresponding adsorbates on FeNC and W_xFeNC(x=1,2,3,4,5,6) through the associative distal and alternating pathway were shown in Figure S13-S19.

With the presence of these void-like defects, the specific surface area of the catalyst was also increased from 113.1 to 207.5 m^2 g^{-1} as determined by the Brunauer-Emmett-Teller (BET) method (Figure S3.3). Moreover, the corresponding pore distribution profiles indicate the appearance of mesopores with diameters of 2.86 and 3.23 nm in P-WFeNC (Figure 3.4 a), which are sufficient to serve as the reservoir for N_2 nanobubbles. The defective structure of P-WFeNC was further studied by XRD and Raman spectroscopy. With the increase of defect level due to plasma etching, the peak located at 25.2° attributed to the (002) plane of the graphitic carbon becomes broader for P-WFeNC in the XRD patterns (Figure 3.4 b). Correspondingly, the intensity ratio of G-band corresponding to graphitic carbons and the D-band assigning to the defect density in the graphitic domains in the Raman spectroscopy also increase from 0.98 for

WFeNC to 1.07 for P-WFeNC (Figure 3.4 c), again demonstrating the presence of enriched defects upon plasma etching. The induced surface heterogeneity would effectively enhance the vdW interactions, such as London dispersion force, between the electrocatalyst and the nitrogen molecules, triggering directional nitrogen transfer toward the catalyst.[125] The oncoming nitrogen nanobubbles can be effectively captured by the voids, providing abundant reactant supply for the nitrogen reduction and thus boosting the whole NRR process.

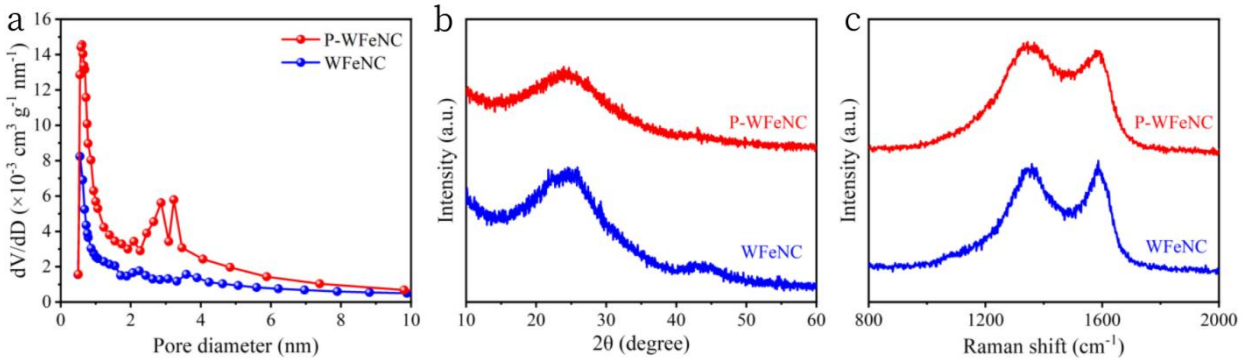

Figure 3.4 (a) The pore size distribution curves, (b) the XRD patterns, and (c) the Raman spectra of WFeNC and P-WFeNC.

Subsequently, the captive bubble experiments were performed to evaluate if P-WFeNC is able to effectively capture the N_2 nanobubbles. For WFeNC-coated electrode, it fails to interact with N_2 bubble, which keeps the “pinning” state once contacting the electrode surface and exhibits no observable change for 3000 ms (Figure 3.5 a). In contrast, with plasma modification, a large number of voids are constructed for capturing N_2 nanobubble, so that it takes only 720 ms to completely burst and enter into the inner part of the P-WFeNC-coated electrode (Figure 3.5 b). Then, in-situ XRD experiments were conducted to demonstrate the N_2 enrichment over the electrode.[126] The in-situ XRD intensity map of the P-WFeNC-coated electrode was collected during chronoamperometric operations under N_2 atmosphere and is displayed in Figure 3.5 c. Obviously, the intensity of the carbon peak, which varies with the concentration of localized N_2, gradually decreases to approximately 53.9 % of the original value in 60 minutes. Furthermore, the electrochemical active surface area (ECSA), which would be reduced by the increased contact of N_2 with the electrocatalyst, was also compared. It can be determined by the double-layer capacitance (C_{dl}) (Figure S3.4), and the data illustrate that the ECSA of P-WFeNC-coated electrode is indeed lower than that of WFeNC-coated electrode (Figure 3.5 d). The above

results give a further indication that N_2 molecules can be effectively captured within the P-WFeNC-coated electrode during the actual experimental condition, thus giving full play to the highly active electrocatalyst by supplying abundant N_2 reactant.

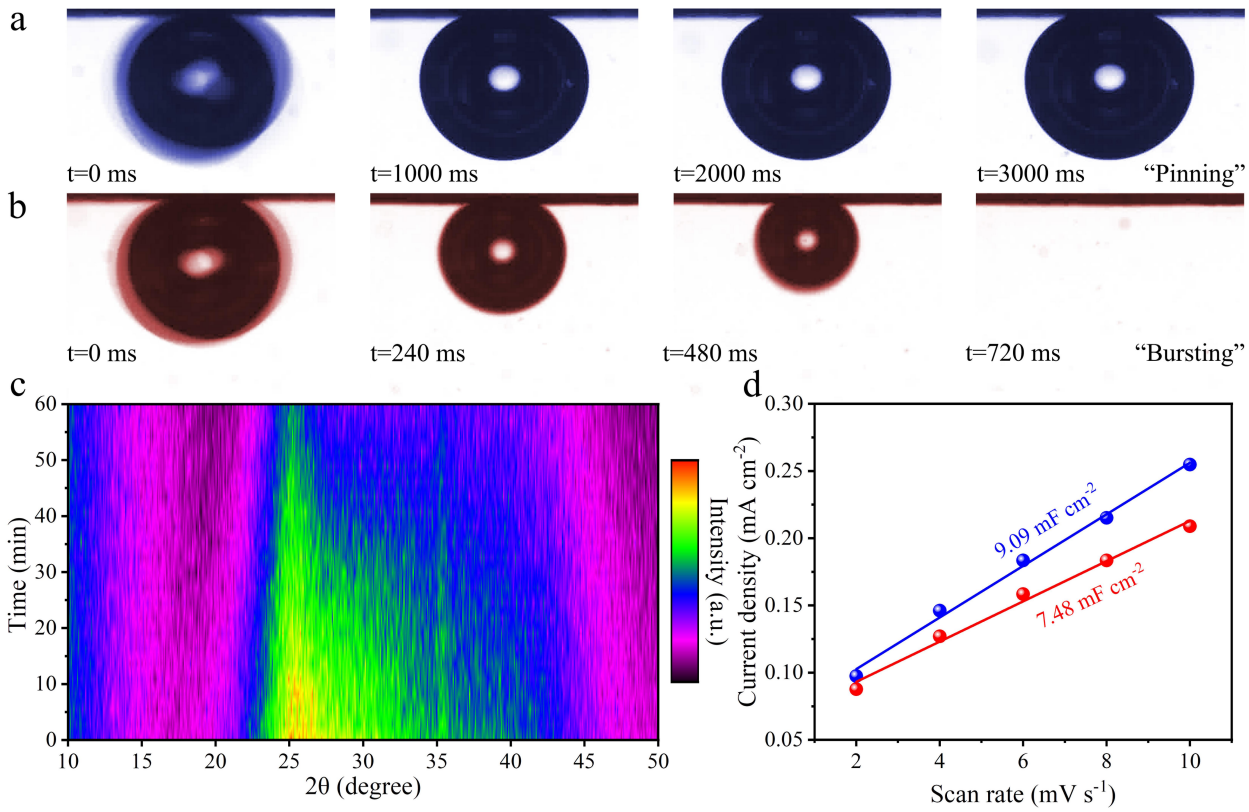

Figure 3.5 A series of optical images showing the N_2 diffusion process on the surface of (a) WFeNC and (b) P-WFeNC measured by the captive bubble method. (c) In situ XRD intensity maps of P-WFeNC under electrochemical testing as a function of time. (d) Double-layer charging current plotted against the CV scan rate for different electrodes.

Considering the beneficial effect of plasma etching on nitrogen confining, the actual NRR performance of P-WFeNC and WFeNC were evaluated in 0.1 M HCl using a gas-tight H-type electrochemical cell under ambient conditions via chronoamperometry measurements (Figure S3.5 and S3.6). During the measurements, a strict experimental protocol was followed to obtain a verification of reliable NRR performance.[127,128] While NH_3 and N_2H_4 have been examined by colorimetric method (Figure S3.7 and S3.8) as possible nitrogen reduction products in the electrolyte, no N_2H_4 by-product was found in this study (Figure S3.9). The NH_3 yield rates and the corresponding Faradaic efficiencies at each given potential of P-WFeNC and WFeNC are

shown in Figure 3.6 a and b. Without abundant supply of nitrogen gas, the NRR performance of WFeNC is quite limited, delivering the largest NH_3 yield rate of 15.29 μg h^{-1} mg^{-1} at -0.3 V vs. RHE and the highest Faradaic efficiency of 21.10 % at -0.2 V vs. RHE. As expected, much improved NRR performance was achieved by P-WFeNC, with an NH_3 yield rate of 35.24 μg h^{-1} mg^{-1} and a corresponding Faradaic efficiency of 53.99 % at -0.3 V vs. RHE, demonstrating the superiority of the proposed nitrogen confining strategy.

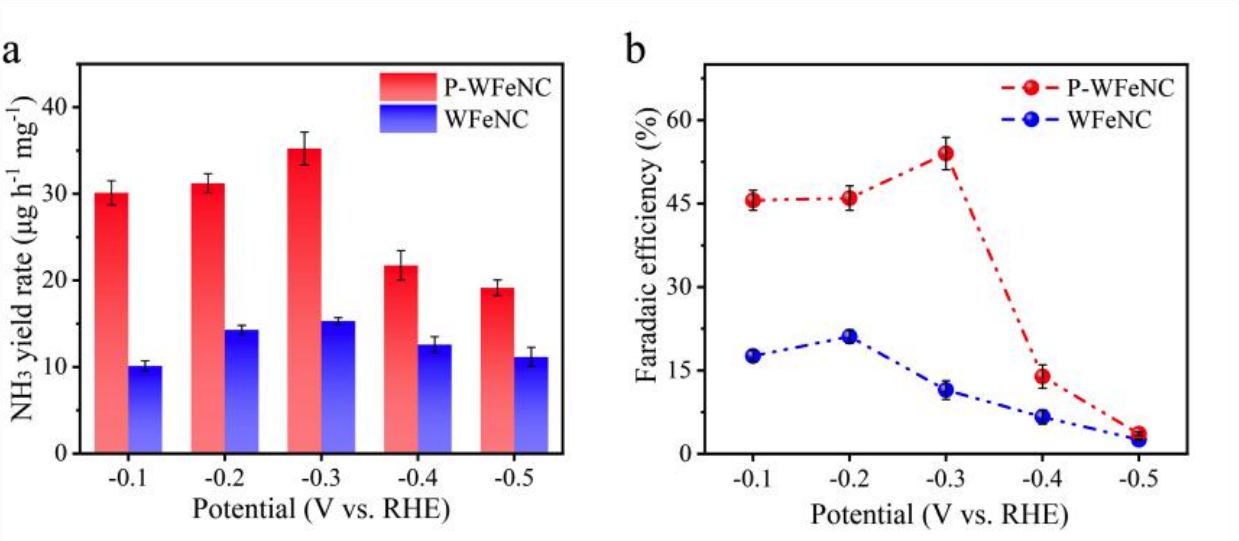

Figure 3.6 (a) NH_3 yield rates and (b) corresponding Faradaic efficiencies of WFeNC and P-WFeNC at various potentials.

Several control experiments were performed to make sure that there were no contaminants in the testing system (Figure 3.7 a).[129] No ammonia was found in the electrolyte when electrolyzing the bare carbon paper in N_2-saturated electrolyte at -0.3 V vs. RHE, the P-WFeNC-coated electrode in Ar-saturated electrolyte at -0.3 V vs. RHE, or the P-WFeNC-coated electrode in N_2-saturated electrolyte under open circuit potential. Furthermore, ^{15}N isotope labeling studies were carried out to investigate the N source of the produced NH_3. As shown in Figure 3.7 b, only a doublet signal for $^{15}NH_4^+$ is found in the ^1H NMR spectra when employing $^{15}N_2$ as the feeding gas, which is consistent with that recorded with standard solutions of $(^{15}NH_4)_2SO_4$. The above results confirm that the NH_3 obtained in the electrolyte originates entirely from the electrochemical NRR process, and thus the electrochemical data can be proved to be reliable.

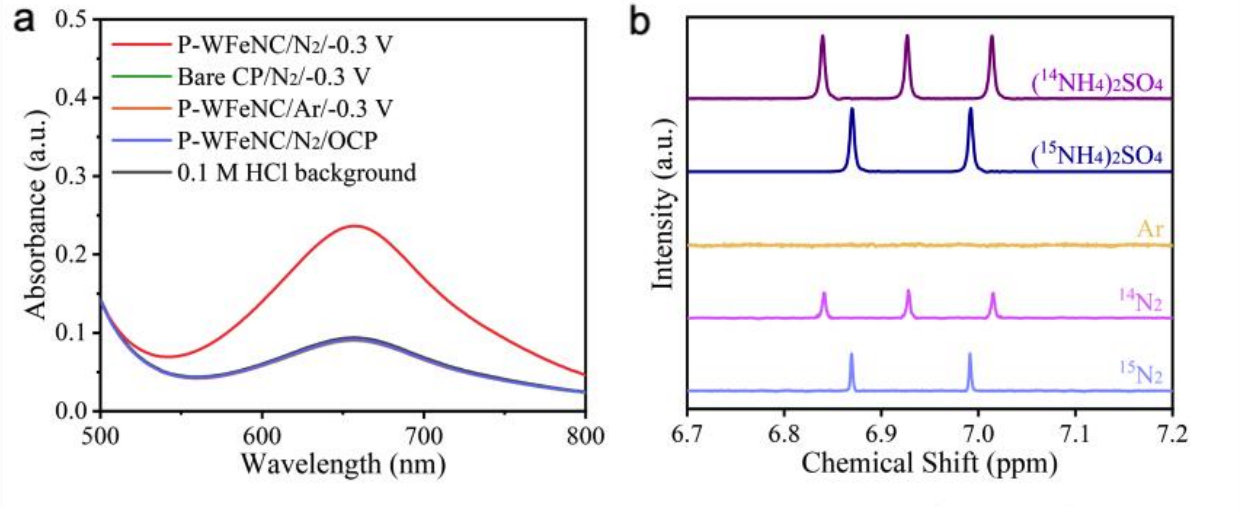

Figure 3.7 (a) The UV-vis absorption spectra the electrolytes under different conditions. (b) ^{1}H NMR spectra of the electrolyte tested with different feeding gases.

Upon comparing with the latest works, such superior NRR performance of P-WFeNC ranks at the top of the state-of-the-arts (Figure 3.8 a). In addition, it can maintain its outstanding performance almost unvaried under 10 continuing cycles of NRR electrolysis (Figure S3.10 and Figure 3.8 b), revealing the robustness of P-WFeNC.

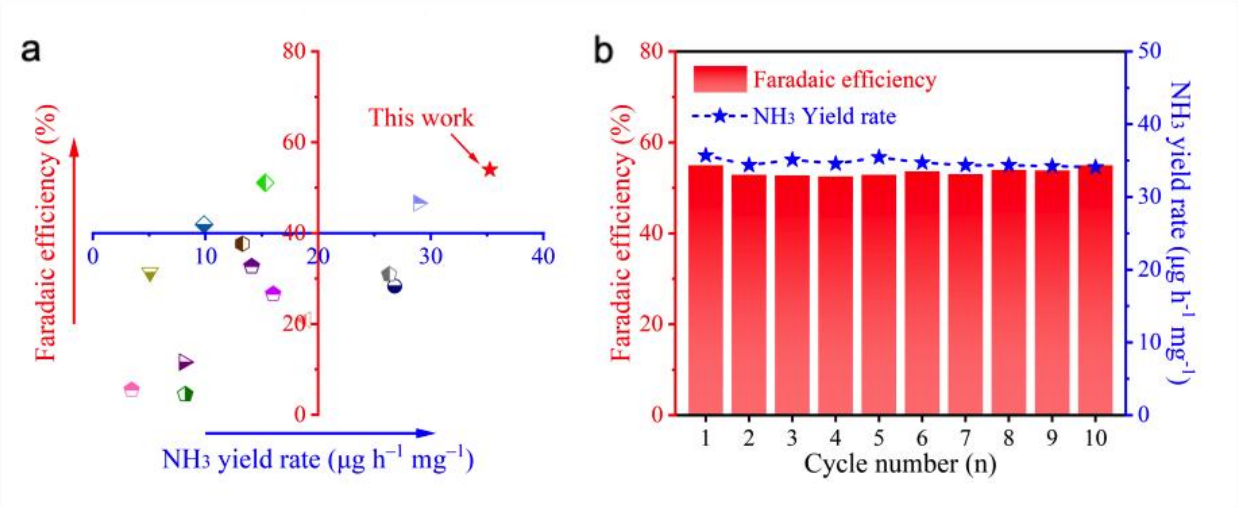

Figure 3.8 (a) Comparison of our results with state-of-the-art electrocatalysts in terms of NH_3 yield rate and Faradaic efficiency. (b) The NRR performance of P-WFeNC in the durability test.

3.3 Conclusion

In summary, a nitrogen confining strategy achieved by plasma etching has been proposed to address the challenge of limited reactant supply for nitrogen reduction reaction under ambient conditions. Upon plasma etching, a large number of voids with diameters of 2.86 and 3.23 nm appeared in the proof-of-concept P-WFeNC, which were totally sufficient to serve as the reservoir for N_2 nanobubbles with an average diameter of approximately 1.5 nm as suggested by MD simulations. Moreover, the void-like defects would induce surface heterogeneity and effectively enhance the vdW interactions between the electrocatalyst and the nitrogen molecules, triggering directional nitrogen transfer toward the catalyst. Consequently, N_2 molecules can be effectively captured within the voids of P-WFeNC, as demonstrated by the combination of captive bubble experiments and in-situ XRD characterizations during the actual experimental condition, thus giving full play to the electrocatalyst by supplying abundant N_2 reactant. As expected, the P-WFeNC exhibited much enhanced NRR performance as compared with WFeNC, with an ammonia yield rate of 35.24 μg h^{-1} mg^{-1} and a Faradaic efficiency of 53.99 % at -0.3 V vs. RHE. This work presents a feasible method for addressing the restricted reaction supply of gas-involved electrochemical reactions.

Acknowledgements

This work was supported by the National Natural Science Foundation of China [Nos. U21A20332, 52103226, 52202275, 52203314, and 12204253], the Distinguished Young Scholars Fund of Jiangsu Province [No. BK20220061], Suzhou Foreign Academician Workstation (project number: SWY2022001), and the Fellowship of China Postdoctoral Science Foundation [No. 2021M702382].

3.4 Supporting Information

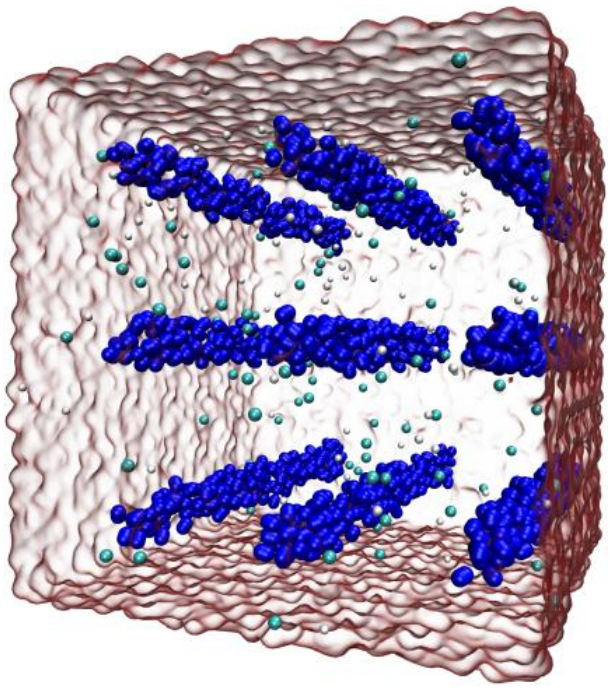

Figure S3.1 The initial model of N_2-saturated 0.1 M HCl system in MD simulations.

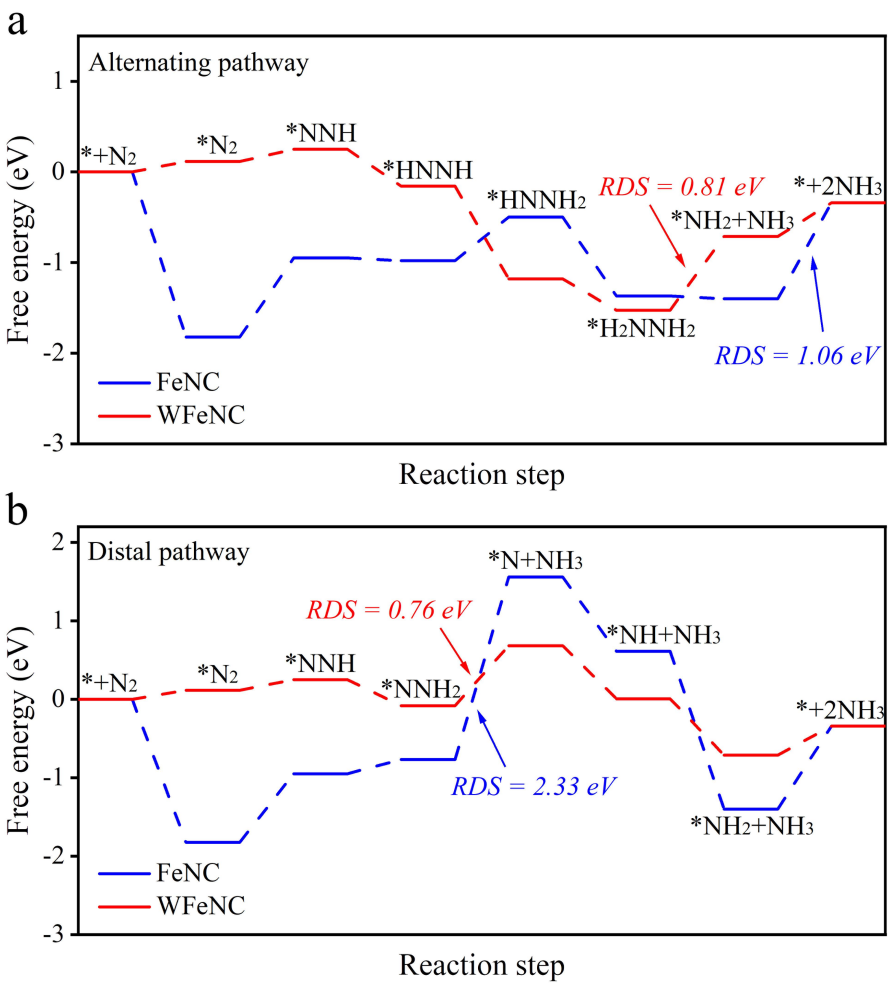

Figure S3.2 Free energy of ammonia synthesis on WFeNC and FeNC through (a) the alternating pathway and (b) the distal pathway.

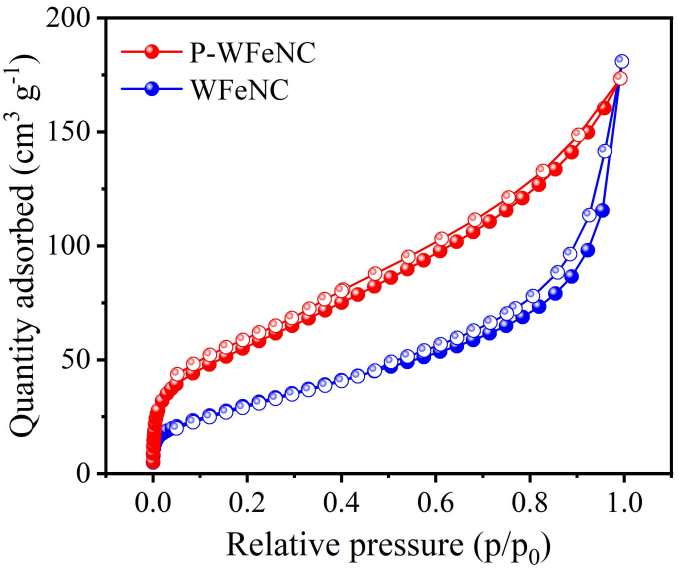

Figure S3.3 Nitrogen adsorption-desorption isotherms of P-WFeNC and WFeNC.

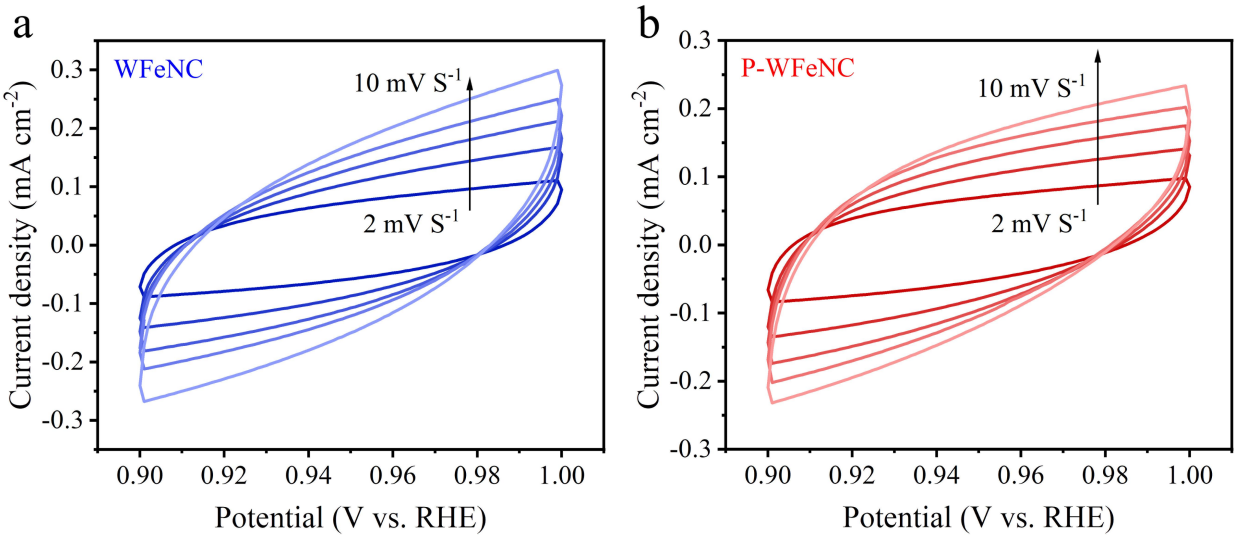

Figure S3.4 Cyclic voltammograms of (a) WFeNC and (b) P-WFeNC taken at different scan rates in a potential window where only double-layer charging and discharging occurs.

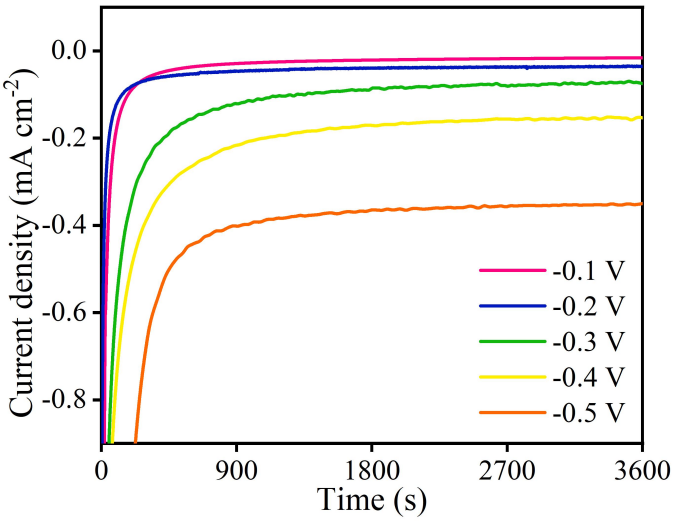

Figure S3.5 Chronoamperometry results of WFeNC tested in the H-cell with 0.1 M HCl at different applied potentials under N_2.

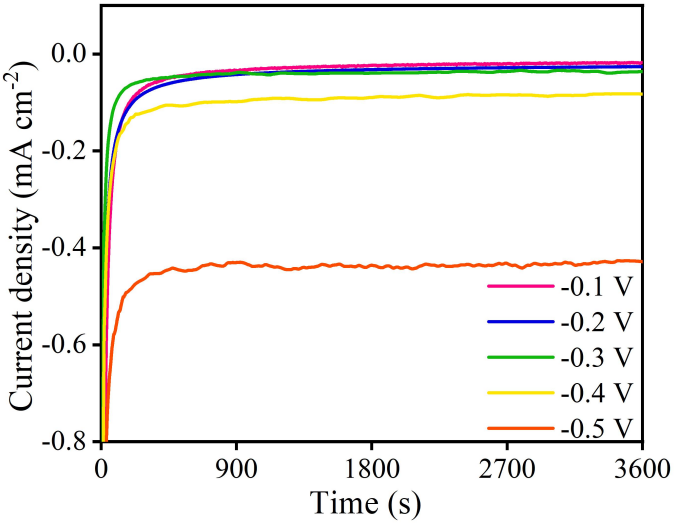

Figure S3.6 Chronoamperometry results of P-WFeNC tested in the H-cell with 0.1 M HCl at different applied potentials under N_2.

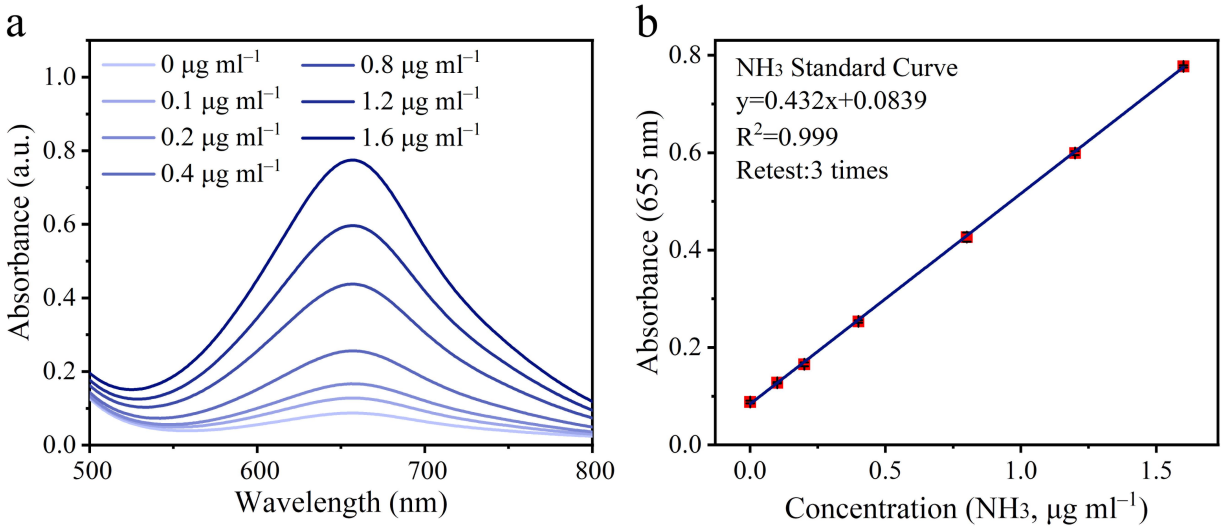

Figure S3.7 (a) The UV-vis absorption spectra and (b) corresponding calibration curves for the colorimetric determination of NH_3 in 0.1 M HCl using the indophenol blue method. The error bars correspond to the standard deviations of three separately prepared samples measured under identical conditions.

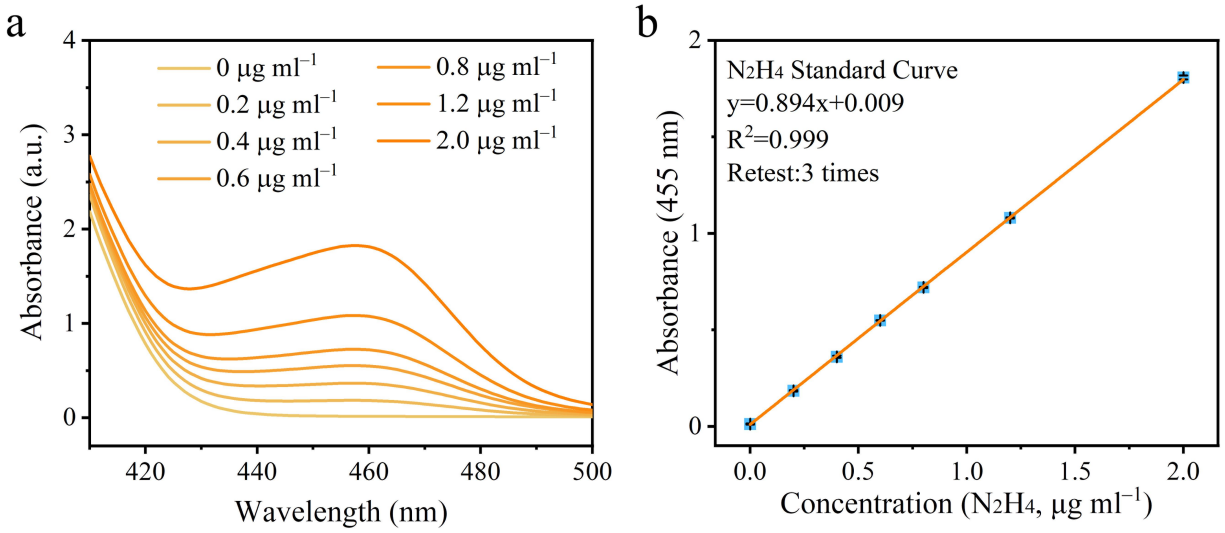

Figure S3.8 (a) The UV-vis absorption spectra and (b) corresponding calibration curves for colorimetric N_2H_4 determination in 0.1 M HCl using the Watt and Chrisp method. The error bars correspond to the standard deviations of three separately prepared samples measured under identical conditions.

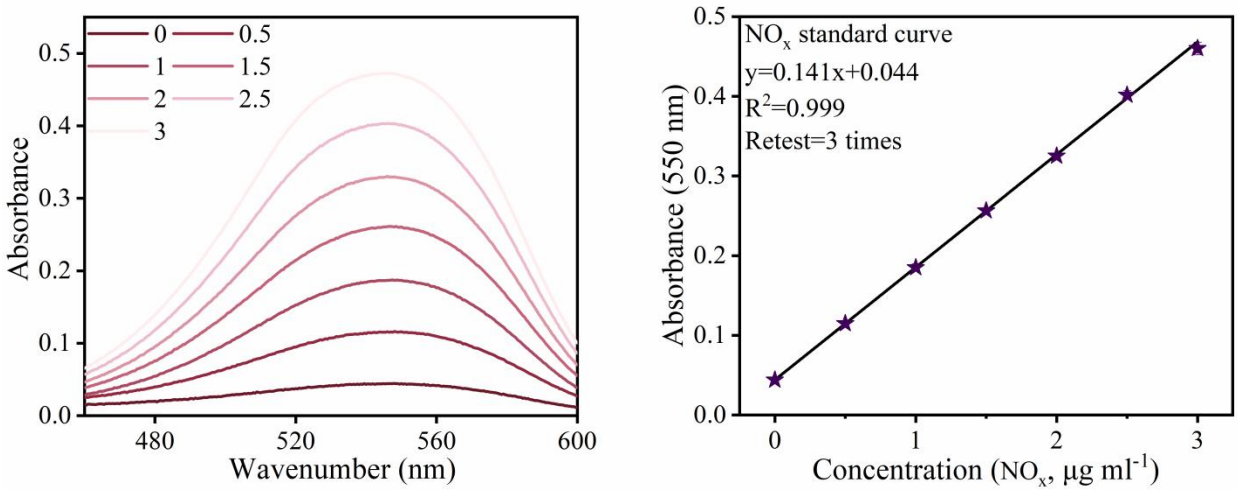

Figure S3.9. Determination of the produced hydrazine in 0.1 M HCl. (a) The UV-Vis absorption spectra and (b) corresponding calibration curves for the colorimetric NOx assay using N-(-1-naphthyl)-ethylenediamine dihydrochloride spectrophotometric method in 0.1 M HCl. The error bars correspond to the standard deviations of measurements over three separately prepared samples under the same conditions.

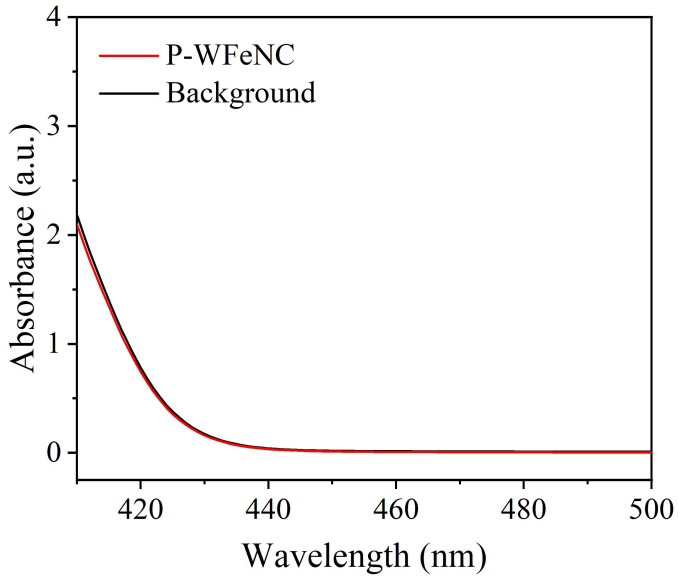

Figure S3.10 The UV-vis absorption spectra of the electrolyte using the Watt and Chrisp method.

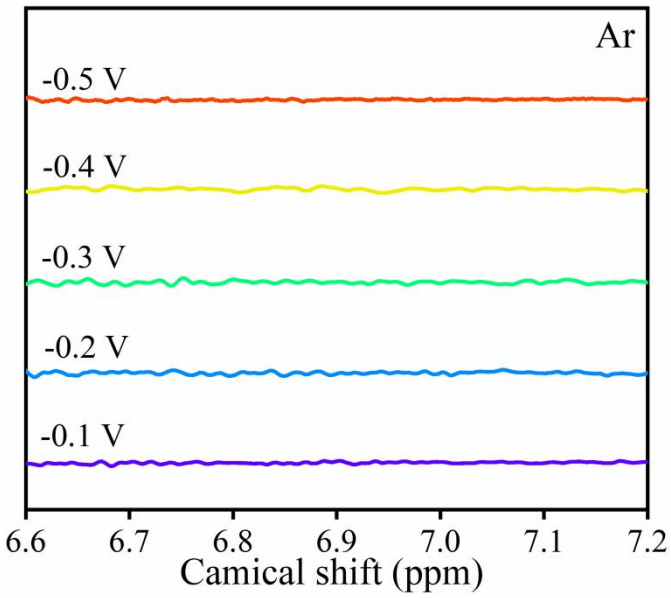

Figure S3.11 The ^{1}H NMR spectra of the corresponding electrolytes tested using WFeNC catalyst after chronoamperometry measurements under Ar.

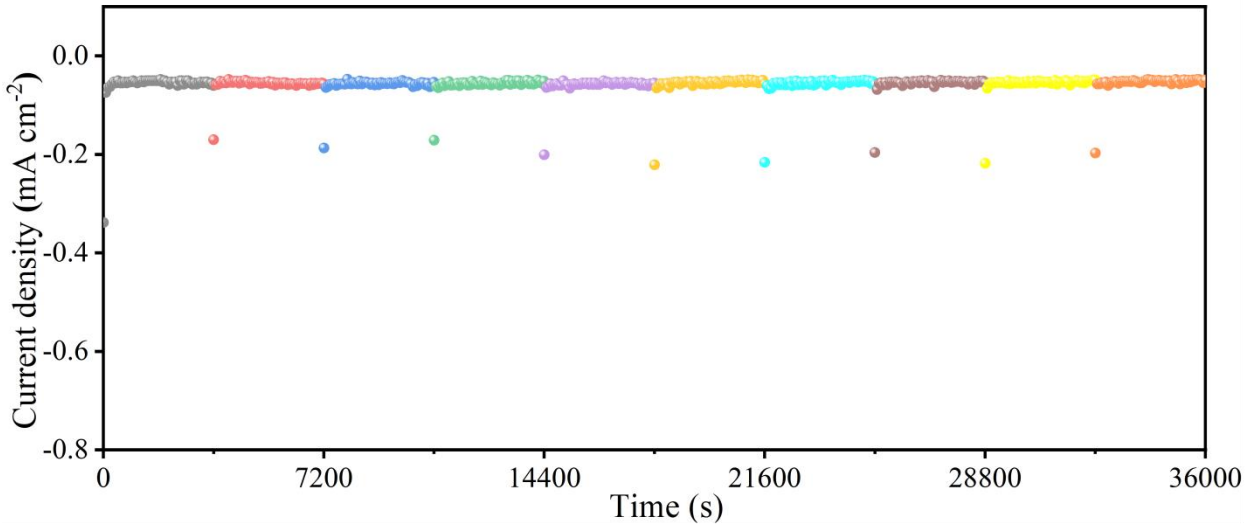

Figure S3.12 Stability test of the P-WFeNC catalyst in N_2-saturated 0.1 M HCl at -0.3 V vs. RHE under consecutive recycling electrolysis.

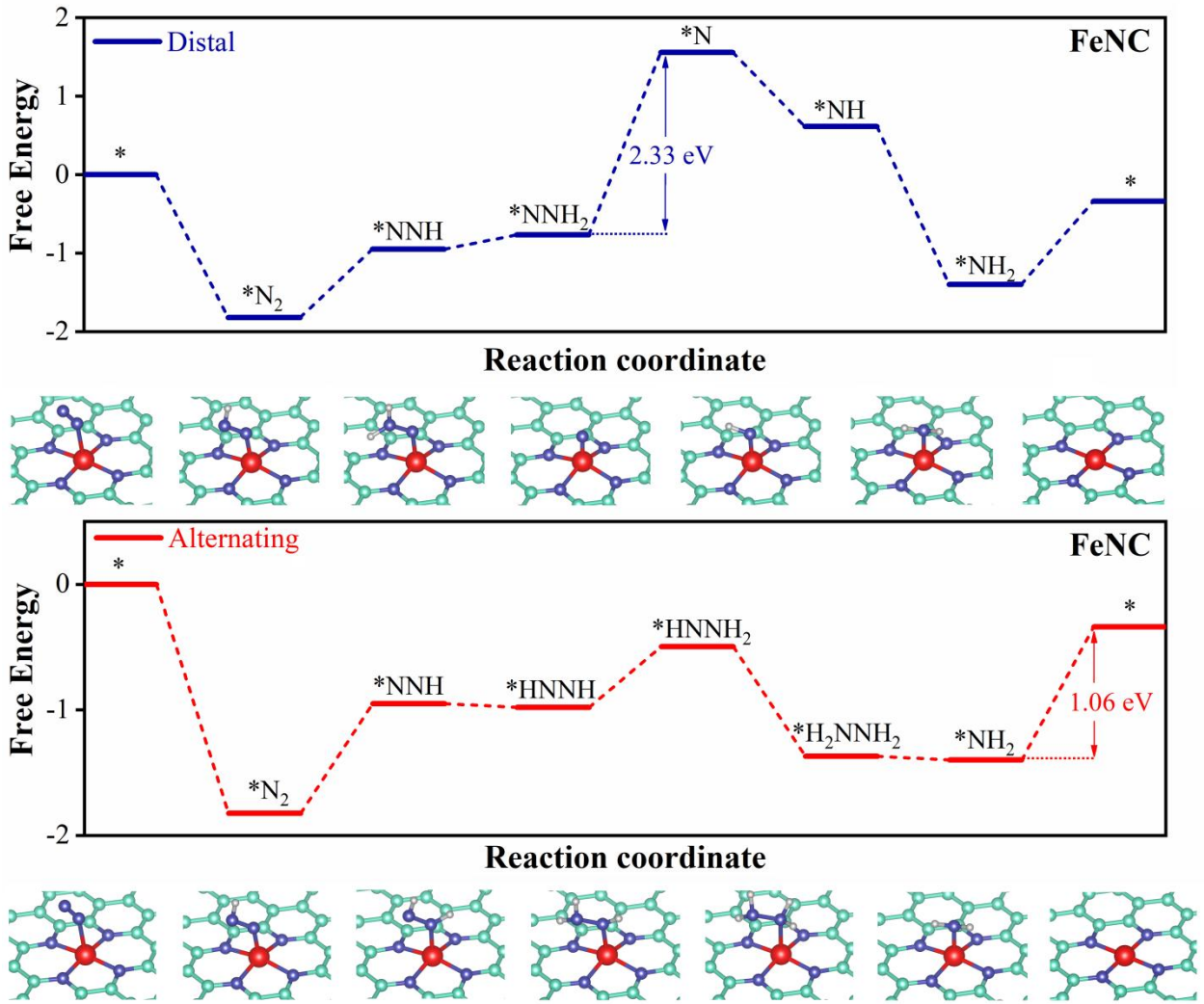

Figure S3.13 Free energy diagram and models represent the corresponding adsorbates on FeNC through the associative (a) distal and (b) alternating pathway. The cyan, blue, red and gray spheres represent C, N, Fe and H atoms, respectively.

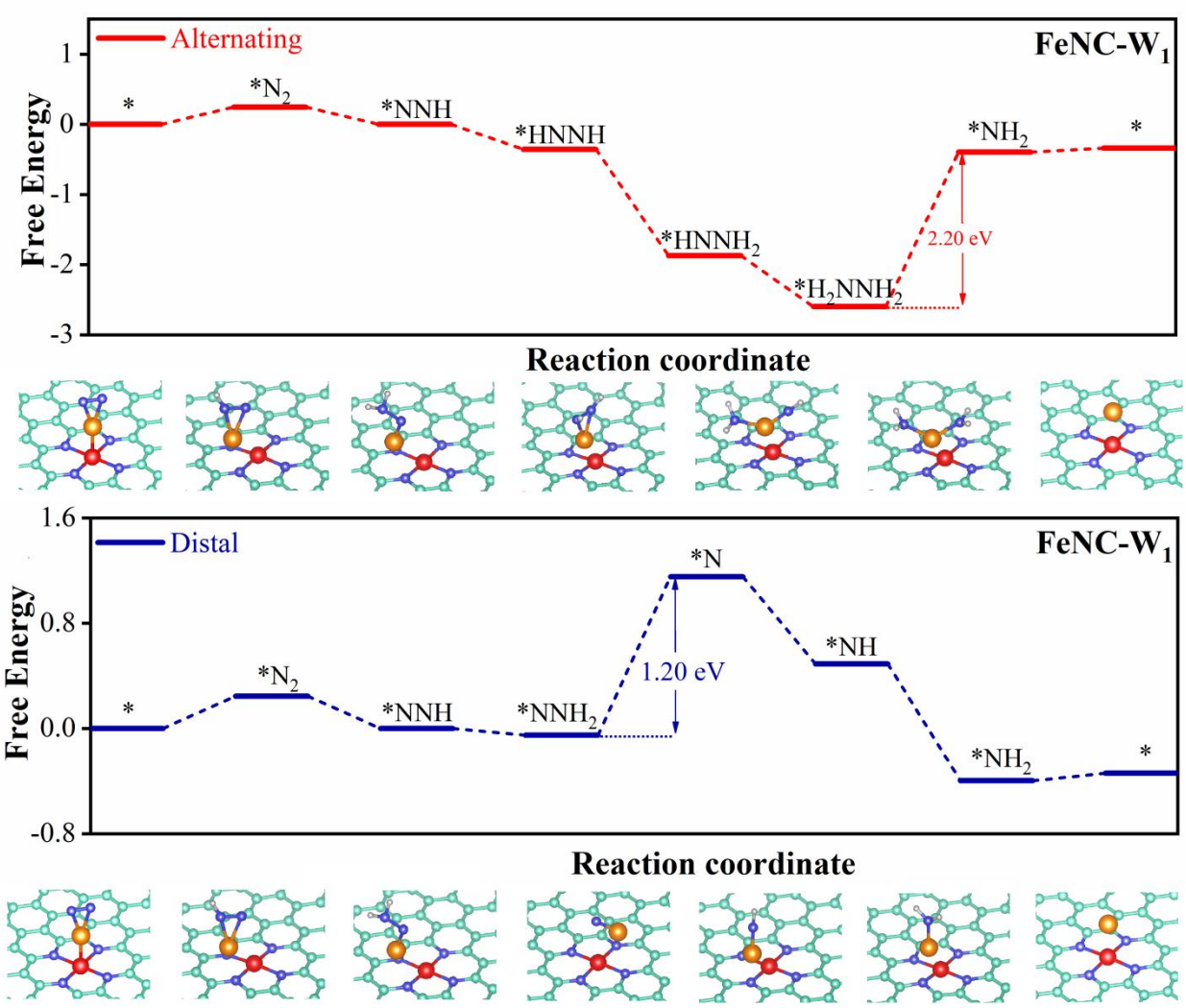

Figure S3.14 Free energy diagram and models represent the corresponding adsorbates on FeNC-W_1 through the associative (a) distal and (b) alternating pathway. The cyan, blue, red, orange and gray spheres represent C, N, Fe, W and H atoms, respectively.

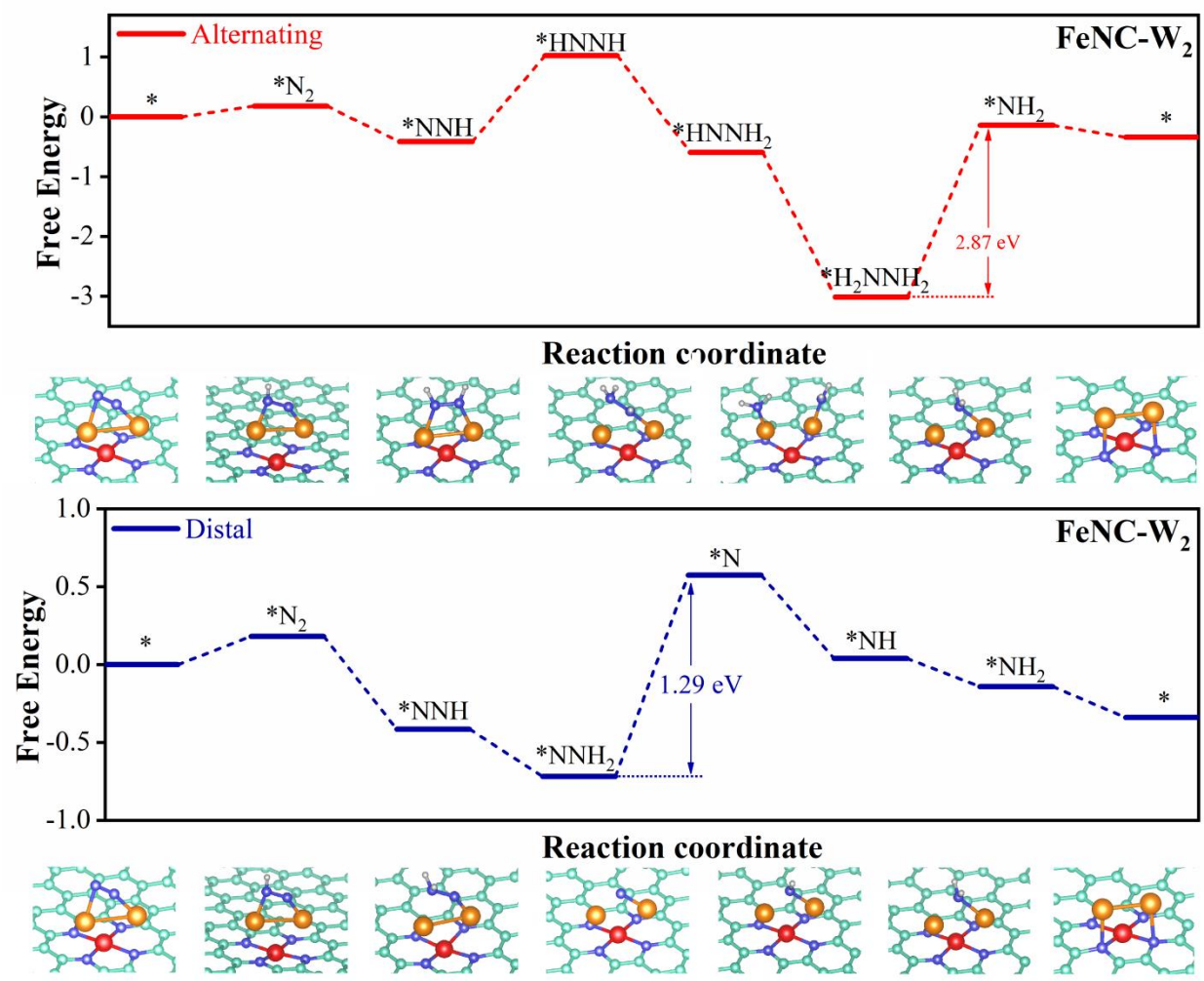

Figure S3.15 Free energy diagram and models represent the corresponding adsorbates on FeNC-W_2 through the associative (a) distal and (b) alternating pathway. The cyan, blue, red, orange and gray spheres represent C, N, Fe, W and H atoms, respectively.

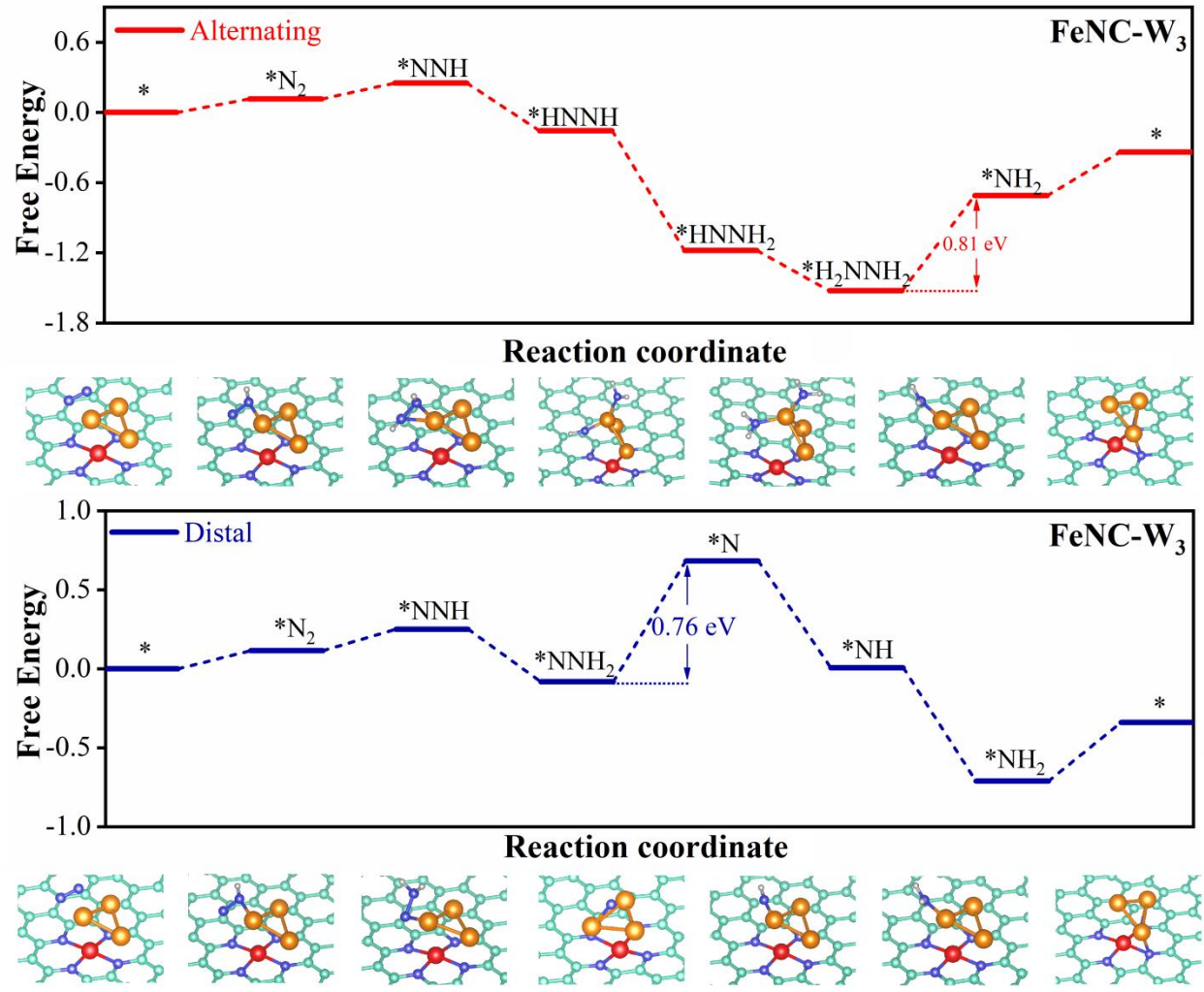

Figure S3.16 Free energy diagram and models represent the corresponding adsorbates on FeNC-W_3 through the associative (a) distal and (b) alternating pathway. The cyan, blue, red, orange and gray spheres represent C, N, Fe, W and H atoms, respectively.

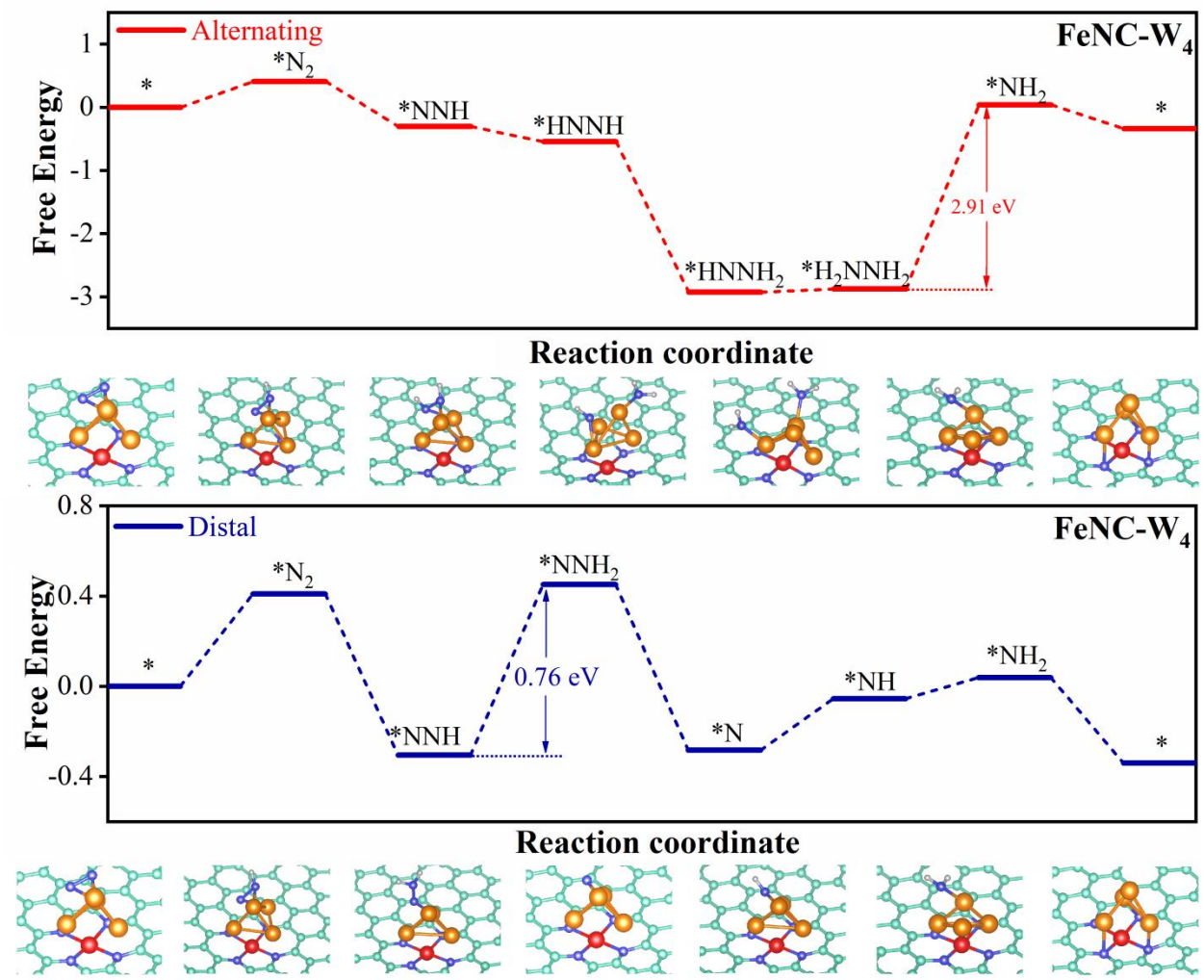

Figure S3.17 Free energy diagram and models represent the corresponding adsorbates on FeNC-W$_4$ through the associative (a) distal and (b) alternating pathway. The cyan, blue, red, orange and gray spheres represent C, N, Fe, W and H atoms, respectively.

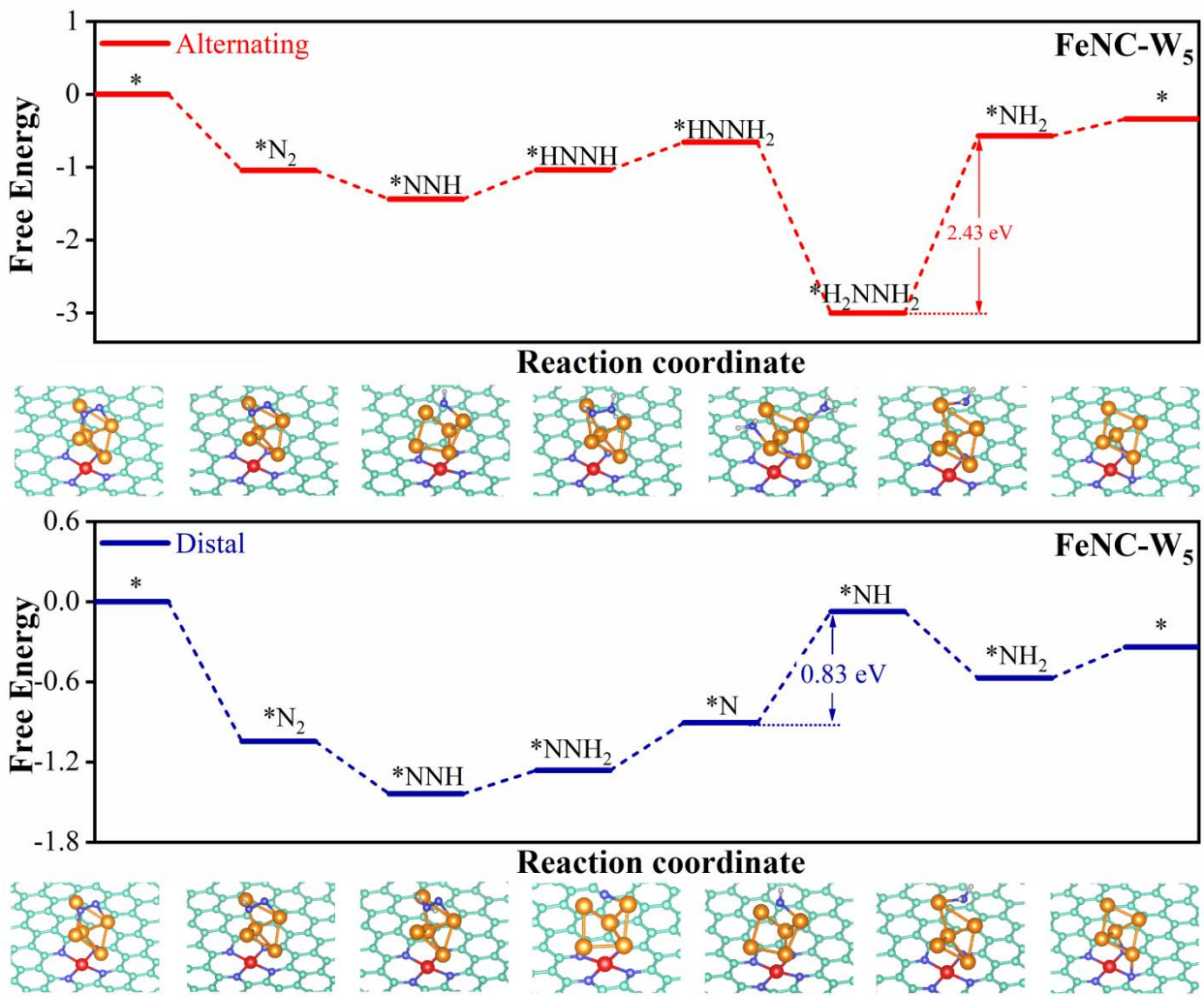

Figure S3.18 Free energy diagram and models represent the corresponding adsorbates on FeNC-W_5 through the associative (a) distal and (b) alternating pathway. The cyan, blue, red, orange and gray spheres represent C, N, Fe, W and H atoms, respectively.

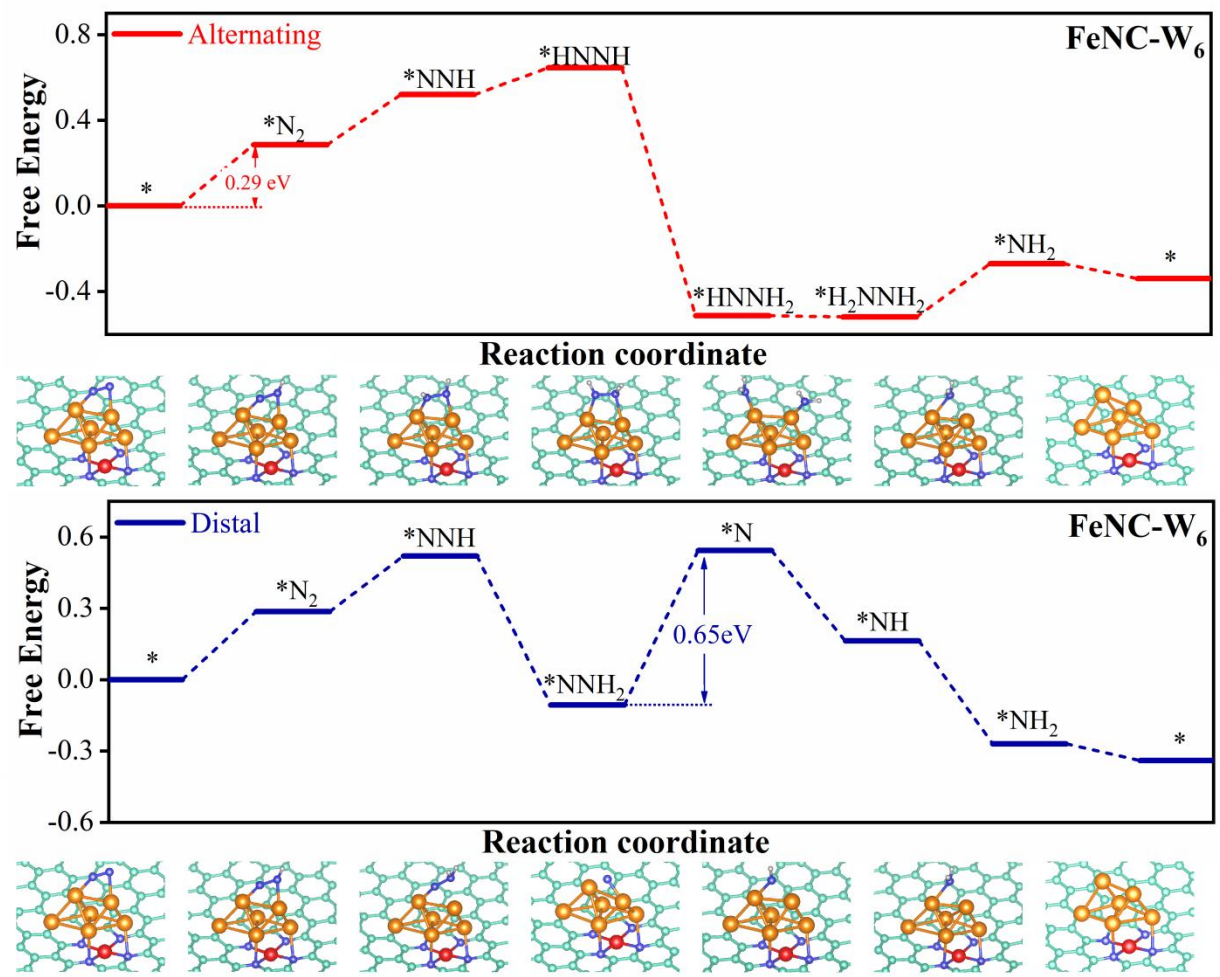

Figure S3.19 Free energy diagram and models represent the corresponding adsorbates on FeNC-W_6 through the associative (a) distal and (b) alternating pathway. The cyan, blue, red, orange and gray spheres represent C, N, Fe, W and H atoms, respectively.

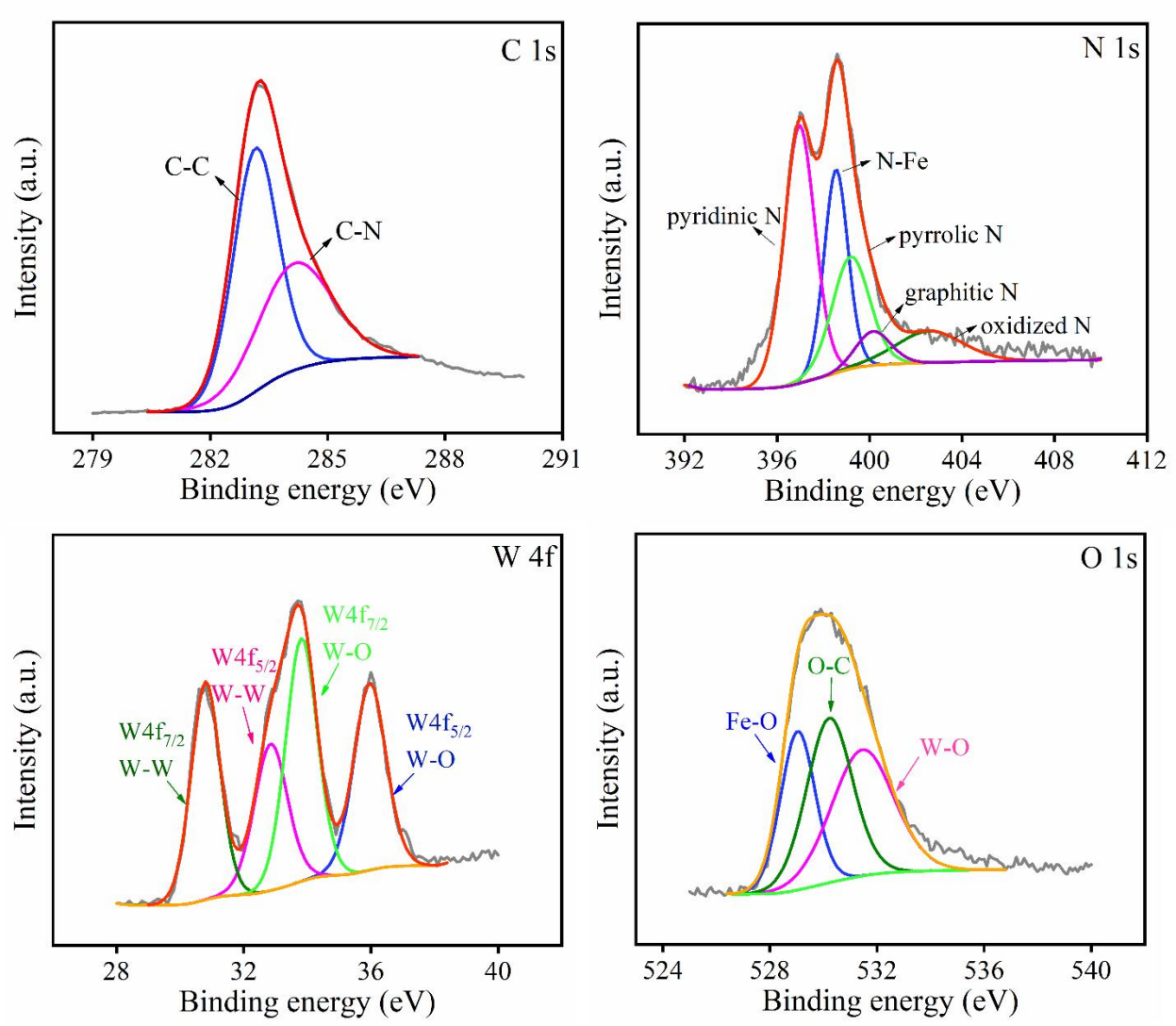

Figure S3.20 The high resolution (a) C1s, (b) N1s, (c) W4f and (d) O1s X-ray photoelectron spectroscopy (XPS).

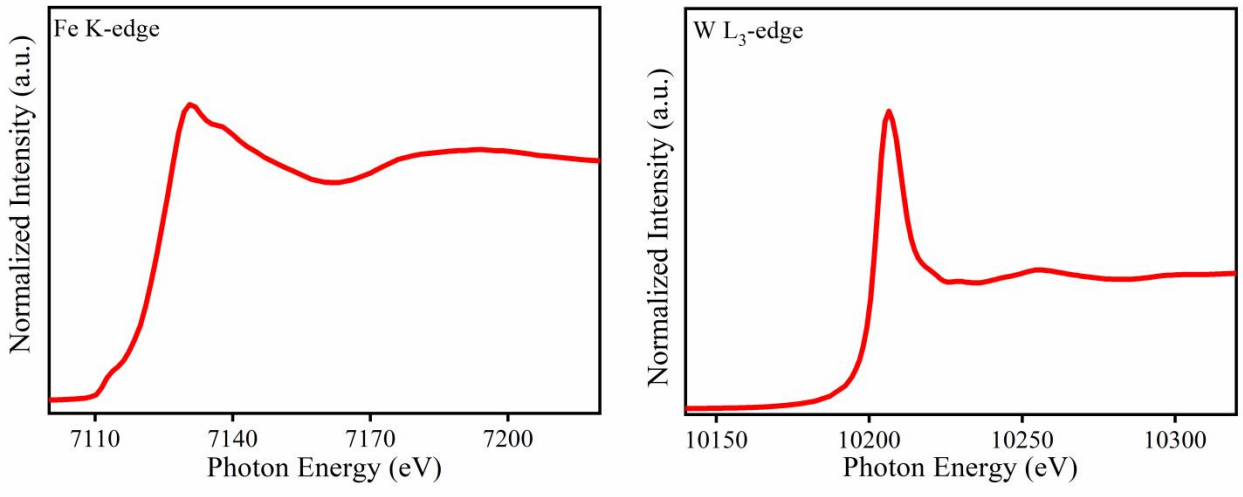

Figure S3.21 XAS results of P@W-FeNC atalysist: (a) Fe K-edge and (b) W L_3-edge XANES spectra

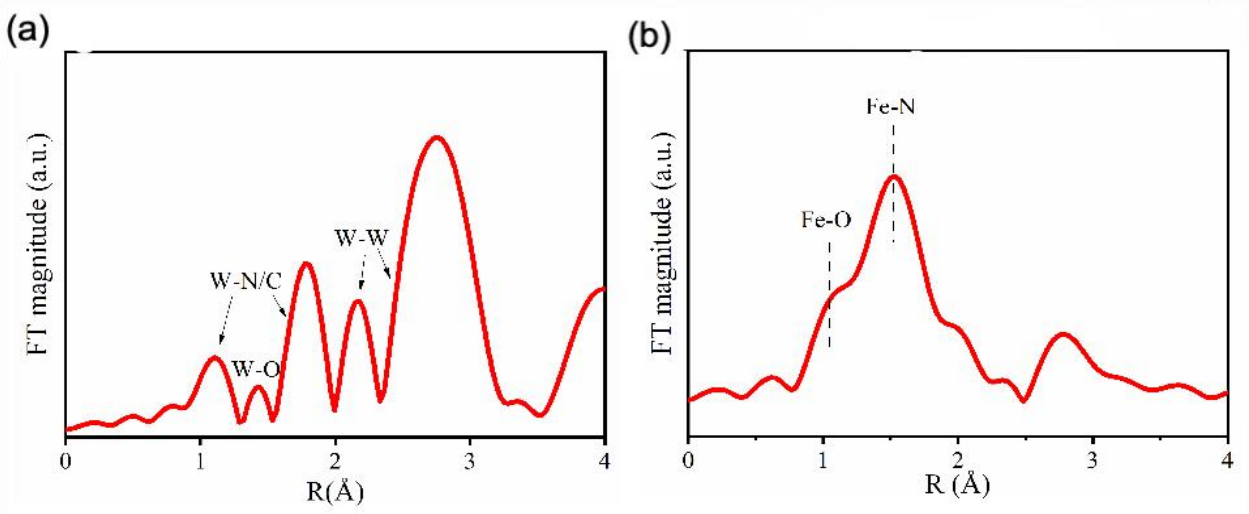

Figure S3.22 (e)W L_3-edge (f) Fe K-edge, X-ray absorption near-edge structure (XANES) fourier transform spectra.

4 OENC catalyst with synergistic electron promotion for NRR

Triggering synergistic electronic promoting effect through oxygen doping to promote electrochemical nitrogen reduction on metal-free electrocatalyst

Déclenchement d'un effet de promotion électronique synergique grâce au dopage à l'oxygène pour favoriser la réduction électrochimique de l'azote sur un électrocatalyseur sans métalAuthors:

Na Xu[a, b], Qiyang Cheng[a], Mengfan Wang[a], Yanzheng He[a], Haoqing Ji[a], Federico Rosei[b]

a. Collaborative Innovation Center of Suzhou Nano Science and Technology, College of Energy, Soochow University, Suzhou 215006, China

b. Institut national de la recherche scientifique1650 Boul. Lionel-Boulet, Varennes, QC J3X1S2, Canada

Publication:

Inorganic Chemistry Frontiers

Publication date: 13 October 2023

Volume 10, Page 7010–7017

DOI: 10.1039/D3QI01673K

4.1 Introduction

Ammonia (NH_3) is a highly important feedstock for synthesizing fertilizers, plastics, and other chemicals.[8,124,130] Recently, it also gains much attention as a liquid energy carrier due to its low liquefaction pressure and high energy density, and thus is projected to play a critical role in the future hydrogen economy.[131-133] Up to now, industrial ammonia production still mainly depends on the energy-intensive Haber-Bosch (HB) process, in which high purity hydrogen and nitrogen react under high temperatures (400-500 °C) and high pressures (150-250 atm). Such widely applied process causes excessive consumption of natural gas for hydrogen production, accounts for 1-3% of the world's energy supply, and is accompanied by massive greenhouse gas emission annually.[110,134] Therefore, it is necessary to develop alternative technologies for ammonia synthesis to avoid the serious energy and environmental issues caused by the conventional HB process. To this end, environmentally benign methods powered by renewable energy, such as photocatalysis and electrocatalysis under ambient conditions, have been rapidly expanding fields of research.[99,118,135] Among them, the electrocatalytic nitrogen reduction reaction (NRR) with N_2 and H_2O as direct reactants has attracted great attention.[113,114] Nevertheless, current NRR process still suffers from inherent inertness of N≡N bond as well as sluggish multi-step reaction kinetics, and the rational design of highly efficient electrocatalysts toward NRR remains a significant challenge.

A series of metal-based electrocatalysts, especially transition metal-based electrocatalysts with unoccupied and occupied d orbitals, have been demonstrated to be able to activate nitrogen and achieve ammonia synthesis under ambient conditions.[136-139] However, the d orbital electrons of transition metal would also favor the formation of metal-H bond, leading to the competition with the undesired hydrogen evolution reaction (HER) and thus low Faradaic efficiency (FE) and yield rate for NRR.[140-143] Compared to transition metal-based materials, metal-free electrocatalysts may provide a new opportunity to achieve efficient NRR,[144-146] since theoretical calculations have suggested that metal-free electrocatalysts with nonmetallic elements featuring weak hydrogen adsorption are unfavorable for HER. Recently, nitrogen-doped carbon materials with the modified electronic structure, the formed defects, and the charge polarization have been experimentally and theoretically proven to be capable of facilitating the adsorption of nitrogen and cleavage of N≡N bond, thus showing a certain NRR activity.[147] Unfortunately, current NRR performance on nitrogen-doped carbon is still far from satisfactory because of the high energy barrier of the following hydrogenation steps. It is previously confirmed that dual-atoms-doped carbon with synergistic coupling effect could obtain

enhanced catalytic performance for electrochemical reactions.[148-151] In this context, the introduction of secondary heteroatom to nitrogen-doped carbon holds great promise to further boost the reaction kinetics of NRR.[152] Among various options, oxygen atom exhibits much larger electronegativity (3.44) with respect to carbon (2.55) and nitrogen (3.04) and its presence as secondary heteroatom provides strong power to manipulate the electronic properties of carbon catalysts, which is conducive to significantly promote the NRR process.[153]

In this work, synergistic electronic promoting effect is deliberately triggered through doping oxygen as secondary heteroatom to boost ambient ammonia synthesis on nitrogen-doped carbon. In 0.1 M HCl, the proof-of-concept oxygen-enriched nitrogen-doped carbon catalyst achieves a superior ammonia yield rate of 67.3 μg h^{-1} mg^{-1} and a high FE of 36.2% at -0.2 V versus reversible hydrogen electrode (vs. RHE), and the reliability has been confirmed by several qualitative and quantitative experiments using $^{14}N_2$ or $^{15}N_2$ as feeding gas. Upon the introduction of oxygen into nitrogen-doped carbon, the electronic structure and the polarity of adjacent carbon atoms are further optimized, significantly lowing the energy barrier of the overall nitrogen reduction process as confirmed by the density functional theory (DFT) calculations. This work opens the window for the rational design of heteroatoms-modified carbon materials.

4.2 Results and discussion

The polymerization of pyrrole can be catalyzed and regulated by adding different amounts of hydrogen peroxide, so that it was chosen as the carbon source in this work.[154] With normal polypyrrole or overoxidized polypyrrole as a precursor, as well as sodium chloride as a template, oxygen-containing or oxygen-enriched nitrogen-doped carbon (denoted as ONC and OENC) was obtained after high temperature pyrolysis in Ar, followed by the removal of salt through aqueous washing. To highlight the critical role of oxygen, nitrogen-doped carbon (NC) was also prepared by annealing the ONC at 300 °C for 2 h under an Ar/H_2 atmosphere to remove the O-groups. All of the three samples show rumpled and wrinkled sheet morphology as indicated by the scanning electron microscopy (SEM) and the transmission electron microscopy (TEM) images (Figure S4.1, Figure 4.1 a and b), which contributes to greatly enhanced exposure of active sites toward reactants and thus the formation of large three-phase reaction region. The corresponding elemental mapping images suggest uniformly distributed elemental C, N, and O within OENC (Figure 4.1 c), indicating the sufficient integration of oxygen and nitrogen in the carbon matrix.

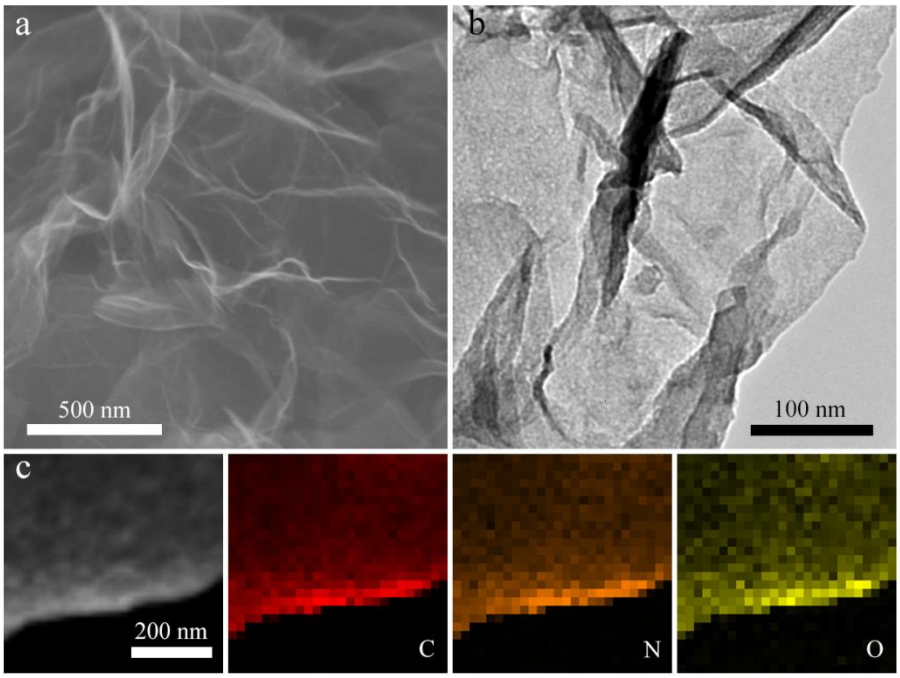

Figure 4.1 (a) Scanning electron microscopy image, (b) transmission electron microscopy image, and (c) corresponding elemental mapping images of OENC.

The powder X-ray diffraction (XRD) and Raman analysis were then conducted to characterize the carbonized product. As shown in Figure 4.2 a, for , for all three samples, the two broad diffraction peaks in the XRD patterns can be attributed to the (002) and (100) planes of graphitized carbon, respectively, which represent the typical properties of carbon materials with low graphitic degree.[155] They also exhibit evident D and G bands in the Raman spectra (Figure 4.2 b). The G band stands for the in-plane vibration of sp^2 carbon structures while the D band represents the defects in the graphitic lattice, namely crystallinity and disorder, respectively.[156] The intensity ratio of D band and G band (I_D/I_G) increases from 0.84 for the NC to 0.93 for ONC to 1.05 for OENC, suggesting more disordered graphitic structure domains in the latter induced by the presence of enriched oxygen.

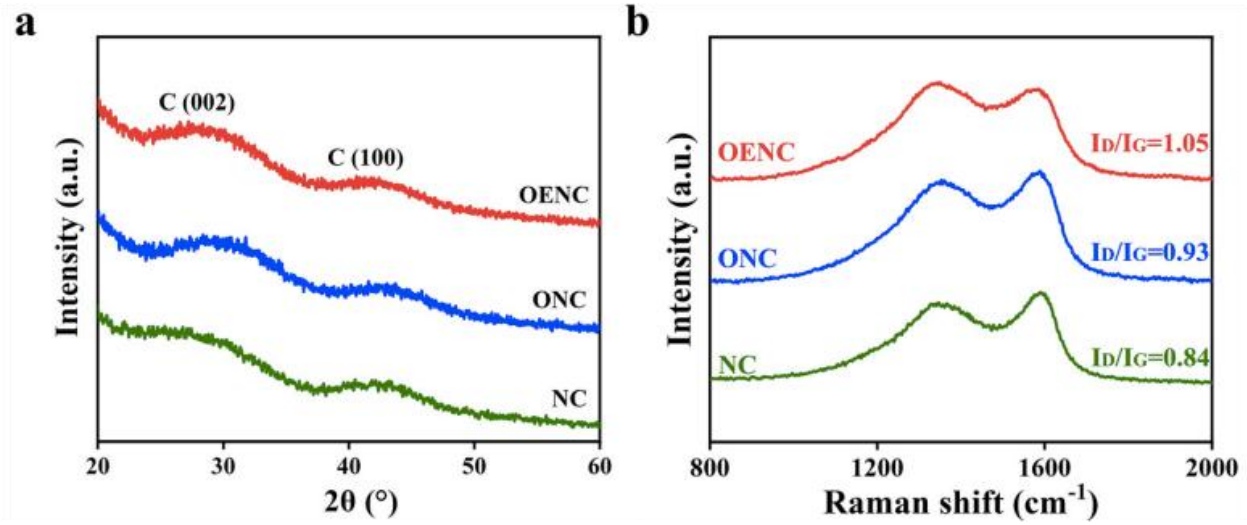

Figure 4.2 (a) XRD patterns and (b) Raman spectra of OENC, ONC and NC.

Subsequently, the chemical nature and bond structure of different structures were investigated by X-ray photoelectron spectroscopy (XPS). The C 1s, N 1s, and O 1s peaks were captured in both ONC and OENC, with a much larger O content of 8.89 at.% in the OENC (Figure 4.3 a). Notably, a trace amount of oxygen is still detected in the NC, which can be attributed to the surface adsorbed adventitious oxygen-containing species such as H_2O or CO_2. The high-resolution C 1s spectra were composed of five peaks relating to basal-plane sp^2 C, defect sp^3 C, C-O, C=O, and π-π* (Figure 4.3 b).[157] The high-resolution N 1s spectra of ONC and OENC consist of four characteristic peaks corresponding to graphitic-N, pyrrolic-N, pyridinic-N, and N-oxides (Figure 4.3 c).[125] Notably, the quantitative analysis of N contents and the deconvolution of these four peaks do not show obvious difference between ONC and OENC, confirming that the enriched oxygen would not influence the N dopants. As for the high-resolution O 1s spectra, they can be deconvoluted into three peaks assignable to physically adsorbed oxygen, ketonic C=O groups, and C-O (hydroxyl and epoxide) groups (Figure 4.3 d).[158-160] Clearly, with overoxidized polypyrrole as precursor, both C=O groups and C-O groups significantly increase in OENC with respect to ONC, which would effectively tailor the electronic structure of nitrogen-doped carbon and make synergistic contribution to the catalytic activity of active sites. Moreover, the introduction of enriched oxygen would not sacrifice electronic conductivity as suggested by electrochemical impedance spectroscopy (EIS) measurements (Figure S4.2).

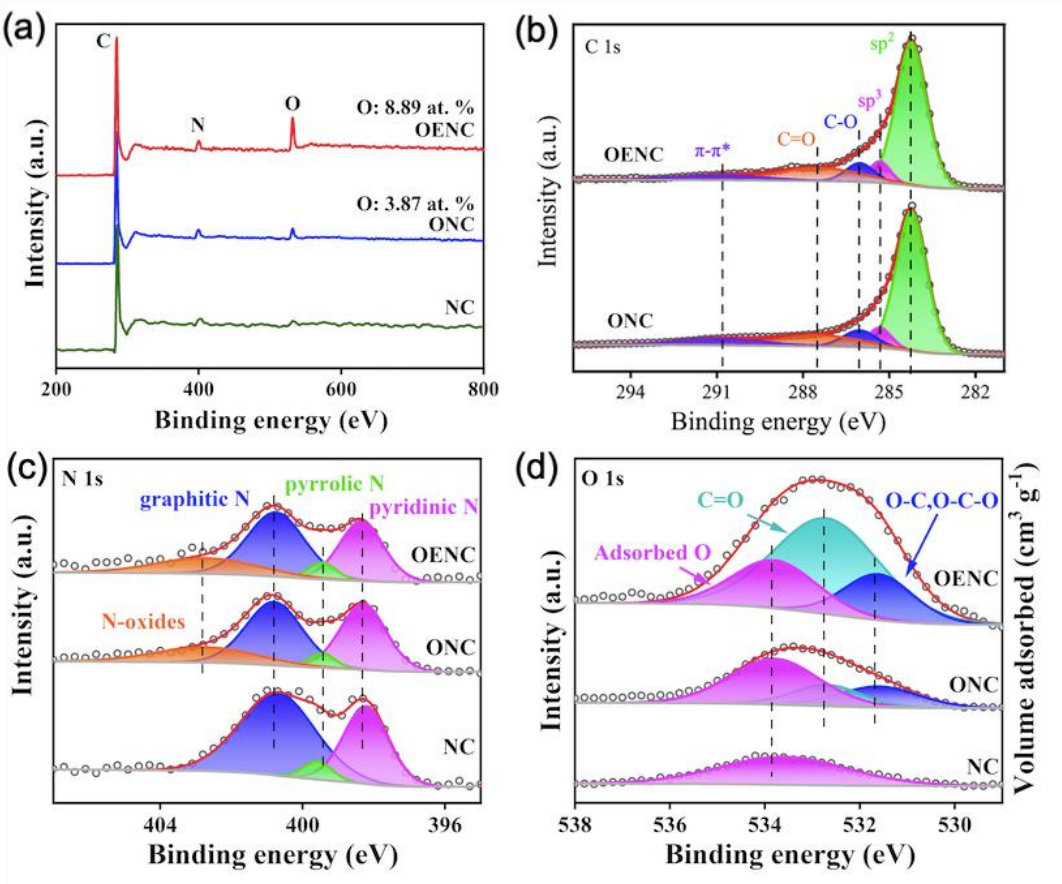

Figure 4.3 (a) The survey XPS spectra of OENC, ONC and NC. High-resolution (b) C 1s, (c) N 1s and (d) O 1s spectra of OENC, ONC and NC.

From the N_2 adsorption-desorption isotherms in Figure 4.4, it can be observed that the OENC also possesses a large specific surface area as determined by the Brunauer–Emmett–Teller (BET) model with a hierarchically porous structure, which matches well with its sheet morphology and is beneficial to the exposure of active sites as well as the facilitation of mass transfer for efficient NRR.

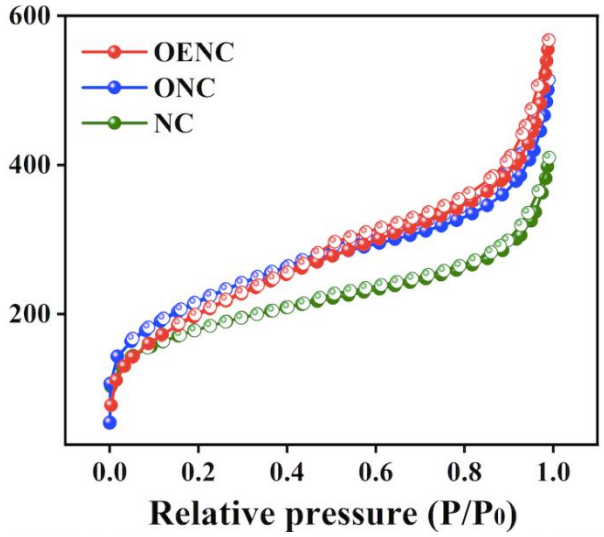

Figure 4.4 N_2 sorption isotherms of OENC, ONC and NC.

To estimate the electrochemically active surface area (ECSA) of each sample, the double layer capacitance (C_{dl}) is then calculated (Figure 4.5). The OENC displays a Cdl of 22.1 mF cm^{-2}, 1.5 times higher than that of the ONC (14.6 mF cm^{-2}) and almost 7 times higher than that of the NC (3.3 mF cm^{-2}), indicating that the OENC presents the largest catalytically active area.

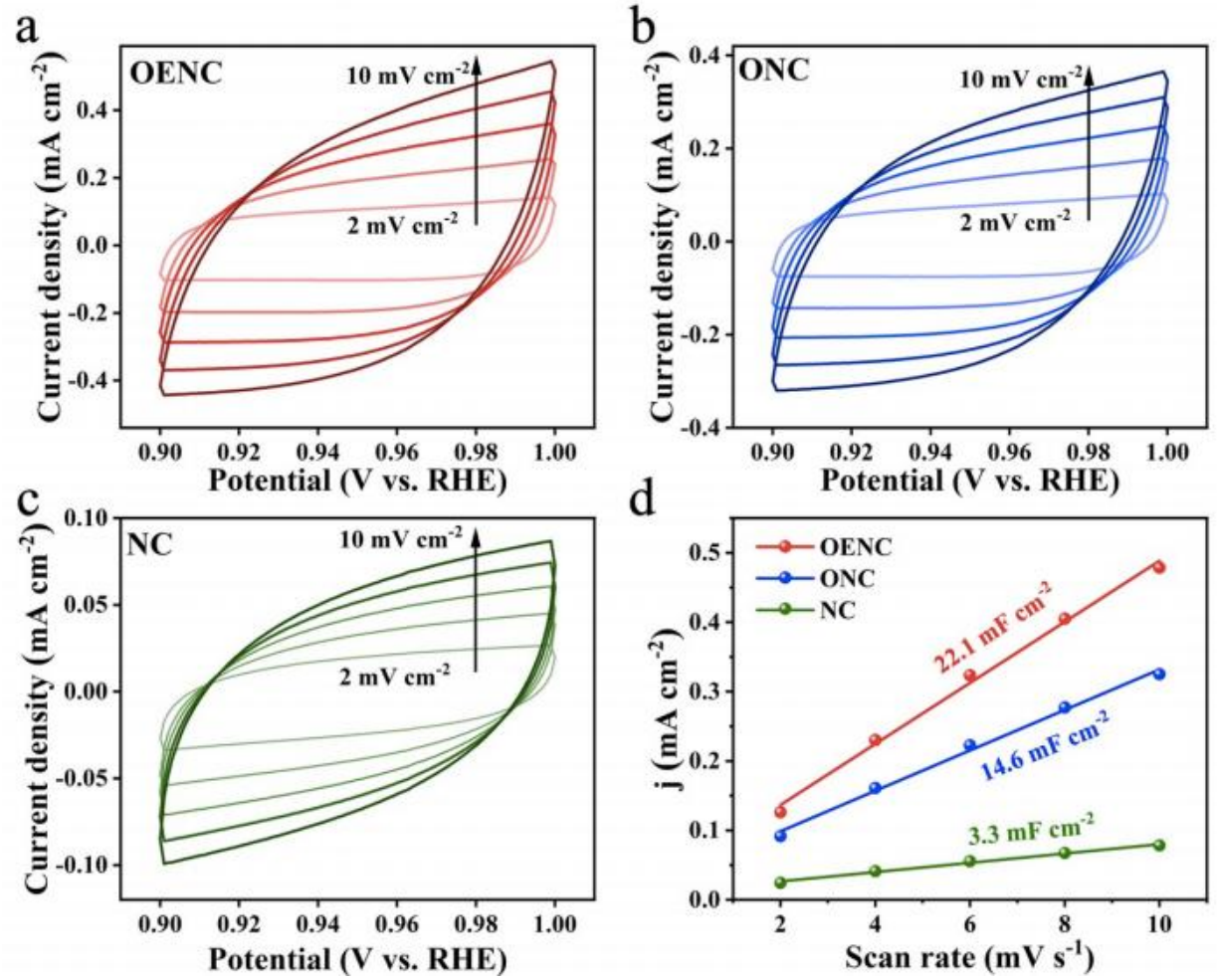

Figure 4.5 Cyclic voltammograms of (a) OENC, (b) ONC, and (c) NC taken at different scan rates in a potential window where only double-layer charging and discharging occurs. (d) Double-layer charging current plotted against the CV scan rate for different electrodes.

The actual NRR performance of OENC, ONC and NC were evaluated in 0.1 M HCl using a gas-tight H-type electrochemical cell under ambient conditions.[161] To obtain a verification of reliable NRR data, a strict experimental protocol was followed and all the contaminations from the electrochemical setup or the feeding gas have been excluded(Figure S4.3 and S4.4).[59,128] Chronoamperometry measurements were performed to achieve quantitative analysis of ammonia production (Figure 4.6), and the possible nitrogen reduction products, including NH_3 and N_2H_4, were examined by the indophenol blue method and the Watt and Chrisp method, respectively (Figure S4.5 and S4.6). Notably, no N_2H_4 by-product was detected here in this study (Figure S4.7).

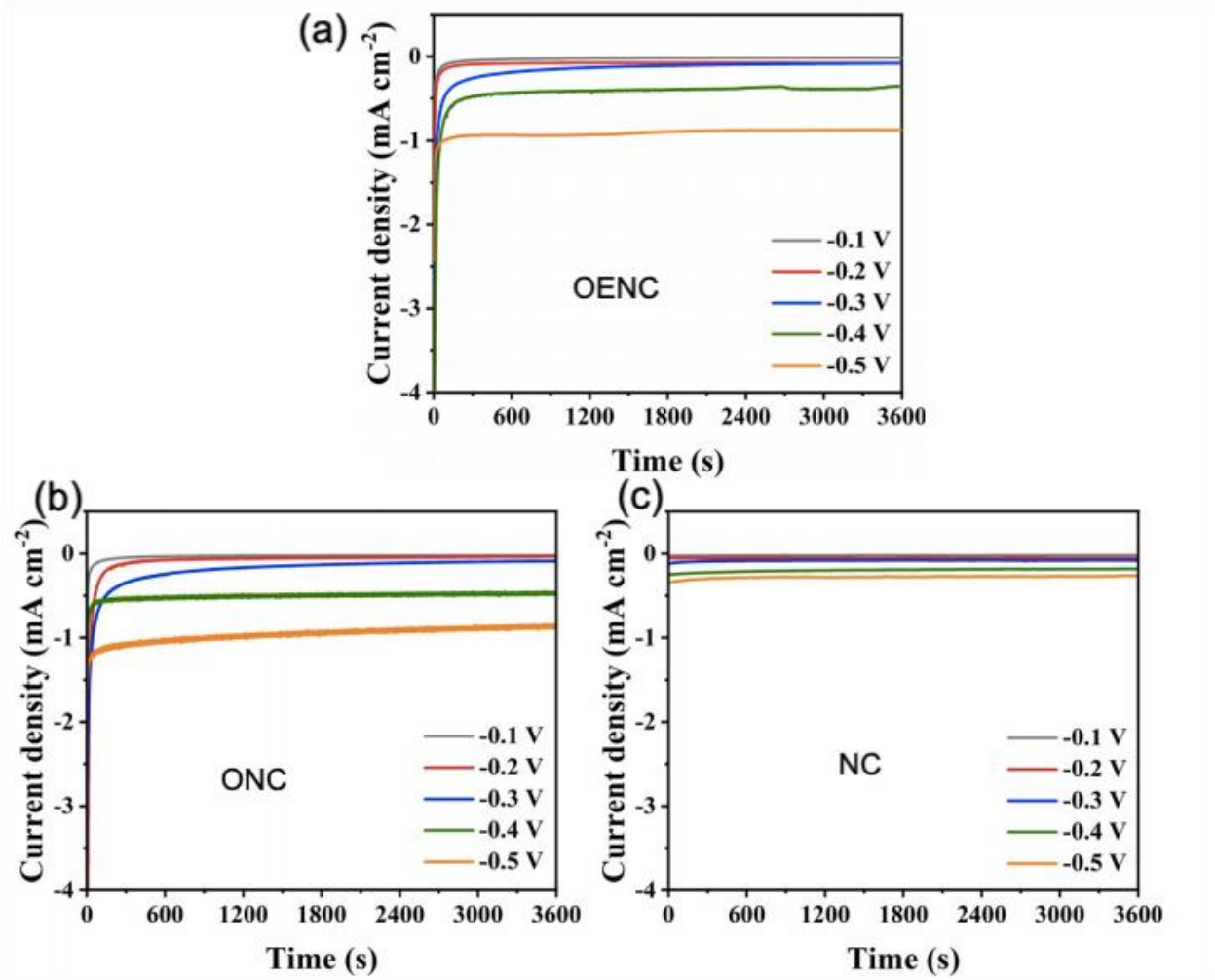

Figure 4.6 Chronoamperometry results of (a) OENC and (b) ONC (c) NC tested in 0.1 M HCl at different applied potentials.

The mean value of NH_3 yield rates and the corresponding FEs of OENC, ONC and NC are compared in Figure 4.7 a and b. Obviously, the OENC catalyst shows better catalytic performance at all applied potentials as compared with ONC and NC. The maximized NH_3 yield rate for OENC is determined to be 67.3 μg h^{-1} mg^{-1} at -0.2 V vs. RHE, much larger than that of ONC (34.4 μg h^{-1} mg^{-1}) or the NC (15.1 μg h^{-1} mg^{-1}). Simultaneously, the highest FE of 36.2% is also attained at -0.2 V vs. RHE, superior to those of the ONC(24.9%) and the NC (12.7%). When the applied potential moves below -0.2 V vs. RHE, both the NH_3 yield rate and FE decrease due to the rising of the competitive HER (Figure 4.8).

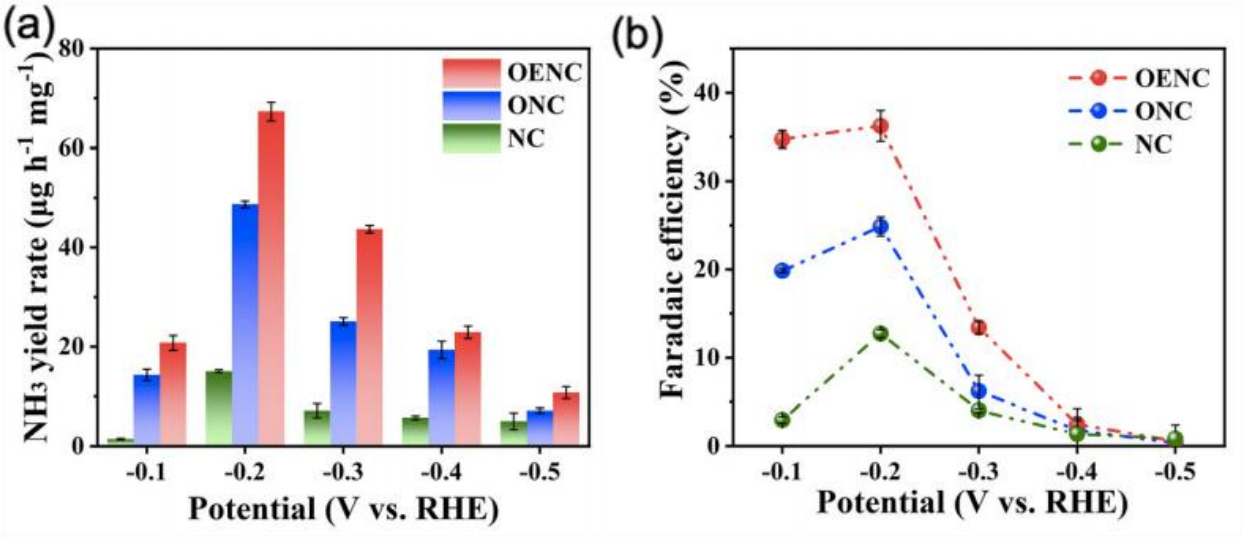

Figure 4.7 (a) NH_3 yield rates and (b) corresponding Faradaic efficiencies of OENC, ONC and NC measured at all given potentials.

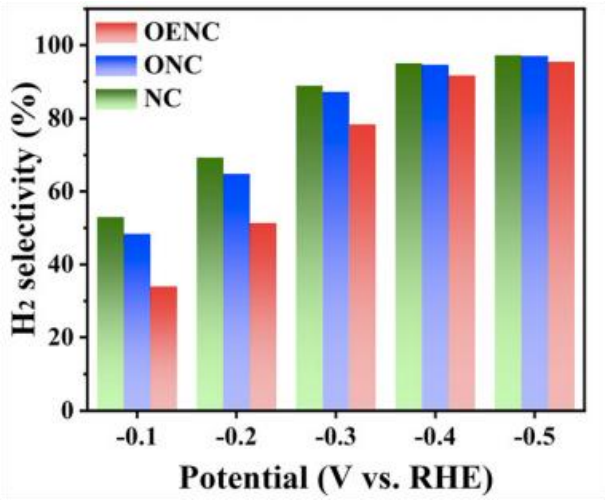

Figure 4.8 H_2 selectivity of OENC, ONC and NC measured at all given potentials.

Upon comparing with the latest works, the superior NRR performance of metal-free OENC is higher than many of the reported electrocatalysts, including noble metal-based catalysts, non-noble metal-based catalysts, and metal-free catalysts (Figure 4.9 a and Table 4.1). In addition, such outstanding performance was further examined by durability experiments at -0.2 V vs. RHE, in which either the ammonia yield rate or the FE shows no marked deteriorations under 10 continuing cycles of NRR electrolysis (Figure 4.9 b), confirming the robust stability of OENC for the electrochemical NRR. Further SEM and XRD characterization shows that the morphology

and structure are well preserved after long-term electrolysis (Figure S4.8 and S4.9), confirming the robust stability of the OENC for the electrochemical NRR.

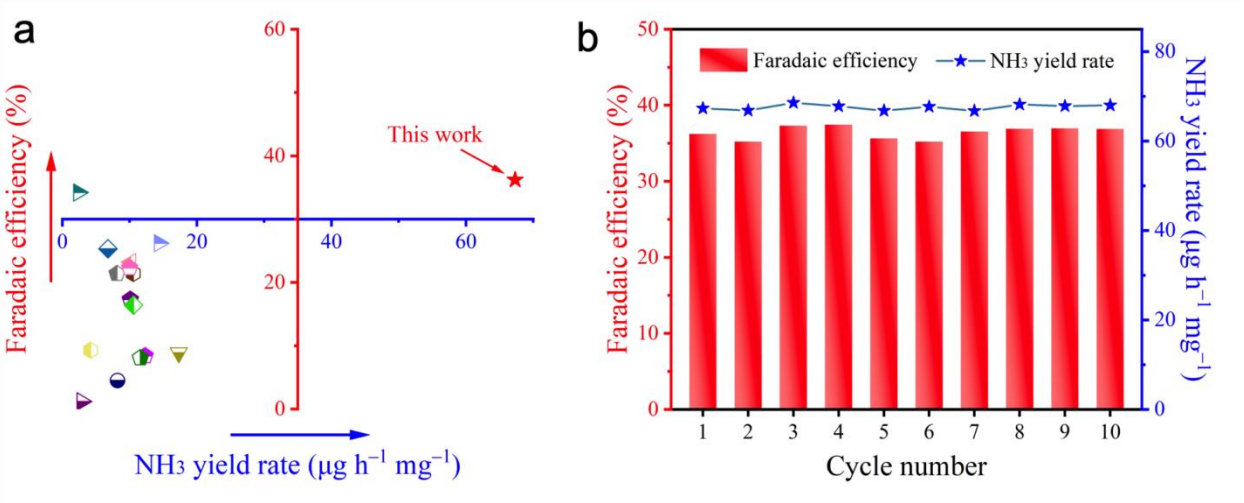

Figure 4.9 **(a) NH_3 yield rate and Faradaic efficiency of OENC compared with other state-of-the-arts; detailed data are provided in Table 4.1. (b) The NRR performance in the durability test of OENC.**

Table 4.1 **Comparison of the electrocatalytic NRR performance at ambient conditions.**

Catalyst	Electrolytre	Faradaic efficiency (%)	NH_3 yield rate ($\mu g\ h^{-1}\ mg_{cat}^{-1}$)	Ref.
OENC	0.1 M HCl	67.3	36.2	This work
Non-noble metal-based catalysts				
$Bi_4V_2O_{11}/CeO_2$	0.1 M HCl	10.16	23.21	[162]
Cr_2O_3 hollow microsphere	0.1 M Na_2SO_4	6.78	25.3	[163]
np-Mo_4P_3	0.1 M PBS	10.1	17.3	[164]
Zr^{4+}-doped anatase TiO_2	0.1 M KOH	17.30	8.90	[165]
$Ni_{0.75}Fe_{0.25}Se_2$	0.1 M Li_2SO_4	12.3	8.4	[166]
Noble metal-based catalysts				
Pd/C	0.1M PBS	8.2	4.5	[167]
Au cluster/TiO_2	0.1 M HCl	8.11	21.40	[168]
$IrTe_4$	0.1 M KOH	14.4	26.2	[169]
Au–Fe_3O_4 Nanoparticles	0.1 M KOH	10.54	21.42	[170]
PdRu nanorod	0.1 M HCl	2.40	34.20	[171]
Metal-free catalysts				
PEBCD	0.5 M Li_2SO_4	2.9	1.2	[172]
Defect-rich fluorographene nanosheets	0.1 M Na_2SO_4	4.2	9.3	[173]

CN_xB_y	0.1 M HCl	10.58	16.40	[152]
NPC-500	0.005 M H_2SO_4	10.0	22.3	[147]
Metal-free polymeric carbon nitride	0.1 M HCl	11.59	8.09	[146]

A series of complementary and controlled experiments were carried out to verify the reliability of the electrochemical data. First, the bare carbon paper (CP) was electrolyzed in N_2-saturated electrolyte at -0.2 V vs. RHE, while the OENC-coated electrode was electrolyzed in Ar-saturated electrolyte at -0.2 V vs. RHE or N_2-saturated electrolyte under open circuit potential. The results suggest that no ammonia was detected by neither indophenol blue method nor the ^1H nuclear magnetic resonance (NMR) spectra (Figure 4.9 a and Figure S4.10). Subsequently, ^{15}N isotope labeling experiments were conducted to further investigate the N source of the produced ammonia. No ammonia can be detected under open circuit potential when employing $^{15}N_2$ as the feeding gas, while an NH_3 yield rate of 66.0 μg h^{-1} mg^{-1} and a FE of 37.2% were obtained at -0.2 V vs. RHE by indophenol blue method (Figure 4.10 b). Furthermore, in contrast to the case of ^{14}NRR experiments, only a doublet signal for $^{15}NH_4^+$ is found in the ^1H NMR spectrum of the electrolyte, which is consistent with that obtained with standard solutions of $(^{15}NH_4)_2SO_4$ (Figure 4.10 c). Moreover, upon quantitative analysis, both NH_3 yield rate and the FE match well with those attained in the ^{14}NRR experiments either by indophenol blue method or the ^1H NMR method (Figure 4.10 d). All the above results strongly evidence that the produced NH_3 entirely originates from the electrochemical NRR process, convincingly proving the reliability of the electrochemical data.

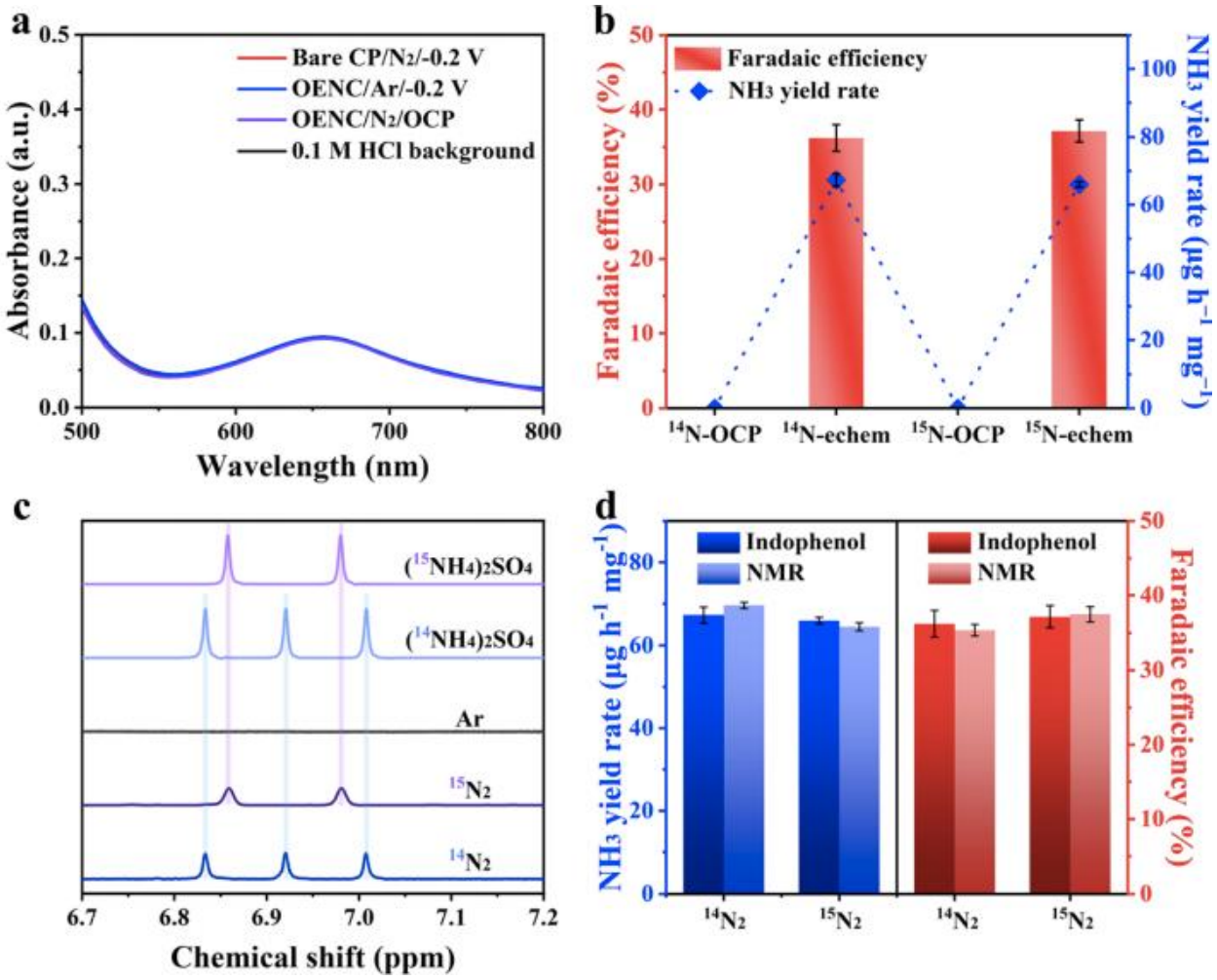

Figure 4.10 (a) The UV-vis absorption spectra of the electrolytes under different conditions. (b) Comparison of the NH_3 yield rate and Faradaic efficiency using different feeding gases for NRR at -0.2 V vs. RHE and open-circuit potential. (c) ^1H NMR spectra of the NRR products using different feed gases. (d) Comparison of the NH_3 yield rate and Faradaic efficiency using different feeding gases for NRR at -0.2 V vs. RHE either by colorimetric or NMR method.

To gain deeper insight into the involved reaction mechanisms of NRR on OENC, DFT calculations were performed to study the free energy profiles, including the distal pathway and the alternating pathway (Figure S4.11 and S4.12).[90] Usually, nitrogen features strong bonding energy, broad energy gap between the highest occupied molecular orbital and the lowest unoccupied molecular orbital, as well as high ionization potential, so that its chemisorption is considered as the rate-determining step (RDS). Previous reports have indicated that nitrogen-doped carbon with modified electronic structure and the charge polarization could facilitate the nitrogen adsorption. Indeed, for N-doped carbon, the nitrogen chemisorption barrier has been

successfully eliminated, which turns into an exothermic step. Unfortunately, as multiple-steps electrochemical reactions, the NRR process is more than just adsorption, but also subsequent nitrogen cleavage and hydrogenation. That is, a superior NRR performance is the result of combined action of all steps. For NC, despite the eliminated barrier of nitrogen chemisorption, the NRR process still suffers from high energy barriers of 1.92 eV during the hydrogenation of $*N_2$ to *NNH as the RDS in the alternating pathway or 3.38 eV during the hydrogenation of $*NNH_2$ to $*N + NH_3$ as the RDS in the distal pathway. The introduction of oxygen as secondary heteroatom could further optimize the electronic structure of active sites, triggering the synergistic electronic promoting effect to boost the NRR process. As expected, the reaction barrier is significantly reduced to 1.14 eV, with the hydrogenation of $*NH_2 + NH_3$ to $* + 2NH_3$ as the RDS. The theoretical calculations well rationalize the electrochemical experiments, and thus emphasize the superiority of oxygen doping toward NRR on nitrogen-doped carbon.

4.3 Conclusion

In conclusion, oxygen is deliberately introduced into nitrogen-doped carbon to trigger synergistic electronic promoting effect and boost ambient ammonia synthesis. The proposed OENC exhibits much enhanced NRR performance as compared with NC, with an ammonia yield rate of 67.3 μg h^{-1} mg^{-1} and a FE of 36.2 % at -0.2 V vs. RHE in 0.1 M HCl. Such superior NRR performance of OENC ranks at the top level among the reported electrocatalysts, and the reliability of the electrochemical data has been verified by a series of complementary and controlled tests including qualitative and quantitative isotope labelling experiments. The DFT calculations suggest that, upon the introduction of oxygen into nitrogen-doped carbon, the electronic structure and the polarity of adjacent carbon atoms are further optimized, greatly reducing the energy barrier of the overall NRR process from 1.92 eV on NC to 1.14 eV on OENC. This work opens up an exciting new avenue to develop multi-heteroatom-doped carbon material and gives a guidance of rational design of metal-free electrocatalysts.

Acknowledgements

This work was supported by the National Natural Science Foundation of China (Nos. U21A20332, 52103226, 52202275, 52203314, and 12204253), the Distinguished Young Scholars Fund of Jiangsu Province (No. BK20220061), Suzhou Foreign Academician

Workstation (project number: SWY2022001), and the Fellowship of China Postdoctoral Science Foundation (No. 2021M702382).

4.4 Supporting information

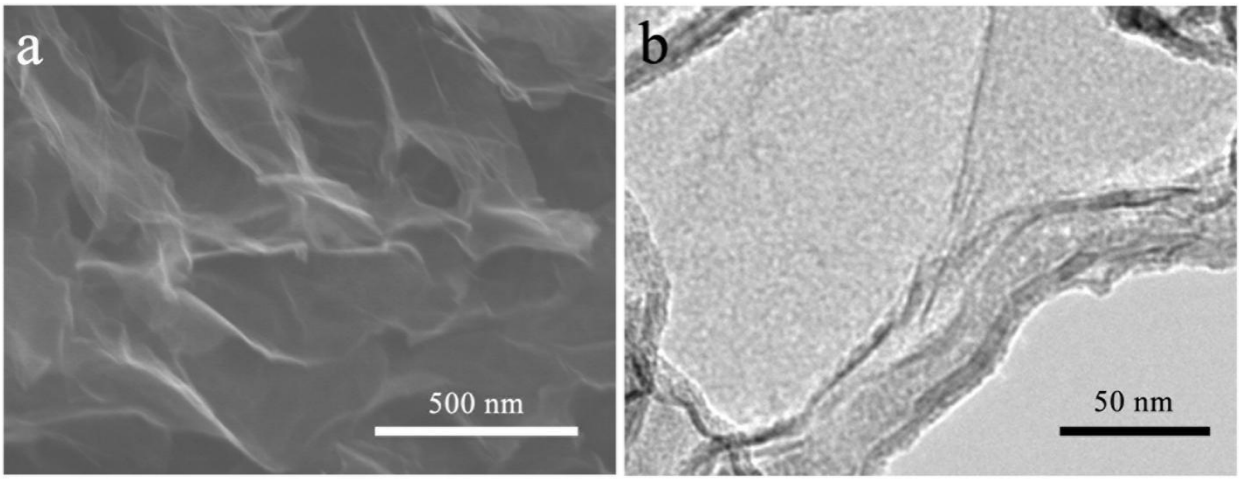

Figure S4.1 (a) Scanning electron microscopy image and (b) transmission electron microscopy image of ONC.

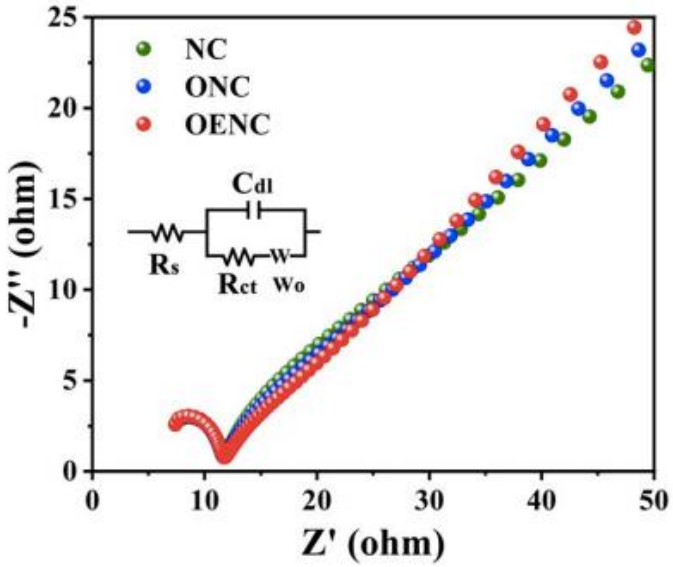

Figure S4.2 Nyquist plots obtained using electrochemical impedance spectroscopy for the different electrodes, inset: the equivalent circuit used to fit the experiment data. Upon impedance spectra fitting, the

charge transfer resistances (R_{ct}) are determined to be 5.983 Ω cm^{-2} for OENC, 5.937 Ω cm^{-2} for ONC, and 5.925 Ω cm^{-2} for NC.

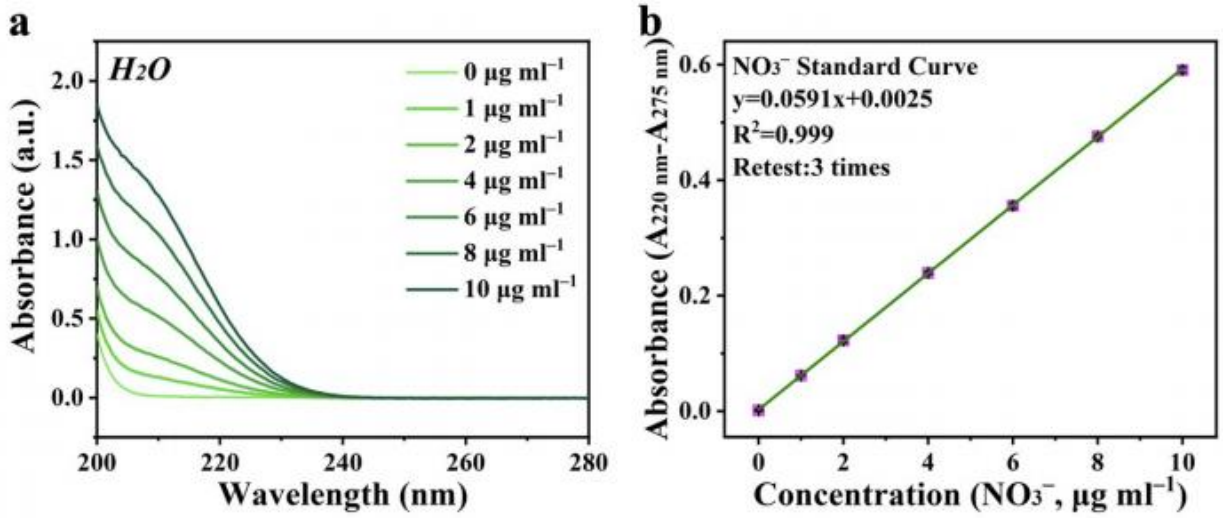

Figure S4.3 (a) The UV-vis absorption spectra and (b) corresponding calibration curves for the colorimetric determination of NO_3^- in H_2O using the sulfamic acid method. The error bars correspond to the standard deviations of three separately prepared samples measured under identical conditions.

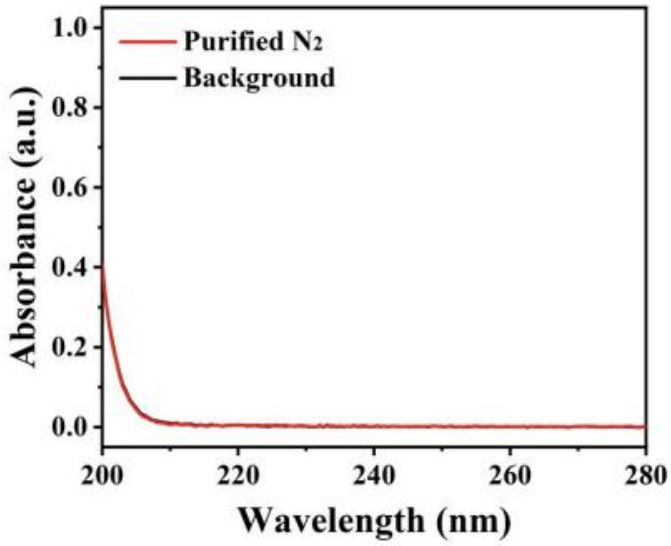

Figure S4.4 The UV-vis absorption spectra of the H_2O background and the purified N_2 treated water using sulfamic acid method.

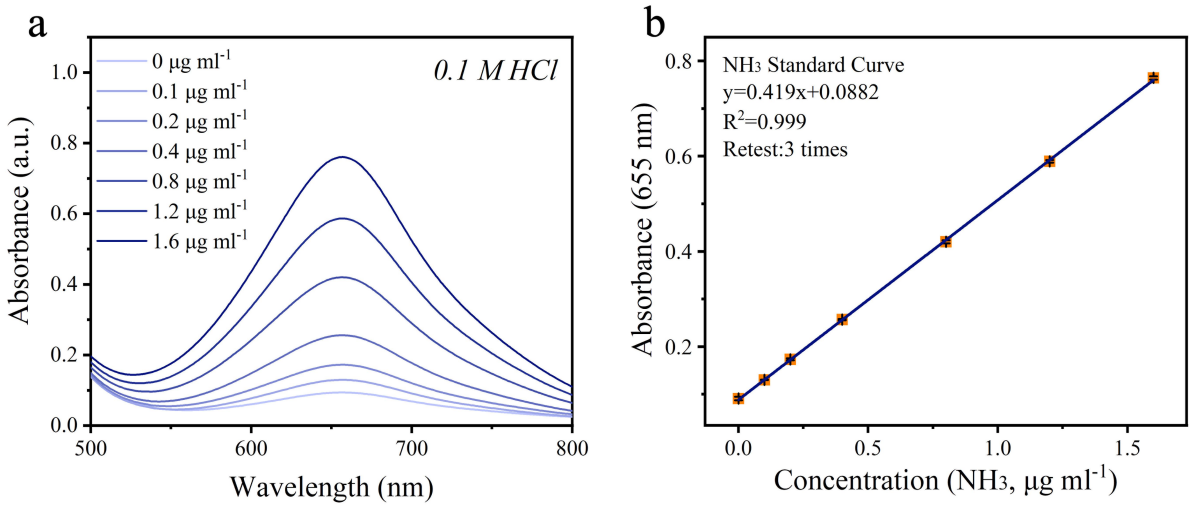

Figure S4.5 (a) The UV-vis absorption spectra and (b) corresponding calibration curves for the colorimetric determination of NH_3 in 0.1 M HCl using the indophenol blue method. The error bars correspond to the standard deviations of three separately prepared samples measured under identical conditions.

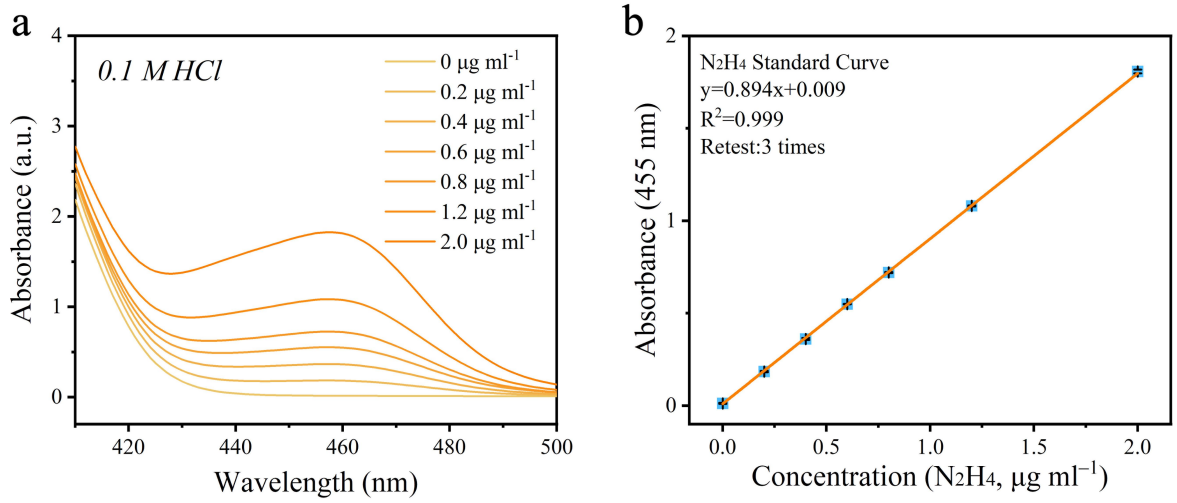

Figure S4.6 (a) The UV-vis absorption spectra and (b) the corresponding calibration curves for colorimetric N_2H_4 determination in 0.1 M HCl using the Watt and Chrisp method. The error bars correspond to the standard deviations of three separately prepared samples measured under identical conditions.

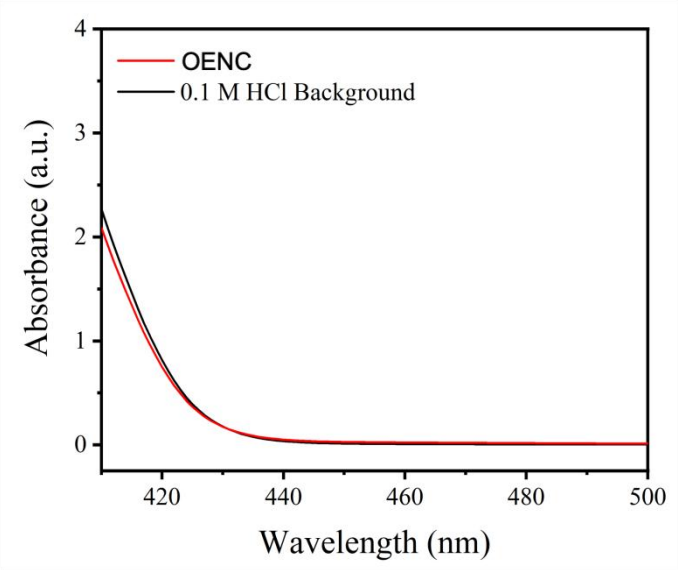

Figure S4.7 The UV-vis absorption spectra of the electrolyte using the Watt and Chrisp method.

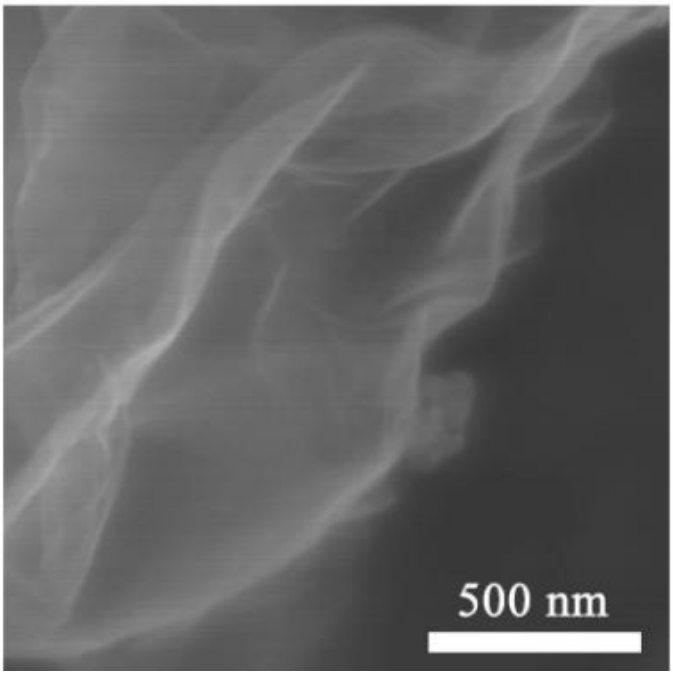

Figure S4.8 Scanning electron microscopy image of the OENC after NRR electrolysis.

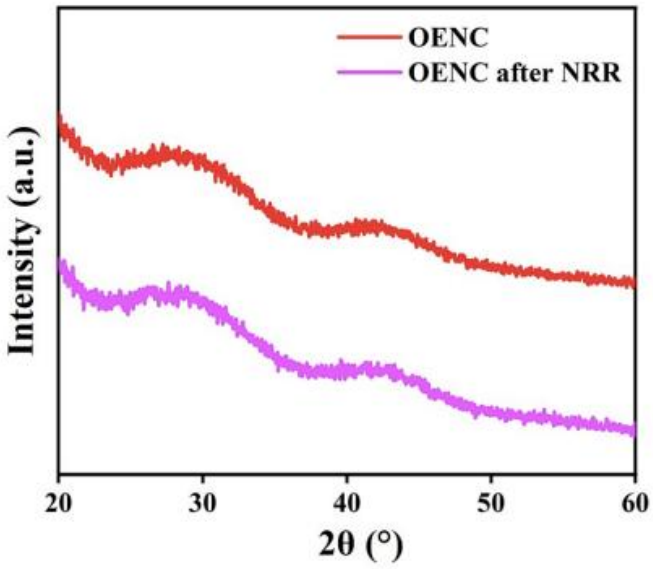

Figure S4.9 XRD of the OENC after NRR electrolysis.

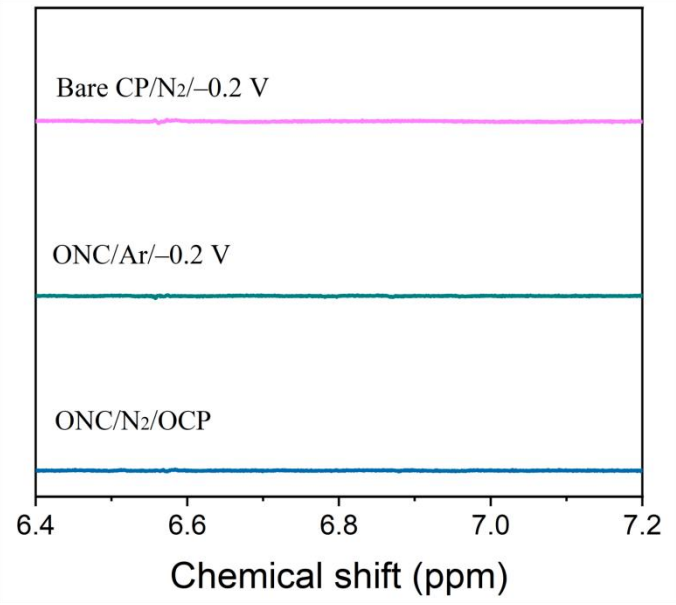

Figure S4.10 ^{1}H NMR spectra of the electrolytes measured under different conditions.

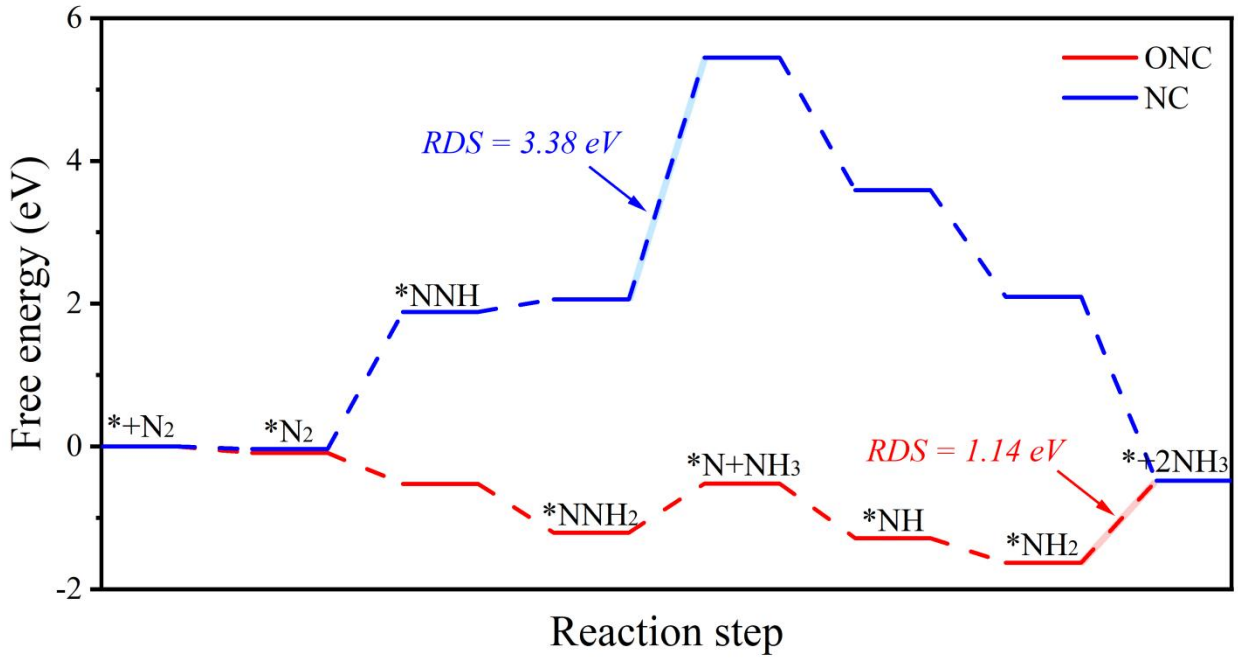

Figure S4.11 Free energy diagram of the NRR on OENC and NC through the distal pathway.

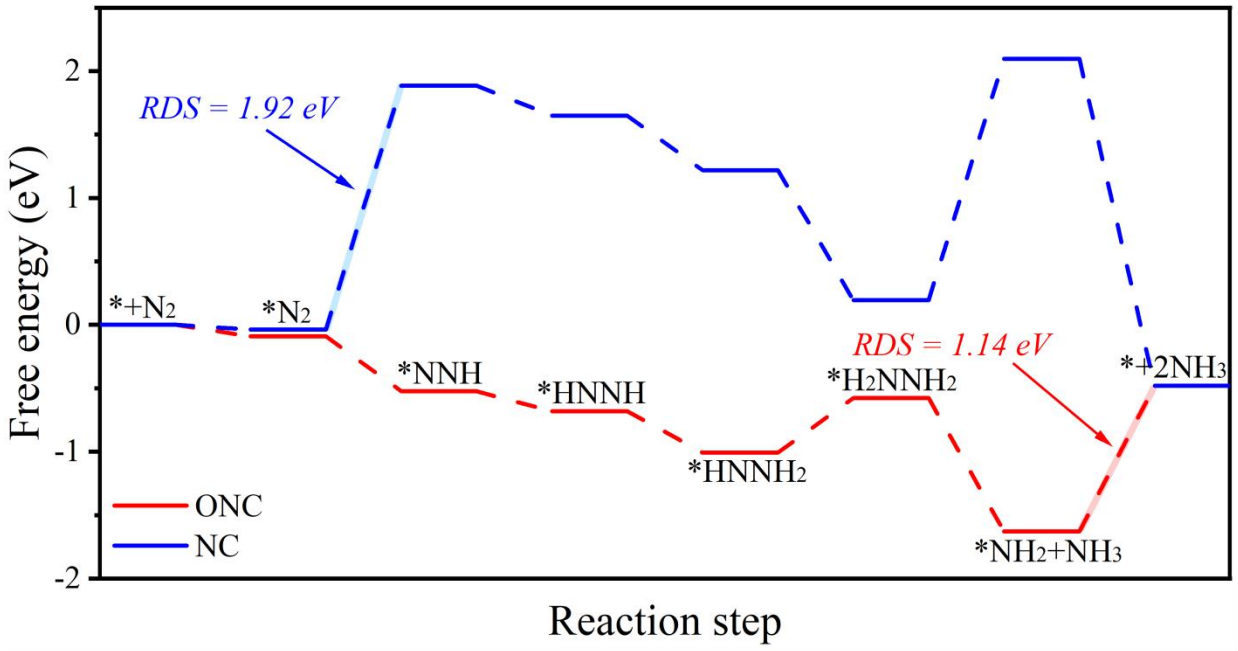

Figure S4.12 Free energy diagram of the NRR on OENC and NC through the alternating pathway.

5 Breaking scaling relations in NRR with FeCoNC catalyst

Breaking scaling relations in nitrogen reduction with asymmetrical heterobimetallic FeCo sites to boost ammonia synthesis

Rompre les relations d'échelle dans la réduction de l'azote avec des sites FeCo hétérobimétalliques asymétriques pour stimuler la synthèse d'ammoniac

Na Xu,[a,b] Yanzheng He,[a] Mengfan Wang,[a] Chen Cheng,[a] Qiyang Cheng,[a] Sisi Liu,[a] Haoqing Ji,[a] Chenglin Yan,[a,c] Federico Rosei[b,d]

a College of Energy, Soochow University, Suzhou 215006, China

b Institut national de la recherche scientifique1650 Boul. Lionel-Boulet, Varennes, QC, J3X1P7, Canada

c School of Petrochemical Engineering, Changzhou University, Changzhou 213164, China

d Department of Chemical and Pharmaceutical Sciences, University of Trieste, Via Giorgeri 1, Trieste 34127, Italy

Publication:

Materials Chemistry Frontiers

Publication date: 5 December 2023

Volume 8, Page 851–858

DOI: 10.1039/D3QM01076G

5.1 Introduction

Ammonia (NH_3) featuring easy liquefaction and high energy density plays a key role in the modern society, which is widely utilized in industry and agriculture.[8,124,130] It also holds great potential to serve as the carrier for renewable energy and thus reduce the use of fossil fuels for green economy.[131,174,175] Nowadays, the century-old Haber-Bosch (HB) process has still been the primary method for industrial ammonia production. However, the required harsh conditions such as high temperatures (300-500 °C) and pressures (150-300 bar) inevitably consume approximately 1~2% global energy and result in the release of over 3 gigatonnes of CO_2 annually.[110,134] Therefore, it is necessary to search for clean and sustainable method to replace the energy-intensive HB process. With the researchers' efforts for decades, several alternative strategies, such as biocatalysis, photocatalysis, and electrocatalysis, have been proved to be able to achieve artificial ammonia synthesis.[99,118,135] Among a variety of options, the electrochemical nitrogen reduction reaction (NRR) by utilization of renewable electricity has gained significant and increasing attentions.[113,114] Nevertheless, although encouraging progresses have been made for NRR, the undesired performance still poses great challenge for developing the ideal electrocatalyst.

Single-atom catalysts (SACs) with isolated metal atom coordinated on carbon substrate have recently been demonstrated to deliver superior performance in various electrocatalysis fields, such as oxygen reduction reaction, hydrogen evolution reaction, and carbon dioxide reduction reaction.[140,141,176-178] The maximum atom-utilization efficiency, together with the unique electronic structure and coordination environment, have been proven to contribute to the high activity and selectivity.[179-181] However, for efficient NRR as multi-intermediate reaction, any ambition by SACs with monotonous active site seems to be in vain. It might be easy to regulate the adsorption energy of single intermediate in reactions with one-intermediate, but it is impossible to tune the adsorption energy of all intermediates simultaneously in multi-intermediate reactions, since the well-known adsorbate scaling relations forbid the binding strength of a certain intermediate from being optimized freely.[182-184] As a result, the ultrahigh limiting potential of the rate-determining step (RDS) remains a great challenge.[137] Taking inspiration from Nature, where the nitrogen is fixed on enzyme complex nitrogenase containing heteronuclear FeMo active centers.[11,125,185] Developing heterobimetallic electrocatalysts featuring synergetic interatomic interactions and more flexible active sites would be a promising strategy to address this issue. Compared with SACs, the heteronuclear dimer sites could provide a bridge active center for the adsorption of nitrogen and the corresponding

intermediates, which is conducive to the polarization of N_2 and makes the optimization of the binding strength of certain intermediates feasible.[186-189]

In this work, asymmetrical heterobimetallic sites is proposed to break the inherent scaling relations between the binding strength of intermediates of NRR as multi-intermediate reaction. The heteronuclear Fe and Co atoms with two occupied d orbitals in the dimer sites can simultaneously trap two lone-pair electrons at two ends of the N_2 molecule and enable the asymmetrical electron backdonation, which is beneficial to the polarization of N≡N bond and thus facilitates its weakening. The strong electronic interaction between N_2 and dimer sites enables maximized activation of N_2 and regulation of the binding strength of the key intermediates, thereby greatly reducing the energy barrier of the overall NRR process as confirmed by the density functional theory (DFT) calculations. In 0.1 M HCl, the proof-of-concept catalyst achieves a superior ammonia yield rate of 70.11 μg h^{-1} mg^{-1} and a high Faradaic efficiency of 32.16% at -0.2 V versus reversible hydrogen electrode (vs. RHE), and the reliability has been confirmed by several qualitative and quantitative experiments using both $^{14}N_2$ and $^{15}N_2$ as feeding gas.

5.2 Results and discussion

Isolated single Fe atoms anchored on nitrogen-doped carbon (FeNC) is well-known to deliver certain degree of NRR performance, and is chosen as the proof-of-concept SACs in this work.[82,190] Co single atoms have also been reported to be able to serve as active sites for N_2 adsorption and dissociation, so that was chosen as the second metal here to assemble the asymmetrical Fe-Co dimers anchored on nitrogen-doped carbon (FeCoNC). Theoretical calculations were first conducted to explore the advantages of asymmetrical heterobimetallic sites in comparison with single site. The proposed configurations of FeNC and FeCoNC are shown in Figure 5.1 a and b. The electrostatic potential of heterobimetallic sites in FeCoNC clearly exhibit asymmetrical charge distribution (Figure 5.1 c), which is beneficial to polarize the adsorbed N_2 and thus weakens the N≡N bond.[56,113] The electron density difference after nitrogen adsorbed at FeNC and FeCoNC are compared to give a deep understanding of the advantages of heterobimetallic sites. The N_2 adsorbed on FeNC configuration ($*N_2$@FeNC) corresponds to the end-on pattern having one N atom binding with the Fe site (Figure 5.1 d), while the N_2 adsorbed on FeCoNC configuration ($*N_2$@FeCoNC) belongs to the side-on pattern with both two N atoms binding simultaneously with the dimers (Figure 5.1 e).[191] Both single

atom site and bimetal sites with empty d-orbitals are capable of accepting lone-pair electrons of nitrogen through σ donation, and then donating back to the antibonding orbitals of the adsorbed molecule with partially filled d-electrons via π backdonation.[192] However, different structures show different behaviors. For *N_2@FeNC with end-on pattern, only one lone-pair electron of adsorbed side of the nitrogen molecule can be trapped by the empty d-orbital of the single Fe atom site, so that the electronic interaction between N_2 and FeNC is rather limited. At the same time, the adsorbed N_2 experiences elongation of the N≡N bond by only 0.022 Å with respect to the calculated distance for a free N_2 molecule (1.154 Å) (Figure 5.1 f).[127] On the contrary, both Fe and Co atoms in the bimetal sites with two occupied d orbitals can simultaneously trap two lone-pair electrons at two ends of the nitrogen molecule, as confirmed by stronger electron accumulation and depletion observed in the *N_2@FeCoNC.[193] Combined with the elongation of N≡N bond length to 1.214 Å, the maximized activation for the following hydrogenation steps is thus demonstrated.

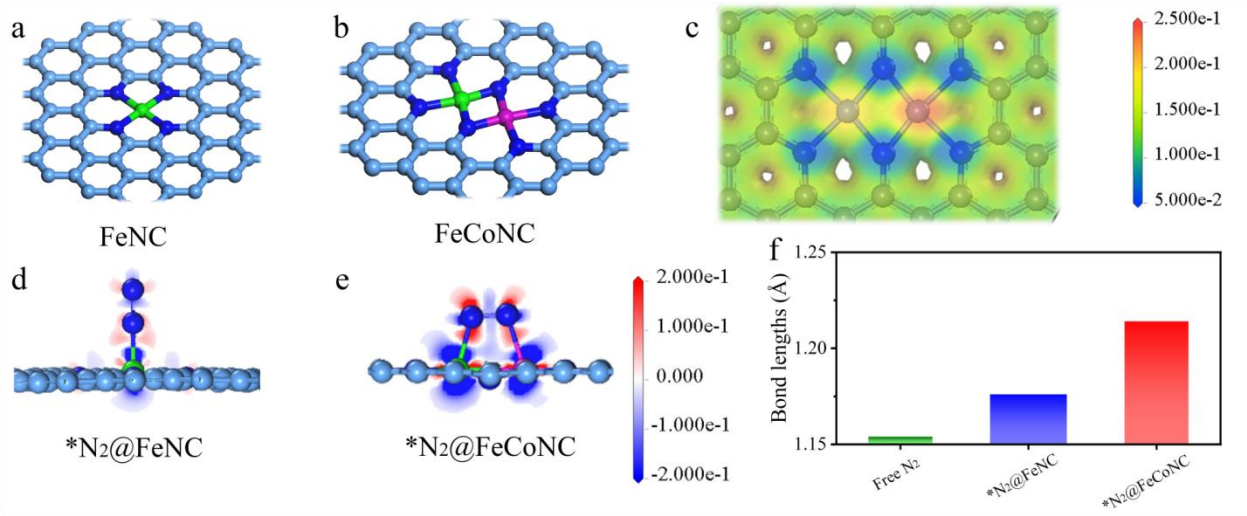

Figure 5.1 Configurations of (a) FeNC and (b) FeCoNC. (c) The electrostatic potential of FeCoNC. The electron density difference after nitrogen adsorbed at (d) FeNC and (e) FeCoNC. (f) Comparison of nitrogen bond length after adsorption at the corresponding active site.

Subsequently, the free energy diagrams for NRR on FeNC and FeCoNC were further calculated by DFT to explore if asymmetrical heterobimetallic sites could indeed break scaling relations limited by the single metal site.[90][40] The proposed NRR mechanisms including the distal pathway and the alternating pathway were considered here.[194,195] For the system of FeNC

following the alternating pathway, the RDS of NRR is the hydrogenation of $*H_2NNH_2$ to $*NH_2$ + NH_3, with a ΔG value of 0.79 eV (Figure 5.2 a). As expected, this RDS can be radically promoted by the bridge site of FeCoNC with an implementable ΔG value of 0.43 eV. As for the distal pathway, bigger energy barrier of the RDS of the hydrogenation of $*NNH_2$ to *N + NH_3 has to be overcome, so that is not considered here (Figure 5.2 b). Overall, the above results reveal that the asymmetrical heterobimetallic sites featuring the polarized surface enable maximized activation of nitrogen and contributes to significantly reduced energy barrier of the overall nitrogen reduction process, thus holding great potential to serve as the electrocatalyst for NRR.

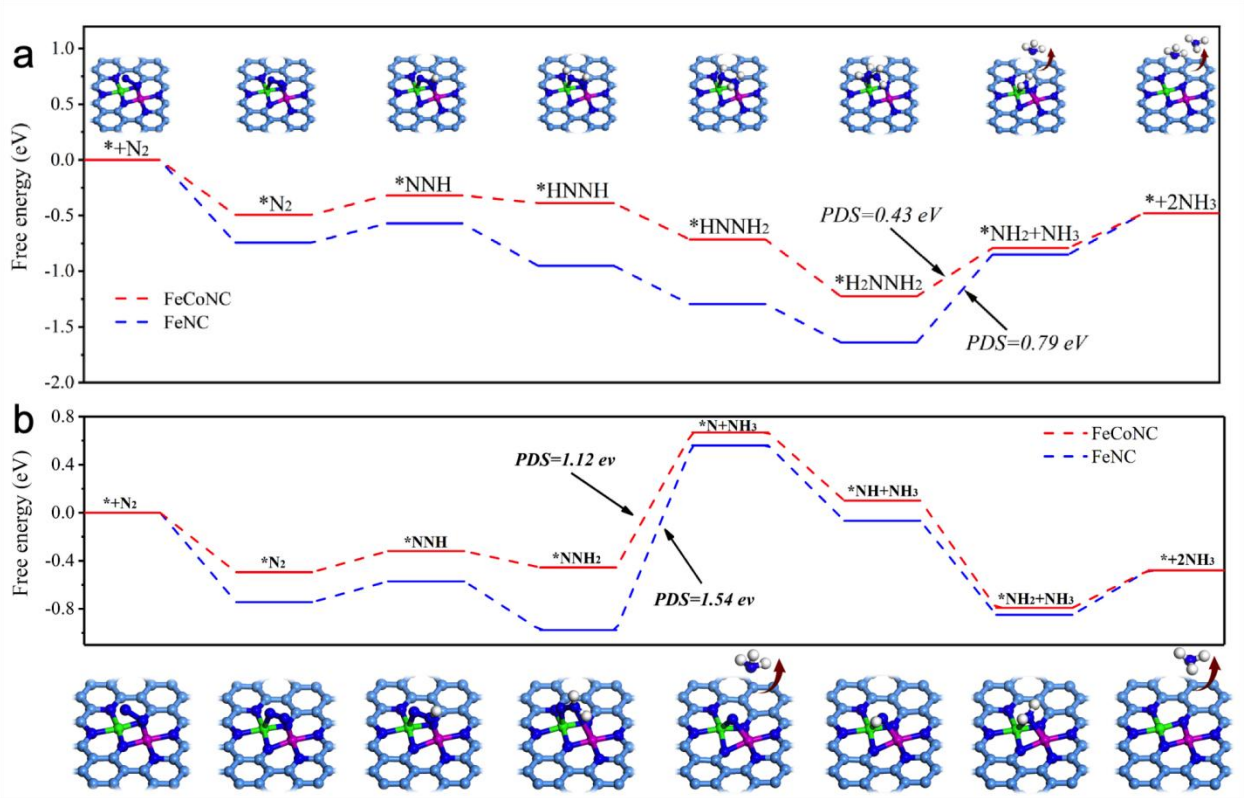

Figure 5.2 (a) Free energy of ammonia synthesis on FeCoNC and FeNC through the alternating pathway and the corresponding configurations of adsorbates on FeCoNC. (b) Free energy of ammonia synthesis on FeCoNC and FeNC through the distal pathway and the corresponding configurations of adsorbates on FeCoNC. The light blue, blue, green, pink, and white spheres represent C, N, Fe, Co, and H atoms, respectively.

Inspired by theoretical calculations, FeNC and FeCoNC were synthesized to evaluate and compare the NRR performance experimentally. Fe single atom/FeCo dual atoms immobilized

on N-doped hollow carbon nanospheres were prepared by optimized pyrolysis of polypyrrole-metal coordination complex.[154] The scanning electron microscopy (SEM) and transmission electron microscopy (TEM) images show that both FeCoNC and FeNC catalysts exhibit the aperture spherical structure (Figure 5.3 a and b, Figure S5.1). The mapping images of FeCoNC exhibit that Fe, Co, C, and N were distributed uniformly over the entire architecture (Figure 5.3 c). Such morphology is conducive to expose the catalytic active sites for NRR, as confirmed by the Brunauer-Emmett-Teller surface area (Figure S5.2) and the electrochemical active surface area calculated by the double layer capacitance (Figure S5.3 and S5.4). The aberration-corrected high-angle annular dark field scanning transmission electron microscopy (AC-HAADF-STEM) was then conducted to elucidate the existential form of Fe and Co atoms (Figure 5.3 d). As expected, the homogeneously distributed small bright dual dots marked with red cycles are observed in the carbon substrate, which can be attributed to heavy Fe and Co atoms than light C, N, and O atoms.

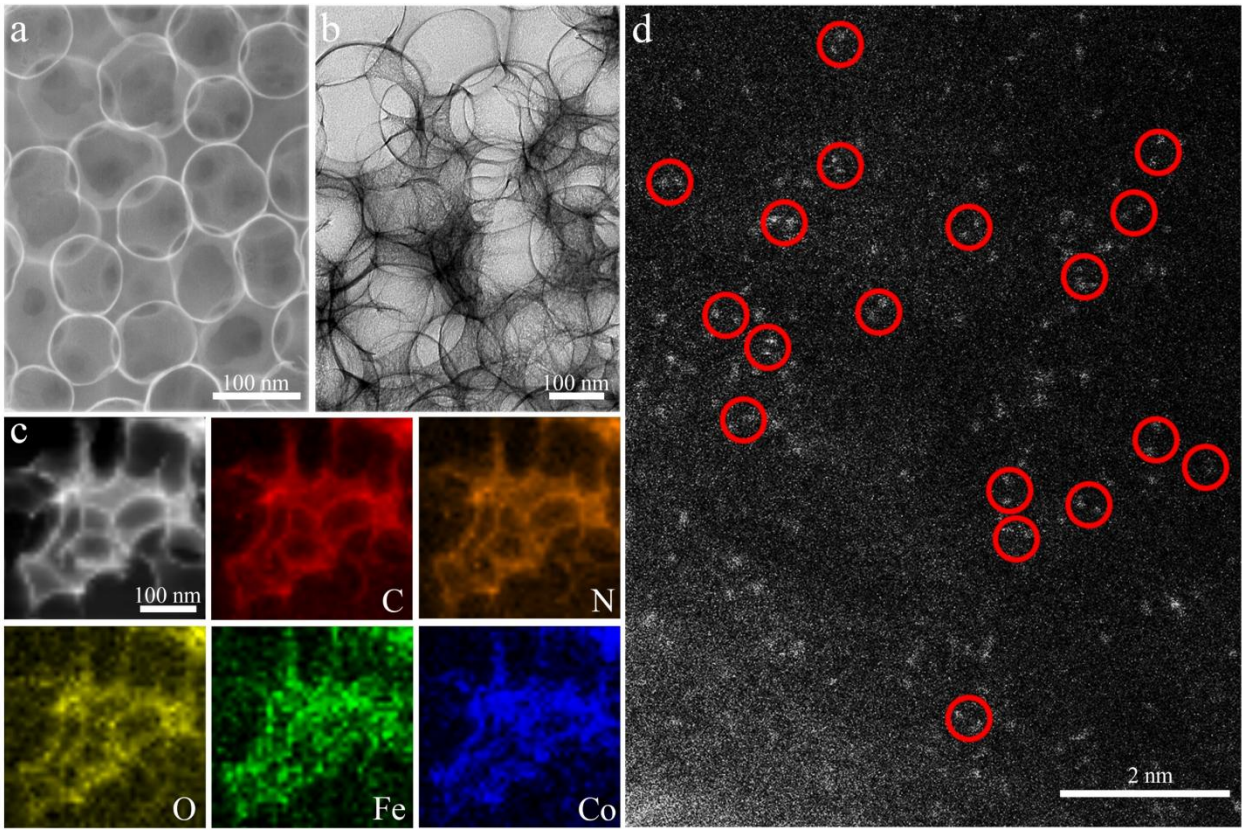

Figure 5.3 (a) Scanning electron microscopy image, (b) transmission electron microscopy image, and (c) element mappings of FeCoNC. (d) Aberration-corrected high-angle annular dark-field scanning transmission electron microscopy image of FeCoNC.

Powder X-ray diffraction (XRD) patterns of FeCoNC and FeNC both exhibit a broad peak ascribed to the (002) plane of graphitic carbon, with no sharp diffraction peak assignable to metallic Fe or Co-based species captured (Figure 5.4 a). The graphitization structure can also be verified by the I_D/I_G value in Raman spectra (Figure 5.4 b).

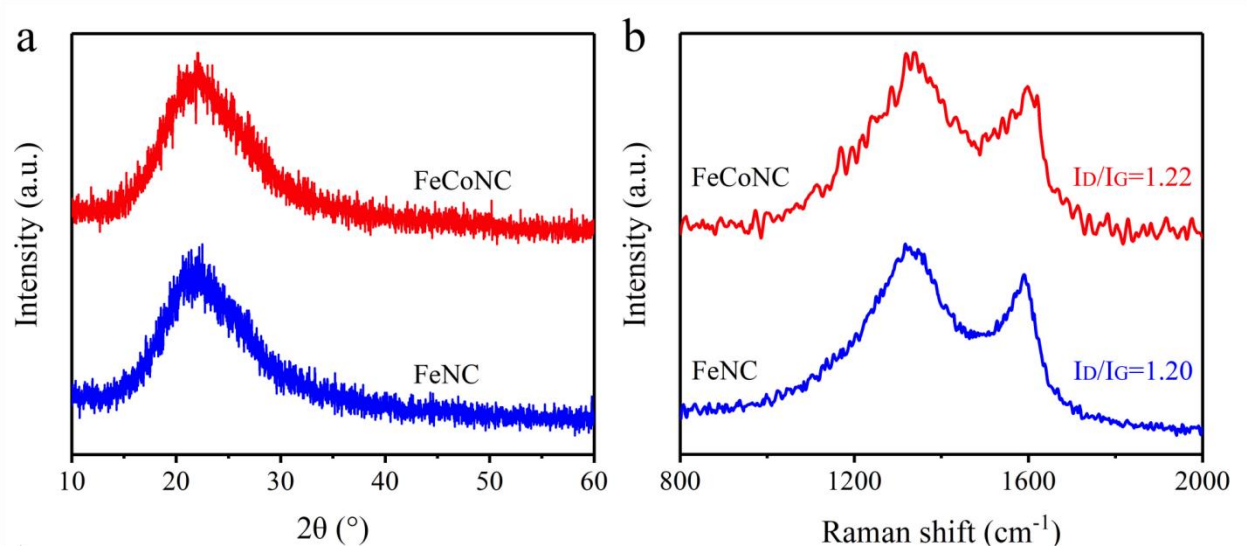

Figure 5.4 (a) XRD pattern and (b) Raman spectra of FeCoNC and FeNC.

X-ray absorption near-edge structure (XANES) and extended X-ray absorption fine structure (EXAFS) analyses were then performed for FeCoNC, with Fe foil and Co foil as references, to further confirm its structure in atomic level. No matter in the Fe K edge or Co K edge XANES spectra, the absorption edge of FeCoNC situates at more positive energy than that of the Fe foil or Co foil (Figure 5.5 a and b), indicating that the valence states of Fe and Co in the heteronuclear active center are positive. The prominent peak at 1.47 Å in the Fe K edge EXAFS spectrum endorses the presence of Fe-N coordination (Figure 5.5 c). In addition, the characteristic peak corresponding to metallic Fe-Fe bonds is absent, confirming its absence in FeCoNC.[196] Similarly, the observed Co K edge EXAFS peak at 1.38 Å can be assigned to the Co-N bond, and the Co-Co peak was not detected. Notably, an evident metal-metal path at 2.02 Å is observed, confirming the presence of Fe-Co bond (Figure 5.5 d). According to above analysis, it could be concluded that FeCo dual sites are atomically dispersed in FeCoNC to serve as efficient NRR active centers.

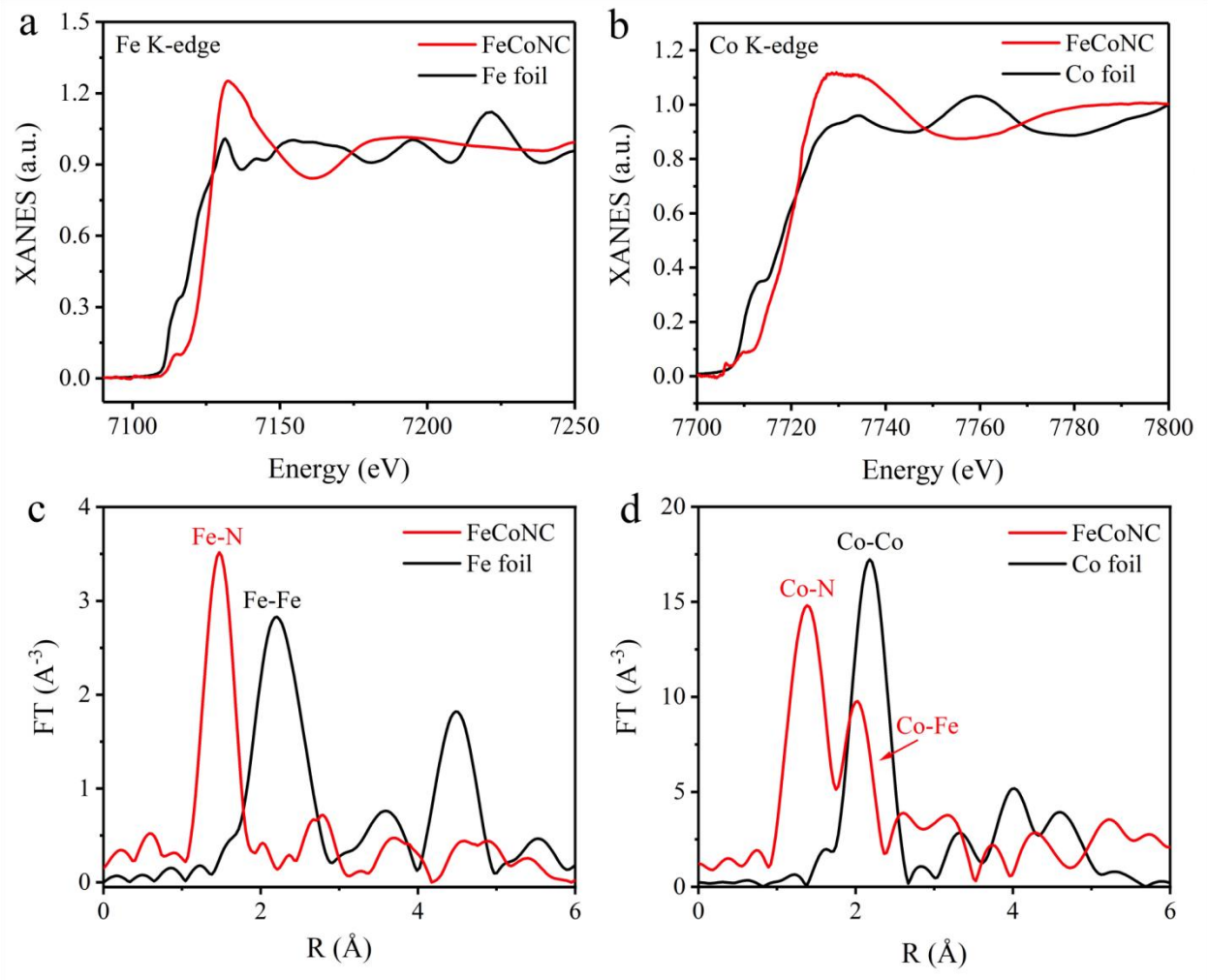

Figure 5.5 (a) X-ray absorption near-edge structure (XANES) spectra of FeCoNC and Fe foil. (b) XANES spectra of FeCoNC and Co foil. (c) Extended X-ray absorption fine structure (EXAFS) spectra at the Fe K-edge of FeCoNC and Fe foil. (d) EXAFS spectra at the Co K-edge of FeCoNC and Co foil.

The actual NRR performance of FeCoNC and FeNC were then evaluated in 0.1 M HCl using a gas-tight H-type electrochemical cell under ambient conditions.[197,198] A strict experimental protocol was followed to obtain a verification of reliable NRR performance during the measurements, and all the contaminations from the feeding gas or the electrochemical setup have been excluded (Figure S5.5-S5.8).[59,199] Quantitative analysis of ammonia production was carried out via chronoamperometry measurements (Figure 5.6 a and b). Both NH_3 and N_2H_4 as possible nitrogen reduction products have been examined by colorimetric method (Figure S5.9 and S5.10), while no N_2H_4 by-product was found in this study (Figure S5.11).

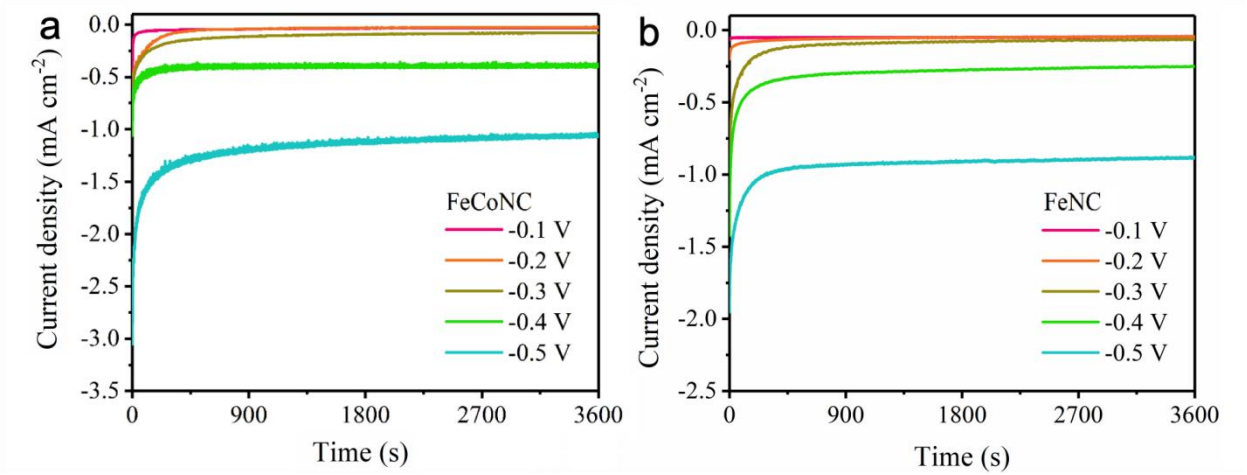

Figure 5.6 Chronoamperometry results of (a) FeCoNC and (b) FNCntested in the H-cell with 0.1 M HCl at different applied potentials.

The mean value of ammonia yield rate and the corresponding Faradaic efficiency of FeCoNC and FeNC are shown in Figure 5.7 a and b. Clearly, compared with FeNC, the FeCoNC catalyst exhibits better catalytic performance at all applied potentials. At -0.2 V vs. RHE, the maximized ammonia yield rate for FeCoNC is determined to be 70.11 μg h^{-1} mg^{-1}, with a Faradaic efficiency of 32.16%, much larger than those of FeNC (37.43 μg h^{-1} mg^{-1} and 17.19%). With the applied potential moves below -0.2 V vs. RHE, both NH_3 yield rate and Faradaic efficiency decrease, which can be attributed to the rising of the competitive HER (Figure 5.7c).

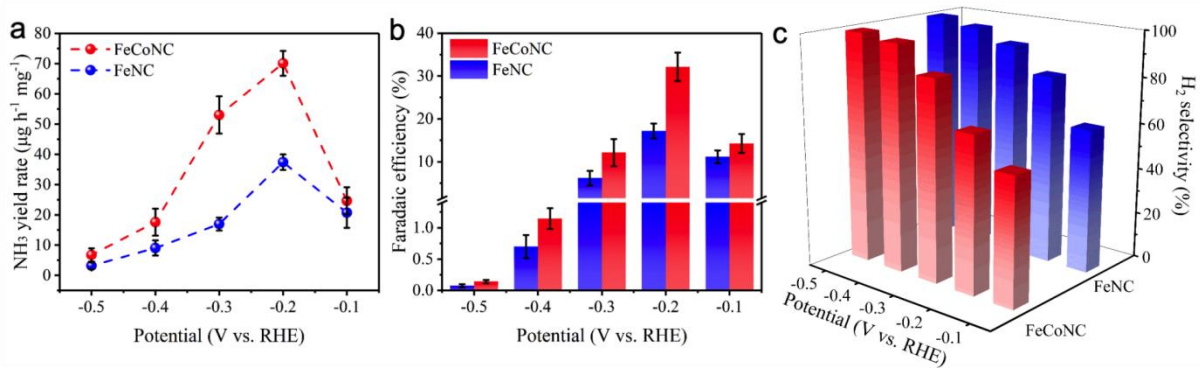

Figure 5.7 (a) NH_3 yield rates, (b) corresponding Faradaic efficiencies, and (c) H_2 selectivity of FeNC and FeCoNC measured at all given potentials.

Such outstanding performance was further examined by stability test at -0.2 V vs. RHE, in which either the ammonia yield rate or the Faradaic efficiency exhibits no marked deteriorations under 10 continuing cycles of NRR electrolysis (Figure 5.8 a), confirming the robustness of FeCoNC. In addition, upon comparing with the latest works, the superior NRR performance of FeCoNC ranks at the top of the state-of-the-arts (Figure 5.8 b and Table 5.1).

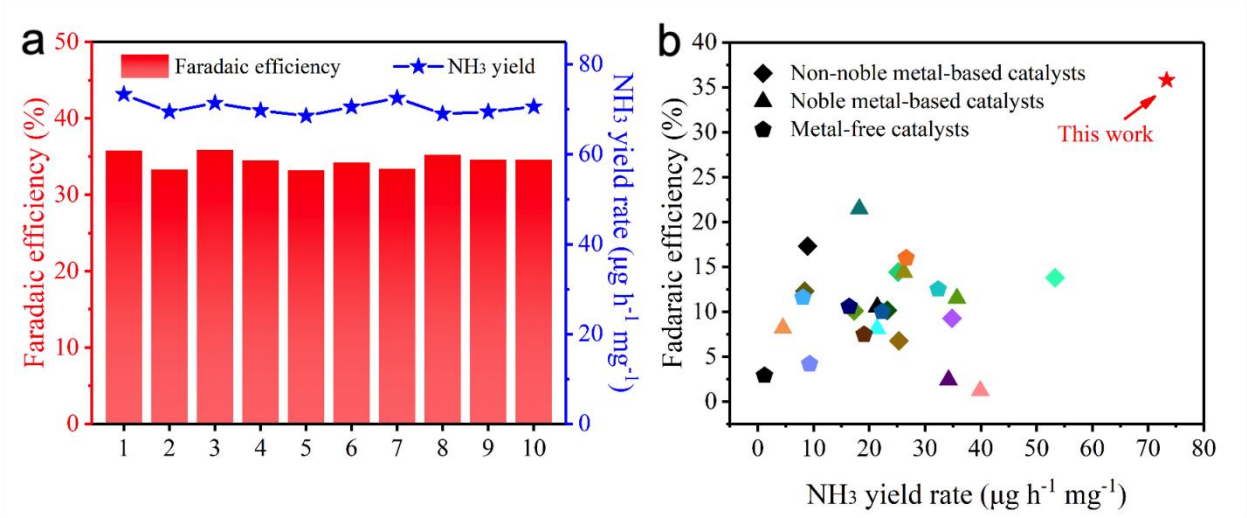

Figure 5.8 (a) The NH_3 production performance in the durability test of FeCoNC. (b) NH_3 yield rate and Faradaic efficiency of FeCoNC compared with other state-of-the-arts; detailed data are provided in Table 5.1.

Table 5.1 Comparison of the electrocatalytic NRR performance at ambient conditions.

Catalyst	Electrolytre	Faradaic efficiency (%)	NH_3 yield rate ($\mu g\ h^{-1}\ mg_{cat}^{-1}$)	Ref.
Non-noble metal-based catalysts				
FeCoNC	0.1 M HCl	35.8	73.34	This work
$Bi_4V_2O_{11}/CeO_2$	0.1 M HCl	10.16	23.21	[162]
Cr_2O_3 hollow microsphere	0.1 M Na_2SO_4	6.78	25.3	[163]
Cu/CN_x	0.1 M KOH	13.80	53.30	[200]
np-Mo_4P_3	0.1 M PBS	10.1	17.3	[164]
Zr^{4+}-doped anatase TiO_2	0.1 M KOH	17.30	8.90	[165]
Mo/FeS_2	0.1 M KOH	14.41	25.15	[169]
Fe-N/C-carbon nanotube	0.1 M KOH	9.28	34.83	[155]
$Ni_{0.75}Fe_{0.25}Se_2$	0.1 M Li_2SO_4	12.3	8.4	[166]
Noble metal-based catalysts				

Pd/C	0.1M PBS	8.2	4.5	[167]
Pd_3Pb nanowire networks	0.1 M Na_2SO_4	21.46	18.20	[201]
Au cluster/TiO_2	0.1 M HCl	8.11	21.40	[168]
Pd_3Cu_1	1 M KOH	1.2	39.9	[202]
$IrTe_4$	0.1 M KOH	14.4	26.2	[169]
Au-Fe_3O_4 Nanoparticles	0.1 M KOH	10.54	21.42	[170]
PdCu	0.5 M LiCl	11.50	35.70	[203]
PdRu nanorod	0.1 M HCl	2.40	34.20	[171]
	Metal-free catalysts			
PEBCD	0.5 M Li_2SO_4	2.9	1.2	[172]
S-doped carbon nanosphere	0.1 M Na_2SO_4	7.47	19.07	[204]
Defect-rich fluorographene nanosheets	0.1 M Na_2SO_4	4.2	9.3	[173]
CN_xB_y	0.1 M HCl	10.58	16.40	[152]
NPC-500	0.005 M H_2SO_4	10.0	22.3	[147]
Metal-free polymeric carbon nitride	0.1 M HCl	11.59	8.09	[146]
B_4C	0.1 M HCl	16.0	26.6	[144]
Oxidized carbon nanotubes	0.1 M $LiClO_4$	12.50	32.33	[67]

Several control experiments were performed to verify the reliability of the electrochemical data. When electrolyzing the bare carbon paper (CP) in N_2-saturated 0.1 M HCl at -0.2 V vs. RHE, the FeCoNC-coated electrode in Ar-saturated 0.1 M HCl at -0.2 V vs. RHE, or the FeCoNC-coated electrode in N_2-saturated 0.1 M HCl under open circuit potential, no ammonia was detected by neither colorimetric method nor the ^1H nuclear magnetic resonance (NMR) method (Figure 5.9 a and Figure S5.12). Subsequently, ^{15}N isotope labeling studies were performed to investigate the N source of the produced ammonia. When employing $^{15}N_2$ as the feeding gas, no ammonia can be detected under open circuit potential, while an ammonia yield rate of 70.09 μg h^{-1} mg^{-1} and a Faradaic efficiency of 33.26% were obtained at -0.2 V vs. RHE by indophenol blue method (Figure 5.9 b). Furthermore, in the ^1H NMR spectra, only a doublet signal for $^{15}NH_4^+$ is found in the electrolyte, which is consistent with that recorded with standard solutions of $(^{15}NH_4)_2SO_4$ (Figure 5.9 c). Upon quantitative analysis, both ammonia yield rate and the Faradaic efficiency are in consistent with those achieved in the ^{14}NRR experiments either by colorimetric method or the ^1H NMR method (Figure 5.9 d), convincingly proving that the produced NH_3 entirely comes from the NRR process.

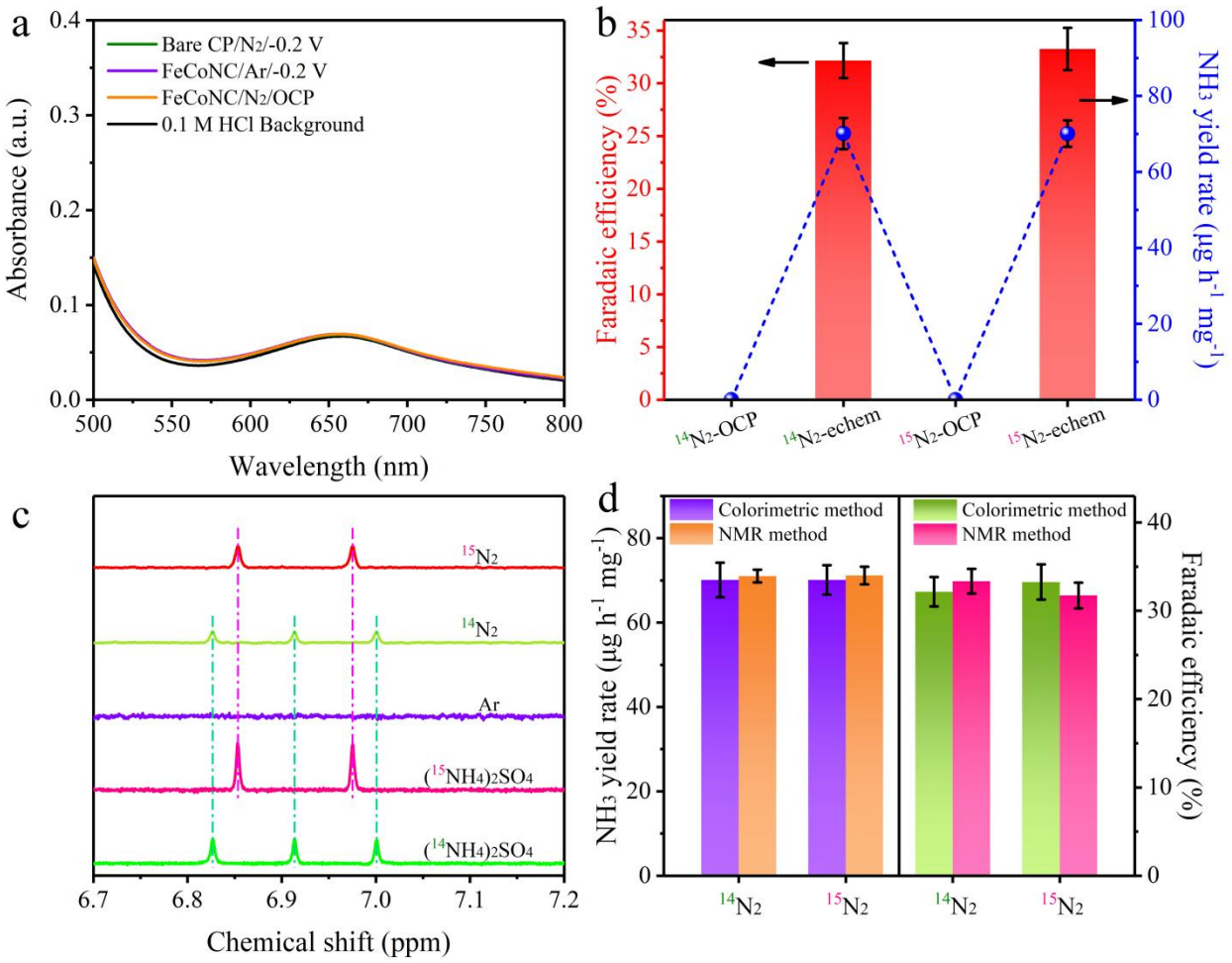

Figure 5.9 (a) The UV-vis absorption spectra of the electrolytes under different conditions. (b) Comparison of the NH_3 yield rate and Faradaic efficiency using different feeding gases for NRR at -0.2 V vs. RHE and open-circuit potential. (c) ^1H NMR spectra of the NRR products using different feed gases. (d) Comparison of the NH_3 yield rate and Faradaic efficiency using different feeding gases for NRR at -0.2 V vs. RHE either by colorimetric or NMR method.

5.3 Conclusion

In conclusion, asymmetrical heterobimetallic active centers containing FeCo dimers has been proposed to tackle the challenge of restrictions from scaling relations in NRR for ammonia synthesis under ambient conditions. In contrast to single metal site, which can only trap one lone-pair electron of adsorbed N_2 molecule and exhibit limited electronic interaction, the bimetal sites are capable of accepting two lone-pair electrons of adsorbed N_2 molecule and thus achieve stronger electron accumulation and depletion to maximize the activation of N_2. The

optimization of the binding strength of certain intermediates thus becomes feasible, and the energy barrier of the overall nitrogen reduction process is significantly reduced from 0.79 eV on FeNC to 0.43 eV on FeCoNC. Experimentally, the proposed FeCoNC exhibited much enhanced NRR performance as compared with FeNC, with an ammonia yield rate of 70.11 μg h^{-1} mg^{-1} and a Faradaic efficiency of 32.16 % at -0.2 V vs. RHE. This work presents a feasible method for breaking scaling relations between the adsorption energies of intermediates and achieving breakthrough in multi-intermediate electrocatalytic reactions.

Acknowledgements

This work was supported by the National Natural Science Foundation of China (Nos. U21A20332, 52103226, 52202275, 52203314, and 12204253), the Distinguished Young Scholars Fund of Jiangsu Province (No. BK20220061), Suzhou Foreign Academician Workstation (project number: SWY2022001), and the Fellowship of China Postdoctoral Science Foundation (No. 2021M702382).

5.4 Supporting information

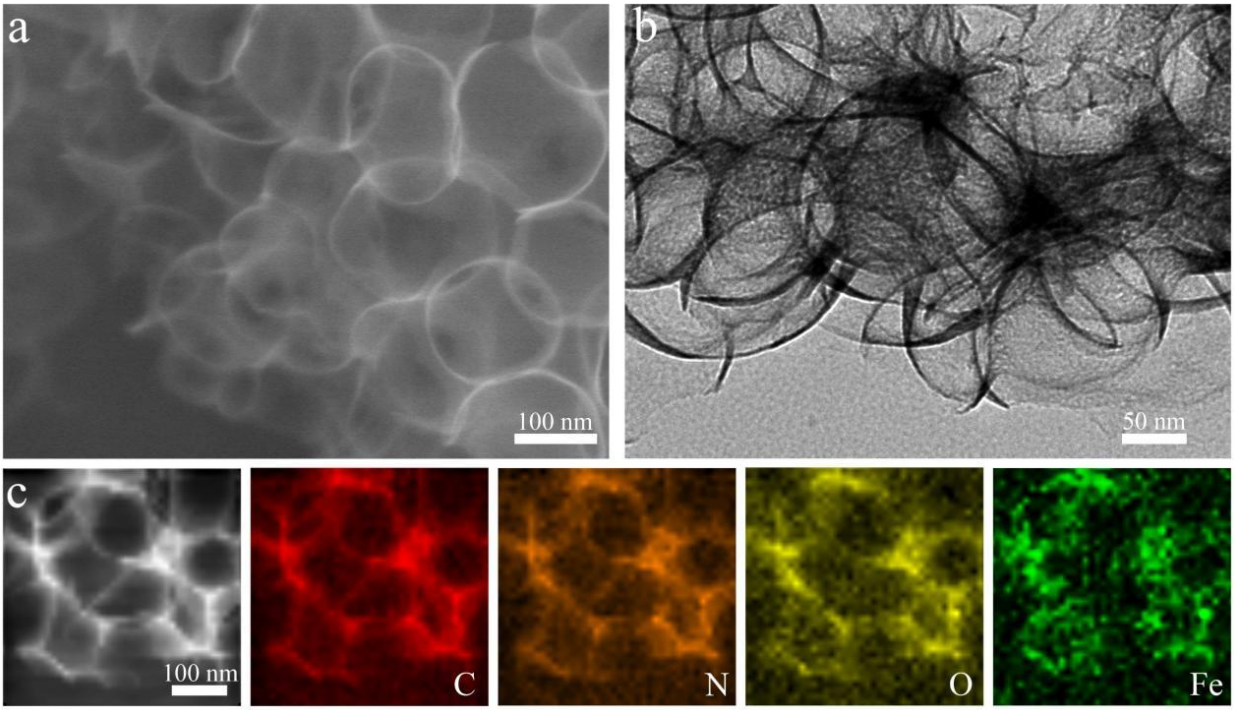

Figure S5.1 (a) Scanning electron microscopy image, (b) transmission electron microscopy image, and (c) element mappings of FeNC.

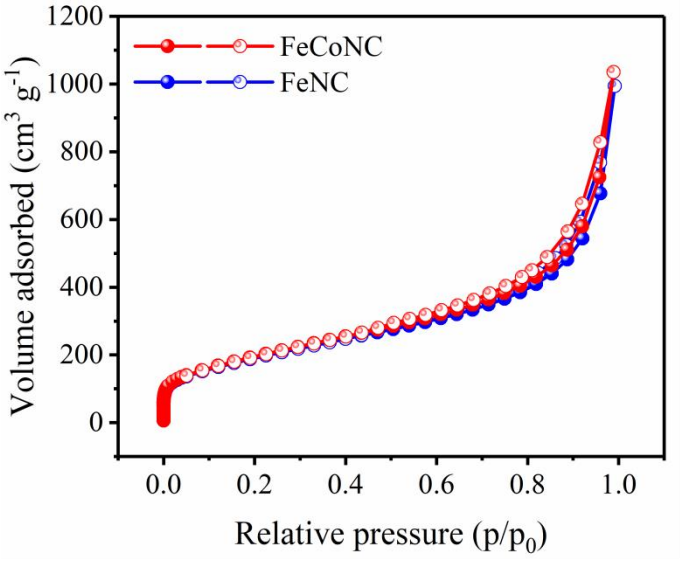

Figure S5.2 N_2 sorption isotherms of FeCoNC and FeNC.

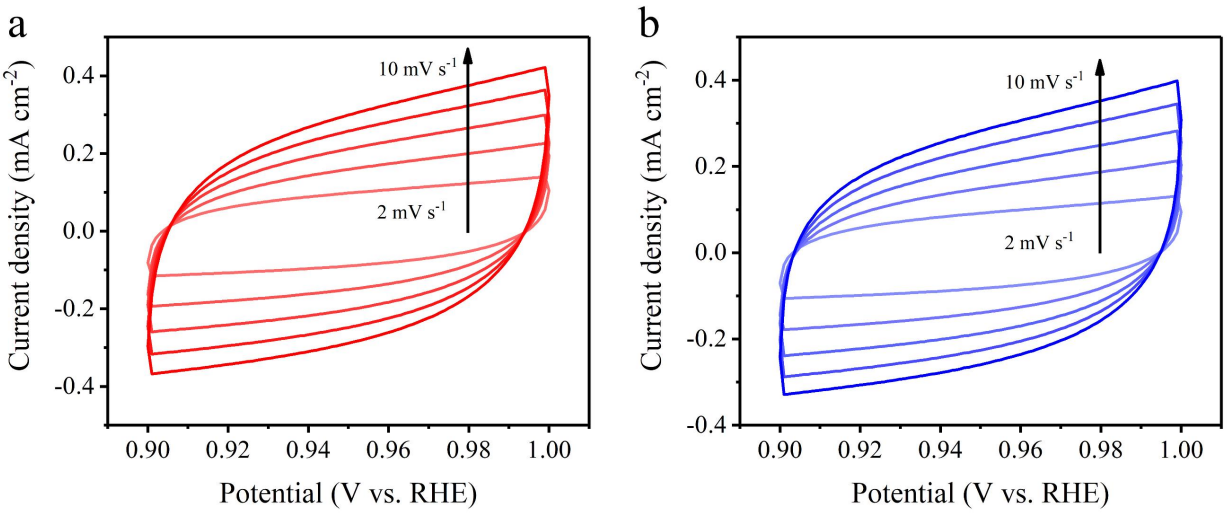

Figure S5.3 Cyclic voltammograms of (a) FeCoNC and (b) FeNC taken at different scan rates in a potential window where only double-layer charging and discharging occurs.

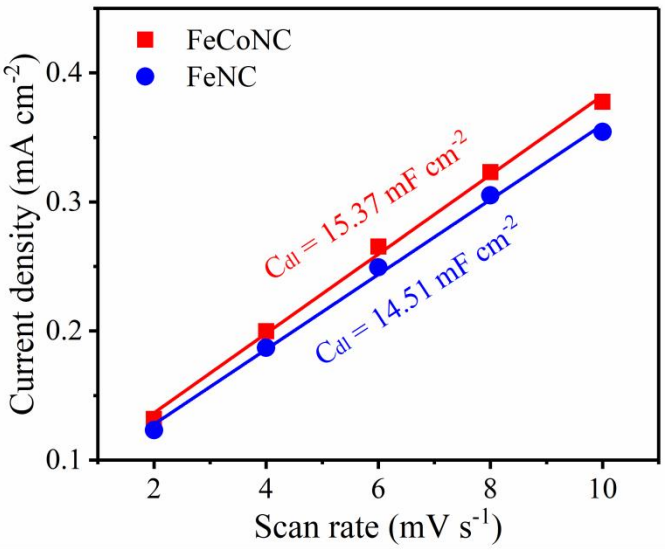

Figure S5.4 Double-layer charging current plotted against the CV scan rate for FeCoNC and FeNC.

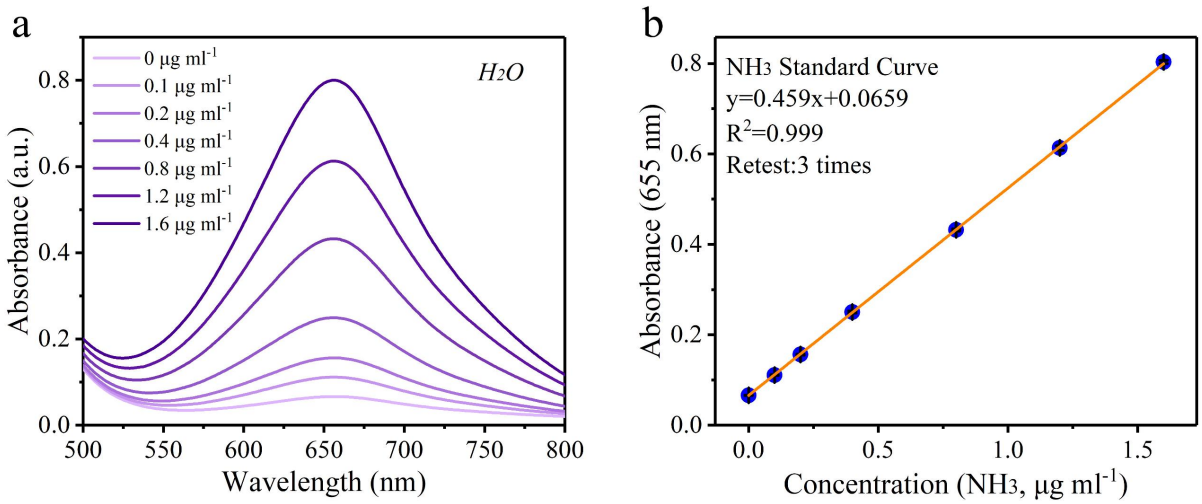

Figure S5.5 (a) The UV-vis absorption spectra and (b) corresponding calibration curves for the colorimetric determination of NH_3 in ultrapure water using the indophenol blue method. The error bars correspond to the standard deviations of three separately prepared samples measured under identical conditions.

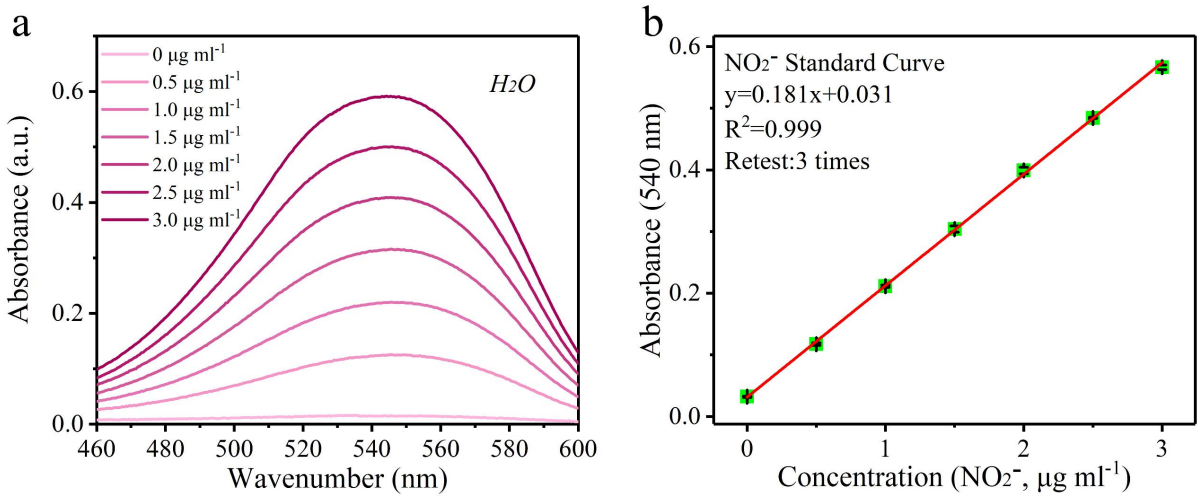

Figure S5.6 (a) The UV-vis absorption spectra and (b) corresponding calibration curves for the colorimetric determination of NO_2^- in ultrapure water using the N-(-1-naphthyl)-ethylenediamine dihydrochloride spectrophotometric method. The error bars correspond to the standard deviations of three separately prepared samples measured under identical conditions.

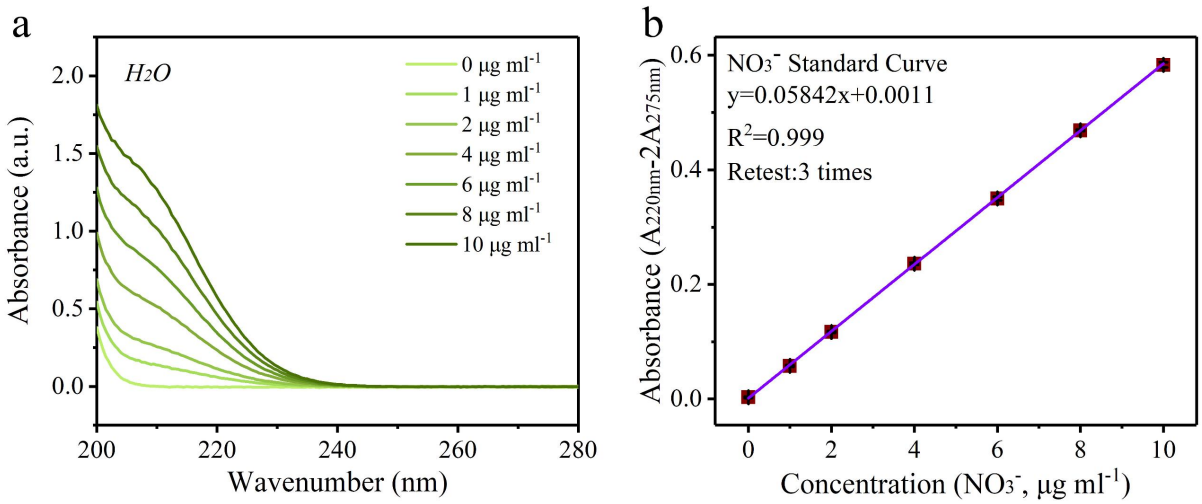

Figure S5.7 (a) The UV-vis absorption spectra and (b) corresponding calibration curves for the colorimetric determination of NO_3^- in ultrapure water using the sulfamic acid spectrophotometric method in water. The error bars correspond to the standard deviations of three separately prepared samples measured under identical conditions.

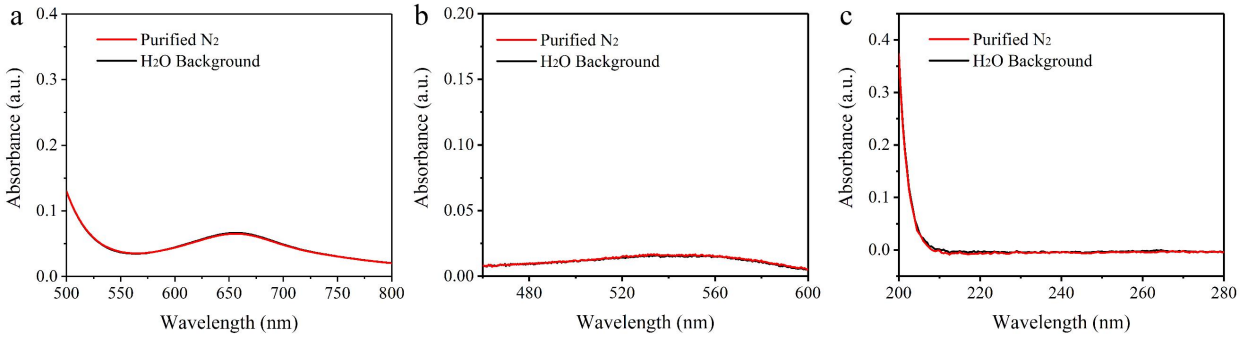

Figure S5.8 The UV-vis absorption spectra of aqueous background and the purified N_2 treated water using (a) the indophenol blue method, (b) the Griess spectrophotometric method, and (c) the sulfamic acid spectrophotometric method.

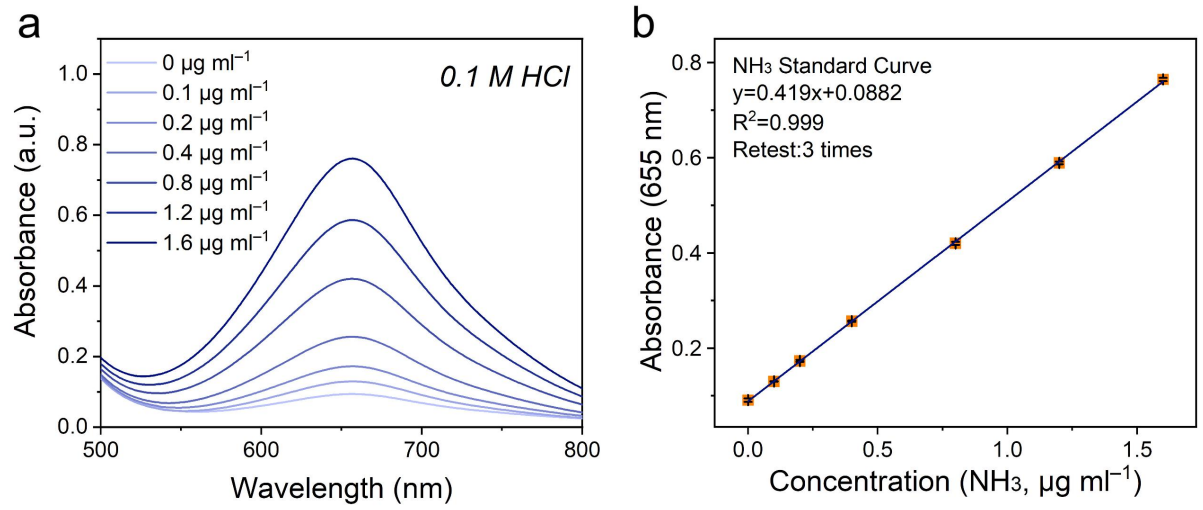

Figure S5.9 (a) The UV-vis absorption spectra and (b) corresponding calibration curves for the colorimetric determination of NH_3 in 0.1 M HCl using the indophenol blue method. The error bars correspond to the standard deviations of three separately prepared samples measured under identical conditions.

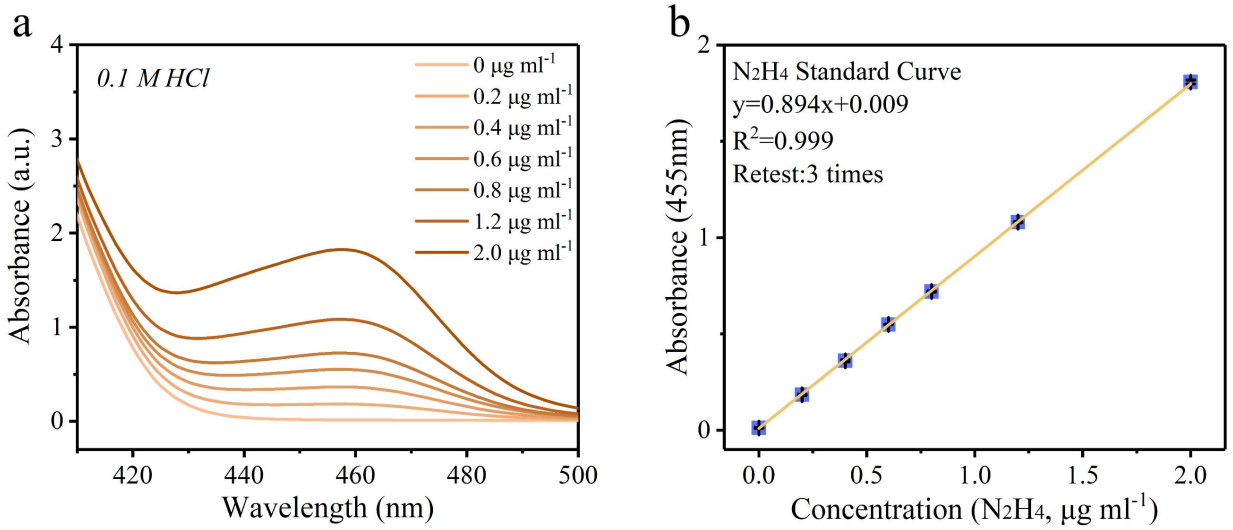

Figure S5.10 (a) The UV-vis absorption spectra and (b) the corresponding calibration curves for colorimetric N_2H_4 determination in 0.1 M HCl using the Watt and Chrisp method. The error bars correspond to the standard deviations of three separately prepared samples measured under identical conditions.

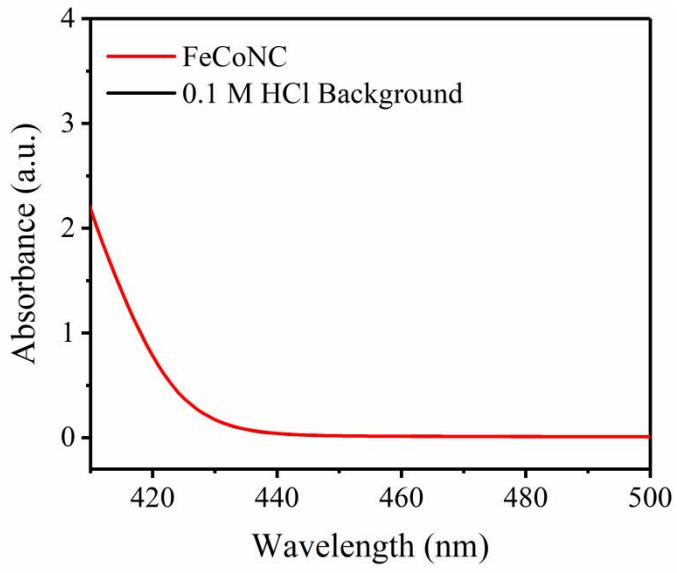

Figure S5.11 The UV-vis absorption spectra of the electrolyte using the Watt and Chrisp method.

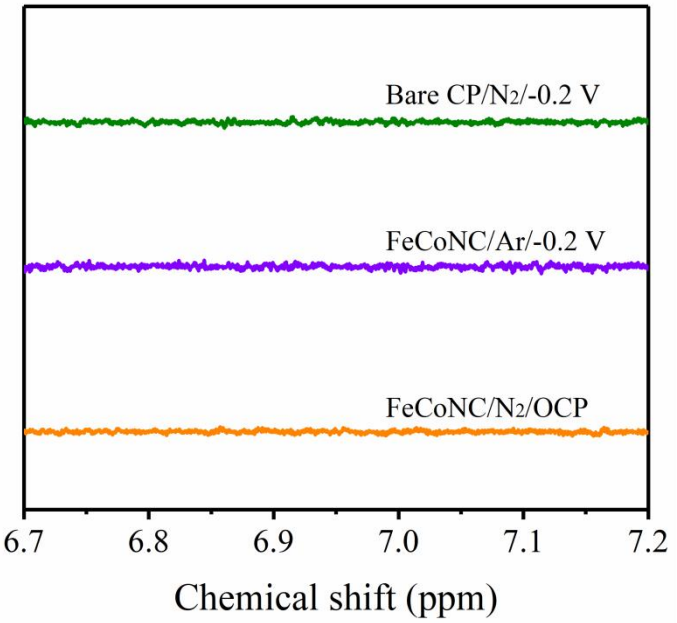

Figure S5.12 ^{1}H NMR spectra of the electrolytes measured under different conditions.

6 CONCLUSION

6.1 Conclusion

In this thesis, we focused on the synthesis of different element-coordinated carbon nitride catalytic materials, starting from the basic nitrogen-doped carbon (NC), to oxygen-enriched nitrogen-doped carbon (OENC), single Fe atoms anchored on nitrogen-doped carbon (FNC), asymmetrical Fe-Co dimers anchored on nitrogen-doped carbon (FeCoNC) and tungsten cluster and single Fe atoms anchored on nitrogen-doped carbon (WFeNC). We tested the performance differences of different catalysts and studied why they can show such excellent NH_3 yield rate and Faradaic efficiency through insitu xrd, theoretical calculations, molecular simulations, BET and other technologies.

Part I: The electrocatalytic nitrogen reduction reaction (NRR) holds great potential for green ammonia synthesis and has aroused interest of the scientific community. However, the restricted nitrogen supply at the reaction interface has always been the major unresolved issue, leaving the actual performance much to be desired, even for the highly active electrocatalyst with much reduced reaction barrier. Herein, a nitrogen confining strategy achieved by plasma etching is proposed to address this challenge, providing abundant nitrogen supply to boost ammonia synthesis under ambient conditions. There are three novel features reported in this work:

1. Upon plasma etching, a large number of voids can be in situ constructed in the basal plane of the catalyst to serve as reservoirs for nitrogen nanobubbles.
2. The nanobubbles can be effectively attracted by the defect-induced surface heterogeneity since it could generate van der Waals interactions between the electrocatalyst and the nitrogen and captured by the voids.
3. As expected, the proof-of-concept plasma etched catalyst delivers a superior ammonia yield rate of 35.24 μg h^{-1} mg^{-1} and an outstanding Faradaic efficiency of 53.99 % at -0.3 V versus reversible hydrogen electrode.

Part II: Electrocatalytic nitrogen reduction reaction (NRR) as an alternative approach to the energy-intensive Haber-Bosch process for artificial ammonia synthesis has attracted extensive attention. Previous reports have suggested that metal-free electrocatalyst, such as nitrogen-doped carbon featuring modified electronic structure and the charge polarization, is able to

eliminate the nitrogen chemisorption barrier and achieve ammonia synthesis with a certain performance. However, the NRR process is more than just adsorption, but also subsequent nitrogen cleavage and hydrogenation, which still pose great challenge. Herein, we tackle this challenge by doping oxygen into nitrogen-doped carbon. There are three novel features reported in this work:

1. Through doping oxygen into nitrogen-doped carbon as secondary heteroatom, synergistic electronic promoting effect is triggered to boost ambient ammonia synthesis.
2. The electronic structure and the polarity of adjacent carbon atoms are further optimized, significantly lowing the energy barrier of the overall nitrogen reduction process.
3. As expected, the proof-of-concept oxygen-enriched nitrogen-doped carbon catalyst delivers a much-enhanced performance with respect to the counterpart, with an ammonia yield rate of 67.3 μg h^{-1} mg^{-1} and a corresponding Faradaic efficiency of 36.2% at -0.2 V versus reversible hydrogen electrode.

Part III: The electrochemical nitrogen reduction reaction (NRR) by utilization of renewable electricity is an attractive method for sustainable ammonia production. However, due to its intrinsic essence as multi-intermediate reaction, the inherent scaling relations between the binding strength of intermediates place restrictions on the overall performance. Herein, asymmetrical heterobimetallic FeCo sites is proposed to break scaling relations in NRR and boost ambient ammonia synthesis. There are three novel features reported in this work:

1. The heteronuclear FeCo dimer sites featuring the polarized surface with multielectron sites enable weakening of N≡N bond and maximized activation of N_2.
2. The optimization of the adsorption energies of certain intermediates thus becomes feasible, contributing to significantly reduced energy barrier of the overall nitrogen reduction process.
3. As expected, the proof-of-concept catalyst delivers a superior ammonia yield rate of 70.11 μg h^{-1} mg^{-1} with a corresponding Faradaic efficiency of 32.16% at -0.2 V versus reversible hydrogen electrode.

We have proposed some applicable approaches shown in the above work to improve NRR performance. The development of doping oxygen into nitrogen-doped carbon as secondary heteroatom would trigger synergistic electronic promoting effect to boost ambient ammonia synthesis, while asymmetrical heterobimetallic FeCo sites would break scaling relations in NRR and boost ambient ammonia synthesis. In addition, a nitrogen confining strategy achieved by plasma etching has been proposed to address the challenge of limited reactant supply for

nitrogen reduction reaction under ambient conditions. This work presents a feasible method for addressing the restricted reaction supply of gas-involved electrochemical reactions. We hope our work in this thesis could provide the platform/useful information to develop efficient novel catalysts for NRR and contribute to the ammonia synthesis with rational NRR catalysts design to achieve high-efficiency and public-acceptable aesthetics. Inspired by the achieved results in this thesis, in the future, we will continue to deeply investigate the strategies to improve the efficiency of NRR.

6.2 Perspectives

We have tried different strategies to enhance the activity and production rate of electrochemical reduction of N_2. In spite of this significant progress, the selectivity and efficiency for the NRR still need to be improved for promoting practical applications, and the following aspects need to be considered:

(i) Building rigorous protocols for precise NH_3 determination

Currently, the amount of NH_3 produced by the electrochemical NRR process is relatively low and remains at the microgram level. Furthermore, possible NH_3 contamination is commonly present in the atmosphere, ion exchange membranes, and even the electrocatalyst itself. Accordingly, precise determination of the produced NH_3 is quite challenging. Rigorous protocols for precise and reliable NH_3 determination have been constructed, where a series of controlled experiments should be carried out under the following conditions such as under an Ar gas atmosphere, at open-circuit potential, in the absence of electrocatalysts, and under a $^{15}N_2$ gas atmosphere, to exclude possible ammonia contamination. Only with these reliable data can we evaluate and design high-efficiency electrocatalysts well, and quickly facilitate the development of the electrocatalytic NRR in the future.

(ii) Regulating the gas–liquid–solid three-phase interface

Electrocatalytic N_2 reduction involves the three gas (N_2), liquid (electrolyte), and solid (catalyst) phases. A series of processes including the diffusion and adsorption of N_2 molecules, the delivery of protons and electrons, and the desorption of N_xH_y intermediates and NH_3 molecules take place simultaneously at the three-phase interface. Previous studies revealed that the local concentration of N_2 molecules and protons near the catalyst surface could remarkably affect the adsorption process of N_2 and protons, respectively. As such, more efforts should also be devoted to interface engineering covering the electrolyte and electrocatalyst.

(iii) Optimizing electrocatalysts to enhance the activation ability towards N_2

Great progress for boosting the activation ability of electrocatalysts towards N_2 has been made up to now, with the focus on defects, heterostructures, strain, crystallinity engineering, *etc.* However, the activation ability of electrocatalysts towards N_2 is still insufficient, which also serves as an elementary roadblock for high-efficiency ammonia synthesis under ambient conditions due to the high activation barrier of N_2 molecules.

7 BIBLIOGRAPHIE

[1] Donald E. Canfield ANG, Paul G. Falkowski (2010) The Evolution and Future of Earth's Nitrogen Cycle. *Science* 330:192-196.

[2] Huang Z, Rafiq M, Woldu AR, Tong Q-X, Astruc D, Hu L (2023) Recent progress in electrocatalytic nitrogen reduction to ammonia (NRR). *Coordination Chemistry Reviews* 478:214981.

[3] Liu H (2014) Ammonia synthesis catalyst 100 years: Practice, enlightenment and challenge. *Chinese Journal of Catalysis* 35(10):1619-1640.

[4] Rouwenhorst KHR, Krzywda PM, Benes NE, Mul G, Lefferts L (2020) Ammonia, 4. Green Ammonia Production. *Ullmann's Encyclopedia of Industrial Chemistry,* 10.1002/14356007.w02_w02. p 1-20.

[5] Smith C, Hill AK, Torrente-Murciano L (2020) Current and future role of Haber–Bosch ammonia in a carbon-free energy landscape. *Energy & Environmental Science* 13(2):331-344.

[6] Carvalho EP, Borges C, Andrade D, Yuan JY, Ravagnani MASS (2014) Modeling and optimization of an ammonia reactor using a penalty-like method. *Applied Mathematics and Computation* 237:330-339.

[7] Chen G-F, Yuan Y, Jiang H, Ren S-Y, Ding L-X, Ma L, Wu T, Lu J, Wang H (2020) Electrochemical reduction of nitrate to ammonia via direct eight-electron transfer using a copper–molecular solid catalyst. *Nature Energy* 5(8):605-613.

[8] Tang C, Qiao SZ (2019) How to explore ambient electrocatalytic nitrogen reduction reliably and insightfully. *Chem Soc Rev* 48(12):3166-3180.

[9] Ishaq H, Crawford C (2024) Review and evaluation of sustainable ammonia production, storage and utilization. *Energy Conversion and Management* 300:117869.

[10] Valera-Medina A, Mashruk S, Pugh D, Bowen P (2022) Ammonia. *Renewable fuels: sources, conversion, and utilization. Cambridge University Press, Cambridge* :245-274.

[11] Guo W, Zhang K, Liang Z, Zou R, Xu Q (2019) Electrochemical nitrogen fixation and utilization: theories, advanced catalyst materials and system design. *Chemical Society Reviews* 48(24):5658-5716.

[12] Jiao F, Xu B (2019) Electrochemical ammonia synthesis and ammonia fuel cells. *Advanced Materials* 31(31):1805173.

[13] Yang B, Ding W, Zhang H, Zhang S (2021) Recent progress in electrochemical synthesis of ammonia from nitrogen: strategies to improve the catalytic activity and selectivity. *Energy & Environmental Science* 14(2):672-687.

[14] Martín AJ, Shinagawa T, Pérez-Ramírez J (2019) Electrocatalytic reduction of nitrogen: from Haber-Bosch to ammonia artificial leaf. *Chem* 5(2):263-283.

[15] Fichter F, Suter R (1922) Zur Frage der kathodischen Reduktion des elementaren Stickstoffs. *Helvetica Chimica Acta* 5(2):246-255.

[16] Van Tamelen EE, Akermark B (1968) Electrolytic reduction of molecular nitrogen. *Journal of the American Chemical Society* 90(16):4492-4493.

[17] Tsuneto A, Kudo A, Sakata T (1994) Lithium-mediated electrochemical reduction of high pressure N_2 to NH_3. *Journal of Electroanalytical Chemistry* 367(1-2):183-188.

[18] Rod TH, Logadottir A, Nørskov JK (2000) Ammonia synthesis at low temperatures. *The Journal of Chemical Physics* 112(12):5343-5347.

[19] Köleli F, Röpke T (2006) Electrochemical hydrogenation of dinitrogen to ammonia on a polyaniline electrode. *Applied Catalysis B: Environmental* 62(3-4):306-310.

[20] Skulason E, Bligaard T, Gudmundsdóttir S, Studt F, Rossmeisl J, Abild-Pedersen F, Vegge T, Jónsson H, Nørskov JK (2012) A theoretical evaluation of possible transition metal electro-catalysts for N_2 reduction. *Physical Chemistry Chemical Physics* 14(3):1235-1245.

[21] Azofra LM, Li N, MacFarlane DR, Sun C (2016) Promising prospects for 2D d^2 – d^4 M_3C_2 transition metal carbides (MXenes) in N_2 capture and conversion into ammonia. *Energy & Environmental Science* 9(8):2545-2549.

[22] Abghoui Y, Skúlason E (2017) Onset potentials for different reaction mechanisms of nitrogen activation to ammonia on transition metal nitride electro-catalysts. *Catalysis Today* 286:69-77.

[23] Zhao J, Zhang L, Xie X-Y, Li X, Ma Y, Liu Q, Fang W-H, Shi X, Cui G, Sun X (2018) Ti $_3C_2T_x$ (T= F, OH) MXene nanosheets: conductive 2D catalysts for ambient electrohydrogenation of N_2 to NH $_3$. *Journal of Materials Chemistry A* 6(47):24031-24035.

[24] Du H-L, Chatti M, Hodgetts RY, Cherepanov PV, Nguyen CK, Matuszek K, MacFarlane DR, Simonov AN (2022) Electroreduction of nitrogen with almost 100% current-to-ammonia efficiency. *Nature* 609(7928):722-727.

[25] Ren Y, Yu C, Tan X, Huang H, Wei Q, Qiu J (2021) Strategies to suppress hydrogen evolution for highly selective electrocatalytic nitrogen reduction: challenges and perspectives. *Energy & Environmental Science* 14(3):1176-1193.

[26] Chen X, Guo Y, Du X, Zeng Y, Chu J, Gong C, Huang J, Fan C, Wang X, Xiong J (2020) Atomic structure modification for electrochemical nitrogen reduction to ammonia. *Advanced Energy Materials* 10(3):1903172.

[27] Mushtaq MA, Arif M, Yasin G, Tabish M, Kumar A, Ibraheem S, Ye W, Ajmal S, Zhao J, Li P (2023) Recent developments in heterogeneous electrocatalysts for ambient nitrogen reduction to ammonia: Activity, challenges, and future perspectives. *Renewable and Sustainable Energy Reviews* 176:113197.

[28] Moon YH, Kim NY, Kim SM, Jang YJ (2022) Recent advances in electrochemical nitrogen reduction reaction to ammonia from the catalyst to the system. *Catalysts* 12(9):1015.

[29] Chanda D, Xing R, Xu T, Liu Q, Luo Y, Liu S, Tufa RA, Dolla TH, Montini T, Sun X (2021) Electrochemical nitrogen reduction: recent progress and prospects. *Chemical Communications* 57(60):7335-7349.

[30] Zhou L, Boyd CE (2016) Comparison of Nessler, phenate, salicylate and ion selective electrode procedures for determination of total ammonia nitrogen in aquaculture. *Aquaculture* 450:187-193.

[31] Utomo WP, Wu H, Ng YH (2022) Quantification methodology of ammonia produced from electrocatalytic and photocatalytic nitrogen/nitrate reduction. *Energies* 16(1):27.

[32] Rocha FS, Gomes AJ, Lunardi CN, Kaliaguine S, Patience GS (2018) Experimental methods in chemical engineering: Ultraviolet visible spectroscopy—UV‐Vis. *The Canadian Journal of Chemical Engineering* 96(12):2512-2517.

[33] Cong M, Chen X, Xia K, Ding X, Zhang L, Jin Y, Gao Y, Zhang L (2021) Selective nitrogen reduction to ammonia on iron porphyrin-based single-site metal‐organic frameworks. *Journal of Materials Chemistry A* 9(8):4673-4678.

[34] Zhang Z, Yao K, Cong L, Yu Z, Qu L, Huang W (2020) Facile synthesis of a Ru-dispersed N-doped carbon framework catalyst for electrochemical nitrogen reduction. *Catalysis Science & Technology* 10(5):1336-1342.

[35] Zhao Y, Shi R, Bian X, Zhou C, Zhao Y, Zhang S, Wu F, Waterhouse GI, Wu LZ, Tung CH (2019) Ammonia detection methods in photocatalytic and electrocatalytic experiments: how to improve the reliability of NH3 production rates? *Advanced Science* 6(8):1802109.

[36] Khalil IE, Xue C, Liu W, Li X, Shen Y, Li S, Zhang W, Huo F (2021) The role of defects in metal‐organic frameworks for nitrogen reduction reaction: when defects switch to features. *Advanced Functional Materials* 31(17):2010052.

[37] Cui X, Tang C, Zhang Q (2018) A review of electrocatalytic reduction of dinitrogen to ammonia under ambient conditions. *Advanced Energy Materials* 8(22):1800369.

[38] Pavia DL, Lampman GM, Kriz GS, Vyvyan JR (2015) Introduction to spectroscopy.

[39] Zia K, Siddiqui T, Ali S, Farooq I, Zafar MS, Khurshid Z (2019) Nuclear magnetic resonance spectroscopy for medical and dental applications: a comprehensive review. *European journal of dentistry* 13(01):124-128.

[40] Jang YJ, Lindberg AE, Lumley MA, Choi K-S (2020) Photoelectrochemical nitrogen reduction to ammonia on cupric and cuprous oxide photocathodes. *ACS Energy Letters* 5(6):1834-1839.

[41] Rigamonti MG, Gatti FG, Patience GS (2019) Experimental methods in chemical engineering: Nuclear magnetic resonance. *The Canadian Journal of Chemical Engineering* 97(3):628-635.

[42] Choe S, Kim SM, Lee Y, Seok J, Jung J, Lee JS, Jang YJ (2021) Rational design of photocatalysts for ammonia production from water and nitrogen gas. *Nano Convergence* 8:1-12.

[43] Zhao Y, Wu F, Miao Y, Zhou C, Xu N, Shi R, Wu LZ, Tang J, Zhang T (2021) Revealing ammonia quantification minefield in photo/electrocatalysis. *Angewandte Chemie International Edition* 60(40):21728-21731.

[44] Ye W, Yang Y, Arif M, Yang S, Fang X, Mushtaq MA, Chen X, Yan D (2020) Fe, Mo‐N/C hollow porous nitrogen-doped carbon nanorods as an effective electrocatalyst for N_2 reduction reaction. *ACS Sustainable Chemistry & Engineering* 8(42):15946-15952.

[45] Das A, Nair AS, Pathak B (2020) Elucidating mechanistic origin of the catalytic activity of the Fe (111) surface and nanoclusters toward the electrochemical nitrogen reduction reaction. *The Journal of Physical Chemistry C* 124(37):20193-20202.

[46] Kong Y, Kong H, Lv C, Chen G (2022) Engineering reductive iron on a layered double hydroxide electrocatalyst for facilitating nitrogen reduction reaction. *Advanced Materials Interfaces* 9(10):2102242.

[47] Wei Y, Yu Y, Chen J, Wei M, Huang Y, Zhou X, Liu W (2023) Fabrication of High Surface Area Fe/Fe_3O_4 with Enhanced Performance for Electrocatalytic Nitrogen Reduction Reaction. *Chemistry – A European Journal* 29(71):e202302734.

[48] Jia L, Xue H, Xian F, Sugahara Y, Sakai N, Nan J, Yamauchi Y, Sasaki T, Ma R (2023) Porous and Partially Dehydrogenated Fe^{2+} – Containing Iron Oxyhydroxide Nanosheets for Efficient Electrochemical Nitrogen Reduction Reaction (ENRR). *Small* 19(42):2303221.

[49] Liu Y, Zhao Z, Wei W, Jin X, Wang G, Li K, Lin Y (2021) Single-atom Fe-N_4 on a carbon substrate for nitrogen reduction reaction. *ACS Applied Nano Materials* 4(12):13001-13009.

[50] Liu X, Jiao Y, Zheng Y, Jaroniec M, Qiao S-Z (2019) Building up a picture of the electrocatalytic nitrogen reduction activity of transition metal single-atom catalysts. *Journal of the American Chemical Society* 141(24):9664-9672.

[51] Chen Z, Zhao J, Cabrera CR, Chen Z (2019) Computational screening of efficient single – atom catalysts based on graphitic carbon nitride (g – C_3N_4) for nitrogen electroreduction. *Small Methods* 3(6):1800368.

[52] He T, Matta SK, Du A (2019) Single tungsten atom supported on N-doped graphyne as a high-performance electrocatalyst for nitrogen fixation under ambient conditions. *Physical Chemistry Chemical Physics* 21(3):1546-1551.

[53] Gu Y, Xi B, Tian W, Zhang H, Fu Q, Xiong S (2021) Boosting selective nitrogen reduction via geometric coordination engineering on single – tungsten – atom catalysts. *Advanced Materials* 33(25):2100429.

[54] Lu Z, Wang H, Tao Y, Zhu S, Hao W, Liu X, Min Y, Fan J (2023) WO x nanoparticles coupled with nitrogen-doped porous carbon toward electrocatalytic N_2 reduction. *Nanoscale* 15(36):14847-14857.

[55] Liu Y, Xu Q, Fan X, Quan X, Su Y, Chen S, Yu H, Cai Z (2019) Electrochemical reduction of N_2 to ammonia on Co single atom embedded N-doped porous carbon under ambient conditions. *Journal of Materials Chemistry A* 7(46):26358-26363.

[56] Gao Y, Han Z, Hong S, Wu T, Li X, Qiu J, Sun Z (2019) ZIF-67-derived cobalt/nitrogen-doped carbon composites for efficient electrocatalytic N_2 reduction. *ACS Applied Energy Materials* 2(8):6071-6077.

[57] Zhang S, Jiang Q, Shi T, Sun Q, Ye Y, Lin Y, Zheng LR, Wang G, Liang C, Zhang H (2020) Laser irradiation in liquid to release cobalt single-atom sites for efficient electrocatalytic N_2 reduction. *ACS Applied Energy Materials* 3(7):6079-6086.

[58] Zhao Y, Yan L, Zhao X (2022) Development of Carbon – Based Electrocatalysts for Ambient Nitrogen Reduction Reaction: Challenges and Perspectives. *ChemElectroChem* 9(3):e202101126.

[59] Liu S, Qian T, Wang M, Ji H, Shen X, Wang C, Yan C (2021) Proton-filtering covalent organic frameworks with superior nitrogen penetration flux promote ambient ammonia synthesis. *Nature Catalysis* 4(4):322-331.

[60] Shahid M, Javed HMA, Ahmad MI, Qureshi AA, Khan MI, Alnuwaiser MA, Ahmed A, Khan MA, Tag-ElDin ESM, Shahid A (2022) A brief assessment on recent developments in efficient electrocatalytic Nitrogen reduction with 2D non-metallic nanomaterials. *Nanomaterials* 12(19):3413.

[61] Zhang W, Mao K, Low J, Liu H, Bo Y, Ma J, Liu Q, Jiang Y, Yang J, Pan Y (2021) Working-in-tandem mechanism of multi-dopants in enhancing electrocatalytic nitrogen reduction reaction performance of carbon-based materials. *Nano Research* :1-6.

[62] Mukherjee S, Cullen DA, Karakalos S, Liu K, Zhang H, Zhao S, Xu H, More KL, Wang G, Wu G (2018) Metal-organic framework-derived nitrogen-doped highly disordered carbon for electrochemical ammonia synthesis using N_2 and H_2O in alkaline electrolytes. *Nano Energy* 48:217-226.

[63] Liu Y, Su Y, Quan X, Fan X, Chen S, Yu H, Zhao H, Zhang Y, Zhao J (2018) Facile ammonia synthesis from electrocatalytic N_2 reduction under ambient conditions on N-doped porous carbon. *ACS Catalysis* 8(2):1186-1191.

[64] Chen Y, Wu B, Sun B, Wang N, Hu W, Komarneni S (2019) N-doped porous carbon self-generated on nickel oxide nanosheets for electrocatalytic N_2 fixation with a faradaic efficiency beyond 30%. *ACS Sustainable Chemistry & Engineering* 7(23):18874-18883.

[65] Wan Y, Xu J, Lv R (2019) Heterogeneous electrocatalysts design for nitrogen reduction reaction under ambient conditions. *Materials Today* 27:69-90.

[66] Wang T, Xia L, Yang J-J, Wang H, Fang W-H, Chen H, Tang D, Asiri AM, Luo Y, Cui G (2019) Electrocatalytic N_2-to-NH_3 conversion using oxygen-doped graphene: experimental and theoretical studies. *Chemical Communications* 55(52):7502-7505.

[67] Zhao J, Wang B, Zhou Q, Wang H, Li X, Chen H, Wei Q, Wu D, Luo Y, You J (2019) Efficient electrohydrogenation of N_2 to NH_3 by oxidized carbon nanotubes under ambient conditions. *Chemical Communications* 55(34):4997-5000.

[68] Wang S, Zhu J, Zhang Y, Liu Q, Chen G, Kong X (2020) Identifying the active site on graphene oxide nanosheets for ambient electrocatalytic nitrogen reduction. *Inorganic Chemistry* 59(15):11108-11112.

[69] Chen JG, Crooks RM, Seefeldt LC, Bren KL, Bullock RM, Darensbourg MY, Holland PL, Hoffman B, Janik MJ, Jones AK (2018) Beyond fossil fuel‐driven nitrogen transformations. *Science* 360(6391):eaar6611.

[70] Battino R, Rettich TR, Tominaga T (1984) The solubility of nitrogen and air in liquids. *Journal of Physical and Chemical Reference Data* 13(2):563-600.

[71] Greenlee LF, Renner JN, Foster SL (2018) The use of controls for consistent and accurate measurements of electrocatalytic ammonia synthesis from dinitrogen. (ACS Publications), p 7820-7827.

[72] Lan R, Irvine JT, Tao S (2013) Synthesis of ammonia directly from air and water at ambient temperature and pressure. *Scientific reports* 3(1):1145.

[73] Chen GF, Ren S, Zhang L, Cheng H, Luo Y, Zhu K, Ding LX, Wang H (2019) Advances in electrocatalytic N_2 reduction—strategies to tackle the selectivity challenge. *Small Methods* 3(6):1800337.

[74] Wang L, Xia M, Wang H, Huang K, Qian C, Maravelias CT, Ozin GA (2018) Greening ammonia toward the solar ammonia refinery. *Joule* 2(6):1055-1074.

[75] Shipman MA, Symes MD (2017) A re-evaluation of Sn (II) phthalocyanine as a catalyst for the electrosynthesis of ammonia. *Electrochimica Acta* 258:618-622.

[76] Du H-L, Gengenbach TR, Hodgetts R, MacFarlane DR, Simonov AN (2019) Critical assessment of the electrocatalytic activity of vanadium and niobium nitrides toward dinitrogen reduction to ammonia. *ACS Sustainable Chemistry & Engineering* 7(7):6839-6850.

[77] Cheng S, Li C, Yu Z, Sun Y, Li L, Yang J (2020) Defective S/N co-doped carbon cloth via a one-step process for effective electroreduction of nitrogen to ammonia. *RSC advances* 10(17):9814-9823.

[78] Chu K, Liu Y-p, Li Y-b, Guo Y-l, Tian Y, Zhang H (2020) Multi-functional Mo-doping in MnO_2 nanoflowers toward efficient and robust electrocatalytic nitrogen fixation. *Applied Catalysis B: Environmental* 264:118525.

[79] Wei Z, Zhang Y, Wang S, Wang C, Ma J (2018) Fe-doped phosphorene for the nitrogen reduction reaction. *Journal of Materials Chemistry A* 6(28):13790-13796.

[80] Choi C, Back S, Kim N-Y, Lim J, Kim Y-H, Jung Y (2018) Suppression of hydrogen evolution reaction in electrochemical N_2 reduction using single-atom catalysts: a computational guideline. *ACS Catalysis* 8(8):7517-7525.

[81] Varghese F, Kabasakal BV, Cotton CA, Schumacher J, Rutherford AW, Fantuzzi A, Murray JW (2019) A low-potential terminal oxidase associated with the iron-only nitrogenase from the nitrogen-fixing bacterium Azotobacter vinelandii. *Journal of Biological Chemistry* 294(24):9367-9376.

[82] Lü F, Zhao S, Guo R, He J, Peng X, Bao H, Fu J, Han L, Qi G, Luo J (2019) Nitrogen-coordinated single Fe sites for efficient electrocatalytic N_2 fixation in neutral media. *Nano Energy* 61:420-427.

[83] Lai F, Zong W, He G, Xu Y, Huang H, Weng B, Rao D, Martens JA, Hofkens J, Parkin IP (2020) N2 electroreduction to NH_3 by selenium vacancy‐rich $ReSe_2$ catalysis at an abrupt interface. *Angewandte Chemie International Edition* 59(32):13320-13327.

[84] Hu L, Xing Z, Feng X (2020) Understanding the electrocatalytic interface for ambient ammonia synthesis. *ACS Energy Letters* 5(2):430-436.

[85] Lee HK, Koh CSL, Lee YH, Liu C, Phang IY, Han X, Tsung C-K, Ling XY (2018) Favoring the unfavored: selective electrochemical nitrogen fixation using a reticular chemistry approach. *Science advances* 4(3):eaar3208.

[86] Zhang K, Lively RP, Dose ME, Brown AJ, Zhang C, Chung J, Nair S, Koros WJ, Chance RR (2013) Alcohol and water adsorption in zeolitic imidazolate frameworks. *Chemical Communications* 49(31):3245-3247.

[87] Liu Y, Huang B, Chen X, Tian Z, Zhang X, Tsiakaras P, Shen PK (2020) Electrocatalytic production of ammonia: Biomimetic electrode‐electrolyte design for efficient electrocatalytic nitrogen fixation under ambient conditions. *Applied Catalysis B: Environmental* 271:118919.

[88] Van Der Spoel D, Lindahl E, Hess B, Groenhof G, Mark AE, Berendsen HJ (2005) GROMACS: fast, flexible, and free. *Journal of Computational Chemistry* 26(16):1701-1718.

[89] Li Y, Gao D, Zhao S, Xiao Y, Guo Z, Fang Y, Lin J, Liu Z, Huang Y, Guo K (2021) Carbon doped hexagonal boron nitride nanoribbon as efficient metal-free electrochemical nitrogen reduction catalyst. *Chemical Engineering Journal* 410:128419.

[90] He Y, Liu S, Wang M, Ji H, Zhang L, Cheng Q, Qian T, Yan C (2022) Advancing the electrochemistry of gas‐involved reactions through theoretical calculations and simulations from microscopic to macroscopic. *Advanced Functional Materials* 32(48):2208474.

[91] Berendsen H-J-C, Grigera J-R, Straatsma TP (1987) The missing term in effective pair potentials. *Journal of Physical Chemistry* 91(24):6269-6271.

[92] Potoff JJ, Siepmann JI (2001) Vapor–liquid equilibria of mixtures containing alkanes, carbon dioxide, and nitrogen. *AIChE Journal* 47(7):1676-1682.

[93] Botti A, Bruni F, Ricci M, Soper A (2006) Eigen versus Zundel complexes in HCl-water mixtures. *The Journal of Chemical Physics* 125(1).

[94] Huo L, Han X, Zhang L, Liu B, Gao R, Cao B, Wang W-W, Jia C-J, Liu K, Liu J (2021) Spatial confinement and electron transfer moderating MoN bond strength for superior ammonia decomposition catalysis. *Applied Catalysis B: Environmental* 294:120254.

[95] Erisman JW, Sutton MA, Galloway J, Klimont Z, Winiwarter W (2008) How a century of ammonia synthesis changed the world. *Nature geoscience* 1(10):636-639.

[96] Galloway JN, Townsend AR, Erisman JW, Bekunda M, Cai Z, Freney JR, Martinelli LA, Seitzinger SP, Sutton MA (2008) Transformation of the nitrogen cycle: recent trends, questions, and potential solutions. *Science* 320(5878):889-892.

[97] Choi C, Gu GH, Noh J, Park HS, Jung Y (2021) Understanding potential-dependent competition between electrocatalytic dinitrogen and proton reduction reactions. *Nature Communications* 12(1):4353.

[98] Licht S, Cui B, Wang B, Li F-F, Lau J, Liu S (2014) RETRACTED: Ammonia synthesis by N_2 and steam electrolysis in molten hydroxide suspensions of nanoscale Fe_2O_3. *Science* 345(6197):637-640.

[99] Liu S, Wang M, He Y, Cheng Q, Qian T, Yan C (2023) Covalent organic frameworks towards photocatalytic applications: Design principles, achievements, and opportunities. *Coordination Chemistry Reviews* 475:214882.

[100] Lu S, Lee DH, Liu C (2019) Modeling of electrocatalytic dinitrogen reduction on microstructured electrodes. *Small Methods* 3(6):1800332.

[101] Liu D, Wang J, Bian S, Liu Q, Gao Y, Wang X, Chu PK, Yu XF (2020) Photoelectrochemical synthesis of ammonia with black phosphorus. *Advanced Functional Materials* 30(24):2002731.

[102] Qin Q, Zhao Y, Schmallegger M, Heil T, Schmidt J, Walczak R, Gescheidt–Demner G, Jiao H, Oschatz M (2019) Enhanced electrocatalytic N_2 reduction via partial anion substitution in titanium oxide–carbon composites. *Angewandte Chemie* 131(37):13235-13240.

[103] Peramaiah K, Ramalingam V, Fu HC, Alsabban MM, Ahmad R, Cavallo L, Tung V, Huang KW, He JH (2021) Optically and electrocatalytically decoupled Si photocathodes with a porous carbon nitride catalyst for nitrogen reduction with over 61.8% faradaic efficiency. *Advanced Materials* 33(18):2100812.

[104] Soloveichik G (2019) Electrochemical synthesis of ammonia as a potential alternative to the Haber–Bosch process. *Nature Catalysis* 2(5):377-380.

[105] Foster SL, Bakovic SIP, Duda RD, Maheshwari S, Milton RD, Minteer SD, Janik MJ, Renner JN, Greenlee LF (2018) Catalysts for nitrogen reduction to ammonia. *Nature Catalysis* 1(7):490-500.

[106] Fajardo Jr J, Peters JC (2017) Catalytic nitrogen-to-ammonia conversion by osmium and ruthenium complexes. *Journal of the American Chemical Society* 139(45):16105-16108.

[107] Xia J, Yang S-Z, Wang B, Wu P, Popovs I, Li H, Irle S, Dai S, Zhu H (2020) Boosting electrosynthesis of ammonia on surface-engineered MXene Ti_3C_2. *Nano Energy* 72:104681.

[108] Fu Y, Li T, Zhou G, Guo J, Ao Y, Hu Y, Shen J, Liu L, Wu X (2020) Dual-metal-driven selective pathway of nitrogen reduction in orderly atomic-hybridized Re2MnS6 ultrathin nanosheets. *Nano Letters* 20(7):4960-4967.

[109] Lin Y-X, Zhang S-N, Xue Z-H, Zhang J-J, Su H, Zhao T-J, Zhai G-Y, Li X-H, Antonietti M, Chen J-S (2019) Boosting selective nitrogen reduction to ammonia on electron-deficient copper nanoparticles. *Nature Communications* 10(1):4380.

[110] Shen X, Liu S, Xia X, Wang M, Ji H, Wang Z, Liu J, Zhang X, Yan C, Qian T (2022) Interfacial microextraction boosting nitrogen feed for efficient ambient ammonia synthesis in aqueous electrolyte. *Advanced Functional Materials* 32(17):2109422.

[111] Li J, Chen G, Zhu Y, Liang Z, Pei A, Wu C-L, Wang H, Lee HR, Liu K, Chu S (2018) Efficient electrocatalytic CO_2 reduction on a three-phase interface. *Nature Catalysis* 1(8):592-600.

[112] Yu J, Li BQ, Zhao CX, Liu JN, Zhang Q (2020) Asymmetric air cathode design for enhanced interfacial electrocatalytic reactions in high‐performance zinc–air batteries. *Advanced Materials* 32(12):1908488.

[113] He Y, Wang M, Liu S, Zhang L, Cheng Q, Yan C, Qian T (2023) A superaerophilic gas diffusion electrode enabling facilitated nitrogen feeding through hierarchical micro/nano channels for efficient ambient synthesis of ammonia. *Chemical Engineering Journal* 454:140106.

[114] Ni J, Cheng Q, Liu S, Wang M, He Y, Qian T, Yan C, Lu J (2023) Deciphering electrolyte selection for electrochemical reduction of carbon dioxide and nitrogen to high‐value‐added chemicals. *Advanced Functional Materials* 33(11):2212483.

[115] He Y, Liu S, Wang M, Cheng Q, Qian T, Yan C (2023) Deciphering engineering principle of three-phase interface for advanced gas-involved electrochemical reactions. *Journal of Energy Chemistry* 80:302-323.

[116] Wang J, Zheng Y, Nie F-Q, Zhai J, Jiang L (2009) Air bubble bursting effect of lotus leaf. *International Conference on Micro/Nanoscale Heat Transfer.* p 667-674.

[117] Jiang Y, Wang M, Liu S, Zhang L, Qian S, Cao Y, Cheng Y, Qian T, Yan C (2023) Eliminating nitrogen chemisorption barrier with single-atom supported yttrium cluster via electronic promoting effect for highly efficient ammonia synthesis. *Nano Research* 16(2):2185-2191.

[118] Liu S, Wang M, Ji H, Zhang L, Ni J, Li N, Qian T, Yan C, Lu J (2023) Solvent‐in‐gas system for promoted photocatalytic ammonia synthesis on porous framework materials. *Advanced Materials* 35(14):2211730.

[119] Peng G, Wu J, Wang M, Niklas J, Zhou H, Liu C (2020) Nitrogen-defective polymeric carbon nitride nanolayer enabled efficient electrocatalytic nitrogen reduction with high faradaic efficiency. *Nano Letters* 20(4):2879-2885.

[120] Kang S, Wang J, Zhang S, Zhao C, Wang G, Cai W, Zhang H (2019) Plasma-etching enhanced titanium oxynitride active phase with high oxygen content for ambient electrosynthesis of ammonia. *Electrochemistry Communications* 100:90-95.

[121] Ren Y, Yu C, Tan X, Wei Q, Wang Z, Ni L, Wang L, Qiu J (2022) Strategies to activate inert nitrogen molecules for efficient ammonia electrosynthesis: current status, challenges, and perspectives. *Energy & Environmental Science* 15(7):2776-2805.

[122] Liu Y, Deng P, Wu R, Zhang X, Sun C, Li H (2021) Oxygen vacancies for promoting the electrochemical nitrogen reduction reaction. *Journal of Materials Chemistry A* 9(11):6694-6709.

[123] Zhao S, Lu X, Wang L, Gale J, Amal R (2019) Carbon‐based metal‐free catalysts for electrocatalytic reduction of nitrogen for synthesis of ammonia at ambient conditions. *Advanced Materials* 31(13):1805367.

[124] Liu S, Wang M, Cheng Q, He Y, Ni J, Liu J, Yan C, Qian T (2022) Turning waste into wealth: sustainable production of high-value-added chemicals from catalytic coupling of carbon dioxide and nitrogenous small molecules. *ACS nano* 16(11):17911-17930.

[125] Wang M, Liu S, Ji H, Liu J, Yan C, Qian T (2020) Unveiling the essential nature of Lewis basicity in thermodynamically and dynamically promoted nitrogen fixation. *Advanced Functional Materials* 30(32):2001244.

[126] Wang H, Yang D, Liu S, Yin S, Yu H, Xu Y, Li X, Wang Z, Wang L (2019) Amorphous sulfur decorated gold nanowires as efficient electrocatalysts toward ambient ammonia synthesis. *ACS Sustainable Chemistry & Engineering* 7(24):19969-19974.

[127] Liu S, Wang M, Qian T, Ji H, Liu J, Yan C (2019) Facilitating nitrogen accessibility to boron-rich covalent organic frameworks via electrochemical excitation for efficient nitrogen fixation. *Nature Communications* 10(1):3898.

[128] Andersen SZ, Čolić V, Yang S, Schwalbe JA, Nielander AC, McEnaney JM, Enemark-Rasmussen K, Baker JG, Singh AR, Rohr BA (2019) A rigorous electrochemical ammonia synthesis protocol with quantitative isotope measurements. *Nature* 570(7762):504-508.

[129] Tevi T, Yaghoubi H, Wang J, Takshi A (2013) Application of poly (p-phenylene oxide) as blocking layer to reduce self-discharge in supercapacitors. *Journal of Power Sources* 241:589-596.

[130] Chu S, Majumdar A (2012) Opportunities and challenges for a sustainable energy future. *Nature* 488(7411):294-303.

[131] Jiang Y, Wang M, Zhang L, Liu S, Cao Y, Qian S, Cheng Y, Xu X, Yan C, Qian T (2022) Distorted spinel ferrite heterostructure triggered by alkaline earth metal substitution facilitates nitrogen localization and electrocatalytic reduction to ammonia. *Chemical Engineering Journal* 450:138226.

[132] Yu H, Xue Y, Hui L, Zhang C, Fang Y, Liu Y, Chen X, Zhang D, Huang B, Li Y (2021) Graphdiyne-based metal atomic catalysts for synthesizing ammonia. *National science review* 8(8):nwaa213.

[133] Liu S, Jiang Y, Wang M, Huan Y, He Y, Cheng Q, Cheng Y, Liu J, Zhou X, Qian T (2023) Awakening (220) as one more active facet of PtMo alloy via single‐atom doping to boost ammonia electrooxidation in direct ammonia fuel cell. *Advanced Functional Materials* 33(47):2306204.

[134] Lazouski N, Chung M, Williams K, Gala ML, Manthiram K (2020) Non-aqueous gas diffusion electrodes for rapid ammonia synthesis from nitrogen and water-splitting-derived hydrogen. *Nature Catalysis* 3(5):463-469.

[135] Li M, Huang H, Low J, Gao C, Long R, Xiong Y (2019) Recent progress on electrocatalyst and photocatalyst design for nitrogen reduction. *Small Methods* 3(6):1800388.

[136] Yandulov DV, Schrock RR (2003) Catalytic reduction of dinitrogen to ammonia at a single molybdenum center. *Science* 301(5629):76-78.

[137] Liu S, Wang M, Ji H, Shen X, Yan C, Qian T (2021) Altering the rate-determining step over cobalt single clusters leading to highly efficient ammonia synthesis. *National science review* 8(5):nwaa136.

[138] Jiang YF, Ma XL, Lu JB, Wang JQ, Xiao H, Li J (2019) N_2 Reduction on Fe‐Based Complexes with Different Supporting Main‐Group Elements: Critical Roles of Anchor and Peripheral Ligands. *Small Methods* 3(6):1800340.

[139] Cheng H, Ding LX, Chen GF, Zhang L, Xue J, Wang H (2018) Molybdenum carbide nanodots enable efficient electrocatalytic nitrogen fixation under ambient conditions. *Advanced Materials* 30(46):1803694.

[140] Hua W, Sun H-H, Xu F, Wang J-G (2020) A review and perspective on molybdenum-based electrocatalysts for hydrogen evolution reaction. *Rare Metals* 39:335-351.

[141] Du Y, Li B, Xu G, Wang L (2023) Recent advances in interface engineering strategy for highly‐efficient electrocatalytic water splitting. *InfoMat* 5(1):e12377.

[142] Li X, Li Z-Q, Liu H-Y, Lu S-Y (2023) Theoretical study on hydrogen evolution reaction in transition metal borides. *Rare Metals* 42(6):1808-1812.

[143] Zhai W, Ma Y, Chen D, Ho JC, Dai Z, Qu Y (2022) Recent progress on the long‐term stability of hydrogen evolution reaction electrocatalysts. *InfoMat* 4(9):e12357.

[144] Qiu W, Xie X-Y, Qiu J, Fang W-H, Liang R, Ren X, Ji X, Cui G, Asiri AM, Cui G (2018) High-performance artificial nitrogen fixation at ambient conditions using a metal-free electrocatalyst. *Nature Communications* 9(1):3485.

[145] Du Y, Jiang C, Xia W, Song L, Li P, Gao B, Wu C, Sheng L, Ye J, Wang T (2020) Electrocatalytic reduction of N_2 and nitrogen-incorporation process on dopant-free defect graphene. *Journal of Materials Chemistry A* 8(1):55-61.

[146] Lv C, Qian Y, Yan C, Ding Y, Liu Y, Chen G, Yu G (2018) Defect engineering metal‐free polymeric carbon nitride electrocatalyst for effective nitrogen fixation under ambient conditions. *Angewandte Chemie* 130(32):10403-10407.

[147] Zhao C, Zhang S, Han M, Zhang X, Liu Y, Li W, Chen C, Wang G, Zhang H, Zhao H (2019) Ambient electrosynthesis of ammonia on a biomass-derived nitrogen-doped porous carbon electrocatalyst: contribution of pyridinic nitrogen. *ACS Energy Letters* 4(2):377-383.

[148] Tang Y, Shen Z, Ma Y, Chen W, Ma D, Zhao M, Dai X (2018) Divacancy-nitrogen/boron-codoped graphene as a metal-free catalyst for high-efficient CO oxidation. *Materials Chemistry and Physics* 207:11-22.

[149] Song P, Wang H, Kang L, Ran B, Song H, Wang R (2019) Electrochemical nitrogen reduction to ammonia at ambient conditions on nitrogen and phosphorus co-doped porous carbon. *Chemical Communications* 55(5):687-690.

[150] Tian Y, Xu D, Chu K, Wei Z, Liu W (2019) Metal-free N, S co-doped graphene for efficient and durable nitrogen reduction reaction. *Journal of materials science* 54:9088-9097.

[151] Kong Y, Li Y, Yang B, Li Z, Yao Y, Lu J, Lei L, Wen Z, Shao M, Hou Y (2019) Boron and nitrogen co-doped porous carbon nanofibers as metal-free electrocatalysts for highly efficient ammonia electrosynthesis. *Journal of Materials Chemistry A* 7(46):26272-26278.

[152] Ren J-T, Wan C-Y, Pei T-Y, Lv X-W, Yuan Z-Y (2020) Promotion of electrocatalytic nitrogen reduction reaction on N-doped porous carbon with secondary heteroatoms. *Applied Catalysis B: Environmental* 266:118633.

[153] Wu T, Li P, Wang H, Zhao R, Zhou Q, Kong W, Liu M, Zhang Y, Sun X, Gong FF (2019) Biomass-derived oxygen-doped hollow carbon microtubes for electrocatalytic N_2-to-NH_3 fixation under ambient conditions. *Chemical Communications* 55(18):2684-2687.

[154] Wang M, Liu S, Xu N, Qian T, Yan C (2017) Active Fe‐N_x sites in carbon nanosheets as oxygen reduction electrocatalyst for flexible all‐solid‐state zinc–air batteries. *Advanced Sustainable Systems* 1(10):1700085.

[155] Wang Y, Cui X, Zhao J, Jia G, Gu L, Zhang Q, Meng L, Shi Z, Zheng L, Wang C (2018) Rational design of Fe–N/C hybrid for enhanced nitrogen reduction electrocatalysis under ambient conditions in aqueous solution. *ACS Catalysis* 9(1):336-344.

[156] Zou H, Rong W, Long B, Ji Y, Duan L (2019) Corrosion-induced Cl-doped ultrathin graphdiyne toward electrocatalytic nitrogen reduction at ambient conditions. *ACS Catalysis* 9(12):10649-10655.

[157] Xiao M, Zhu J, Feng L, Liu C, Xing W (2015) Meso/macroporous nitrogen-doped carbon architectures with iron carbide encapsulated in graphitic layers as an efficient and robust catalyst for the oxygen reduction reaction in both acidic and alkaline solutions. *Advanced Materials (Deerfield Beach, Fla.)* 27(15):2521-2527.

[158] Liu Z, Zhao Z, Wang Y, Dou S, Yan D, Liu D, Xia Z, Wang S (2017) In situ exfoliated, edge‐rich, oxygen‐functionalized graphene from carbon fibers for oxygen electrocatalysis. *Advanced Materials* 29(18):1606207.

[159] Lu X, Yim W-L, Suryanto BH, Zhao C (2015) Electrocatalytic oxygen evolution at surface-oxidized multiwall carbon nanotubes. *Journal of the American Chemical Society* 137(8):2901-2907.

[160] Li L, Yang H, Miao J, Zhang L, Wang H-Y, Zeng Z, Huang W, Dong X, Liu B (2017) Unraveling oxygen evolution reaction on carbon-based electrocatalysts: effect of oxygen doping on adsorption of oxygenated intermediates. *ACS Energy Letters* 2(2):294-300.

[161] Bao D, Zhang Q, Meng FL, Zhong HX, Shi MM, Zhang Y, Yan JM, Jiang Q, Zhang XB (2017) Electrochemical reduction of N2 under ambient conditions for artificial N2 fixation and renewable energy storage using N2/NH3 cycle. *Advanced Materials* 29(3):1604799.

[162] Lv C, Yan C, Chen G, Ding Y, Sun J, Zhou Y, Yu G (2018) An amorphous noble‐metal‐free electrocatalyst that enables nitrogen fixation under ambient conditions. *Angewandte Chemie* 130(21):6181-6184.

[163] Zhang Y, Qiu W, Ma Y, Luo Y, Tian Z, Cui G, Xie F, Chen L, Li T, Sun X (2018) High-performance electrohydrogenation of N_2 to NH_3 catalyzed by multishelled hollow Cr2O3 microspheres under ambient conditions. *ACS Catalysis* 8(9):8540-8544.

[164] Xiao L, Zhu S, Liang Y, Li Z, Wu S, Luo S, Chang C, Cui Z (2021) Effects of hydrophobic layer on selective electrochemical nitrogen fixation of self-supporting nanoporous Mo4P3 catalyst under ambient conditions. *Applied Catalysis B: Environmental* 286:119895.

[165] Cao N, Chen Z, Zang K, Xu J, Zhong J, Luo J, Xu X, Zheng G (2019) Doping strain induced bi-Ti^{3+} pairs for efficient N_2 activation and electrocatalytic fixation. *Nature Communications* 10(1):2877.

[166] Yang S, Ye W, Zhang D, Fang X, Yan D (2021) Layered double hydroxide derived bimetallic nickel–iron selenide as an active electrocatalyst for nitrogen fixation under ambient conditions. *Inorganic Chemistry Frontiers* 8(7):1762-1770.

[167] Wang J, Yu L, Hu L, Chen G, Xin H, Feng X (2018) Ambient ammonia synthesis via palladium-catalyzed electrohydrogenation of dinitrogen at low overpotential. *Nature Communications* 9(1):1795.

[168] Shi MM, Bao D, Wulan BR, Li YH, Zhang YF, Yan JM, Jiang Q (2017) Au sub‐nanoclusters on TiO_2 toward highly efficient and selective electrocatalyst for N_2 conversion to NH_3 at ambient conditions. *Advanced Materials* 29(17):1606550.

[169] Wang H-B, Wang J-Q, Zhang R, Cheng C-Q, Qiu K-W, Yang Y-j, Mao J, Liu H, Du M, Dong C-K (2020) Bionic design of a Mo (IV)-doped FeS_2 catalyst for electroreduction of dinitrogen to ammonia. *ACS Catalysis* 10(9):4914-4921.

[170] Zhang J, Ji Y, Wang P, Shao Q, Li Y, Huang X (2020) Adsorbing and activating N_2 on heterogeneous Au‐Fe_3O_4 nanoparticles for N_2 fixation. *Advanced Functional Materials* 30(4):1906579.

[171] Wang H, Li Y, Yang D, Qian X, Wang Z, Xu Y, Li X, Xue H, Wang L (2019) Direct fabrication of bi-metallic PdRu nanorod assemblies for electrochemical ammonia synthesis. *Nanoscale* 11(12):5499-5505.

[172] Chen G-F, Cao X, Wu S, Zeng X, Ding L-X, Zhu M, Wang H (2017) Ammonia electrosynthesis with high selectivity under ambient conditions via a Li^+ incorporation strategy. *Journal of the American Chemical Society* 139(29):9771-9774.

[173] Zhao J, Yang J, Ji L, Wang H, Chen H, Niu Z, Liu Q, Li T, Cui G, Sun X (2019) Defect-rich fluorographene nanosheets for artificial N_2 fixation under ambient conditions. *Chemical Communications* 55(29):4266-4269.

[174] Yao Y, Wang J, Shahid UB, Gu M, Wang H, Li H, Shao M (2020) Electrochemical synthesis of ammonia from nitrogen under mild conditions: current status and challenges. *Electrochemical Energy Reviews* 3:239-270.

[175] Shi L, Yin Y, Wang S, Sun H (2020) Rational catalyst design for N_2 reduction under ambient conditions: strategies toward enhanced conversion efficiency. *ACS Catalysis* 10(12):6870-6899.

[176] Wei Z-X, Zhu Y-T, Liu J-Y, Zhang Z-C, Hu W-P, Xu H, Feng Y-Z, Ma J-M (2021) Recent advance in single-atom catalysis. *Rare Metals* 40:767-789.

[177] Xue K, Mo Y, Long B, Wei W, Shan C, Guo S, Niu L (2022) Single‐atom catalysts supported on ordered porous materials: Synthetic strategies and applications. *InfoMat* 4(6):e12296.

[178] Zhang L, Ren Y, Liu W, Wang A, Zhang T (2018) Single-atom catalyst: a rising star for green synthesis of fine chemicals. *National science review* 5(5):653-672.

[179] Hu P, Huang Z, Amghouz Z, Makkee M, Xu F, Kapteijn F, Dikhtiarenko A, Chen Y, Gu X, Tang X (2014) Electronic metal‐support interactions in single‐atom catalysts. *Angewandte Chemie International Edition* 53(13):3418-3421.

[180] Liu J, Kong X, Zheng L, Guo X, Liu X, Shui J (2020) Rare earth single-atom catalysts for nitrogen and carbon dioxide reduction. *ACS nano* 14(1):1093-1101.

[181] Xue Y, Huang B, Yi Y, Guo Y, Zuo Z, Li Y, Jia Z, Liu H, Li Y (2018) Anchoring zero valence single atoms of nickel and iron on graphdiyne for hydrogen evolution. *Nature Communications* 9(1):1460.

[182] He T, Santiago ARP, Du A (2020) Atomically embedded asymmetrical dual-metal dimers on N-doped graphene for ultra-efficient nitrogen reduction reaction. *Journal of Catalysis* 388:77-83.

[183] Wang S, Shi L, Bai X, Li Q, Ling C, Wang J (2020) Highly efficient photo-/electrocatalytic reduction of nitrogen into ammonia by dual-metal sites. *ACS central science* 6(10):1762-1771.

[184] Ma D, Wang Y, Liu L, Jia Y (2021) Electrocatalytic nitrogen reduction on the transition-metal dimer anchored N-doped graphene: performance prediction and synergetic effect. *Physical Chemistry Chemical Physics* 23(6):4018-4029.

[185] Yan X, Liu D, Cao H, Hou F, Liang J, Dou SX (2019) Nitrogen reduction to ammonia on atomic‐scale active sites under mild conditions. *Small Methods* 3(9):1800501.

[186] Qiu N, Li J, Wang H, Zhang Z (2022) Emerging dual-atomic-site catalysts for electrocatalytic CO_2 reduction. *Science China Materials* 65(12):3302-3323.

[187] Ma D, Zeng Z, Liu L, Jia Y (2021) Theoretical screening of the transition metal heteronuclear dimer anchored graphdiyne for electrocatalytic nitrogen reduction. *Journal of Energy Chemistry* 54:501-509.

[188] Zheng G, Li L, Hao S, Zhang X, Tian Z, Chen L (2020) Double Atom Catalysts: Heteronuclear Transition Metal Dimer Anchored on Nitrogen‐Doped Graphene as Superior Electrocatalyst for Nitrogen Reduction Reaction. *Advanced Theory and Simulations* 3(12):2000190.

[189] Guo X, Gu J, Lin S, Zhang S, Chen Z, Huang S (2020) Tackling the activity and selectivity challenges of electrocatalysts toward the nitrogen reduction reaction via atomically dispersed biatom catalysts. *Journal of the American Chemical Society* 142(12):5709-5721.

[190] Wang M, Liu S, Qian T, Liu J, Zhou J, Ji H, Xiong J, Zhong J, Yan C (2019) Over 56.55% Faradaic efficiency of ambient ammonia synthesis enabled by positively shifting the reaction potential. *Nature Communications* 10(1):341.

[191] Chen ZW, Yan JM, Jiang Q (2019) Single or double: which is the altar of atomic catalysts for nitrogen reduction reaction? *Small Methods* 3(6):1800291.

[192] Légaré M-A, Bélanger-Chabot G, Dewhurst RD, Welz E, Krummenacher I, Engels B, Braunschweig H (2018) Nitrogen fixation and reduction at boron. *Science* 359(6378):896-900.

[193] Li Y, Zhang Q, Li C, Fan H-N, Luo W-B, Liu H-K, Dou S-X (2019) Atomically dispersed metal dimer species with selective catalytic activity for nitrogen electrochemical reduction. *Journal of Materials Chemistry A* 7(39):22242-22247.

[194] Shen H, Choi C, Masa J, Li X, Qiu J, Jung Y, Sun Z (2021) Electrochemical ammonia synthesis: mechanistic understanding and catalyst design. *Chem* 7(7):1708-1754.

[195] Van der Ham CJ, Koper MT, Hetterscheid DG (2014) Challenges in reduction of dinitrogen by proton and electron transfer. *Chemical Society Reviews* 43(15):5183-5191.

[196] Zhang S, Han M, Shi T, Zhang H, Lin Y, Zheng X, Zheng LR, Zhou H, Chen C, Zhang Y (2023) Atomically dispersed bimetallic Fe‐Co electrocatalysts for green production of ammonia. *Nature Sustainability* 6(2):169-179.

[197] Wang S, Ichihara F, Pang H, Chen H, Ye J (2018) Nitrogen fixation reaction derived from nanostructured catalytic materials. *Advanced Functional Materials* 28(50):1803309.

[198] Guo C, Ran J, Vasileff A, Qiao S-Z (2018) Rational design of electrocatalysts and photo (electro) catalysts for nitrogen reduction to ammonia (NH_3) under ambient conditions. *Energy & Environmental Science* 11(1):45-56.

[199] Suryanto BH, Du H-L, Wang D, Chen J, Simonov AN, MacFarlane DR (2019) Challenges and prospects in the catalysis of electroreduction of nitrogen to ammonia. *Nature Catalysis* 2(4):290-296.

[200] Zang W, Yang T, Zou H, Xi S, Zhang H, Liu X, Kou Z, Du Y, Feng YP, Shen L (2019) Copper single atoms anchored in porous nitrogen-doped carbon as efficient pH-universal catalysts for the nitrogen reduction reaction. *ACS Catalysis* 9(11):10166-10173.

[201] Guo J, Wang H, Xue F, Yu D, Zhang L, Jiao S, Liu Y, Lu Y, Liu M, Ruan S (2019) Tunable synthesis of multiply twinned intermetallic Pd_3Pb nanowire networks toward efficient N_2 to NH_3 conversion. *Journal of Materials Chemistry A* 7(35):20247-20253.

[202] Pang F, Wang Z, Zhang K, He J, Zhang W, Guo C, Ding Y (2019) Bimodal nanoporous Pd_3Cu_1 alloy with restrained hydrogen evolution for stable and high yield electrochemical nitrogen reduction. *Nano Energy* 58:834-841.

[203] Tong W, Huang B, Wang P, Li L, Shao Q, Huang X (2020) Crystal‐phase‐engineered PdCu electrocatalyst for enhanced ammonia synthesis. *Angewandte Chemie* 132(7):2671-2675.

[204] Xia L, Wu X, Wang Y, Niu Z, Liu Q, Li T, Shi X, Asiri AM, Sun X (2019) S‐doped carbon nanospheres: an efficient electrocatalyst toward artificial N_2 fixation to NH_3. *Small Methods* 3(6):1800251.

8 SOMMAIRE RÉCAPITULATIF

8.1 Introduction

En tant que produit chimique de base, l'ammoniac est l'un des produits chimiques les plus produits au monde. Il est largement utilisé dans l'industrie chimique, l'agriculture et d'autres domaines. Elle occupe donc une place importante dans l'économie mondiale. Jusqu'à présent, la méthode traditionnelle Haber-Bosch reste la principale méthode de synthèse de NH_3. Cependant, il est difficile de réduire doucement N_2 en NH_3 en raison de la forte triple liaison N (941 kJ mol^{-1}). Par conséquent, le procédé industriel Haber-Bosch actuel nécessite la synthèse d'ammoniac dans des conditions de haute température (400 ~ 450 ℃) et de haute pression (10-30 MPa), où une température élevée pour une cinétique accélérée et une pression élevée pour déplacer favorablement l'équilibre. En 2021, la production mondiale d'ammoniac a atteint 182 millions de tonnes grâce au procédé Haber-Bosch. Parmi eux, environ 70 % de l'ammoniac est utilisé dans la production d'engrais chimiques, et environ 50 % de la production alimentaire mondiale repose sur des engrais chimiques dérivés de l'ammoniac. Les données ci-dessus montrent clairement le grand impact de la technologie de synthèse de l'ammoniac sur les êtres humains. Cependant, le procédé Haber de synthèse de l'ammoniac présente une consommation d'énergie élevée et une pollution importante. L'hydrogène de haute pureté utilisé consomme non seulement une grande quantité de gaz naturel fossile à convertir, mais libère également environ 1,6 tonne de gaz à effet de serre de dioxyde de carbone pour chaque tonne d'ammoniac produite. La consommation d'énergie de ce processus représente 1 % de la consommation mondiale d'énergie et les émissions de dioxyde de carbone représentent 1,5 % des émissions mondiales totales. Par conséquent, trouver une méthode de synthèse de l'ammoniac verte, respectueuse de l'environnement et à faible consommation d'énergie revêt une grande importance pour le développement durable de l'environnement et de l'énergie.

La réaction de réduction électrocatalytique de l'azote (NRR) est un processus écologique et durable qui convertit directement le N_2 en NH_3 en utilisant l'eau comme source de protons et d'électrons à un potentiel inférieur. Le NRR électrocatalytique présente les avantages d'utiliser des énergies renouvelables (énergie éolienne, énergie solaire, etc.), de larges sources de matières premières (N_2 et H_2O) et une réaction à température et pression ambiantes.

Cependant, NRR est encore confronté à d'énormes défis. En général, les principaux défis auxquels nous sommes confrontés dans la recherche de percées dans le domaine du NRR électrocatalytique ambiant peuvent être classés comme des limitations inhérentes et des énigmes techniques. D'une part, bien qu'il soit thermodynamiquement possible de réduire N_2 en NH_3 ou NH^{4+} dans des conditions modérées, la fenêtre potentielle entre le NRR et la réaction de dégagement d'hydrogène (HER) est assez étroite sur toute la plage de pH. En outre, la faible solubilité du N_2 dans l'eau (0,66 mmol L^{-1} dans des conditions ambiantes) limite considérablement les performances du NRR, ce qui remet encore en question la possibilité d'une activité et d'une sélectivité élevées du NRR simultanément. D'un autre côté, la contamination ambiante par l'ammoniac au cours des expériences est inévitable et importante, ce qui rend très difficile la détection précise de l'ammoniac généré par le NRR. En raison de sa polarité élevée et de sa solubilité aqueuse, l'ammoniac (sous forme de NH_3 ou NH^{4+}) peut être omniprésent dans toutes les solutions aqueuses et de nombreuses surfaces, notamment l'atmosphère, le four, la respiration humaine, les gants en latex, la blouse de laboratoire, les tubes d'échantillon, la membrane de nafion, échantillons stockés, eau Milli-Q viciée, etc. Par conséquent, la contamination ambiante par l'ammoniac pourrait très probablement conduire à des incertitudes, à la non-répétabilité et même à des résultats faussement positifs si l'expérience n'était pas menée correctement et avec soin.

Jusqu'à présent, une large gamme de matériaux, tels que des catalyseurs à base d'oxydes métalliques (TiO_2, $Bi_4V_2O_{11}$, etc.), de sulfures métalliques (MoS_2), de catalyseurs à base de métaux (Ag, Cu, W, Mo Co, Fe, etc.), les catalyseurs sans métaux (Cl, B, F, P, S, O, N, etc.) et les matériaux à base de carbone (graphdiyne, g-C_3N_4, carbone dopé N, etc.) ont fait de grands progrès sur l'activité électrocatalytique et sélectivité pour le NRR. Diverses stratégies, notamment le contrôle de surface, l'ingénierie des défauts, l'hybridation, etc., ont été proposées en permanence pour augmenter le nombre de sites actifs exposés ou améliorer l'activité intrinsèque d'un site unique, améliorant ainsi davantage les performances catalytiques. Par exemple, le dopage de l'électrocatalyseur d'origine avec des atomes de tailles et de charges différentes a été largement suggéré dans diverses applications électrocatalytiques. Les dopants peuvent modifier la structure électronique de l'électrocatalyseur et modifier la force de liaison du réactif, de l'intermédiaire ou du produit sur les sites actifs. Ainsi, ils régissent les performances électrocatalytiques. Parallèlement, la synthèse de catalyseurs à atome unique (SAC) a également été considérée comme une technique prometteuse pour le développement de catalyseurs. Les SAC préparés présentent des performances catalytiques exceptionnelles avec un nombre extrêmement élevé de sites actifs et des propriétés électroniques uniques affectant

les voies catalytiques. Des SAC métalliques, tels que Au, Cu, Fe, etc., ont été proposés et ont présenté d'excellentes performances ENRR. Plus particulièrement, la formation de la limite triphasée (TPB) N_2(g)-catalyseur-H_2O(l) est cruciale pour la pratique de l'ENRR. Le TPB avancé peut supprimer efficacement HER, la réaction concurrentielle représentative, et développer le taux de production de NH_3. Dans les systèmes ENRR aqueux typiques, la faible solubilité du N_2 (0,0126 mg g^{-1}) empêche le transfert efficace du N_2, contrairement à la libre accessibilité du H_2O, provoquant une concentration de N_2 significativement plus faible à proximité des catalyseurs que celle du H_2O. Il fournit une condition TPB insuffisante, ce qui entraîne un FE et un taux de production inefficaces pour l'ENRR. Une stratégie pour faire progresser le TPB consiste à modifier la surface de l'électrode qui a une nature partiellement hydrophobe.

8.2 Objects

Cet article vise à optimiser le taux de rendement et l'efficacité faradique de la synthèse de l'ammoniac à température et pression normales en développant une série de catalyseurs NRR à base de NC dopés avec d'autres éléments, tels que OENC, WFeNC et FeCoNC.

(1) Dans ce travail, un catalyseur NRR au carbone bimétallique dopé à l'azote (WFeNC) est synthétisé et une stratégie de limitation de l'azote est proposée par gravure plasma du catalyseur pour résoudre le problème de l'approvisionnement limité en réactifs pour le NRR dans des conditions ambiantes. Après gravure plasma, un grand nombre de vides apparaissent sur le catalyseur P-WFeNC, largement suffisants pour servir de réservoir aux nanobulles de N_2. Un grand nombre de méthodes de caractérisation sont utilisées pour vérifier les conclusions ci-dessus. Tout d'abord, nous utilisons des simulations moléculaires pour comprendre l'état d'agglomération de l'azote dans une solution de HCl 0,1 M et la taille des agglomérats. BET est ensuite utilisé pour tester si la taille des vides dans le matériau après gravure au plasma correspond à la taille des agglomérats d'azote dans la simulation moléculaire. Ensuite, nous caractérisons la surface du catalyseur soumis au NRR grâce à la technologie XRD in situ pour confirmer si l'azote y est adsorbé et stocké. Par la suite, la question de savoir si P-WFeNC peut piéger efficacement les nanobulles de N_2 est évaluée sur la base d'expériences de piégeage de bulles. Enfin, en comparant si le taux de rendement en NH_3 et l'efficacité faradique du catalyseur avant et après gravure plasma sont améliorés pour vérifier si cette stratégie est adaptée au NRR.

(2) Dans ce travail, nous concevons un catalyseur (OENC) dopé à l'oxygène comme hétéroatome secondaire qui peut favoriser la synthèse d'ammoniac ambiant sur du carbone dopé à l'azote en déclenchant un effet coopératif de promotion des électrons. Pour mieux comprendre les mécanismes de réaction impliqués du NRR sur OENC, des calculs DFT sont effectués pour étudier les profils d'énergie libre, y compris la voie distale et la voie alternée. Grâce aux tests Raman, le rapport d'intensité de la bande D et de la bande G (I_D/I_G) pour NC et OENC est comparé pour confirmer la présence d'oxygène enrichi. Ensuite, la nature chimique et la structure des liaisons de différentes structures sont étudiées par spectroscopie photoélectronique à rayons X (XPS). Par la suite, en testant et en comparant le rendement en NH_3, l'efficacité faradique et la sélectivité H_2 de NC et OENC pour vérifier si l'effet promoteur électronique stimulera la synthèse d'ammoniac ambiant. Enfin, des expériences de marquage isotopique ^{15}N sont menées pour étudier plus en détail la source de N de l'ammoniac produit.

(3) Étant donné que les deux atomes métalliques hétéronucléaires orbitaux d occupés dans le site dimère peuvent simultanément piéger deux électrons libres aux deux extrémités de la molécule N_2 et permettre le rétrodon asymétrique d'électrons, ce qui est bénéfique pour la polarisation de la liaison N≡N et facilite ainsi sa affaiblissement. Dans ce travail, des sites hétérobimétalliques asymétriques (Fe, Co) sont proposés pour rompre les relations d'échelle inhérentes entre la force de liaison des intermédiaires du NRR en tant que réaction multi-intermédiaire. Les calculs de la théorie fonctionnelle de la densité (DFT) sont utilisés pour vérifier si la forte interaction électronique entre N_2 et les sites dimères permet une activation maximisée de N_2 et une régulation de la force de liaison des intermédiaires clés, réduisant ainsi considérablement la barrière énergétique du processus NRR global. La microscopie électronique à transmission par balayage à champ sombre annulaire à grand angle et corrigée des aberrations (AC-HAADF-STEM) est ensuite réalisée pour élucider la forme existentielle des atomes de Fe et de Co. Pour confirmer davantage la structure de FeCoNC au niveau atomique, nous prendrons des analyses de structure d'absorption des rayons X proche du bord (XANES) et de structure fine d'absorption étendue des rayons X (EXAFS) avec une feuille de Fe et une feuille de Co comme références. Par la suite, en testant et en comparant le rendement en NH_3, l'efficacité faradique et la sélectivité H_2 de FeNC et FeCoNC pour vérifier si l'effet promoteur électronique stimulera la synthèse d'ammoniac ambiant. Enfin, des expériences de marquage isotopique ^{15}N sont menées pour étudier plus en détail la source de N de l'ammoniac produit.

8.3 Résultats et discussions

8.3.1 Confiner des nanobulles d'azote dans des vides gravés au plasma

Dans ce travail, une stratégie de confinement de l'azote obtenue par gravure plasma est proposée pour résoudre le problème de l'apport limité d'azote pour une synthèse améliorée de l'ammoniac dans des conditions ambiantes (Figure 8.1). Lors de la gravure au plasma, de nombreux vides peuvent être construits in situ pour servir de réservoirs aux nanobulles d'azote. Les nanobulles peuvent être efficacement attirées par l'hétérogénéité de surface induite par les défauts, car elle pourrait générer des interactions de Van der Waals (vdW) entre l'électrocatalyseur et l'azote. Grâce au transfert directionnel, les nanobulles d'azote peuvent être capturées par les vides, fournissant ainsi une source continue d'azote pour le NRR.

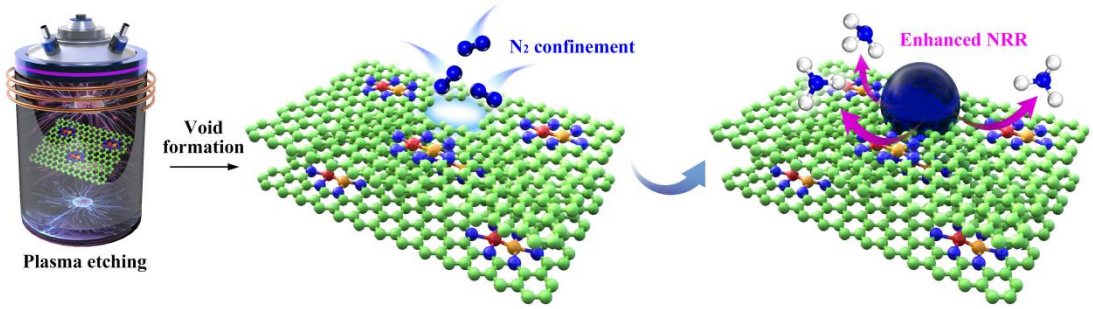

Figure 8.1 Illustration schématique du mécanisme permettant d'améliorer la synthèse électrochimique de l'ammoniac en confinant les amas d'azote dans des vides gravés au plasma.

Afin de parvenir à une capture précise du gaz N_2, sa forme d'existence dans l'électrolyte a d'abord été étudiée par des simulations MD. Étant donné que l'azote est continuellement introduit dans le système pendant les expériences réelles, le modèle initial a été construit en plaçant uniformément 9 colonnes de gaz composées de molécules d'azote dans la boîte de simulation avec une longueur de bord de 12 nm. Un tel modèle a d'abord été minimisé en énergie et équilibré pendant 30 ps, suivi d'une exécution MD de 5 ns. Des instantanés de la distribution de N_2 à 2, 3, 4 et 5 ns sont présentés dans la figure 8.1 a. On voit clairement que les molécules d'azote ont tendance à converger en nanobulles d'un diamètre moyen d'environ 1,5 nm en très peu de temps, puis à conserver cette taille pendant la simulation. Trois simulations distinctes ont été réalisées et le diamètre moyen de l'amas représentatif de N_2 en fonction du temps présente une cohérence supérieure (Figure 8.2 b). Sous cette condition préalable, des vides supérieurs à 1,5 nm doivent être construits dans l'électrocatalyseur pour capturer les nanobulles d'azote et servir de réservoir d'azote à alimenter pour le processus NRR.

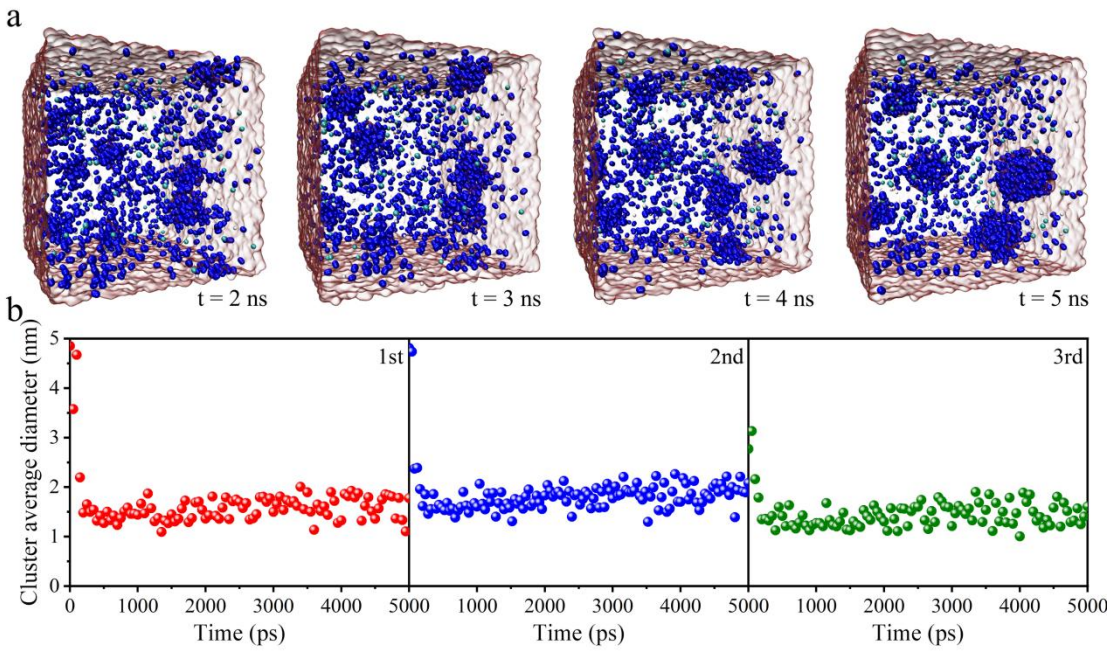

Figure 8.2 (a) Instantanés de simulation MD de la distribution de N_2 dans 0,1 M HCl à 2, 3, 4 et 5 ns. (b) Le diamètre moyen du cluster N_2 représentatif en fonction du temps dans trois simulations distinctes.

Il a été rapporté que la gravure au plasma était capable de perturber les surfaces basales des matériaux à base de carbone pour générer un grand nombre de défauts ressemblant à des vides et a été appliquée ici dans ce travail. Il est bien connu que des atomes de Fe uniques isolés ancrés sur du carbone dopé à l'azote (FeNC) offrent un certain degré de performances NRR. De plus, selon les travaux antérieurs ainsi que les calculs de la théorie fonctionnelle de la densité, l'introduction du deuxième métal tel que le tungstène (WFeNC) pourrait réguler efficacement la structure électronique de la zone active et réduire davantage la barrière réactionnelle de réduction de l'azote. Par conséquent, WFENC a été soigneusement synthétisé comme catalyseur modèle. Le WFeNC vierge présente une morphologie semblable à celle du graphène, comme le montrent les images de microscopie électronique à balayage (MEB) et de microscopie électronique à transmission (TEM) (Figure 8.3 a et b). Lors de la gravure au plasma, de nombreux vides ont été construits in situ dans le plan basal de WFeNC, déclenchant une hétérogénéité de surface et conduisant à une masse de rides dans la surface semblable au graphène (Figure 8.3 c et d). L'image TEM haute résolution (HRTEM) et les cartes d'éléments correspondantes du WFeNC gravé au plasma (P-WFeNC) décrivent la distribution uniforme des éléments C, N, O, Fe et W sur toute l'architecture pleine de vides (Figure 8.3 e). Avec la présence de ces défauts ressemblant à des vides, la surface spécifique du catalyseur a

également été augmentée de 113,1 à 207,5 m^2 g^{-1}, comme déterminé par la méthode Brunauer-Emmett-Teller (BET). De plus, les profils de répartition des pores correspondants indiquent l'apparition de mésopores de diamètres de 2,86 et 3,23 nm dans P-WFeNC (Figure 8.3 f), suffisants pour servir de réservoir aux nanobulles de N_2. La structure défectueuse de P-WFeNC a été étudiée plus en détail par spectroscopie XRD et Raman. Avec l'augmentation du niveau de défauts dû à la gravure plasma, le pic situé à 25,2° attribué au plan (002) du carbone graphitique devient plus large pour le P-WFeNC dans les diagrammes XRD (Figure 8.3 g). De manière correspondante, le rapport d'intensité de la bande G correspondant aux carbones graphitiques et de la bande D attribuée à la densité de défauts dans les domaines graphitiques dans la spectroscopie Raman augmente également de 0,98 pour WFeNC à 1,07 pour P-WFeNC (Figure 8.3 h), démontrant le présence de défauts enrichis lors de la gravure plasma. L'hétérogénéité de surface induite améliorerait efficacement les interactions vdW, telles que la force de dispersion de Londres, entre l'électrocatalyseur et les molécules d'azote, déclenchant ainsi un transfert directionnel d'azote vers le catalyseur. Les nanobulles d'azote entrantes peuvent être efficacement capturées par les vides, fournissant ainsi un apport abondant de réactifs pour la réduction de l'azote et stimulant ainsi l'ensemble du processus NRR.

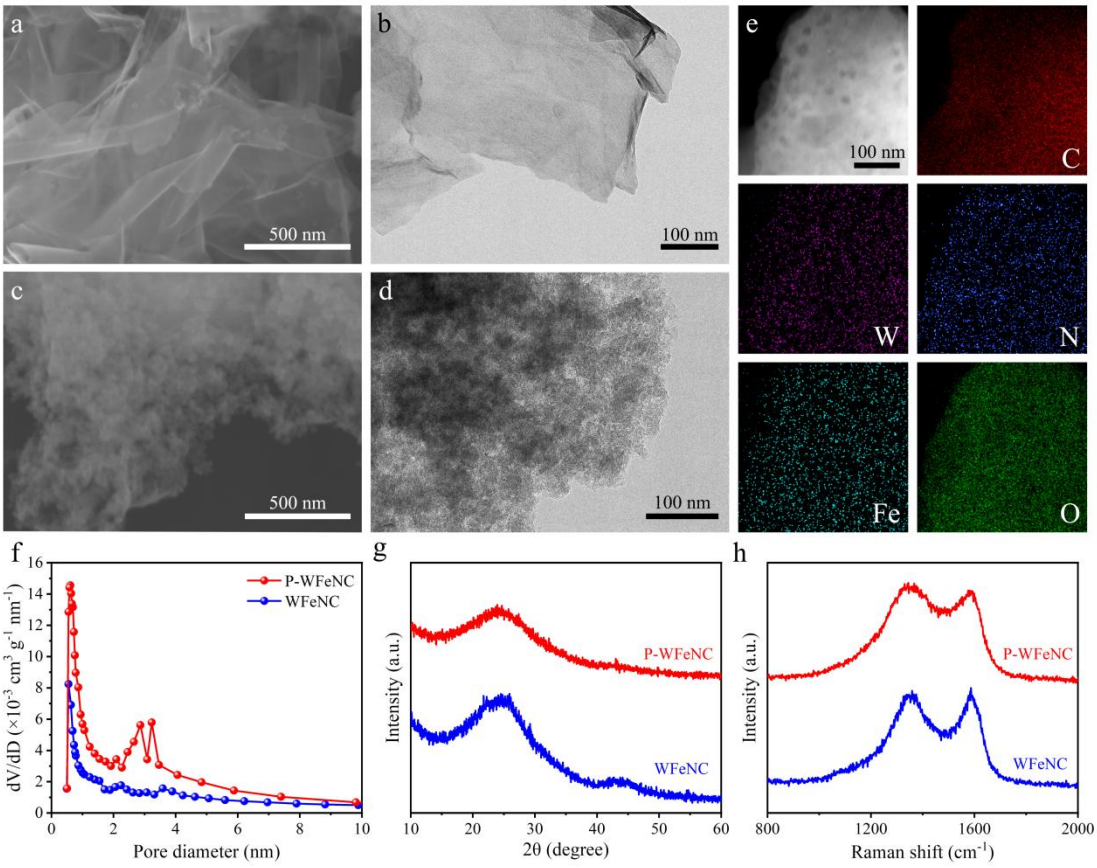

Figure 8.3 (a) Images SEM et (b) TEM de WFeNC. (c) Images SEM et (d) TEM de P-WFeNC. (e) Image HRTEM et cartes d'éléments correspondantes de P-WFeNC. (f) Les courbes de distribution de la taille des pores, (g) les modèles XRD et (h) les spectres Raman de WFeNC et P-WFeNC.

Par la suite, des expériences sur des bulles captives ont été réalisées pour évaluer si le P-WFeNC est capable de capturer efficacement les nanobulles de N_2. Pour l'électrode recouverte de WFeNC, elle ne parvient pas à interagir avec la bulle de N_2, qui conserve l'état de « blocage » une fois en contact avec la surface de l'électrode et ne présente aucun changement observable pendant 3 000 ms (Figure 8.4 a). En revanche, avec la modification du plasma, un grand nombre de vides sont construits pour capturer les nanobulles de N_2, de sorte qu'il ne faut que 720 ms pour éclater complètement et pénétrer dans la partie interne de l'électrode recouverte de P-WFeNC (Figure 8.4 b). Ensuite, des expériences XRD in situ ont été menées pour démontrer l'enrichissement en N_2 sur l'électrode. La carte d'intensité XRD in situ de l'électrode recouverte de P-WFeNC a été collectée lors d'opérations chronoampérométriques sous atmosphère de N_2 et est affichée sur la figure 8.4 c. Évidemment, l'intensité du pic de carbone, qui varie avec la concentration de N_2 localisé, diminue progressivement jusqu'à

environ 53,9 % de la valeur initiale en 60 minutes. En outre, la surface active électrochimique (ECSA), qui serait réduite par le contact accru du N_2 avec l'électrocatalyseur, a également été comparée. Cela peut être déterminé par la capacité double couche (Cdl), et les données montrent que l'ECSA de l'électrode revêtue de P-WFeNC est en effet inférieure à celle de l'électrode revêtue de WFeNC (Figure 8.4 d). Les résultats ci-dessus donnent une indication supplémentaire que les molécules de N_2 peuvent être efficacement capturées dans l'électrode recouverte de P-WFeNC dans les conditions expérimentales réelles, donnant ainsi libre cours à l'électrocatalyseur hautement actif en fournissant un réactif N_2 abondant.

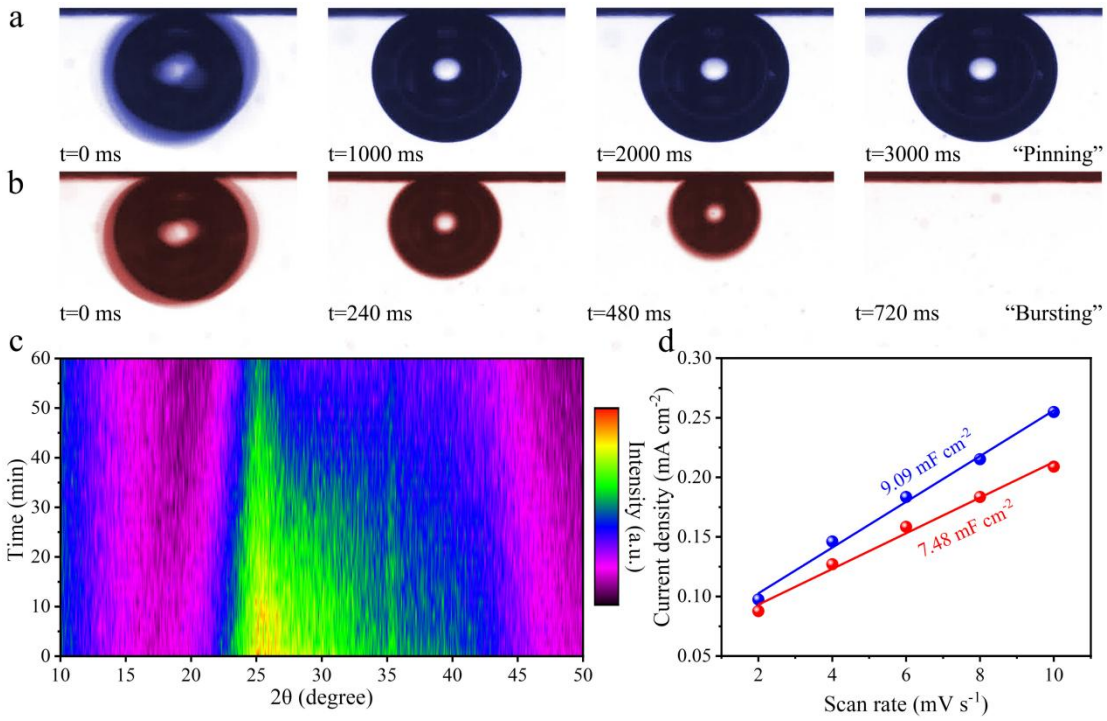

Figure 8.4 Une série d'images optiques montrant le processus de diffusion de N_2 à la surface de (a) WFeNC et (b) P-WFeNC mesuré par la méthode des bulles captives. (c) Cartes d'intensité XRD in situ de P-WFeNC sous test électrochimique en fonction du temps. (d) Courant de charge double couche comparé au taux de balayage CV pour différentes électrodes.

Compte tenu de l'effet bénéfique de la gravure au plasma sur le confinement de l'azote, les performances réelles du NRR du P-WFeNC et du WFeNC ont été évaluées dans 0, 1 M de HCl à l'aide d'une cellule électrochimique de type H étanche aux gaz dans des conditions ambiantes via des mesures de chronoampérométrie. Lors des mesures, un protocole expérimental strict a été suivi pour obtenir une vérification des performances fiables du NRR. Bien que NH_3 et N_2H_4

aient été examinés par méthode colorimétrique comme produits possibles de réduction de l'azote dans l'électrolyte, aucun sous-produit N_2H_4 n'a été trouvé dans cette étude. Les taux de rendement de NH_3 et les efficacités faradiques correspondantes à chaque potentiel donné de P-WFeNC et WFeNC sont présentés dans les figures 8.5 a et b. Sans un apport abondant d'azote gazeux, les performances NRR du WFeNC sont assez limitées, offrant le plus grand taux de rendement de NH_3 de 15,29 μg h^{-1} mg^{-1} à -0,3 V par rapport au RHE et le rendement faradique le plus élevé de 21,10 % à -0,2 V. contre RHE. Comme prévu, des performances NRR bien améliorées ont été obtenues par P-WFeNC, avec un taux de rendement de NH_3 de 35,24 μg h^{-1} mg^{-1} et une efficacité faradique correspondante de 53,99 % à -0,3 V par rapport au RHE, démontrant la supériorité du proposé. stratégie de confinement de l'azote. Plusieurs expériences de contrôle ont été réalisées pour s'assurer qu'il n'y avait aucun contaminant dans le système de test (Figure 8.5 c). Aucun ammoniac n'a été trouvé dans l'électrolyte lors de l'électrolyse du papier carbone nu dans un électrolyte saturé de N_2 à -0,3 V par rapport à RHE, de l'électrode revêtue de P-WFeNC dans un électrolyte saturé d'Ar à -0,3 V par rapport à RHE, ou du P- Électrode revêtue de WFeNC dans un électrolyte saturé en N_2 sous potentiel de circuit ouvert. En outre, des études de marquage isotopique ^{15}N ont été réalisées pour étudier la source de N du NH_3 produit. Comme le montre la figure 8.5 d, seul un signal doublet pour $^{15}NH_4^+$ est trouvé dans les spectres RMN ^1H lors de l'utilisation de $^{15}N_2$ comme gaz d'alimentation, ce qui est cohérent avec celui enregistré avec des solutions standards de $(^{15}NH_4)_2SO_4$. Les résultats ci-dessus confirment que le NH_3 obtenu dans l'électrolyte provient entièrement du processus électrochimique NRR et que les données électrochimiques peuvent donc s'avérer fiables. En comparaison avec les travaux les plus récents, ces performances NRR supérieures du P-WFeNC se classent au sommet de l'état de l'art (Figure 8.5 e). De plus, il peut maintenir ses performances exceptionnelles presque inchangées sous 10 cycles continus d'électrolyse NRR (Figure 8.5 f), révélant la robustesse du P-WFeNC.

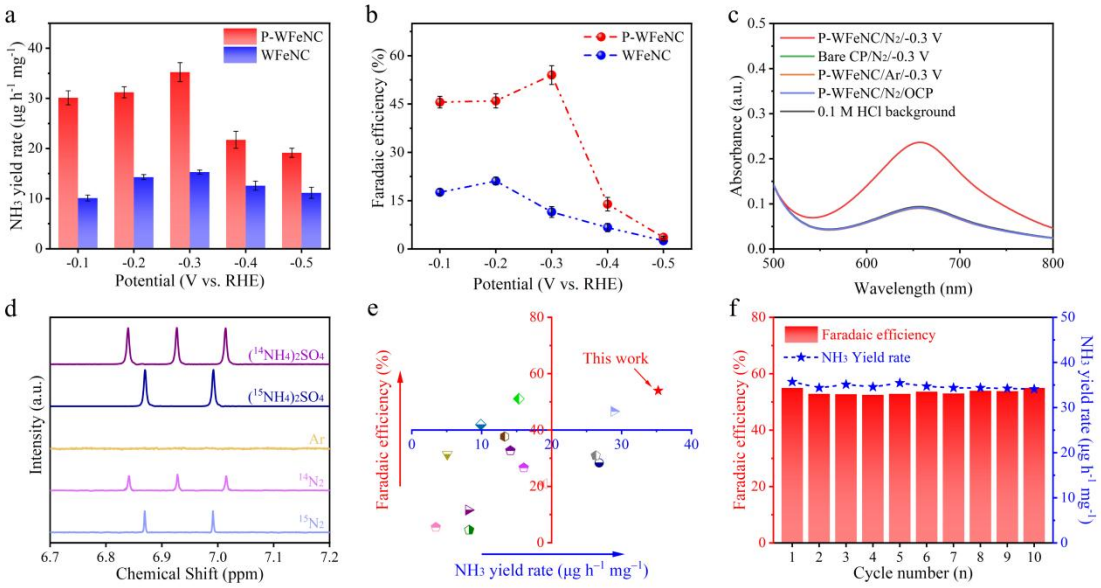

Figure 8.5 (a) Taux de rendement de NH_3 et (b) efficacités faradiques correspondantes de WFeNC et P-WFeNC à différents potentiels. (c) Les spectres d'absorption UV-visible des électrolytes dans différentes conditions. (d) Spectres RMN ^1H de l'électrolyte testé avec différents gaz d'alimentation. (e) Comparaison de nos résultats avec des électrocatalyseurs de pointe en termes de taux de rendement en NH_3 et d'efficacité faradique. (f) Les performances NRR du P-WFeNC dans le test de durabilité.

8.3.2 Catalyseur OENC avec promotion synergique d'électrons pour NRR

Dans ce travail, un effet de promotion électronique synergique est délibérément déclenché par le dopage de l'oxygène en tant qu'hétéroatome secondaire pour stimuler la synthèse d'ammoniac ambiant sur du carbone dopé à l'azote. La polymérisation du pyrrole peut être catalysée et régulée en ajoutant différentes quantités de peroxyde d'hydrogène, de sorte qu'il a été choisi comme source de carbone dans ce travail. Avec du polypyrrole normal ou du polypyrrole suroxydé comme précurseur, ainsi que du chlorure de sodium comme matrice, du carbone dopé à l'azote (NC) et du carbone dopé à l'azote (OENC) enrichi en oxygène ont été obtenus après la pyrolyse à haute température dans Ar et l'élimination du sel qui a suivi. par lavage aqueux. NC et OENC présentent toutes deux une morphologie de feuille froissée et ridée, comme l'indiquent les images de microscopie électronique à balayage (MEB) et de microscopie électronique à transmission (TEM) (Figure 8.6 a et b), ce qui contribue à une exposition considérablement améliorée des sites actifs aux réactifs et donc la formation d'une grande région de réaction triphasée. Les images de cartographie élémentaire correspondantes

suggèrent des éléments C, N et O uniformément distribués au sein de l'OENC (Figure 8.6 c), indiquant l'intégration suffisante de l'oxygène et de l'azote dans la matrice de carbone.

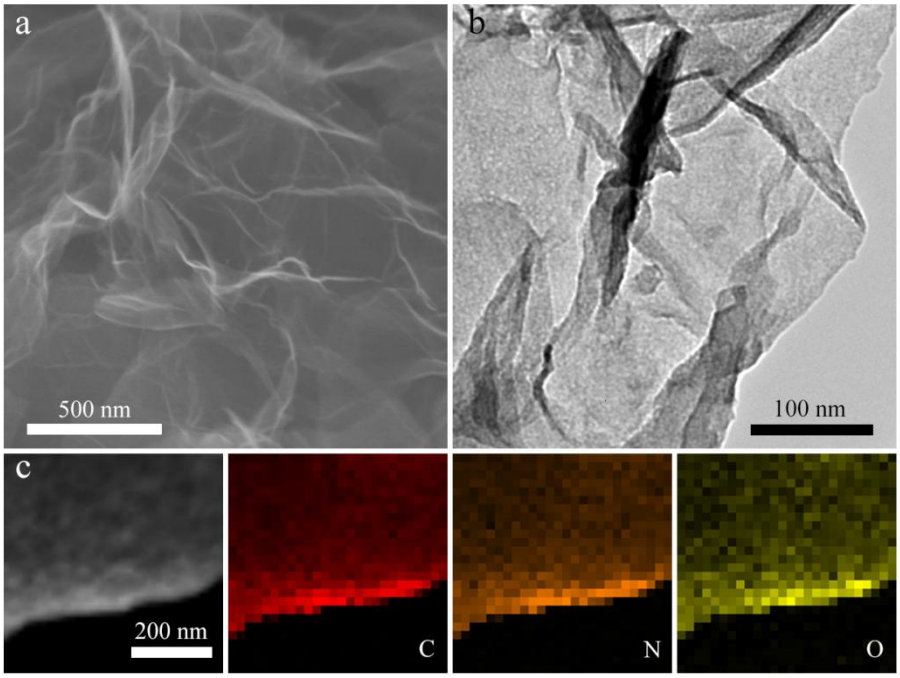

Figure 8.6 (a) Image de microscopie électronique à balayage, (b) image de microscopie électronique à transmission et (c) images de cartographie élémentaire correspondantes de l'OENC.

La diffraction des rayons X sur poudre (XRD) et l'analyse Raman ont ensuite été réalisées pour caractériser le produit carbonisé. Comme le montre la figure 8.7 a, pour NC et OENC, les deux larges pics de diffraction dans les diagrammes XRD peuvent être attribués respectivement aux plans (002) et (100) du carbone graphité, qui représentent les propriétés typiques des matériaux carbonés avec faible degré graphique. Ces deux matériaux présentent également des bandes D et G évidentes dans les spectres Raman (Figure 8.7 b). La bande G représente la vibration dans le plan des structures de carbone sp^2 tandis que la bande D représente les défauts du réseau graphitique, à savoir respectivement la cristallinité et le désordre. Le rapport d'intensité de la bande D et de la bande G (I_D/I_G) augmente de 0,93 pour NC à 1,05 pour OENC, suggérant des domaines de structure graphitique plus désordonnés dans cette dernière induits par la présence d'oxygène enrichi. Par la suite, la nature chimique et la structure des liaisons de différentes structures ont été étudiées par spectroscopie photoélectronique à rayons X (XPS). Les pics C 1s, N 1s et O 1s peuvent être capturés à la fois en NC et en OENC, avec une teneur

en O beaucoup plus élevée de 8,89 at. % en OENC (Figure 8.7 c). Les spectres C 1s haute résolution étaient composés de cinq pics relatifs au sp^2 C du plan basal, au défaut sp^3 C, C-O, C = O et π-π*. Les spectres N 1s haute résolution de NC et OENC sont constitués de quatre pics caractéristiques correspondant au N graphitique, au N pyrrolique, au N pyridinique et aux N-oxydes (Figure 8.7 d). Notamment, l'analyse quantitative des teneurs en N et la déconvolution de ces quatre pics ne montrent pas de différence évidente entre NC et OENC, confirmant que l'oxygène enrichi n'influencerait pas les dopants N. Quant aux spectres O 1s à haute résolution, ils peuvent être déconvolués en trois pics attribuables à l'oxygène physiquement adsorbé, aux groupes C = O cétoniques et aux groupes C-O (hydroxyle et époxyde) (Figure 8.7 e). De toute évidence, avec le polypyrrole suroxydé comme précurseur, les groupes C = O et C-O augmentent de manière significative en OENC par rapport à NC, ce qui adapterait efficacement la structure électronique du carbone dopé à l'azote et apporterait une contribution synergique à l'activité catalytique des sites actifs. D'après les isothermes d'adsorption-désorption de N_2 de la figure 8.7 f, OENC possède également une grande surface spécifique déterminée par le modèle Brunauer-Emmett-Teller (BET) avec une structure hiérarchiquement poreuse, qui correspond bien à la morphologie de sa feuille et est bénéfique pour l'exposition de sites actifs ainsi que la facilitation du transfert de masse pour un NRR efficace.

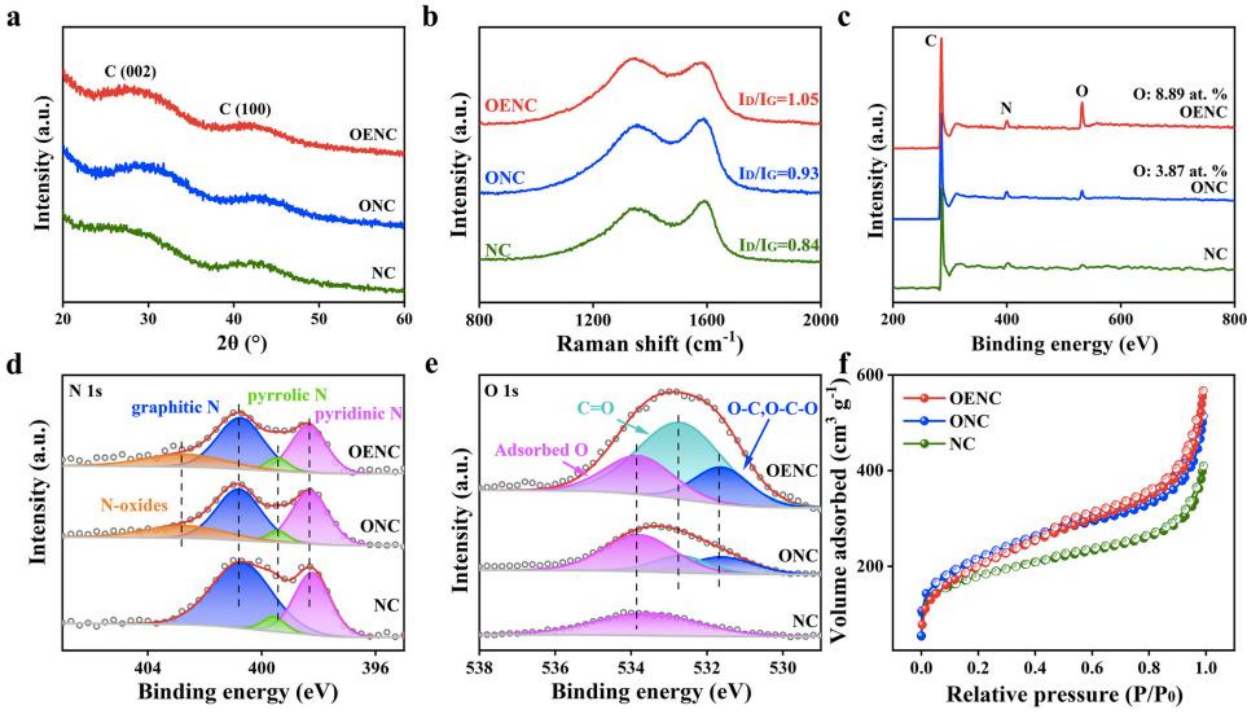

Figure 8.7 (a) Modèles XRD et (b) Spectres Raman de OENC et NC. (c) Les spectres XPS d'enquête d'OENC et de NC. (d) Spectres N 1s à haute résolution et (e) spectres O 1s à haute résolution e l'OENC, de l'ONC et du NC. (f) Isothermes de sorption N_2 de l'OENC, de l'ONC et du NC.

Les performances NRR réelles de OENC et NC ont été évaluées dans 0, 1 M de HCl en utilisant une cellule électrochimique de type H étanche aux gaz dans des conditions ambiantes. Pour obtenir une vérification des données NRR fiables, un protocole expérimental strict a été suivi et toutes les contaminations provenant de l'installation électrochimique ou du gaz d'alimentation ont été exclues. Des mesures chronoampérométriques ont été effectuées pour réaliser une analyse quantitative de la production d'ammoniac (Figure 8.8 a), et les produits possibles de réduction de l'azote, notamment NH_3 et N_2H_4, ont été examinés respectivement par la méthode au bleu d'indophénol et la méthode de Watt et Chrisp. Notamment, aucun sous-produit N_2H_4 n'a été détecté ici dans cette étude. La valeur moyenne des taux de rendement de NH_3 et les FE correspondants de OENC et NC sont comparés dans les figures 8.8 b et c. De toute évidence, le catalyseur OENC présente de meilleures performances catalytiques à tous les potentiels appliqués par rapport au catalyseur NC. Le taux de rendement maximisé de NH_3 pour OENC est déterminé à 67,3 μg h^{-1} mg^{-1} à -0,2 V par rapport à RHE, bien supérieur à celui de NC (34,4 μg h^{-1} mg^{-1}). Simultanément, le FE le plus élevé de 36,2 % est également atteint à -0,2 V par rapport à RHE, supérieur à NC (17,6 %). Lorsque le potentiel appliqué descend en dessous de -0,2 V par rapport au RHE, le taux de rendement du NH_3 et du FE diminuent en raison de l'augmentation du HER compétitif (Figure 8.8 d). En comparaison avec les travaux les plus récents, les performances NRR supérieures de l'OENC sans métal sont supérieures à celles de la plupart des électrocatalyseurs rapportés, y compris les catalyseurs à base de métaux nobles, les catalyseurs à base de métaux non nobles et les catalyseurs sans métal (Figure 8.8 e). De plus, ces performances exceptionnelles ont été examinées plus en détail par des expériences de durabilité à -0,2 V par rapport au RHE, dans lesquelles ni le taux de rendement de l'ammoniac ni le FE ne montrent aucune détérioration marquée sous 10 cycles continus d'électrolyse NRR (Figure 8.8 f), confirmant la robustesse stabilité de l'OENC pour le NRR électrochimique.

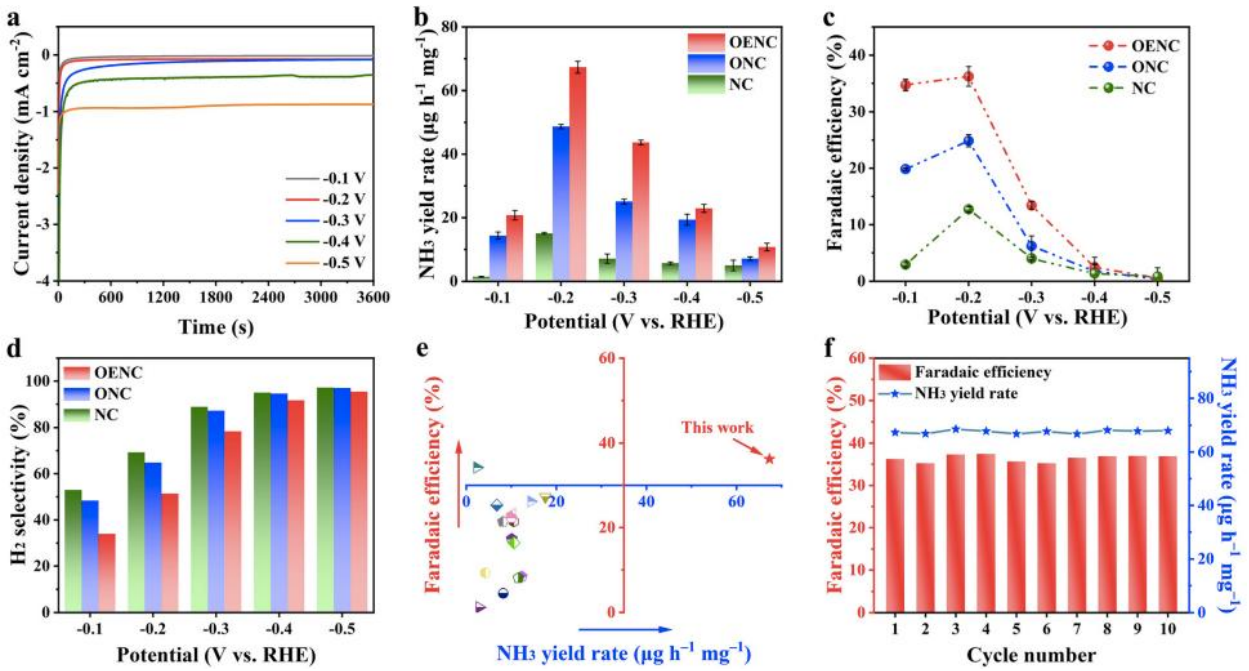

Figure 8.8 (a) Résultats de chronoampérométrie de l'OENC testé dans 0,1 M HCl à différents potentiels appliqués. (b) Taux de rendement en NH_3, (c) efficacités faradiques correspondantes et (d) sélectivité H_2 de OENC et NC mesurée à tous les potentiels donnés. (e) Taux de rendement en NH_3 et efficacité faradique de l'OENC par rapport à d'autres technologies de pointe; des données détaillées sont fournies dans le tableau 5.1. (f) La performance NRR dans le test de durabilité de l'OENC.

Une série d'expériences complémentaires et contrôlées ont été réalisées pour vérifier la fiabilité des données électrochimiques. Tout d'abord, le papier carbone nu (CP) a été électrolysé dans un électrolyte saturé de N_2 à -0,2 V par rapport à RHE, tandis que l'électrode revêtue d'OENC a été électrolysée dans un électrolyte saturé d'Ar à -0,2 V par rapport à RHE ou un électrolyte saturé de N_2 sous potentiel de circuit ouvert. Les résultats suggèrent qu'aucun ammoniac n'a été détecté ni par la méthode au bleu d'indophénol ni par les spectres de résonance magnétique nucléaire (RMN) ^1H (Figure 8.9 a). Par la suite, des expériences de marquage isotopique ^{15}N ont été menées pour étudier plus en détail la source d'azote de l'ammoniac produit. Aucun ammoniac ne peut être détecté sous potentiel de circuit ouvert lors de l'utilisation de $^{15}N_2$ comme gaz d'alimentation, tandis qu'un taux de rendement de NH_3 de 66,0 μg h^{-1} mg^{-1} et un FE de 37,2 % ont été obtenus à -0,2 V par rapport au RHE par la méthode au bleu d'indophénol. (Figure 8.9 b). De plus, contrairement au cas des expériences ^{14}NRR, seul un signal doublet pour $^{15}NH_4^+$ est trouvé dans le spectre RMN ^1H de l'électrolyte, ce qui est cohérent avec celui obtenu avec des solutions standards de $(^{15}NH_4)_2SO_4$ (Figure 8.9 c). De plus, après analyse quantitative, le taux de rendement de NH_3 et le FE correspondent bien à ceux

obtenus dans les expériences ^{14}NRR, soit par la méthode au bleu d'indophénol, soit par la méthode RMN ^{1}H (Figure 8.9 d). Tous les résultats ci-dessus prouvent clairement que le NH_3 produit provient entièrement du processus électrochimique NRR, prouvant ainsi de manière convaincante la fiabilité des données électrochimiques.

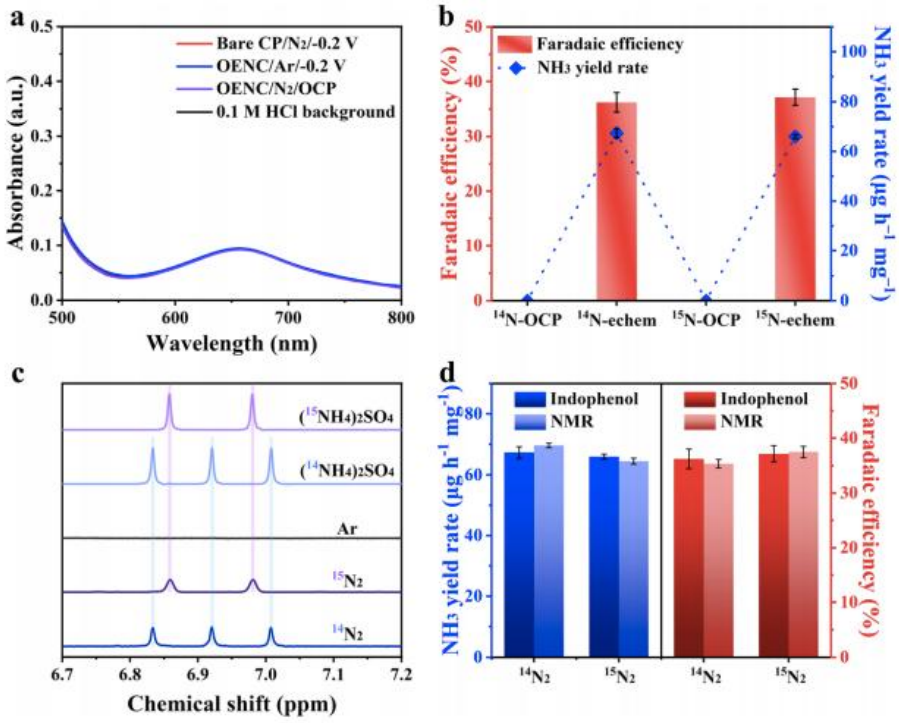

Figure 8.9 (a) Les spectres d'absorption UV-visible des électrolytes dans différentes conditions. (b) Comparaison du taux de rendement de NH_3 et de l'efficacité faradaïque en utilisant différents gaz d'alimentation pour NRR à -0,2 V par rapport au RHE et au potentiel de circuit ouvert. (c) Spectres RMN ^{1}H des produits NRR utilisant différents gaz d'alimentation. (d) Comparaison du taux de rendement de NH_3 et de l'efficacité faradaïque en utilisant différents gaz d'alimentation pour NRR à -0,2 V par rapport au RHE, soit par méthode colorimétrique ou RMN.

Pour mieux comprendre les mécanismes de réaction impliqués du NRR sur l'OENC, des calculs DFT ont été effectués pour étudier les profils d'énergie libre, y compris la voie distale et la voie alternée. Habituellement, l'azote présente une forte énergie de liaison, un large écart énergétique entre l'orbitale moléculaire occupée la plus élevée et l'orbitale moléculaire inoccupée la plus basse, ainsi qu'un potentiel d'ionisation élevé, de sorte que sa chimisorption est considérée comme l'étape déterminante du taux (RDS). Des rapports antérieurs ont indiqué que le carbone dopé à l'azote avec une structure électronique modifiée et une polarisation de

charge pourrait faciliter l'adsorption de l'azote. En effet, pour la NC, la barrière de chimisorption de l'azote a été éliminée avec succès, ce qui se transforme en une étape exothermique. Malheureusement, en tant que réactions électrochimiques en plusieurs étapes, le processus NRR est plus qu'une simple adsorption, mais également un clivage et une hydrogénation de l'azote. Autrement dit, une performance NRR supérieure est le résultat de l'action combinée de toutes les étapes. Pour NC, malgré l'élimination de la barrière de chimisorption de l'azote, le procédé NRR souffre toujours de barrières énergétiques élevées de 1,92 eV lors de l'hydrogénation de $*N_2$ en *NNH comme RDS dans la voie alternée ou 3,38 eV lors de l'hydrogénation de $*NNH_2$ en * N + NH_3 comme RDS dans la voie distale. L'introduction de l'oxygène en tant qu'hétéroatome secondaire pourrait optimiser davantage la structure électronique des sites actifs, déclenchant ainsi l'effet synergique de promotion électronique pour stimuler le processus NRR. Comme prévu, la barrière réactionnelle est considérablement réduite à 1,14 eV, avec l'hydrogénation de $*NH_2$ + NH_3 en * + $2NH_3$ comme RDS. Les calculs théoriques rationalisent bien les expériences électrochimiques, et soulignent ainsi la supériorité du dopage à l'oxygène vers le NRR sur le carbone dopé à l'azote.

8.3.3 Rompre les relations d'échelle dans NRR avec le catalyseur FeCoNC

Les atomes de Fe uniques isolés ancrés sur du carbone dopé à l'azote (FeNC) sont bien connus pour offrir un certain degré de performances NRR et sont choisis comme SAC de preuve de concept dans ce travail. Il a également été rapporté que les atomes uniques de Co peuvent servir de sites actifs pour l'adsorption et la dissociation du N_2, c'est pourquoi ils ont été choisis comme deuxième métal ici pour assembler les dimères asymétriques Fe-Co ancrés sur du carbone dopé à l'azote (FeCoNC). Des calculs théoriques ont d'abord été effectués pour explorer les avantages des sites hétérobimétalliques asymétriques par rapport aux sites uniques. Les configurations proposées de FeNC et FeCoNC sont présentées dans les figures 8.10 a et b. Le potentiel électrostatique des sites hétérobimétalliques dans FeCoNC présente clairement une distribution de charge asymétrique (Figure 8.10 c), ce qui est bénéfique pour polariser le N_2 adsorbé et affaiblit ainsi la liaison N≡N. La différence de densité électronique après l'absorption de l'azote par FeNC et FeCoNC est comparée pour donner une compréhension approfondie des avantages des sites hétérobimétalliques. Le N_2 adsorbé sur la configuration FeNC ($*N_2$@FeNC) correspond au modèle d'extrémité ayant un atome de N se liant au site Fe (Figure 8.10 d), tandis que le N_2 adsorbé sur la configuration FeCoNC ($*N_2$@FeCoNC) appartient à la motif latéral avec les deux atomes de N se liant simultanément

aux dimères (Figure 8.10 e). Les sites d'atomes uniques et les sites bimétalliques avec des orbitales d vides sont capables d'accepter des électrons d'azote en paire isolée par don σ, puis de les redonner aux orbitales antiliantes de la molécule adsorbée avec des électrons d partiellement remplis via un rétrodon π. Cependant, différentes structures montrent des comportements différents. Pour $*N_2$@FeNC avec motif d'extrémité, un seul électron de paire isolée du côté adsorbé de la molécule d'azote peut être piégé par l'orbitale d vide du site unique de l'atome de Fe, de sorte que l'interaction électronique entre N_2 et FeNC soit plutôt limité. Dans le même temps, le N_2 adsorbé subit un allongement de la liaison N≡N de seulement 0,022 Å par rapport à la distance calculée pour une molécule de N_2 libre (1,154 Å) (Figure 8.10 f). Au contraire, les atomes de Fe et de Co dans les sites bimétalliques avec deux orbitales d occupées peuvent simultanément piéger deux électrons libres aux deux extrémités de la molécule d'azote, comme le confirme une plus forte accumulation et un appauvrissement électronique observés dans le $*N_2$@FeCoNC. Combinée à l'allongement de la longueur de la liaison N≡N à 1,214 Å, l'activation maximisée pour les étapes d'hydrogénation suivantes est ainsi démontrée.

Par la suite, les diagrammes d'énergie libre pour NRR sur FeNC et FeCoNC ont été calculés davantage par DFT pour déterminer si les sites hétérobimétalliques asymétriques pouvaient effectivement rompre les relations d'échelle limitées par le site métallique unique. Les mécanismes NRR proposés, y compris la voie distale et la voie alternée, ont été pris en compte ici. Pour le système de FeNC suivant la voie alternée, le RDS du NRR est l'hydrogénation de $*H_2NNH_2$ en $*NH_2 + NH_3$, avec une valeur ΔG de 0,79 eV (Figure 8.10 g). Comme prévu, ce RDS peut être radicalement favorisé par le site pont de FeCoNC avec une valeur ΔG implémentable de 0,43 eV. En ce qui concerne la voie distale, une plus grande barrière énergétique du RDS de l'hydrogénation de $*NNH_2$ en $*N + NH_3$ doit être surmontée, ce qui n'est donc pas pris en compte ici. Dans l'ensemble, les résultats ci-dessus révèlent que les sites hétérobimétalliques asymétriques présentant la surface polarisée permettent une activation maximisée de l'azote et contribuent à réduire considérablement la barrière énergétique du processus global de réduction de l'azote, offrant ainsi un grand potentiel pour servir d'électrocatalyseur pour le NRR.

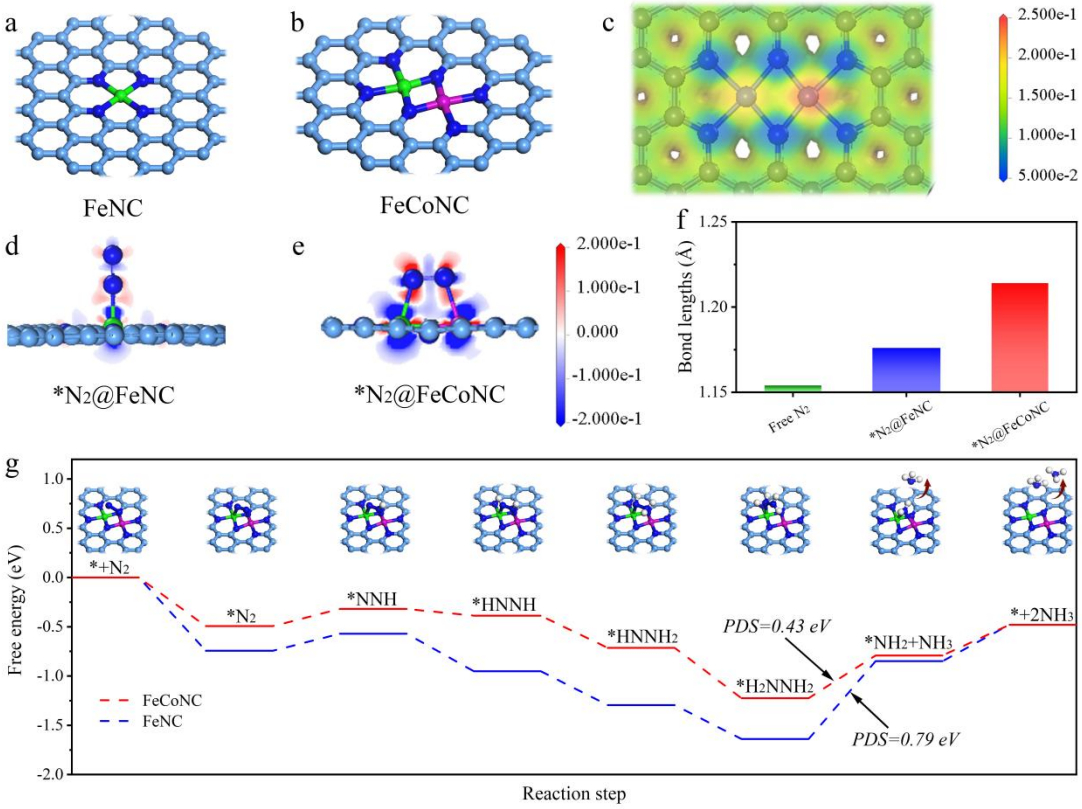

Figure 8.10 Configurations de (a) FeNC et (b) FeCoNC. (c) Le potentiel électrostatique de FeCoNC. La différence de densité électronique après l'azote adsorbé par (d) FeNC et (e) FeCoNC. (f) Comparaison de la longueur de la liaison azote après adsorption sur le site actif correspondant. (g) Énergie libre de synthèse d'ammoniac sur FeCoNC et FeNC par la voie alternée.

Inspirés par des calculs théoriques, FeNC et FeCoNC ont été synthétisés pour évaluer et comparer expérimentalement les performances du NRR. Des atomes doubles Fe/FeCo immobilisés sur des nanosphères de carbone creuses dopées au N ont été préparés par pyrolyse optimisée d'un complexe de coordination polypyrrole-métal. Les images de microscopie électronique à balayage (MEB) et de microscopie électronique à transmission (TEM) montrent que les catalyseurs FeCoNC et FeNC présentent la structure sphérique d'ouverture (Figure 8.11 a et b). Les images cartographiques de FeCoNC montrent que Fe, Co, C et N étaient répartis uniformément sur toute l'architecture (Figure 8.11 c). Une telle morphologie est propice à l'exposition des sites actifs catalytiques pour le NRR, comme le confirment la surface de Brunauer-Emmett-Teller et la surface active électrochimique calculée par la capacité double couche. La microscopie électronique à transmission à balayage sur champ sombre annulaire à grand angle et corrigée des aberrations (AC-HAADF-STEM) a

ensuite été réalisée pour élucider la forme existentielle des atomes de Fe et de Co (Figure 8.11 d). Comme prévu, des petits points doubles brillants répartis de manière homogène et marqués de cycles rouges sont observés dans le substrat de carbone, qui peuvent être attribués aux atomes lourds de Fe et de Co plutôt qu'aux atomes légers de C, N et O.

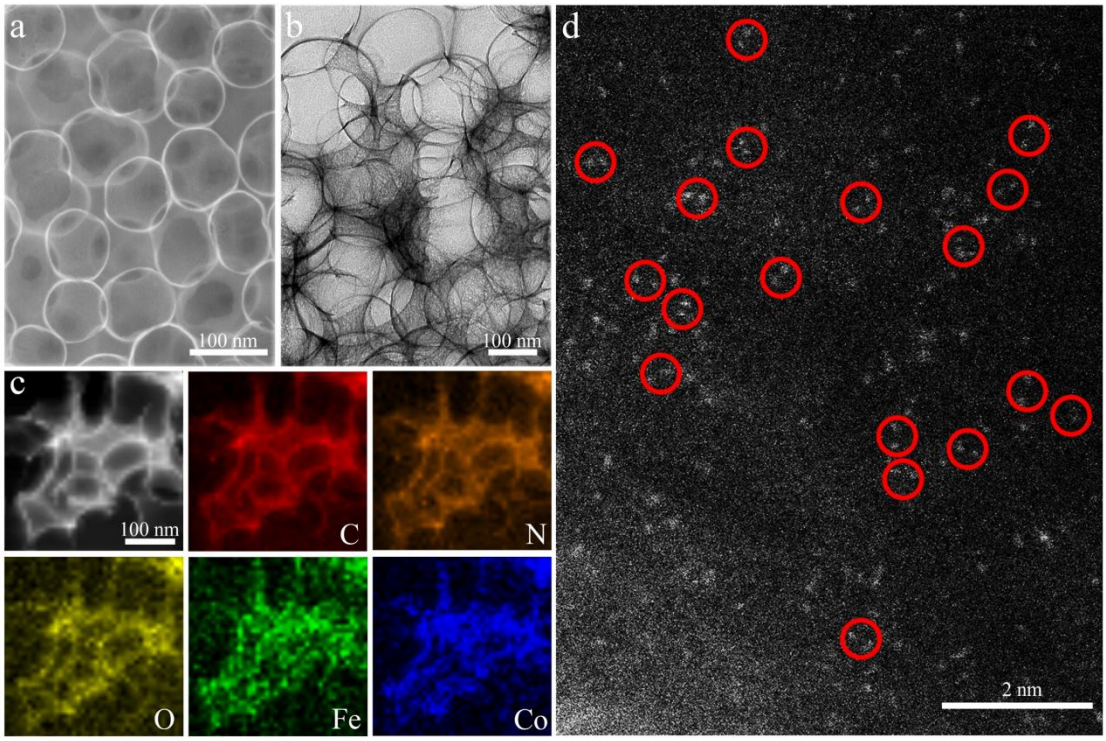

Figure 8.11 (a) Image de microscopie électronique à balayage, (b) image de microscopie électronique à transmission et (c) cartographies d'éléments de FeCoNC. (d) Image de microscopie électronique à transmission par balayage à champ sombre annulaire à grand angle corrigée des aberrations de FeCoNC.

Les diagrammes de diffraction des rayons X sur poudre (DRX) de FeCoNC et FeNC présentent tous deux un large pic attribué au plan (002) du carbone graphitique, sans pic de diffraction net attribuable aux espèces métalliques à base de Fe ou de Co capturées (Figure 8.12 a). La structure de graphitisation peut également être vérifiée par la valeur I_D/I_G dans les spectres Raman (Figure 8.12 b). Des analyses de structure proche d'absorption des rayons X (XANES) et de structure fine d'absorption étendue des rayons X (EXAFS) ont ensuite été effectuées pour FeCoNC, avec une feuille de Fe et une feuille de Co comme références, afin de confirmer davantage sa structure au niveau atomique. Quel que soit le spectre XANES du bord Fe K ou du bord Co K, le bord d'absorption de FeCoNC se situe à une énergie plus positive que celle de

la feuille de Fe ou de la feuille de Co (Figure 8.12 c et d), indiquant que les états de valence de Fe et Co dans le centre actif hétéronucléaire sont positifs. Le pic important à 1, 47 Å dans le spectre EXAFS du bord Fe K confirme la présence d'une coordination Fe-N (Figure 8.12 e). De plus, le pic caractéristique correspondant aux liaisons métalliques Fe-Fe est absent, confirmant son absence dans FeCoNC. De même, le pic EXAFS du bord Co K observé à 1, 38 Å peut être attribué à la liaison Co-N, et le pic Co-Co n'a pas été détecté. Notamment, un chemin métal-métal évident à 2,02 Å est observé, confirmant la présence d'une liaison Fe-Co (Figure 8.12 f). Selon l'analyse ci-dessus, on pourrait conclure que les sites doubles FeCo sont atomiquement dispersés dans FeCoNC pour servir de centres actifs NRR efficaces.

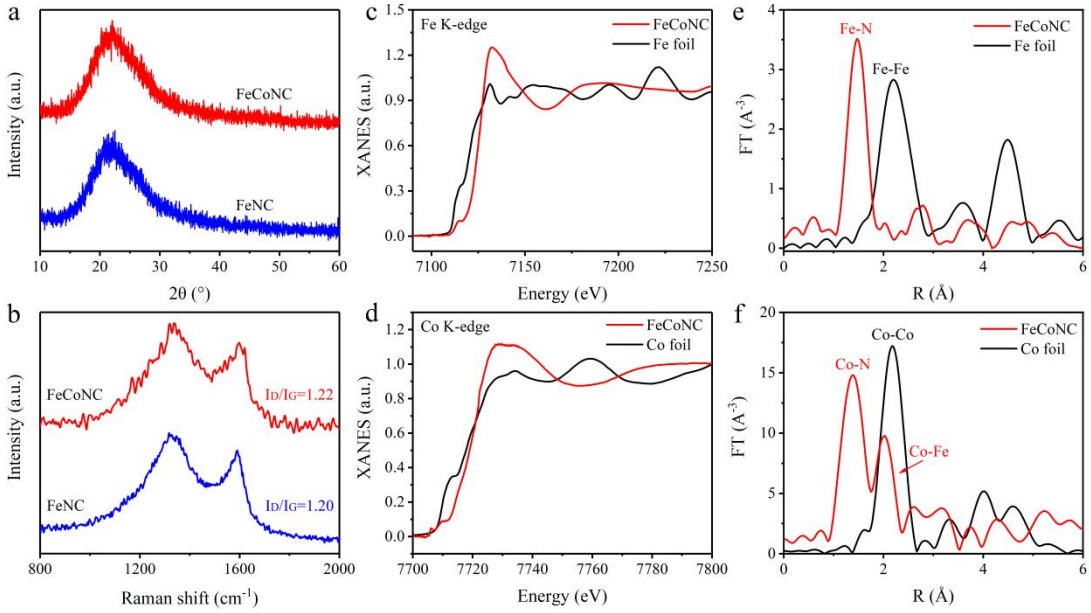

Figure 8.12 (a) Modèle XRD et (b) Spectres Raman de FeCoNC et FeNC. (c) Spectres de structure proche du bord d'absorption des rayons X (XANES) de FeCoNC et de feuille de Fe. (d) Spectres XANES des feuilles FeCoNC et Co. (e) Spectres étendus de structure fine d'absorption des rayons X (EXAFS) au bord Fe K de FeCoNC et de la feuille de Fe. (f) Spectres EXAFS au bord Co K de la feuille FeCoNC et Co.

Les performances NRR réelles de FeCoNC et FeNC ont ensuite été évaluées dans 0, 1 M de HCl en utilisant une cellule électrochimique de type H étanche aux gaz dans des conditions ambiantes. Un protocole expérimental strict a été suivi pour obtenir une vérification des performances fiables du NRR pendant les mesures, et toutes les contaminations provenant du gaz d'alimentation ou de l'installation électrochimique ont été exclues. L'analyse quantitative de la production d'ammoniac a été réalisée via des mesures chronoampérométriques (Figure 8.13

a). Le NH_3 et le N_2H_4, en tant que produits possibles de réduction de l'azote, ont été examinés par méthode colorimétrique, alors qu'aucun sous-produit N_2H_4 n'a été trouvé dans cette étude. La valeur moyenne du taux de rendement en ammoniac et l'efficacité faradique correspondante de FeCoNC et FeNC sont présentées sur les figures 8.13 b et c. De toute évidence, comparé au FeNC, le catalyseur FeCoNC présente de meilleures performances catalytiques à tous les potentiels appliqués. À -0,2 V par rapport au RHE, le taux de rendement maximisé en ammoniac pour FeCoNC est déterminé à 70,11 μg h^{-1} mg^{-1}, avec une efficacité faradique de 32,16 %, bien supérieure à celle de FeNC (37,43 μg h^{-1} mg^{-1} et 17,19 %). Avec le potentiel appliqué se déplaçant en dessous de -0,2 V par rapport au RHE, le taux de rendement du NH_3 et l'efficacité faradique diminuent, ce qui peut être attribué à l'augmentation du HER compétitif (Figure 8.13 d). Ces performances exceptionnelles ont été examinées plus en détail par un test de stabilité à -0,2 V par rapport au RHE, dans lequel ni le taux de rendement en ammoniac ni l'efficacité faradique ne présentent aucune détérioration marquée sous 10 cycles continus d'électrolyse NRR (Figure 8.13 e), confirmant la robustesse de FeCoNC. De plus, en comparaison avec les travaux les plus récents, les performances NRR supérieures de FeCoNC se classent au sommet de l'état de l'art (Figure 8.13 f et Tableau 6.1).

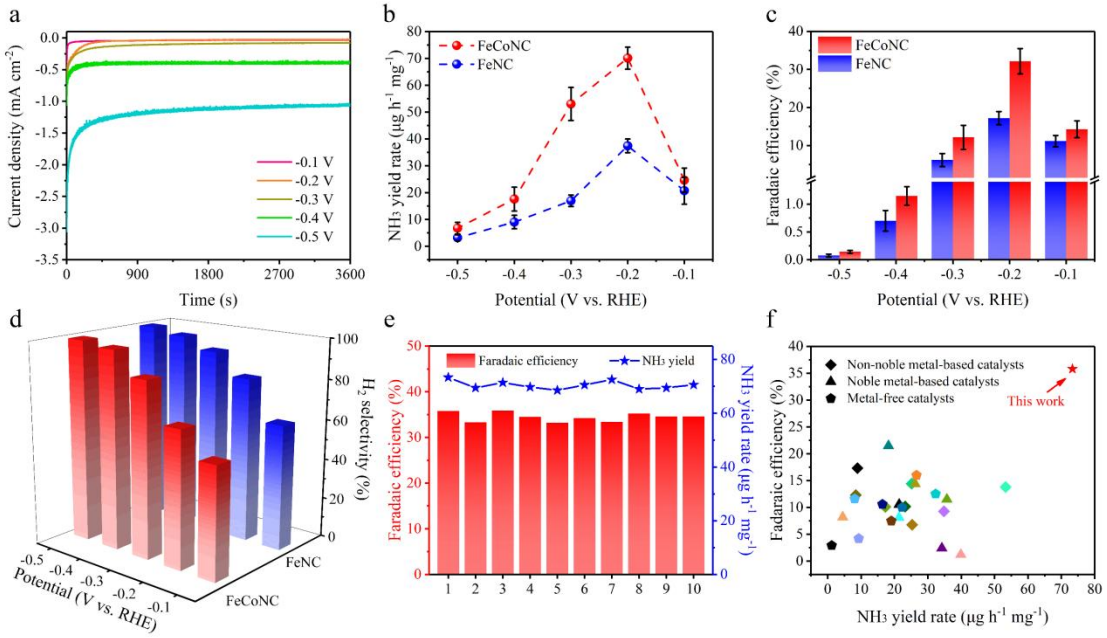

Figure 8.13 (a) Résultats de chronoampérométrie de FeCoNC testés dans la cellule H avec 0,1 M HCl à différents potentiels appliqués. (b) Taux de rendement en NH_3, (c) efficacités faradiques correspondantes et (d) sélectivité H_2 de FeNC et FeCoNC mesurée à tous les potentiels donnés. (e) Les performances de production de NH_3 dans le test de durabilité du FeCoNC. (f) Taux de rendement en NH_3 et efficacité faradique

de FeCoNC par rapport à d'autres technologies de pointe; des données détaillées sont fournies dans le tableau 6.1.

Plusieurs expériences de contrôle ont été réalisées pour vérifier la fiabilité des données électrochimiques. Lors de l'électrolyse du papier carbone nu (CP) dans du HCl 0,1 M saturé de N_2 à -0,2 V par rapport au RHE, de l'électrode recouverte de FeCoNC dans du HCl 0,1 M saturé d'Ar à -0,2 V par rapport au RHE, ou de l'électrode revêtue de FeCoNC dans du HCl 0,1 M saturé en N_2 sous potentiel de circuit ouvert, aucun ammoniac n'a été détecté ni par la méthode colorimétrique ni par la méthode de résonance magnétique nucléaire (RMN) ^1H (Figure 8.14 a). Par la suite, des études de marquage isotopique ^{15}N ont été réalisées pour étudier la source de N de l'ammoniac produit. Lors de l'utilisation de $^{15}N_2$ comme gaz d'alimentation, aucun ammoniac ne peut être détecté sous potentiel de circuit ouvert, tandis qu'un taux de rendement d'ammoniac de 70,09 μg h^{-1} mg^{-1} et un rendement faradique de 33,26 % ont été obtenus à -0,2 V par rapport au RHE par l'indophénol. méthode bleue (Figure 8.14 b). De plus, dans les spectres RMN ^1H, seul un signal doublet pour $^{15}NH_4^+$ est trouvé dans l'électrolyte, ce qui est cohérent avec celui enregistré avec les solutions standards de $(^{15}NH_4)_2SO_4$ (Figure 8.14 c). Après analyse quantitative, le taux de rendement en ammoniac et l'efficacité faradaïque sont cohérents avec ceux obtenus dans les expériences ^{14}NRR, soit par la méthode colorimétrique, soit par la méthode RMN ^1H (Figure 8.14 d), prouvant de manière convaincante que le NH_3 produit provient entièrement du processus NRR.

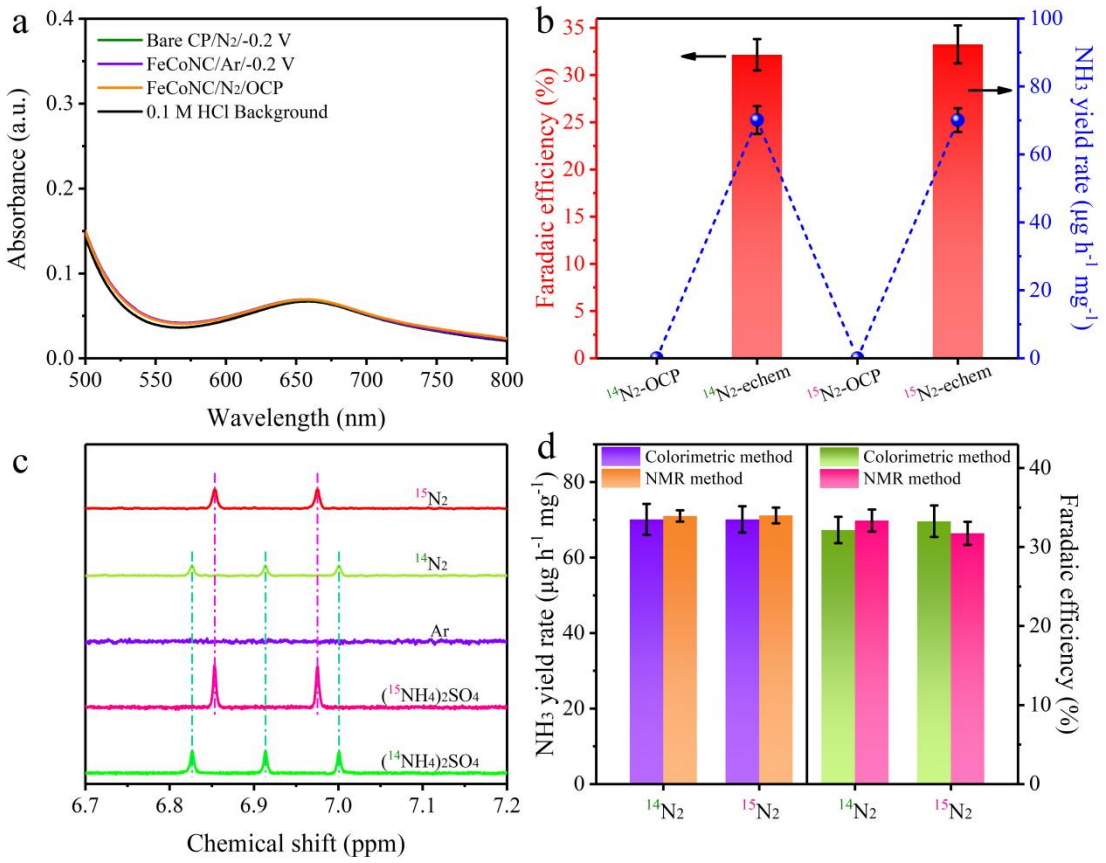

Figure 8.14 (a) Les spectres d'absorption UV-visible des électrolytes dans différentes conditions. (b) Comparaison du taux de rendement de NH_3 et de l'efficacité faradique en utilisant différents gaz d'alimentation pour NRR à -0,2 V par rapport au RHE et au potentiel de circuit ouvert. (c) Spectres RMN ^1H des produits NRR utilisant différents gaz d'alimentation. (d) Comparaison du taux de rendement de NH_3 et de l'efficacité faradaïque en utilisant différents gaz d'alimentation pour NRR à -0,2 V par rapport au RHE, soit par méthode colorimétrique ou RMN.

8.4 Conclusions et perspectives

8.1 Conclusions

Dans cet article, nous nous concentrons sur la synthèse de différents matériaux catalytiques de nitrure de carbone coordonnés par éléments, du carbone basique dopé à l'azote (NC) au carbone dopé à l'azote (OENC) riche en oxygène, avec un seul atome de Fe ancré dans du carbone dopé à l'azote. carbone (FeNC), des dimères asymétriques Fe-Co ancrés sur du carbone dopé à l'azote (FeCoNC) et des amas de tungstène et des atomes de Fe uniques ancrés sur du carbone dopé à l'azote (WFeNC). Nous avons testé les différences de performances de différents catalyseurs et étudié pourquoi ils peuvent montrer un rendement en

NH_3 et une efficacité Faradaïque aussi excellents grâce à la DRX in situ, aux calculs théoriques, aux simulations moléculaires, au BET et à d'autres technologies.

Partie I: La réaction électrocatalytique de réduction de l'azote (NRR) recèle un grand potentiel pour la synthèse de l'ammoniac vert et a suscité l'intérêt de la communauté scientifique. Cependant, l'apport restreint d'azote à l'interface de réaction a toujours été le principal problème non résolu, laissant les performances réelles beaucoup à désirer, même pour l'électrocatalyseur hautement actif avec une barrière de réaction très réduite. Ici, une stratégie de confinement de l'azote réalisée par gravure au plasma est proposée pour relever ce défi, en fournissant un apport abondant d'azote pour stimuler la synthèse d'ammoniac dans des conditions ambiantes. Trois nouveautés sont rapportées dans ce travail:

1. Lors de la gravure au plasma, un grand nombre de vides peuvent être construits in situ dans le plan basal du catalyseur pour servir de réservoirs aux nanobulles d'azote.
2. Les nanobulles peuvent être efficacement attirées par l'hétérogénéité de surface induite par les défauts, car elles pourraient générer des interactions de Van der Waals entre l'électrocatalyseur et l'azote, et capturées par les vides.
3. Comme prévu, le catalyseur gravé au plasma de preuve de concept offre un taux de rendement en ammoniac supérieur de 35,24 μg h^{-1} mg^{-1} et une efficacité faradique exceptionnelle de 53,99 % à -0,3 V par rapport à une électrode à hydrogène réversible.

Partie II: La réaction électrocatalytique de réduction de l'azote (NRR) en tant qu'approche alternative au procédé Haber-Bosch, à forte intensité énergétique, pour la synthèse artificielle de l'ammoniac a suscité une grande attention. Des rapports antérieurs ont suggéré qu'un électrocatalyseur sans métal, tel que le carbone dopé à l'azote présentant une structure électronique modifiée et une polarisation de charge, est capable d'éliminer la barrière de chimisorption de l'azote et de réaliser une synthèse d'ammoniac avec une certaine performance. Cependant, le processus NRR ne se limite pas à l'adsorption, mais également au clivage et à l'hydrogénation ultérieurs de l'azote, qui posent encore de grands défis. Ici, nous relevons ce défi en dopant l'oxygène dans du carbone dopé à l'azote. Trois nouveautés sont rapportées dans ce travail:

1. En dopant l'oxygène dans du carbone dopé à l'azote en tant qu'hétéroatome secondaire, un effet de promotion électronique synergique est déclenché pour stimuler la synthèse d'ammoniac ambiant.

2. La structure électronique et la polarité des atomes de carbone adjacents sont encore optimisées, réduisant considérablement la barrière énergétique du processus global de réduction de l'azote.
3. Comme prévu, le catalyseur au carbone dopé à l'azote et enrichi en oxygène de preuve de concept offre des performances bien améliorées par rapport à son homologue, avec un taux de rendement en ammoniac de 67,3 μg h^{-1} mg^{-1} et une efficacité faradique correspondante. de 36,2 % à -0,2 V par rapport à une électrode à hydrogène réversible.

Partie III: La réaction électrochimique de réduction de l'azote (NRR) par utilisation d'électricité renouvelable est une méthode intéressante pour la production durable d'ammoniac. Cependant, en raison de son essence intrinsèque en tant que réaction multi-intermédiaire, les relations d'échelle inhérentes entre la force de liaison des intermédiaires imposent des restrictions sur les performances globales. Ici, il est proposé que des sites FeCo hétérobimétalliques asymétriques rompent les relations d'échelle dans le NRR et stimulent la synthèse d'ammoniac ambiant. Trois nouveautés sont rapportées dans ce travail:

1. Les sites dimères hétéronucléaires FeCo présentant la surface polarisée avec des sites multiélectroniques permettent un affaiblissement de la liaison N≡N et une activation maximisée de N_2.
2. L'optimisation des énergies d'adsorption de certains intermédiaires devient ainsi réalisable, contribuant à réduire considérablement la barrière énergétique du processus global de réduction de l'azote.
3. Comme prévu, le catalyseur de validation de principe offre un taux de rendement en ammoniac supérieur de 70,11 μg h−1 mg−1 avec une efficacité faradique correspondante de 32,16 % à -0,2 V par rapport à une électrode à hydrogène réversible.

Nous avons proposé certaines approches applicables présentées dans les travaux ci-dessus pour améliorer les performances du NRR. Le développement du dopage de l'oxygène en carbone dopé à l'azote en tant qu'hétéroatome secondaire déclencherait un effet de promotion électronique synergique pour stimuler la synthèse de l'ammoniac ambiant, tandis que les sites FeCo hétérobimétalliques asymétriques rompraient les relations d'échelle dans le NRR et stimuleraient la synthèse de l'ammoniac ambiant. De plus, une stratégie de confinement de l'azote obtenue par gravure plasma a été proposée pour relever le défi de l'approvisionnement limité en réactifs pour la réaction de réduction de l'azote dans des conditions ambiantes. Ce travail présente une méthode réalisable pour résoudre l'offre restreinte de réactions

électrochimiques impliquant des gaz. Nous espérons que nos travaux dans cette thèse pourront fournir la plate-forme/informations utiles pour développer de nouveaux catalyseurs efficaces pour le NRR, et contribuer à la synthèse de l'ammoniac avec une conception rationnelle de catalyseurs NRR pour obtenir une esthétique à haut rendement et acceptable par le public. Inspirés par les résultats obtenus dans cette thèse, nous continuerons à l'avenir à étudier en profondeur les stratégies visant à améliorer l'efficacité du NRR.

8.2 Perspectives

Nous avons essayé différentes stratégies pour améliorer l'activité et le taux de production de réduction électrochimique du N_2. Malgré ces progrès significatifs, la sélectivité et l'efficacité du NRR doivent encore être améliorées pour promouvoir des applications pratiques, et les aspects suivants doivent être pris en compte :

(i) Élaborer des protocoles rigoureux pour une détermination précise du NH_3

Actuellement, la quantité de NH_3 produite par le procédé électrochimique NRR est relativement faible et reste au niveau du microgramme. De plus, une éventuelle contamination par NH_3 est généralement présente dans l'atmosphère, les membranes échangeuses d'ions et même l'électrocatalyseur lui-même. En conséquence, la détermination précise du NH_3 produit est assez difficile. Des protocoles rigoureux pour une détermination précise et fiable de NH_3 ont été élaborés, dans lesquels une série d'expériences contrôlées doivent être réalisées dans les conditions suivantes, par exemple sous une atmosphère de gaz Ar, au potentiel de circuit ouvert, en l'absence d'électrocatalyseurs et sous une atmosphère de $^{15}N_2$. atmosphère gazeuse, pour exclure une éventuelle contamination par l'ammoniac. Ce n'est qu'avec ces données fiables que nous pourrons évaluer et concevoir correctement des électrocatalyseurs à haut rendement et faciliter rapidement le développement du NRR électrocatalytique à l'avenir.

(ii) Régulation de l'interface triphasée gaz-liquide-solide

La réduction électrocatalytique du N_2 implique les trois phases gazeuse (N_2), liquide (électrolyte) et solide (catalyseur). Une série de processus comprenant la diffusion et l'adsorption de molécules de N_2, la délivrance de protons et d'électrons et la désorption des intermédiaires N_xH_y et des molécules de NH_3 se déroulent simultanément à l'interface triphasée. Des études antérieures ont révélé que la concentration locale de molécules de N_2 et de protons à proximité de la surface du catalyseur pourrait affecter considérablement le processus d'adsorption du N_2 et des protons, respectivement. À ce titre, davantage d'efforts devraient également être consacrés à l'ingénierie des interfaces couvrant l'électrolyte et l'électrocatalyseur.

(iii) Optimisation des électrocatalyseurs pour améliorer la capacité d'activation vers le N_2

De grands progrès ont été réalisés jusqu'à présent pour augmenter la capacité d'activation des électrocatalyseurs vers N_2, en mettant l'accent sur les défauts, les hétérostructures, les déformations, l'ingénierie de la cristallinité, etc. Cependant, la capacité d'activation des électrocatalyseurs vers N_2 est encore insuffisante, ce qui sert également de un obstacle élémentaire à la synthèse d'ammoniac à haute efficacité dans des conditions ambiantes en raison de la barrière d'activation élevée des molécules de N_2.